PREMELTING AND THE MECHANISMS OF MELTING IN THE ALKALI HALIDES

JEFFERY LEWIS TALLON, B.Sc. (HONS), M. INST. P.

A Thesis submitted in partial fulfillment of the requirements for the degree of Doctor in Philosophy.

DEPARTMENT OF CHEMISTRY

VICTORIA UNIVERSITY OF WELLINGTON

NEW ZEALAND

NOVEMBER, 1976

ACKNOWLEDGEMENTS

It is with pleasure that I wish to thank my supervisors Drs S.I. Smedley and W.H. Robinson for friendly and helpful guidance during the course of this work. I would also like to thank Mr C. Snell of the Chemistry Department, Victoria University for technical assistance and members of the staff of the Physics and Engineering Laboratory (P.E.L.), D.S.I.R. for indispensible service work. Particularly I thank Mr G.D. Walker for the scanning electron microscopy, and Messrs J. Brownlie and T. Ransfield for the photographic work contained herein. I am grateful to Dr M.C. Probine, the Director of P.E.L., and to the Department of Scientific and Industrial Research for allowing this work to be undertaken. Finally, I thank my wife Mary for support and encouragement throughout this work and for carrying out the onerous task of typing the text.

ABSTRACT

An experimental and theoretical study of premelting behaviour and mechanisms of melting in the alkali-halides is presented. Theories of melting and previous premelting experiments are first reviewed, then an elastic strain theory of melting is developed, which includes dilatation and shear contributions to the elastic energy and to the vibrational entropy, as well as a communal entropy and an entropy due to the isothermal expansion on melting. By fitting experimental melting parameters, dislocation-like local strains are implicated. The bulk and shear moduli are shown to be continuous with respect to dilatation through the melting expansion and one of the shear moduli vanishes at the dilatation of the melt at the melting temperature. A modified Born instability theory of melting is thus valid. Premelting rises in the apparent specific heat and electrical conductivity within 6 K of the melting point are studied and are shown to occur at the surfaces only. The use of guard rings to eliminate surface conduction is essential at all temperatures above the extrinsic/intrinsic conductivity 'knee', and electrical fringing must be taken into account for typical specimen sizes. For various surface orientations, the rises in surface conductivity occur at lower temperatures the lower the surface packing density, and for deformed specimens, the greater the deformation. The results are interpreted in terms of an atomic-scale surface melting below the melting point, and a consequent rapid rise in vaporisation rate. A dislocation theory of surface melting, melting and the solid-liquid interface is developed which gives good agreement with experimental values for the melting temperatures and the interfacial energies.

GLOSSARY OF SYMBOLS

A	Electrode area, p. 66, total specimen area, p. 101 ff.
a	Lattice parameter i.e. the cation-cation distance for alkali-halides
a	Facetting parameter, p. 25, radius of cylindrical superheating specimen, Appendix C
A_B	Born-Mayer constant
b	Burgers vector
C	Lindemann constant, p. 8. Constant relating shear and dilatation strain, p. 54 only. Capacitance, Appendix C
C_d	Concentration of gas molecules dissolved in the melt
C_g	Concentration of gas molecules in the gas
C_p	Specific heat at constant pressure
C_v	Specific heat at constant volume
c_{ij}	Elastic modulus reduced matrix elements
D	Separation of wire electrodes, p. 76
d	Diameter of wire electrodes, p. 76. Diameter of a stable dislocation cell, p. 133
$\underset{\sim}{D}$	Electric displacement
e	Electronic charge. Emissivity, p. 101 only
e_i	Shear strains, i = 1,5
$\hat{e}_i$	Rms shear strains
f	Atomic force constant for the unstrained lattice
f_{kk}	Diagonal elements of the dynamical matrix
G	Electrical conductance. Free energy
G^*	Free energy of a critical surface island
g	Gruneisen parameter
G_{eff}	Effective activation energy for dislocation pair formation
$g_s(j)$	Shear frequency modulation parameters
g_β	Gruneisen type parameter for the dilatation dependence of β
g_μ	Gruneisen type parameter for the dilatation dependence of μ
$g_{\mu'}$	Gruneisen type parameter for the dilatation dependence of μ'

H	Enthalpy
H_{eff}	Effective activation enthalpy for vaporisation at T_m
h_s	Surface enthalpy
J	Vaporisation flux
J_p	Saturated vaporisation flux
k	Boltzmann's constant
l	Subscript or superscript denoting melt or liquid
M	Molecular weight
m	Subscript denoting the melting point, otherwise specimen mass
n	Number of ion-pairs in a surface island
N^*	Critical number of ion-pairs on a surface
n^*	Critical number of ion-pairs in a surface island
$\underline{\hat{n}}$	Unit vector in the surface plane normal to a dislocation line
n_d	Dislocation density
N_o	Avogadro's number
P	Power density in the superheating specimen, p. 82 and Appendix C only. Elsewhere, ambient gas pressure
R	Gas constant
r	Particle radius or radial co-ordinate
R_c	Dislocation cut-off radius
r_c	Frank's dislocation core radius, Appendix E
r_d	Constant with dimensions of distance, eqn. E4
r_l	Radius of a curved liquid-vapour interface
r_m	Constant with dimensions of distance, eqn. E4
r_{sl}	Radius of a curved s-l interface
r_o	Radius of the first minimum in the ionic pair potential, p. 6, elsewhere the core radius of a dislocation
r_∞	Radius of a molten dislocation core
r^+	Cation radius
r^-	Anion radius
S	Surface charge density, or, entropy
s	Subscript or superscript denoting solid
S_c^s	Dislocation core entropy for the slip system, s

S_{conf}	Configurational entropy
S_{ie}	Entropy of isothermal expansion
S_l	Entropy of the melt
S_s	Entropy of the solid
s_s	Surface entropy
S_1	Constant defined in eqn.(6.3), p. 104
S_2	Constant defined in eqn.(6.5), p. 106
T	Temperature (K)
T_b	Boiling temperature
T_c	Critical Temperature
T_d	Melting temperature from dislocation theory
T_L	Lindemann instability temperature
T_m	Melting temperature
T_{sm}	Surface melting temperature
t	Separation of electrodes,p.66, thereafter, time.
U	s-l interfacial velocity p.82 only, elsewhere the energy of a dislocation
U_{am}	Binding energy of an adsorbed monomer
U_c	Core energy of a dislocation
U_e	Elastic energy of a dislocation
V	Molar volume
v	Total specimen volume
V_l	Molar volume of the melt
v_p	Volume of a dislocation melt pit
$V(r,\theta)$	Local potential in cylindrical co-ordinates
V_s	Molar volume of the solid
V_l^*	Molar free volume of the melt
V_s^*	Molar free volume of the solid
V_o	Applied voltage
W	Strain energy density
W_δ	Dilatation contribution to the strain energy density
W_e	{100} shear " " " " " "
$W_{e'}$	{110} " " " " " " "
x	Cartesian co-ordinate
y	" "
z	" "

α	Proportion of solid-like degrees of freedom in the theory of significant structures, p. 14. Half angle subtended by uncoated area of cylindrical superheating specimen, p. 82 and Appendix C.
α_v	Coefficient of volume thermal expansion
β	Bulk modulus
β_{ad}	Adiabatic bulk modulus
β_{is}	Isothermal bulk modulus
β_o	$\beta(\delta=0)$, p. 51.
γ	$a/2\rho_B$, p. 46 and Appendix A
γ_d	Estimate of γ_{sl} from dislocation theory
γ_l	Liquid-vapour interfacial free energy
γ_M	Molar s-l interfacial free energy, p. 159
Γ_p	Number of planes cut perpandicularly by a dislocation per unit length of dislocation
γ_s	Solid-vapour interfacial free energy
γ_{sl}	Solid-liquid interfacial free energy
γ'	$(1+\delta)^{\frac{1}{3}}\gamma$
γ_δ	Surface step free energy
δ	Dilatation
$\overline{\delta}$	Mean dilatation
$\hat{\delta}$	Rms dilatation
ΔH_m	Enthalpy of melting
ΔH_s	Enthalpy of sublimation
ΔH_v	Enthalpy of vaporisation
ΔJ	Premelting increment in vaporisation flux
δ_m	$\Delta V_m/V_m$
$\Delta_m T$	$T_m - T$
$\Delta_m T_R$	Raoult depression of melting point
$\Delta_m T_{sm}$	$T_m - T_{sm}$
ΔS	Change in entropy
ΔS_m	Entropy of melting
ΔS_{vib}	Change in vibrational entropy
ΔT	Temperature difference between specimen and specimen chamber
ΔT_{lin}	ΔT below the premelting region
ΔT_{ss}	Steady state temperature increase in internally heated specimen
ΔV_m	Change in molar volume on melting
$\Delta\mu_l$	Change in chemical potential of the melt

$\Delta\mu_s$	Change in chemical potential of the solid
$\Delta\nu_i$	Change in normal mode lattice frequency
ϵ_{ij}	Strain tensor
η	Number of dimensions of the local melt strain, $\eta = 2$ or 3
η_m	Viscosity of the melt
Θ	Time constant for the temperature rise in the internally heated specimens
θ	Angular co-ordinate
Λ	Ion-pair area
λ	Length of wire electrode, p. 73. Lagrange multiplier, Appendix C
λ_o	Atomic jump distance, p. 82
λ_1	Length of specimen electrode, p. 66
λ_2	Breadth of specimen electrode, p. 66
μ	Shear modulus, c_{44}
μ'	Shear modulus, $\frac{1}{2}(c_{11} - c_{12})$
μ_e	Effective shear modulus for an edge dislocation
μ_s	Effective shear modulus for a screw dislocation
μ_o'	$\mu(\delta=0)$, p. 54
μ_o'	$\mu'(\delta=0)$, p. 57
ν	Poisson's constant
ν_E	Einstein frequency
ν_i	Normal mode lattice frequency
ξ	Core energy factor
ρ	Lindemann fraction of the lattice parameter, p. 8, mass density thereafter until Appendix E where it is the radius of the bottom of a dislocation melt dimple
ρ_B	Born-Mayer repulsion distance
ρ_l	Mass density of the liquid (usually at T_m)
ρ_s	Mass density of the solid (usually at T_m)
Σ	Shape factor, p. 146
σ	Electrical conductivity
σ_B	Stefan-Boltzmann constant
σ_{ij}	Stress tensor
τ	Thickness of the premelting surface layer

Υ The equilibrium number of surface islands of critical size

ϕ Interionic potential

Φ_m Cosine coefficients of the potential expansion, Appendix C

ϕ_m Sine coefficients of the potential expansion, Appendix C

χ Compressibility

ψ $A_B \gamma (\gamma - 2) e^{-\gamma}$

ϑ Volume expansion of the core per unit length of a dislocation

$\varkappa$ Mole fraction of impurity

LIST OF TABLES

LIST OF FIGURES

CONTENTS

1 INTRODUCTION

Melting of a crystalline state of matter is classically understood to be a first order phase transition involving an absorbtion of heat and an increase in specific volume with accompanying increase in fluidity and isotropy. The first quantitative measurements of the enthalpy of fusion appear to have been made by Black[1] in 1762 and independently ten years later by Wilcke[2] on the melting of ice, while the effect of pressure on phase changes dates back 100 years earlier to the experiments of Boyle[3] on the boiling of water under vacuum. Yet, in spite of such a prolonged period of intensive study, the mechanism of fusion is not well understood, and to date there exists no theory of melting which accurately predicts the melting parameters solely from the interatomic potentials. This of course arises more from the difficulty in describing the melt than the solid. At the same time, it is well known that the melting parameters[4] provide rudimentary information regarding the structure of the melt. In particular the enthalpy of fusion is smaller than the enthalpy of sublimation by a factor of 20 to 40 for ionic and metallic crystals and of 5 to 10 for molecular crystals, while the change in specific volume may range from 3% to 25% which requires a change in apparent interatomic distance as small as 1 to 8%. Both these results suggest that the melt relates far more closely to the solid than the vapour. This is borne out more decisively by X-ray diffraction which reveals a retention of short range order on melting[5] i.e. the immediate environment of any atom or molecule is little altered by fusion. However, the atomic ordering falls off rapidly to

1 J. Black, Lectures on the Elements of Chemistry 1, Edinburgh 1803, p.166 ff.

2 J.C. Wilcke, K. Svenska Vet. Akad. Handl., 33, 97 (1772).

3 R. Boyle, New Experiments Physico-Mechanicall, etc. Oxford, 1660, p.388.

4 Melting parameters are reviewed and discussed in detail in § 4.

5 For alkali halides see H.A. Levy and M.D. Danford in Molten Salt Chemistry, ed. by M. Blander (Interscience, N.Y., 1964). For metals see B.R.T. Frost "Progress in Metal Physics", ed. by B. Chalmers and R. King, 5, 96, Pergamon, London, 1954. This result was first established by G. Stewart, Phys. Rev., 30, 232 (1927); 31, 174 (1928).

zero over 3 to 4 atom spacings. To these results we may add that the phonon spectra[1], specific heat[2], and thermal conductivity[3] show only small changes on melting. Indeed this is the case with most of the properties which in the crystalline state are termed 'structure insensitive'. On the other hand, very substantial changes do occur on melting in the so called 'structure sensitive' properties such as self diffusion, plasticity and conductivity (in the case of ionic crystals) and it is possibly for this reason that many theories of melting resort to the use of the structural defects which occur in the solid state to characterise the liquid state. There is little justification for many of these models apart from the great simplification in mathematical complexity they afford. These properties which exhibit substantial change on melting trace to a single event the onset of fluidity on fusion or more rigorously the decrease in relaxation time for mechanical shear. This arises from the small increase in specific volume, which, since the repulsion potentials are very short range, decreases the activation barriers for self diffusion, or co-operative flow.

In general, it is assumed that the free energy surfaces of the solid and liquid phases are independent and consequently it must be expected that a potential barrier must be traversed during transformation from one phase to the other. This means metastable solid and liquid states may exist over a finite range above and below the melting temperature, T_m under isobaric conditions, requiring fusion and crystallisation to be described as nucleation and growth processes. Supercooling was discovered early in the quantitative study of heat by Fahrenheit[4] and is of course well known. On the other hand, melting generally occurs with little or no super-

1 A.J. Barker, J. Phys. C: Sol. St. Phys., 5, 2276 (1972).

2 e.g. A.S. Dworkin and M.A. Bredig, J. Phys. Chem 67, 697 (1963).

3 B.R.T. Frost, loc. cit.

4 D.G. Fahrenheit, Phil. Trans., 33, 78, 1724.

heating and only very few instances have been reported of genuine superheatings in excess of 0.2 K above T_m. This raises the question of symmetry in the melting/crystallisation processes, in particular whether the mechanism of melting is identically the mechanism of crystallisation in reverse. Crystallisation is understood to be a heterogeneous atom by atom, plane by plane building process[1]. However, it is easy to conceive that in melting the lattice, due to some instability, transforms homogeneously to the liquid phase. The absence of superheating is claimed as evidence of this. Arguing for symmetry, Tamman[2] takes the view that the rarity of superheating derives from the fact that most melts 'wet' their parent crystals, with the result that melting readily nucleates on the crystal surfaces at T_m. This is indeed borne out by more recent melting experiments on crystals which have high viscosity melts wherein superheatings of 50 K in tetragonal phosphorus pentoxide[3] and up to 300 K in crystalline quartz[4] are accessable. A successful theory of melting must, it would seem, allow a metastable solid phase above T_m and describe the progression of the solid-liquid interface into the solid as a nucleation and growth process.

Finally, we have noted the assumption that the free energy surfaces or Gibb's function surfaces of the solid and liquid phases are independent. Ubbelohde[5] suggests that as the structure of the melt and solid are not greatly dissimilar the two surfaces near T_m may curve towards each other such that they intersect at a reduced angle. This would give rise to premelting and prefreezing effects in a number of properties, certainly including the second intensive derivatives of the Gibb's function: the thermal expansion, specific heat and compressibility. In fact a wide range of precursary effects[5]

1 For reviews of crystallization see R.A. Laudise, J.R. Carruthers and K.A. Jackson, Ann. Rev. Materials Science 1, 253 (1971), and A.A. Chernov, ibid. 3, 397 (1973).
2 G. Tamman, The States of Aggregation, Van Nostrand. N.Y., 1925.
3 R.L. Cormia, J.D. McKenzie, and D. Turnbull, J. Appl. Phys. 34, 2239 (1963).
4 N.G. Ainslie, J.D. McKenzie, and D. Turnbull, J. Phys. Chem. 65, 1718 (1961).
5 A.R. Ubbelohde, Melting and Crystal Structure, Clarendon, Oxford, 1965.

have been reported on both sides of T_m . At the same time, as a number of careful investigations have failed to locate any premelting or prefreezing, the effects are therefore by no means general. The subject of §3 is Premelting and some of these examples will be considered there. Of particular interest to this study however are the premelting rises in ionic conductivity reported by Allnatt and Sime[1] in the case of NaCl and KCl. They obtained reproducible rapid rises in conductivity with effective activation energy ranging about 200 eV for NaCl and about 400 eV for KCl beginning up to 4 K below T_m. The effect was reported as neither impurity nor deformation dependent as no significant alteration obtained for specimens doped to 3×10^{-4} mole % with Sr^{2+} or compressed to 5% strain. It seemed to us that if this were a genuine intrinsic effect precursory to melting, its study might lend some elucidation of the actual mechanism of melting in those crystals. For this reason the present study was undertaken, to give closer examination in the first instance to the premelting conductivity anomaly and also to changes in heat content in alkali halides close to T_m.

Firstly, we review critically theories of melting which have appeared throughout the past 60 years, and observations of premelting phenomena. Then we tabulate the data appropriate to melting of the rock salt structured alkali halides, examine the various contributions to melting parameters and establish some interesting correlations with other properties. Our experimental data on ionic conductivity, differential thermal analysis and an attempt at superheating are presented and finally discussed in the light of possible mechanisms of melting.

1 A.R. Allnatt and S.J. Sime, Trans. Faraday Soc. 67, 674 (1971).

2 THEORIES OF MELTING

In the above brief sketch of some of the more important facets of melting, the similarities between the liquid and parent solid states near T_m were emphasised. However, it would be totally misleading to give the impression that the melt may be viewed simply as a defective form of the high temperature solid. The fact is, that in many respects the liquid state at least qualitatively resembles the gaseous state also. Both are described as fluids, the difference being that a liquid has a free surface; both are isotropic while single crystals are in general anisotropic; both allow their individual atomic or molecular constituents access to the entire fluid volume so that both possess a communal entropy. (This is at least the case in the alkali halides[1]). We might say then that liquids are at once solid like and gas like. Accordingly, the complexities of the liquid state, for the sake of tractability, often have been avoided by modelling on the solid or the gaseous states, more often the former. However, theories of melting of this kind, while instructive, are often physically unconvincing and enjoy only limited success. It seems fair to say that only those theories which see the liquid state as a distinctive state with properties peculiar to that state can have the potential of ubiquitous success. In this section we gather together under various categories some of the melting theories which have been advanced, with a view to assessing which kinds of theory are physically convincing. The usual approach is to divide descriptions of melting and of the liquid state into two groups comprising firstly modelled theories then formal theories. However, we would like to use a higher resolution in our grouping scheme for the purpose of emphasizing the distinctive features of different theories, although some of the theories belong in part to more than one category. Three broad categories are discussed: (i) Phenomenological, (ii) Non-structural and (iii) Structural theories. Within these are firstly two subgroups of non-structural theories namely, Instability and Thermodynamic theories and three subgroups: Lattice model, Statistical geometrical and Statistical mechanical of structural theories. In addition, two

1 L.V.Woodcock and K.Singer, Trans.Faraday Soc.67, 12 (1971).

further general groupings are shown to be necessary, these comprising Homogeneous and Heterogeneous theories. A tabulated summary of our classification is given at the end of this chapter in Table 2.2 on p. 28.

2.1 Phenomenological Theories

These make use of or assume certain correlations between physical properties and melting parameters often by using dimensional arguments or simple generalised macroscopic theory and an example of this is a general elastic strain approach which we develop in § 4. Correlations in physical properties are to be expected as they each have a common ancestry in the atomic potentials. Consequently, such descriptions of melting are often only useful for classifying various kinds of solids and their melts, and at best may provide information regarding the kind of structural model which should be used for a realistic theory. Again we shall see an example of the latter in § 4. The phenomenological description of melting is discussed fully by Ubbelohde[1] and correlations of a wide range of properties to Debye and melting temperatures may be found in a paper by Grimvall and Sjödin[2]. We shall elaborate at this point on only one kind of phenomenological theory, that known as the corresponding states theory. The essential feature of this approach is that the melting parameters of solids of a similar kind may be expected to be in quantitative agreement provided they are reduced in some appropriate manner. Thus e.g. melting temperatures are expressed as reduced dimensionless quantites viz. T_m/T where T is some characteristic temperature such as the critical temperature T_c or an equivalent temperature such as e^2/kr_o in the case of the alkali halides[3], where e is the electronic charge, k Boltzmann's constant and r_o the radial position of the minimum in the ionic pair potential. As first formulated by Pitzer[4] the principle of corresponding states is that the total potential energy of an ensemble of atoms is proportional to the same function of reduced inter-

1 A.R.Ubbelohde,Melting and Crystal Structure,(Clarendon Press, Oxford 1965), p.43.
2 G.Grimvall and S.Sjödin,Physica Scripta 10, 340 (1974).
3 L.V.Woodcock, Proc.R.Soc.Lond. A 348, 187 (1976).
4 K.S. Pitzer, J.Chem.Phys. 7, 583 (1939).

atomic distances for all conformable materials. Where this principle applies reduced melting temperatures, enthalpies and volume changes will be constant within a group. This principle has some degree of success with the inert gases, but for most solids is not applicable.[1] Corresponding states theory has been applied to the alkali halides[2] working from the interionic potentials, however conformality obtains only within subgroups and the overall range of reduced melting temperatures varies by a factor of 1.8. These deviations are explained by Woodcock[3] by developing a first order correction to the conformal potential and thence to T_m. Presumably since the entropies of melting for the alkali halides are fairly constant (see § 4), deviations in the reduced melting enthalpy $r_o \Delta H_m / e^2$ are thus also explained. However, the basic questions of mechanism of melting and how to calculate the absolute T_m remain unanswered by this approach.

2.2 Non-Structural Theories

The non-structural theories which have been applied to the melting process use, in general, macroscopic thermodynamics and often are phenomenological in their application. We may consider two distinct categories, firstly those which invoke some kind of mechanical instability and attempt to locate a critical instability temperature which is equal to, or at least an upper limit to, the melting temperature. The second category encompasses purely thermodynamic theories which are unable to identify absolute values for T_m but at best are able to determine relative shifts in T_m.

2.2.1 Mechanical Instability Theories:

(a) Vibration instability. The regular lattic sites within a crystal are defined internally by the mean positions of the vibrating constituent atoms and as long as the vibrations are small the mean positions are well defined. However, if the crystal temperature is steadily raised the atomic

1 E.A. Guggenheim, J.Chem.Phys. 13, 253 (1945).

2 H. Reiss, S.W. Mayer and J.L. Katz, J.Chem.Phys. 35, 820 (1961).

3 L.V. Woodcock, Proc. R. Soc. Lond. A348, 187 (1976).

vibration amplitudes increase to the stage where it is no longer possible to approximate the motion of one atom as in the potential field of stationary neighbours. Vibrations become increasingly more anharmonic giving rise to a thermal expansion and ultimately the point must be reached where lattice sites lose their definition and we may no longer speak of long range order within the crystal. This is the essential idea behind Lindemann's vibrational theory of melting[1] wherein, according to a more recent version[2] of the theory, melting is assumed to occur when the rms amplitude of thermal vibration reaches a certain critical fraction ϱ of the lattice parameter. The temperature of this instability is given by

$$T_L = C\nu_E^2 V^{\frac{2}{3}} M \quad ; \quad C = 4.2^{\frac{1}{3}} \pi^2 \varrho^2 / 3RN_o^{\frac{2}{3}} , \qquad (2.1)$$

where ν_E is the Einstein frequency of the solid, V the molar volume, M the molar weight, R the gas constant and N_o Avogadro's number. T_L correlates fairly well with T_m with $\varrho = 0.072$ for the metals, in good agreement with X-ray data. Furthermore, the coexistence curve or melting curve giving the pressure dependence of T_m obtained by differentiating (2.1) with respect to volume and using Gruneisen's constant (see §4) is also in reasonable agreement with experimental data.[3] The Lindemann type theories, however, do not explain why a particular value of the vibration amplitude should be critical. In this respect a more plausible theory has been advanced by Ida[4] which shows that anharmonicity arising from an added thermal expansion due to transverse waves causes a maximum to appear in the vibrational energy at a critical temperature, above which the lattice is presumably unstable. However these theories as such do not predict first order transitions at T_L, the Lindemann theory becomes somewhat phenomenological in the important choice of ϱ, and along with all instability

1 F.A. Lindemann, Physik. Z. 11, 609 (1910).

2 J.J. Gilvarry, Phys. Rev. 102, 308 (1956).

3 C.L. Reynolds, K.A. Faughnan and R.E. Barker, J. Chem. Phys. 59, 2943 (1973).

4 Y.Ida, Phys. Rev. 187, 951 (1969).

theories these are incomplete in the sense that they are single phase theories which take no account of the liquid state. Finally, they fail to describe the dynamic character of melting and crystallisation. The most that can be said is that T_L is the maximum upper limit for T_m i.e.

$$T_L \geq T_m \tag{2.2}$$

(b) Elastic instability. Closely related to the Lindemann hypothesis is the elastic instability theory of melting based on the vanishing (or near vanishing) of one of the elastic moduli i.e. the crystal becomes completely soft at some critical temperature. Thermal expansion in solids is accompanied by increasing compressibility χ or a decreasing bulk modulus β and this theory has its origins in the work of Herzfeld and Göppert-Mayer[1] and Frenkel[2] who supposed that at the fusion point $\beta = 0$. A more general theory was presented by Born[3] wherein the free energy was formulated as a function of P, T and 6 strain components, although he did not use the 6 independent strains as we do in § 4. A cubic crystal has 3 independent elastic moduli $\beta = \frac{1}{3}(c_{11}+2c_{12})$ and the two shear moduli c_{44} and $\frac{1}{2}(c_{11} - c_{12})$.[4] For elastic stability each modulus must be positive and non-zero. Born following Brillouin[5] earlier, suggested a more realistic criterion for melting that the shear modulus vanishes in accordance with the common experience that liquids have a finite compressibility but cannot support a shear stress. He selected c_{44} as the appropriate modulus and showed that this modulus decreased first linearly with temperature then increasingly more rapidly, vanishing at a temperature given by an equation of the form of Lindemann's (2.1) differing only in the constant C, which, Furth[6] has shown, is close in value to

1 K. Herzfeld and M. Göppert-Mayer, Phys. Rev. 46, 995 (1934).

2 J. Frenkel, Acta Physicochimica U.R.S.S. 3, 913 (1935).

3 M. Born, J. Chem. Phys. 7, 591 (1939).

4 J.F. Nye, Physical Properties of Crystals (Clarendon Press, Oxford 1957) p.140.

5 L. Brillouin, Phys. Rev. 54, 916 (1938).

6 R. Furth, Proc. Camb. Phil. Soc. 37, 34 (1941).

Lindemann's C. What is evident in the elastic constant data[1] for NaCl type alkali halides, however, is that c_{44} at T_m is not zero and because of its temperature insensitivity would not be near zero until temperatures in excess of 2000 K. Born has chosen $c_{44} = 0$ as his melting criterion but apparently was unaware of the earlier suggestion by Durand[2] that melting might occur when the other shear modulus $\mu' = \frac{1}{2}(c_{11} - c_{12}) = 0$. This criterion gives much more realistic melting temperatures (although admittedly a little in excess of the actual values) and almost exact pressure derivatives of T_m for all the NaCl type alkali halides.[3] Further support for the model derives from theory[4] which shows the acoustic normal mode with modulus μ' becomes unstable under a critical thermal expansion. The stability criterion for the CsCl group of alkali halides appears to be Born's $c_{44} = 0$, and there is a very close correspondence between the instability and melting parameters of LiF and MgO, NaF and CaO, and KF and SrO in accordance with Godschmidt's suggestion[6] of general correspondence between these pairs.

Again, in criticism of the instability hypothesis, it is a single phase theory, the transition is not first order and marked pretransition behaviour would occur over a broad temperature range. Therefore we may not equate the critical temperatures T_c with melting temperatures T_m. However, there is much evidence which attests the close relationship between the two and possibly T_c does not much exceed T_m, premelting in some cases being the precursor to instability rather than to melting. This is essentially the conclusion of Fritsch and Lüscher[7] from careful premelting thermal and electrical

1 R.F.S. Hearmon in Landolt-Bornstein New Series, Group III, Vol. 1 (Springer-Verlag, Berlin, 1966).

2 M.A. Durand, Phys. Rev. 50, 449 (1936).

3 I.N.S. Jackson and R.C. Liebermann, J.Phys.Chem.Solids 35, 1115 (1974).

4 J.H.C. Thompson, Phil. Mag. 44, 131 (1953).

5 O.D. Slagle and H.A. McKinstry, J. Appl. Phys. 38, 451, (1967).

6 V.M. Goldschmidt, Ceram. Abstracts 6, 308 (1927).

7 G. Fritsch and E. Lüscher, Phys. Rev. B4, 3292, (1971).

conductivity studies of sodium. We shall show in §4 how many of these difficulties can be removed by modifying just one detail of the instability hypothesis. It is pertinent to add that Kirkwood and Boggs[1] found a stability limit for the liquid state based on loose packing of hard spheres. Whether this corresponds to the freezing point or is just the lower limit for the freezing point is not, however, clear.

2.2.2 Thermodynamic theories.

(a) Surface theories. In contrast to the above essentially homogeneous theories of melting, the theories of Tammann and Stranski viewed melting as a surface process. Tammann[2] considered that all crystal surfaces were wettable by their own melt and that the melting of crystals proceeded as a dissolution of the crystal in its own melt, commencing at the surface. Because of the wetting condition

$$\gamma_s > \gamma_l + \gamma_{sl} , \qquad (2.3)$$

where the gammas are the specific surface free energies, the free energy surfaces for the solid and liquid states in the vicinity of a crystal surface intersect prior to the bulk melting point so that the surface melts prematurely and superheating is impossible. The latter statement is certainly borne out by general experience. This view finds its origins at least as early as 1859 when in order to explain the sintering of ice Faraday[3] proposed that for some degrees below 0 °C a liquid-like layer exists on the surface of ice, although the theoretical basis for surface melting of ice was not established until more than 100 years after.[4] Then somewhat later in 1881 Poynting[5] raised the question as to whether the melting point of a substance would differ if the freshly formed melt were to be removed as quickly as it was formed. Tammann's ideas were consolidated by subsequent experiments by Volmer and Schmidt[6] on Hg and Ga which showed that in fact not all

1 J.G. Kirkwood and E.M. Boggs, J.Chem.Phys. 10, 3942).
2 G. Tammann, Z. physik. Chem. 68, 205 (1910).
3 M. Faraday, Phil. Mag. 17, 162 (1859).
4 N. Fletcher, Phil. Mag. 18, 1287 (1968).
5 N. Poynting, Phil. Mag. 12, 32 (1881).
6 M. Volmer and O. Schmidt, Z. physik. Chem. B 35, 467 (1937).

surfaces were completely self wettable and those which were not could be superheated. Stranski[1], employing considerations of matching the less dense melt with the crystal at the solid-liquid interface, developed this viewpoint with the idea that it is the close packed surfaces which are least wettable, and which retain facets in the high temperature equilibrium shape of the crystal. Less densely packed surfaces tend to become rounded at high temperature and near the melting point a quasi-liquid layer should form across the surface, becoming increasingly thicker as T_m is approached. We may supplement these ideas with the observation that at T_m the thickness of the surface melt will be such that the solid-liquid interface is just 'unaware' of the presence of the external surface. Surface effects in solid alkali halides disappear at a depth of 2 cation-anion spacings under a (100) surface, 4 spacings under a (110) and 6 spacings under a (111) surface[2], while in the melt, periodicity in the radial distribution function is fully damped at $\sim$ 4 spacings[3]. We might expect then that the quasi-melt layers at T_m have depths $\sim$ 3, 4 and 5 cation-anion spacings on the (100), (110) and (111) surfaces respectively. Considerations of surface free energy have become very important in the study of crystallisation but curiously tend to be overlooked in the reverse process of melting. We shall return to this very important topic of surface melting later in this chapter. In the context of the kinetics of crystallisation, the concept of the interfacial tension γ_{sl}, or more correctly the interfacial free energy of the interface between the solid and liquid phases, has become of paramount importance.[4] The existence of metastable supercooled (and sometimes superheated) states make it clear that there is a nucleation barrier to the new phase and the new phase must grow into the old phase. This barrier is the interfacial free energy, and normally in a freezing liquid it is traversed at only small supercoolings by heterogeneous nucleation at strained sites such as impurities or the surface of the containing vessel. Under special

1 I.N. Stranski, Naturwissenschaften 28, 425 (1942).

2 D.E. Parry, Surface Sci. 49, 433 (1975).

3 L.V. Woodcock and K. Singer, Trans. Faraday Soc. 67, 12 (1971).

4 D. Turnbull, Phase Changes, in Solid State Physics, ed. by F. Seitz and D. Turnbull, (Academic Press, N.Y.) 3, 225 (1956).

circumstances e.g. when the liquid is in the form of very small droplets lying on clean amorphous substrates, there are no preferred nucleation sites and large supercoolings are possible. Here nucleation occurs when by thermal fluctuations sufficiently large spherical regions of the new phase occur for the decrease in volume free energy to just offset the increase in surface interfacial free energy. Once critical nuclei form they may grow rapidly, so that for growth, nucleation should be the rate controlling step. This is the basis of the Volmer-Weber-Becker-Doring (VWBD) theory of nucleation and growth[1], and has been used by Turnbull[2] to determine γ_{sl} from the homogeneous nucleation temperatures for metals and more important to the present work by Buckle and Ubbelohde[3] for the alkali halides. These are listed later in Table 4.1. γ_{sl} is also important in the depression of equilibrium melting temperature for very small particles[4]. If we imagine a particle to have a molten surface layer, as the radius r decreases the relative contribution of γ_{sl} to the molar free energy increases and T_m falls proportionate to r^{-1}. The effect is observable for particles less than 100 nm in diameter and the radius dependence becomes a little more complex below 10 nm. [5] A similar effect results for the melting point of substances in capillaries and of course if the solid-liquid interface is concave T_m is increased. As a final reference to the use of γ_{sl} in theories of melting we recall Frenkel's theory of heterophase fluctuations[6] in which a distribution of embryos or micro-regions of the new phase are formed near T_m by thermodynamic fluctuations. These supposedly grow in volume at the expense of the old phase as T_m is approached and beyond T_m regions of the old phase diminish. It is claimed[7] that premelting and prefreezing phenomena may

1 ibid.

2 D. Turnbull, J. Appl. Phys. 21, 1022 (1950).

3 E.R. Buckle and A.R. Ubbelohde, Proc. Roy. Soc. A 261, 197 (1961).

4 H. Reiss and I.B. Wilson, J. Colloid Sci. 3, 551 (1948).

5 C.R.M. Wronski, Brit. J. Appl. Phys. 18, 1731 (1967).

6 J. Frenkel, J. Phys. 1, 315 (1939).

7 A.R. Ubbelohde, Melting and Crystal Structure, loc. cit.

find their explanation in this theory. However it is apparent that the theory is little different in principle from the above nucleation theory which, rather than predicting precursors to the melting or freezing transition, actually postpones the transition. γ_{sl} raises the free energy of melt embryos in the solid and of solid embryos in the melt so that both are unfavourable fluctuations, and since the homogeneous nucleation transitions occur over a very small temperature range no premelting or prefreezing behaviour can result.

(b) Bulk theories. Some bulk non-structural theories of melting have appeared e.g. Fritsch[1] has used the Landau model[2] of second order transitions which differentiates between the free energies of two phases by a function of long range order, and by including a function of short range order obtained a system which exhibits a melting point and an instability point. Common to many of this kind of theory is the inability to predict absolute values for T_m, and the approach often becomes basically phenomenological. This is not the case however for the theory of significant liquid structures as developed by Eyring and co-workers[3]. Although in its detail this theory is an extension of the hole theory discussed as a structural theory in § 2.3 (i), the essential feature is that a liquid is envisaged as comprising proportions α of solid-like and $(1-\alpha)$ of gas-like degrees of freedom. Liquid properties are estimated, surprisingly accurately, as averages of the solid and the gas properties, weighted in those proportions, without necessarily any considerations of structure. The rationale for this simplistic view is that vacancies within the liquid will tend to behave much as molecules in a gas, in the same way that holes in the valence band of a metal correspond to electrons in the conduction band, or holes in negative energy space are equivalent to elementary particles in Dirac's theory of matter. By formulating the partition function for the liquid as a weighted product of solid and gas partition functions a range of prop-

1 G. Fritsch, Phys. Stat. Solidi, 31, 107 (1975).

2 L.D. Landau and E.M. Lifshits, Course of Theoretical Physics 5 (Pergamon, London), chapter 14.

3 H. Eyring and R.P. Marchi, J.Chem.Edu. 40, 562 (1963); H. Eyring and M.S. Jhon, Significant Liquid Structures (Wiley, N.Y. 1969).

erties from melting parameters, thermodynamic and transport properties to the dielectric constant of liquids can be accurately characterised. The shortfall of this approach and even more so of the lattice model approach summarised in the next section is the assumption of solid-like structure in a substantial proportion of the liquid. While the average radial distribution function and average co-ordination number suggest this is an approximation which is not unreasonable, however, the instantaneous structure revealed by Monte-Carlo computations shows a large degree of irregularity at all points in the liquid, some molecules being virtually unco-ordinated. This is particularly well displayed by a model constructed by Woodcock[1] from an instantaneous configuration of KCl melt near its triple point. Nevertheless, in terms of quantitative results, the significant structures theory is probably the single most successful and at the same time simple theory to have been applied to melting and the liquid state.

2.3 Structural Theories.

We consider three kinds of structural theories of melting which range in their paradymes from the solid to the gaseous states: (i) lattice (ii) statistical geometrical and (iii) statistical mechanical.

2.3.1 Lattice Theories. These attempt to represent the melt structure as a modification of the structure of a perfect crystal. The isotropy of the liquid state together with the similarity between X-ray diffraction patterns of liquids and their powdered solids suggests the analogy between a melt and its very finely powdered parent crystal. A model of this kind was suggested by Stewart[2] who proposed to describe a liquid as having 'cybotactic regions' of perfect crystallites each separated by thin amorphous layers. Later Gurney and Mott[3] elaborated this view using more familiar terms to

1 L.V. Woodcock, Nature Physical Science 232, 63 (1971).
2 G.W. Stewart, Rev. Mod. Phys. 2, 116 (1930).
3 R.W. Gurney and N.F. Mott, Trans. Faraday Soc. 35, 364 (1939).

describe a liquid as a limiting form of a polycrystalline solid with very small grain size, the enthalpy of melting ΔH_M being identified with the grain boundary energy. The latter may be expressed in terms of the shear modulus μ and attention was drawn[1] to the correlation between μ and ΔH_M. Various claims to priority exist for a vacancy or hole model of fusion[2] which in its simplest form views the melt as a solid with a large density of vacancies. This appears to have been suggested first by Frenkel in 1926. The error in this simplistic view is that it presupposes the existence of a lattice with long range order, the very thing that is lost on melting. A rather more plausible approach was initiated by Lennard-Jones and Devonshire[3] using a point defect structure which allows loss of long range order, that of interstitials as well as vacancies. They propose that in a fcc crystal there are two sets of lattice sites of interest: those occupied by the atoms and those defined by interstitial sites, which at low temperature are completely vacant but as temperature rises become increasingly occupied after the fashion of a Bragg-Williams[4] order-disorder transition. Under the assumption that the interaction energy of atoms on adjacent lattice and interstitial sites decreases with increase in volume of the system, they showed that a first order transition identifiable with melting occurred. Above T_m each of the two lattices have equal random occupancy with the result that long range order is absent while short range order is still retained but with a decrease in co-ordination number. This is at least in good qualitative agreement with melt structure. Quantitatively, predicted values of T_m and $(V_l - V_s)/V_s$ are reasonably accurate for a number of gases and Lindemann's formula is predicted. More recently[5] under the assumption that the interaction energy maximises at low volume, this theory has been

1 J.K. MacKenzie and N.F. Mott, Phys. Soc. Proc. 63, 411 (1950).

2 J. Frenkel, loc.cit., p.176; H. Eyring, J.Chem.Phys. 4, 283 (1935); W. Altar, J. Chem. Phys. 5,577 (1937); R. Furth, L.S. Ornstein and J.M.W. Milatz, Proc.Amst.Acad.Sci. 42,107 (1939).

3 J.E. Lennard-Jones and F. Devonshire, Proc. Roy. Soc. Lond. A169, 317 (1939); A170, 464 (1939).

4 W.L. Bragg and E.J. Williams, Proc. Roy. Soc. A145,699 (1934).

5 T. Yoshida and H. Okamoto, Prog. Theoret. Phys. 45,663 (1971).

used to explain the maximum observed in the melting curves of a number of substances at high pressures[1].

An important development of the lattice models is the cell model[2] which abandons the regular lattice but requires molecules to be confined for much but not all of the time in a cell volume delineated by its neighbours. Subject to this constraint, the liquid molecules are treated much as though they were an ideal gas with the result that a 'communal' entropy R appears on melting. Adding to this entropy that due to the isothermal expansion of free volume on melting Hirschfelder et al[2] obtain values of ΔS_M in reasonable agreement with experimental values, however other contributions such as vibrational entropy are not considered and in the mathematical and conceptual development rather arbitrary approximations are made.

So far we have considered point and surface (grain boundary) defect melting theories, and linear defects such as dislocations also have not escaped the attention of those interested in the melting process. A dislocation is a source of shear and it is by virtue of these that crystals deform plastically under external shear stresses. The importance of shear in melting has already been emphasised and it is the opinion of many researchers that the numerous factors involved in melting are best explained using a dislocation model. Rothstein[3] first drew attention to the possibility that the increase in free volume for a given expenditure of formation enthalpy is far greater for a single dislocation than for a distribution of isolated vacancies. This co-operative effect should at a suitably high temperature lead to a rapid spontaneous formation of dislocations with an accompanying loss of shear resistance tantamount to melting. As grain boundaries may be resolved into arrays of dislocations, the cybotactic theory (of Stewart, and Gurney and Mott) may be considered to be a special case of the dislocation theory. The detailed calculations appropriate to this model were performed by Mizushima[4] by setting up the free energy function for an

1 e.g. F.P. Bundy, J. Chem. Phys. 38, 618 (1963).
2 J. Hirschfelder, D. Stevenson and H. Eyring, J. Chem. Phys. 5, 896 (1937).
3 J. Rothstein, J. Chem. Phys. 23, 218 (1955).
4 S. Mizushima, J. Phys. Soc. Japan 15, 70 (1960).

array of dislocations including the long range elastic and core energies and the configurational and vibrational entropies as functions of the dislocation density, n_d. Up to a certain temperature, the equilibrium value of n_d is zero, and above that temperature n_d assumes its maximum value where adjacent dislocation cores are just touching such that the long range elastic stress fields cancel. The enthalpy of melting given by the dislocation core energy agrees with the measured value fairly satisfactorily for a number of metals.

A rather more rigorous formulation of the dislocation model was subsequently presented by Ookawa[1] in terms of the partition function for a dislocated lattice using in particular an anharmonic shear frequency modulation parameter analagous to the Gruneisen parameter for dilatation. The theory is however limited by the assumption of a regular periodic dislocation array and a uniform state of shear. These assumptions are made for the sake of mathematical tractability, however Bernal has emphasized the importance of variability in co-ordination (and hence shear) as a fundamental characteristic of the liquid state.

Still later, using a very simple and admittedly incomplete model, Kulmann-Wilsdorf[2] discussed a wide range of physical implications of the dislocation theory deriving a number of well known phenomenological relationships including, again, Lindemann's law. It has become quite apparent by now that almost any theory of melting would seem to roughly predict melting parameters as well as phenomenological laws (particularly Lindemann's). Doubtless, this is because some of these relationships can be derived by dimensional considerations and because of the ubiquitous influence of the force constants in physical properties. One learns therefore to regard agreement between melting theories and experiment with some caution. The dislocation model however is compelling both in its implications and simplicity. The long range stress field of a dislocation which must be cancelled by adjacent

1 A. Ookawa, J. Phys. Soc. Japan 15, 2191 (1960).

2 D. Kulmann-Wilsdorf, Phys. Rev. A 140, 1599 (1965).

dislocations provides a nucleation barrier so that the kinetic aspects of melting are successfully represented and the important solid-liquid (s-l) interfacial free energy is calculated[1] as one half the free energy of a dislocation sub-grain boundary since such a boundary may be interpreted as two s-l interfaces back to back. These estimates agree remarkably closely to the values of γ_{sl} determined by Turnbull[2] from homogeneous nucleation experiments for 18 different metals. Also, as the nucleation of fresh melt is probably via glide and multiplication of dislocations the rarity of superheating is attributed to the universal presence of isolated dislocations in crystals which would act as nucleation sites. It may be significant that gallium which can be grown relatively dislocation-free can be superheated by small amounts. Finally, Kotzé and Kulmann-Wilsdorf[3] have computed radial correlation functions of metallic melts using two models suggested by the dislocation theory: one of planar glide where order is retained on the glide plane, and pencil glide where order is retained along rows in the slip direction. Agreement with experimental correlation functions is best using the former model for f.c.c. metals which show pronounced planar glide in the solid state, and using the second model for b.c.c. metals which in their solid state show pencil glide. A strong link therefore exists between the liquid structure and the dislocated solid structure.

A rather different approach has been extensively employed by Cotterill and coworkers[4] using molecular dynamics computer experiments on melting. They find a liquid-like pair distribution function appearing at a critical temperature in which the structure is characterised by Shockley partial dislocation loops on close packed planes. The

1. I.A. Kotzé and D. Kulmann-Wilsdorf, Appl. Phys. Letters 9, 96 (1966).

2 D. Turnbull, J. Appl. Phys. 21, 1022 (1950).

3 I.A. Kotzé and D. Kulmann-Wilsdorf, Phil. Mag. 23, 1133 (1971)

4 R.M.J. Cotterill, E.J. Jensen and W. Damgaard Kristensen, Phys. Lett. A 44, 127 (1973); Phil. Mag. 27, 623 (1973); 30, 229 (1974); 30, 245 (1974).

equivalent of premature surface melting, discussed above, was demonstrated by showing that a thin crystal consisting of 6 layers melted at a temperature 4% lower than the bulk melting temperature.[1]

2.3.2 Statistical geometrical theory of melting.

Crystals are characterised by close regular packing of the constituent atoms in general in a manner which 'fills space'. Frank[2] suggested that the packing in liquids may possess basic units which are not space-filling e.g. in hcp crystals there are 12 first co-ordinated atoms so that the appropriate liquid co-ordination may be 12 atoms at the vertices of a regular icosahedran which is a non space-filling unit. This may account for the increase in free volume on melting but does not deal with the essential irregularity of packing in liquids.

Bernal[3] has been accredited with pioneering a geometrical approach to the study of liquids which draws attention to the coherent but irregular packing and variability in co-ordination of atoms in liquids. In fact, some of the important features were examined much earlier both analytically and by model making. Morrell and Hildebrand[4] examined the loose packing of hard gelatin spheres suspended in a liquid of the same density and found radial distribution curves rather similar to those found by X-ray diffraction of liquids. Then Kirkwood and Boggs[5] presented an approximate theory of three-dimensional loose packing of hard spheres which gave a liquid-like radial distribution function (rdf) and above a critical maximum density the rdf became undamped as for a crystal with long range order. The critical density therefore resembles the melting point and interestingly this density is less than that for close packing, indicating the essential discontinuity of melting.

1 R.M.J. Cotterill, Phil. Mag. 32, 1283 (1975).

2 F.C. Frank, Proc. Roy. Soc. A215, 43 (1952).

3 J.D. Bernal, Nature 183, 141 (1959); Proc. Roy. Soc. A280, 299 (1964); J.D. Bernal and J. Mason, Nature 188, 910 (1960).

4 W.E. Morrell and J.H. Hildebrand, J. Chem. Phys. 4, 224 (1936).

5 J.G. Kirkwood and E.M. Boggs, J.Chem.Phys. 10, 394 (1942).

Bernal, in the absence of an exact mathematical formalism, which he described as statistical geometry, resorted to examining compressed irregular stacks of plasticene balls and ball bearings.[1] Three important features consistently revealed themselves. The already mentioned variation in first co-ordination, the preference for surface co-ordination of 5 (as shown by the predominance of pentagonal faces on the compressed plasticene balls), and the impossibility of obtaining densities intermediate between those for long range order and for closest packed disorder. The last point explains the physical necessity for melting to be a first order transition and precludes the possibility of critical melting.

An interesting relationship with the dislocation melting theory is obtained by Pang, Franklin and Miller[2] who find that close packed planes become warped sheets in random packing as predicted by the planar glide dislocation model.[3] Unfortunately, Bernal's approach suffers from the lack of exact mathematical procedures for analysing random packing, particularly at high densities, but is important as it points up the need to discuss liquids in terms of their own intrinsic properties rather than those of solids or gases.

2.3.3 Statistical mechanical theories of melting. These find their origins in the success of the van der Waals equation of state in the kinetic theory of gases and particularly in the theory of dense gases. The basic difference however of a liquid from a gas is the multiple correlations or interactions between a molecule and its neighbours and the lack of a concept of a molecular free path. Thus various approximations were required to extend the dense gas theory to apply to liquids. The earliest and most successful of such theories are due to Kirkwood and Munroe[4] and Born and Green[5] although their approximations and particularly the

1 See also G.D. Scott, Nature 188, 908 (1960).

2 T.W.S. Pang, U.M. Franklin and W.A. Miller, Mat. Sci. Eng. 12, 167 (1973).

3 I.A. Kotzé and D. Kulmann-Wilsdorf, Phil. Mag. 23, 1133 (1971).

4 J.G. Kirkwood and E. Monroe, J.Chem.Phys. 9, 514 (1941).

5 M. Born and H.S. Breen, Proc. Roy. Soc. A188, 10 (1946); A189, 103 (1947).

manner in which irreversibility is introduced are open to question. These and other like theories are well reviewed by Green.[1]

We may add to these theories a special class of computation: the molecular dynamics (MD) and Monte-Carlo (MC) computer studies which, given the interatomic potentials, identify allowable displacements of atoms and thus simulate the evolving kinetic behaviour of ensembles of atoms. We have already referred to the MD studies of dislocation generation at T_m by Cotterill and shall have occasion to refer to the MC studies by Woodcock and co-workers on the melting of alkali halides.[2] The latter have provided melting data very close to experimental values and furthermore have provided values of some parameters which are not accessible by experiment. However, these studies are classified as experiments rather than theories as they contain no analytical formulation of the statistical, kinetic and co-operative behaviour of the atoms.

The last theoretical approach to melting we shall discuss here is one which has recently given successful results for the melting of simple metals by the use of variational principles to calculate the solid and liquid free energies. Stroud and Ashcroft[3], using known pseudo-potentials for Na, set up general solid and liquid free energies which were evaluated by minimising the free energy with respect to each phonon frequency. The melting curve thus obtained is in reasonable agreement with experiment, and along the curve the rms displacements in the solid were virtually constant, thus verifying Lindemann's law. In the melt the effective hard sphere packing fraction was constant along the curve, giving what they call an analog to the Lindemann law for the liquid

1 H.S. Green, The Structure of Liquids, in Handb. der Physik, ed. by S. Flugge (Springer-Verlag, Berlin 1960).

2 L.V. Woodcock and K. Singer, loc. cit.

3 D. Stroud and N.W. Ashcroft, Phys. Rev. B 5,371 (1972).

state.

We have now reviewed the main kinds of melting theories, in detail where the theory particularly applies to the remainder of this work. Where we have been very brief, we have done so because there exists a thorough review in that area which is referred to. The remainder of this chapter will be devoted to emphasizing one further important classification of melting theories.

2.4 Heterogeneous Theories of Melting.

When considering surface thermodynamic theories in § 2.2, attention was directed to the need to describe the onset of melting as a nucleation problem and the development of melting as interfacial growth. This is demonstrated most clearly by the ability to cause the s-l interface to oscillate by thermal cycling[1] and the ability to superheat the relatively defect free interior of a crystal when internally heated[2], indicating the existence of a nucleation barrier to melting. McKenzie, Turnbull and others[3,4] showed that quartz, cristobalite and phosphorus pentoxide could be superheated (by up to 300 K above T_m for the first, and 40 K to 50 K above T_m for the second two) by virtue of the high viscosity of their melts and the consequent slow movement of the s-l interface. Even at the highest superheatings, melting began at surfaces and grain boundaries but never in the crystal interior. The weight of experimental evidence therefore appears to suggest that melting must be seen as a heterogeneous process and homogeneous theories of melting such as the instability theories are unacceptable or must be modified. The actual structure of the s-l interface and indeed of the crystal surface thus become important in the theory of melting and crystalisation. These have been well

1 J.J. Kramer and W.A. Tiller, J.Chem.Phys. 37, 841 (1962).

2 S.E. Haykin and N.P. Benet, C.R. (Doklady) Acad. Sci. URSS 23, 31 (1939).

3 N.G. Ainslie, J.D. McKenzie and D. Turnbull, J. Phys. Chem. 65, 1718 (1961).

4 R.L. Cormia, J.D. McKenzie and D. Turnbull, J. Appl. Phys. 34, 2239 (1963).

studied[1] although largely from the point of view of growth of crystals from melt, vapour or solution rather than melting. Three types of interfaces obtain[2], namely singular which are atomically smooth or facetting, non singular which are atomically rough, and where a surface or interface is misoriented to a low index crystallographic plane and therefore consists of a sequence of singular terraces separated by steps, vicinal.

The statistical thermodynamics of surfaces was first presented by Burton, Cabrera and Frank[3] as a classical two dimensional co-operative problem using the exact Onsager solution for the two level case and the Bethe approximation for the multi level case. The picture that emerges is that at low temperatures low index faces are singular while above a transition temperature T_c those faces become non-singular i.e. they contain a high density of adatoms, holes, kinks on ledges etc. For the close packed surfaces in which interactions between atoms are dominated by nearest neighbour interactions T_c may exceed T_m and certainly is greater than the value of T_c for the less densely packed surfaces where next nearest neighbour interacrions are also important. This agrees precisely with Stranski's non-structural view of surface melting already elaborated in § 2.2.

Gurney[4] independently proposed a different model of surface melting to explain the high mobility found on surfaces. He suggested that the increased chemical potential in surface regions would cause a diffusion of molecules away from these regions leaving vacancies behind, ultimately to the extent that the density of vacancies would be sufficient to cause the surface to melt. The surface tension of the melt on the solid would be just such that the chemical potentials of

1 D.P. Woodruff, The Solid-Liquid Interface (Cambridge University Press 1973).

2 N. Cabrera, Trans. Faraday Soc. 55, 16 (1959).

3 W.K. Burton, N. Cabrera and F.C. Frank, Phil. Trans. Roy. Soc. A243, 299 (1951).

4 R.W. Gurney, Proc. Phys. Soc. 62, 639 (1949).

surface molecules and bulk molecules could be equated.

The structure of the s-l interface was worked out by Jackson[1] as a two level problem using the Bragg-Williams approximation. His results are expressible in terms of a parameter α given by

$$\alpha = (\eta_1/\nu)(L_o/kT) \quad , \qquad (2.4)$$

where L_o is the change in internal energy between bulk solid and bulk liquid, η_1 is the number of nearest neighbours in the plane of the interface and ν is the total number of nearest neighbours in the crystal bulk. When $\alpha \leq 2$ the interface is completely rough and interface movement may readily take place at any point on its surface, while for $\alpha > 2$ the interface is singular so that it may progress only by two dimensional nucleation and is therefore much slower moving and cannot move until a critical supercooling or superheating is reached. (We note in passing that a growing singular surface may avoid two dimensional nucleation by growing on the ledge of a spiral about a screw dislocation existing on the surface[2]. However, such a surface strictly is vicinal rather than singular). Table 2.1 lists values of α calculated for the alkali halides at their melting points for the three lowest index planes and it appears that the sodium and potassium salts and possibly RbCl may facet on (100) near T_m but certainly not on any higher index plane. This is indeed what is found in the case of KCl by depositing argon bubbles just under the s-l interface, quenching, then examining the bubble surfaces by electron microscopy.[3] Only (100) faces grow from the melt as singular ones and these being poorly wetted by the melt may be completely stripped of the melt by the bubble.

We thus have a process which may be very important in

1 K.A. Jackson, Liquid Metals and Solidification, (ASM, Cleveland, 1958) p.174.

2 F.C. Frank, Adv. Phys. 1, 91 (1952).

3 G. Grange, R. Landers and B. Mutaftschiev, Surf. Sci. 54, 445 (1976).

the study of premelting behaviour. At a critical temperature T_c below the melting temperature, surfaces will become disordered i.e. they will melt, with resultant high diffusivity pathways around the exterior of the crystal. T_c decreases the higher the index of the surface plane. These ideas are confirmed by a study by Pavlovska and Nenow[1] on surface melting in diphenyl. They find that {201} faces melt 20-25 K below the melting temperature (342.7 K), {110}

Salt	Orientation of Interface		
	(100)	(110)	(111)
LiF	1.94	0.97	0
LiCl	1.80	0.90	0
LiBr	1.72	0.86	0
LiI	1.58	0.79	0
NaF	2.11	1.05	0
NaCl	2.10	1.05	0
NaBr	2.05	1.03	0
NaI	2.03	1.02	0
KF	1.93	0.96	0
KCl	2.03	2.02	0
KBr	2.03	1.02	0
KI	2.02	1.01	0
RbF	1.82	0.91	0
RbCl	2.06	1.03	0
RbBr	1.82	0.91	0
RbI	1.56	0.78	0

Table 2.1. Values of α for various orientations of s-l interfaces at the melting point.

faces 10-15 K below T_m, while for {001} faces $T_c \geq T_m$.

1 A. Pavlovska and D. Nenow, Surf. Sci. 27, 211 (1971).

By the same token, premature melting at grain boundaries might be expected, and indeed beginning with the experiments of Chaudron et al on high purity aluminium[1] this has been found, although controversy developed regarding the possibility of melting point depression due to accumulation of impurities at the grain boundaries. The general consensus now appears to be that preferential melting occurs at the boundary due to ease of nucleation rather than intrinsic depression of the melting point.[2]

2.5 Summary.

The various melting theories which have been examined in this chapter are summarised accoring to their categories in Table 2.2. Each displays at least some degree of predictive success and many are quantitatively convincing. So many in fact that it has had to be stressed that satisfactory theories must be judged not so much on quantitative results but more on how physically realistic the description is.

In view of the dynamic character of melting, the existence of a solid-liquid interface and a nucleation barrier to melting, we found it necessary to distinguish between homogeneous and heterogeneous theories, as is done in Table 2.2, and retain as viable only those theories which fall in the latter group. Ofcourse some of the presently homogeneous theories could, with further complexity, be modified so as to include a description of the s-l interface, however we have simply tabulated these theories according to present rather than potential status. The assignment of theories to the two groups is in most instances obvious, except that the Bernal and molecular dynamics approaches have been included in both groups because the first has been applied to the interface between close and loose packing and MD computations applied to thin crystals reveal a depressed melting point. Presumably MD or MC computations on semi-infinite arrays of atoms would display the morphology of surface melting and the

1 G. Chaudron, P. Lacombe and N. Yannaquis, Compt. Rend. 226, 1372 (1948).

2 S. Amelinckx and W. Dekeyser, Sol. St. Phys. 8, 473(1959).

	Phenomenological	Non-structural		Structural		
		Instability	Thermodynamic	Lattice	Statistical Geometry	Statistical Mechanical & Thermodynamic
Homogeneous	Corresponding States.	Vibrational Theories Lindemann. Anharmonic. Elastic Shear modulus = 0.	Bulk Theories Modified Landau. Significant Structures.	Cybotactic. Vacancy. Order/ Disorder. Cell.	Icosahedral. Bernal. Kirkwood and Boggs.	Dense gas. Molecular dynamics (MD). Monte Carlo (MC). Variational.
Heterogeneous			Surface Theories Surface wetting. Equilibrium form. Nucleation.	Dislocation	Bernal.	MD MC Surface melting - Burton, Cabrera Frank. S-L Interface - Jackson.

Table 2.2 Theories of Melting

appearance of a s-l interface which progresses into the lattice as the bulk melting point is approached. This has not yet been done but should be possible with only little modification to existing computer programmes and is strongly recommended to further elucidate the dynamics and mechanism of melting.

We have suggested that a truly successful theory of melting must view the liquid in terms of its own distinctive properties rather than in terms of gas-like or solid-like models. At the same time the complexities involved in the formulation of such a theory are so great that one is forced to a compromise, and the model approach remains attractive. All things considered, two model theories present themselves as being at once both simple and successful - Eyring's Significant Liquid Structures theory and the dislocation model. The success of the former lies in its accurate quantitative characterisation of a wide range of properties, the latter more in its capability of meeting a number of physical requirements particularly the nucleation and kinetics of the s-l interface. We will show in §7 how the dislocation model may be applied to describe surface melting as predicted by the theory of Burton, Cabrera and Frank and the movement of the s-l interface from the surface into the crystal bulk. Nevertheless, it must be understood that the model is physically realistic only when dislocations are packed so closely that the base lattice can no longer be recognised, and under these conditions the formulation of dislocation properties in terms of those usually studied for isolated dislocations is likely to be inaccurate.

3 PREMELTING

The diversity of theories of melting arises, as we have seen, from the general lack of success in obtaining a single realistic and quantitatively precise theory. This is due, in turn, to the difficulty in formulating the structure of the melt. The interest in premelting behaviour, then, is that processes possibly pertaining to the mechanism of melting may be studied in the better understood solid state.

Before we discuss some of these premelting events, it is necessary to state that by premelting we mean intrinsic effects which are precursory to melting. Thus we exclude all extrinsic effects, particularly the 'two-phase premelting' as described by Ubbelohde, including the Raoult freezing depression by insoluble impurities and the appearance of a melting region due to soluble impurities. In addition we exclude depressed melting points in very small crystalline particles[1] and also intrinsic effects which first appear well below T_m (at $\sim \frac{2}{3} T_m$) and are directly attributable to the thermal formation of point defects. Prominent examples of the latter are the high temperature rises in volume thermal expansion α_v and specific heat C_p above their vibrational values. (For example, for α_v in NaCl see ref. 2 and in AgCl see ref. 3. The temperature dependence of C_p for many ionic crystals is given in ref. 4.) It is not superfluous to state that one must consider specific heat C_v at constant volume, for C_p contains the effect of thermal expansion and consequently rises well above the Dulong and Petit value 6 R, particularly at high temperatures where vacancies contribute to α_v. The effects we are left with, then, are those which appear within about

1 S.J. Peppiat and J. R. Sambles, Proc. R. Soc. Lond. A 345, 387 (1975).

2 F.D. Enck and J.G. Dommel, J. Appl. Phys. 36, 839 (1965).

3 R. Nicklow and R. Young, Phys. Rev. 129, 1936 (1963).

4 D.R. Stull and H. Prophet, JANAF Thermochemical Tables, 2nd Edn., NSRDS - NBS 37 (1971).

10 K of the melting temperature and are not attributable to the presence of impurities.

Because of the impurity problem, particularly the possible presence of unknown or unexpected impurity, and more subtly the accumulation of impurities at grain boundaries and surfaces, the results of many studies are at variance with each other. Moreover, the situation is further complicated by the fact that even when impurities are taken into account, or are absent in high purity specimens, premelting data from separate studies of the one system are not entirely consistent. We quote just a few examples. Ubbelohde[1] found distinct premelting rises in specific heat near T_m in carefully purified paraffins. The intrinsic character of the results was checked by deliberate doping and this work was substantiated by others[2], yet Hoffman and Decker[3] particularly referring to pure C-18 paraffin found cooling curves characteristic of an ideal first order transition with no premelting specific heat anomaly. Abrupt increases in self diffusion observed in indium within one half a degree of the melting point[4] led Meyer and Nachtrieb[5] to examine the tracer self diffusion in sodium up to T_m. No anomalous changes in diffusion coefficient occurred to within 0.08 K of T_m. Again, apart from the usual vacancy contribution, no premelting is evident in the specific heat measurements in sodium reported by Martin[6]. In contrast to both these results Fritsch and Lüscher[7], after carefully allowing for deliberately introduced potassium impurity, found a steep rise in thermal conductiv-

1 A. Ubbelohde, Trans. Faraday Soc. 34, 282 (1938).

2 H. Finke, M. Gross, G. Waddington and H. Huffman, J. Am. Chem. Soc. 76, 333 (1954).

3 J. Hoffman and B. Decker, J. Phys. Chem. 57, 520 (1953).

4 R.E. Eckert and H.G. Drickamer, J. Chem. Phys. 20, 13 (1952).

5 R. E. Meyer and N.H. Nachtrieb, J. Chem, Phys. 23, 405 (1955).

6 D.L. Martin, Phys. Rev. 154, 571 (1967).

7 G. Fritsch and E. Lüscher, Phys. Rev. B4, 3292 (1971).

ity below the solidus point. As a final example, Jach and Sebba[1] have reported differential thermal analysis of the melting of gallium at a constant heating rate which shows a slow climb in temperature in two stages at the melting point. The temperature/time curve, rather than turning over sharply at the onset of melting, is rounded. They interpret their results in turns of anisotropic melting in two different crystallographic directions. We may compare this with a recent precision melting study[2] on 99.9999% purity gallium which for a heating rate of 3×10^{-3} K/h showed very sharp edges on the melting plateau and a constancy in temperature of both melt and crystal within at least 10^{-4} K during melting.

The fact that many premelting anomalies may be eliminated by careful experimentation and the use of very high purity samples tempts one to dismiss premelting in general as spurious. Even where there are strong theoretical reasons for believing that surfaces should melt prematurely, low energy electron diffraction studies[3] of various crystals under ultra-high vacuum where there are no gasious surface contaminants show that the surfaces remain ordered up to the bulk melting point. However, it must be recognised that the mechanism of melting will vary from one substance to the other, and generalisations would be most unsafe. (We might, in fact, expect for example that gallium, which has a negative volume change on melting, should not exhibit premelting but rather, if possible, 'post melting' effects. This would be consistent with the superheating of certain crystalline faces of gallium observed by Volmer and Schmidt[4].) Nevertheless, the possibility of spurious results near T_m must be recognised e.g. Mundy, Barr and Smith[5] point out that a very small impurity

1 J. Jach and F. Sebba, Trans. Faraday Soc. 50, 226 (1954).

2 H. Wenzl and G. Mair, Z. Physik B 21, 95 (1975).

3 R.M. Goodman and G.A. Somorjai, J. Chem. Phys. 52, 6325 (1970).

4 M. Volmer and O. Schmidt, Z. Physik. Chem. B 35, 467 (1937).

5 J.N. Mundy, L.W. Barr and F.A. Smith, Phil. Mag. 14, 785 (1966).

concentration is sufficient for impurity accumulations along dislocations to cause premature melting there, giving an enhanced pipe diffusion likely to effect all transport processes.

With these cautions in mind, we now turn to those premelting studies on ionic crystals which more closely relate to the present work. The most thorough study is that of Allnatt and Sime[1] on the rises in electrical conductivity beginning about 4 K prior to melting in NaCl and KCl. Care was taken not to deform the specimens and thus alter the geometrical factor during an experiment, a KCl crystal was doped with 3.3 10^{-4} mole % of $SrCl_2$ and NaCl crystals were strained up to 5% in simple compression. They observe that the anomalous rise is unaffected by the doping or the deformation and has an effective activation energy of $\sim$ 200 eV for NaCl and $\sim$ 400 eV for KCl. We note, however, that their tabulated activation energies show 120 eV for the first rise and 210 eV for the second rise on a 2% strained NaCl specimen. There may therefore be a deformation dependence which is annealed out by the end of the first rise. Discounting impurities as the cause of the effect, and not having measured surface conductivity, Allnatt and Sime are unable to present an explanation. Subsequently, Robinson[2] has interpreted their results in terms of a dislocation theory of melting, the excess conductivity being attributable to 'pipe diffusion' along thermally formed dislocation lines. Earlier observations of premelting conductivity have been made in sodium nitrate[3] amd caesium chloride[4].

These results are complemented by a number of measurements of elastic constants in alkali halides up to the melting

1 A.R. Allnatt and S.J. Sime, Trans. Faraday Soc. 67, 674 (1971).

2 W.H. Robinson, J. Appl. Phys. (in press).

3 M. Bizouard and P. Cerisier, C.R. Acad. Sc. Paris 262, 1 (1966).

4 W.W. Harpur, R.L. Moss and A.R. Ubbelohde, Proc. Roy. Soc. A 232, 196 (1955).

point. The first of these by Hunter and Siegel[1] using NaCl single crystals in composite piezoelectric oscillators in the longitudinal and torsional modes, revealed up to 6% decreases in the shear moduli c_{44} and $\frac{1}{2}(c_{11} - c_{12})$ and the compressibility χ , beginning about 5 K below T_m. This means, surprisingly, that the lattice becomes 'harder' near the melting point. No explanation is given except to say that the calculated compressibility is the adiabatic value which is less than the isothermal value by an amount $\alpha_v^2 VT/C_p$ where V is the molar volume. A rapid rise, they say, in α_v prior to melting may therefore account for the drop in $\chi_{adiabatic}$ and give a $\chi_{isothermal}$ which remains normal or even rises close to T_m. This leaves the problem of explaining a rapid increase in α_v as well as, since the adiabatic shear moduli equal the isothermal shear moduli, the decrease in shear moduli. A similar result obtains for KCl[2]. Slagle and McKinstry[3], however, using a 20 MHz acoustic pulse technique found no deviations in c_{44} and $\frac{1}{2}(c_{11} - c_{12})$ and contrary to the above results an increase in isothermal compressibility near T_m. To these results we may add that Robinson and co-workers using the piezoelectric composite oscillator technique have observed, near T_m, rapidly increasing mechanical damping in single crystals of KCl[4,5,6] and Al[7] and rapidly decreasing dislocation charge in KCl[5].

1 L. Hunter and S. Siegel, Phys. Rev. 61, 84 (1942).

2 R.D. Enck, Phys. Rev. 119, 1873 (1960).

3 O.D. Slagle and H.A. McKinstry, J. Appl. Phys. 38, 437 (1967).

4 W.H. Robinson and H.K. Birnbaum, J. Appl. Phys. 37, 3754 (1966).

5 W.H. Robinson, J.L. Tallon and P.H. Sutter, Phil. Mag. (to be published).

6 W.H. Robinson and H.K. Birnbaum, (to be published).

7 A. Wolfenden and W.H. Robinson, private communication.

There are some interesting pre- and post-melting effects observed in the vaporisation kinetics of NaCl, KBr and CsI[1]. In each case at about 100 K below T_m, vaporisation flux departs from simple lower temperature Arrhenius behaviour passing through a minimum in gradient at T_m then rising quickly above T_m towards the extrapolated Arrhenius line. On the other hand, LiF shows no such irregularities, the vaporisation flux increasing uniformly through the melting point. The anomalous behaviour was tentatively ascribed to a change of the rate controlling step in a two step vaporisation process.

It is not unlikely that these various electrical and mechanical changes near melting are related and it is possible the climb in vaporisation rate at T_m is also connected to or even causing these effects.

We have briefly reviewed a number of premelting observations in alkali halides and as a final example we shall consider an interesting type of behaviour which has not been located amongst the alkali halides but may be possible in this kind of binary system. This is a first or second order solid state transition involving the disordering, if not melting, of one of the sublattices. Perhaps the best known example is AgI[2] which undergoes an isothermal transition from the β to the α form at 418 K, with an accompanying jump in electrical conductivity rather characteristic of the usual change on melting of other ionic crystals. Above the transition temperature the Ag^+ sublattice has no long range order and the relatively small Ag^+ ions are highly mobile. The actual melting temperature is much higher at $\sim$ 830 K. α - AgI and the α phases of a whole range of related substitutional salts[3] such as Ag_2HgI_4 are described as solid electrolytes and have received much attention in recent years in relation to high power density galvanic cells.[4] Many

1 C. Ewing and K. Stern, J.Phys.Chem. 79, 2007 (1975).

2 W. Jost, J. Krug and L. Sieg, Proc. Intern. Symp. Reactivity Solids, Gothenburg, 1952, pp 81-82.

3 T. Takahashi, J. Appl. Electrochem. 3, 79 (1973).

4 R.T. Foley, J. Electrochem. Soc. 116, 13 C (1969).

substances possessing the fluorite (MX_2) or anti-fluorite (M_2Y) type of structure show similar, though second order, transitions[1]. The anion sublattices in CaF_2, $SrCl_2$, $SrBr_2$ and $BaCl_2$ become, at high temperatures, increasingly randomly distributed over the octahedral and tetrahedral sites within the fcc cation sublattice. As a result the specific heat rises to a maximum at some critical temperature and the entropies of melting are correspondingly about half those of other alkaline earth halides which do not exhibit transitions. Other crystals with similar transitions are K_2S, Li_2SO_4, NdI_3 and probably UO_2, ThO_2 and Na_2O. It is particularly interesting to note that $SrBr_2$ shows a transition only 12 K below its melting point[1] and the question arises, if in a substance the transition were much closer to T_m, whether experimentally it would be distinguished from melting or interpreted as an impurity effect. Premelting effects in some binary compounds might in fact be due to a disordering of one sublattice premature to melting. In possible connection with this idea, we observe that cryoscopic studies on the premelting of KCNS[2] reveal a continuous transition within 1 or 2 K of the melting point. Thus, for example, premelting in the alkali halides may be due to disordering of the cation (in general) sublattice before melting and we might expect that the smaller the radius ratio, r^+/r^-, the earlier the premelting. This is consistent with the above noted results for NaCl and KCl obtained by Allnatt and Sime wherein the breadth of the premelting region for NaCl was twice that for KCl. This and other possible premelting processes will be considered in detail in §7 in relation to our own experimental results. Lastly we recall that Frenkel's heterophase fluctuation theory[3] was rejected in § 2.2 as a possible explanation of premelting.

1 A.S. Dworkin and M.A. Bredig, J. Phys. Chem. 67, 697 (1963); ibid. 72, 1277 (1968).

2 E. Rhodes and A.R. Ubbelohde, Trans. Faraday Soc. 55, 1705 (1959).

3 J. Frenkel, J. Phys. 1, 315 (1939).

4 MELTING DATA OF ALKALI HALIDES AND AN ELASTIC STRAIN THEORY OF MELTING.

In this section we collect together the values of a number of important physical parameters, some of which will be required for later computation and others which will receive some comment in the present section. Then we develop a generalised elastic strain description of melting and show that, with one important alteration, Born's shear instability theory of melting applies for a large number of the alkali halides.

4.1 Physical Data

Table 4.1 contains the basic data for the alkali halides with the rocksalt structure, and these show some interesting contrasting trends. Some quantities, while remaining roughly constant within homologous groups, overall show a marked variation e.g. the melting temperature T_m which varies by a factor of 2. Another, $\Delta V/V$ varies monotonically down the column, and still others such as the entropy of melting are remarkably constant. The last feature suggests that the structural disorder in the melts is the same in each case. We have cited the smallness of the enthalpy of melting ΔH_m relative to the enthalpy of sublimation ΔH_s as being proof of the greater similarity of the melt near T_m to the crystal than to the gas. In the case of metals $\Delta H_s/\Delta H_m$ is as high as 40 whereas here we find values scattered about 10 which suggests the distinction between melt and vapour is rather less in the alkali halides than in the metals. This is because the vapours of the alkali halides largely consist of ion pairs and even dimers as gaseous molecules[1]. Adding the dissociation energy of these molecules gives a final ratio $\Delta H_s / \Delta H_m$ averaging around 30 which is in closer agreement with the metals. A contributing factor to the greater similarity between melt and vapour may also derive from the inclination to ion pairing in the melt which is apparent even

1 D. Stull and H. Prophet, JANAF Thermochemical Tables NSRDS - NBS 37 (1971).

Table 4.1 Physical data for the alkali halides. Molar weight, M, melting temperature, T_m, enthalpy of melting, ΔH_m, enthalpy of sublimation, ΔH_s, and the specific heats of the solid and liquid at the melting point, C_{ps} and C_{pl} are all from D. Stull and H. Prophet, JANAF Thermochemical Table NSRDS - NBS 37 (1971). The fractional changes in volume on melting $\Delta V_m/V_s$ are from H. Schinke and F. Sauerwald, Z. anorg. Chem. 287, 313 (1956). The Gruneisen parameters g are from J.C. Slater, Introduction to Chemical Physics (McGraw-Hill, N.Y., 1939). The solid-liquid interfacial energies γ_{sl} are from E.R. Buckle and A.R. Ubbelohde, Proc. Roy. Soc. A 261, 197 (1961). The melt surface tensions γ_ℓ and melt densities are from G.J. Janz et al, NSRDS -NBS 15 (1968). The solid densities at the melting point are calculated from the melt densities and the volume changes $\Delta V_m/V_s$. Where values of ΔH_s were not available they were calculated from the cohesive energies of the crystals (given in F. Seitz, Modern Theory of Solids (McGraw-Hill, N.Y., 1940)) and the binding energies of the gasious ion-pairs. The values of $\Delta H_s/\Delta H_m$ thus obtained are marked by asterisks.

Salt	$10^3 M$ / kg/mol	T_m / K	ΔH_m / 10^5 J/kg	$\Delta H_s / \Delta H_m$	$\Delta S / R$	$\Delta V_m / V_s$	a / 10^{-10} m	r^+ / r^-	g	γ_{sl} / N/m²	γ_l / N/m²	ρ_s / kgm.$^{-3}$	C_{ps}/R	C_{pl}/R
LiF	25.9	1121	10.44	10.2	2.91	.294	4.02	0.51	1.34	0.181	0.236	2.340	7.44	7.72
LiCl	42.4	883	4.68	12.6*	2.70	.262	5.14	0.38	1.52	0.089	0.129	1.895	7.42	7.82
LiBr	86.8	823	2.33	14.1*	2.58	.243	5.50	0.35	1.70	0.047		3.144	7.87	7.85
LiI	133.8	742	1.09	17.5*	2.38		6.00	0.31					7.67	7.60
NaF	42.0	1269	7.94	8.54	3.16	.274	4.62	0.74		0.179	0.187	2.509	7.95	8.45
NaCl	58.4	1074	4.82	8.16	3.16	.250	5.638	0.55	1.63	0.084	0.114	1.945	8.10	8.50
NaBr	102.9	1020	2.54	8.33	3.08	.224	5.96	0.51	1.56	0.072	0.104	2.866	7.38	7.50
NaI	149.9	933	1.57	9.68*	3.04	.186	6.46	0.45			0.100	3.251	7.21	7.80
KF	58.1	1131	4.68	8.89	2.89	.172	5.34	1.06	1.45		0.143	2.239	7.79	8.66
KCl	74.6	1044	3.53	7.90*	3.03	.173	6.29	0.78	1.60	0.066	0.101	1.792	8.31	8.85
KBr	119.0	1007	2.15	8.37*	3.05	.166	6.58	0.72	1.68	0.057	0.089	2.479	8.22	8.41
KI	166.0	954	1.45	8.43	3.03	.159	7.06	0.64	1.63	0.047	0.079	2.832	8.12	8.71
RbF	104.5	1033	1.65	13.3*	2.73		5.64	1.19			0.127			
RbCl	120.9	988	1.5	11.5*	3.06	.143	6.54	0.87		0.056	0.099	2.846		
RbBr	165.4	965	0.94	12.8*	2.73	.135	6.86	0.81	1.37		0.089	3.463		
RbI	212.4	915	0.59	16.5*	1.64		7.32	0.72	1.41		0.082			
CsF	151.9	976	1.43	9.13	2.68		6.00			0.060	0.108			

at the melting point[1].

The tendency of properties to vary monotonically within homologous groups in a similar manner for each group allows one to obtain many correlations between solid state properties and melting parameters which must be regarded with some degree of caution. We shall consider just one type of correlation: that of the elastic moduli with the enthalpies of melting. For other property correlations, the paper of Grimvall and Sjödin[2] may be referred to. Mott and McKenzie[3] noted the correspondence between grain boundary energy via the shear modulus and the enthalpy of melting and this has, as we have seen, subsequently led to a number of dislocation theories of melting. Better correspondence obtains, certainly in the case of the alkali halides, if proper consideration is given to the parameters which should be combined. On dimensional grounds, or by considering simple models, it can be seen that one should look for constancy in the shear modulus divided by $\rho_s \Delta H_m$ where ρ_s is the density of the solid at the melting point. For example, in the case of a dislocation model of melting in the alkali halides one migh assume that the active planes and directions for spontaneous dislocation generation are $\{110\}\langle 110\rangle$ as for normal slip. The appropriate moduli for edge and screw dislocations on these planes are respectively[4]

$$\mu_e = \frac{(c_{11} + c_{12})\,\mu_s}{[\frac{1}{2}c_{11}(c_{11} + c_{12} + 2c_{44})]^{\frac{1}{2}}} \quad , \qquad (4.1)$$

and

$$\mu_s = [\tfrac{1}{2}c_{44}\,(c_{11} - c_{12})]^{\frac{1}{2}} \qquad (4.2)$$

The three independent elastic constants c_{11}, c_{12} and c_{44}[5] are tabulated in Table 4.2. and from these we calculate the quantities $\mu_e/\rho_s \Delta H_m$ and $\mu_s/\rho_s \Delta H_s$ shown in the 3rd and 4th

1 L.V. Woodcock, Nature Physical Science 232, 63 (1971).
2 G. Grimvall and S. Sjödin, Physica Scripta 10, 340 (1974).
3 J.K. McKenzie and N.F. Mott, Phys. Soc. Proc., 63, 411 (1950).
4 J.D. Eshelby, W.T. Read and W. Shockley, Acta Met. 1, 251 (1953).
5 R.F.S. Hearmon in Landolt-Bornstein, New Series, Group III Vol.1 (Springer-Verlag, Berlin, 1966).

Table 4.2 Elastic moduli and reduced moduli $\mu/\rho\Delta H_m$ for shear on various orientation planes. Values given in brackets are for elastic moduli at T_m. Room temperature moduli are from Hearmon ref. 5 p. 40 and high temperature moduli are from refs. 1-7 p. 44 .

Crystal	C_{11} 10^{10}Pa	C_{44} 10^{10}Pa	C_{12} 10^{10}Pa	μ_e $\rho\Delta H_m$	μ_s $\rho\Delta H_m$	β $\rho\Delta H_m$	C_{44} $\rho\Delta H_m$	$C_{11}-C_{12}$ $2\rho\Delta H_m$	$C_{11}+C_{12}+2C_{44}$ $4\rho\Delta H_m$	$C_{11}-C_{12}+10C_{44}$ $12\rho\Delta H_m$	$\frac{1}{3}(C_{11}-C_{12}+C_{44})$ $\rho\Delta H_m$
LiF	11.2	6.32	4.5	23.5	18.9	27.6 (6.22)	25.9 (19.1)	13.7 (4.63)	19.8	23.9	17.8
LiCl	4.94	2.46	2.28	27.0	20.4	35.8	27.8	15.0	21.4	25.6	19.3
LiBr	3.94	1.93	1.87	25.7	19.2	35.0	26.4	14.2	20.3	24.3	18.2
LiI											
NaF	9.7	2.81	2.44	20.9	16.0	24.4 (9.48)	14.2 (10.7)	18.2 (8.58)	16.2	14.8	16.9
NaCl	4.85	1.27	1.25	21.4	16.1	26.2 (16.9)	13.6 (9.9)	19.2 (6.3)	16.4	14.5	17.4
NaBr	3.97	0.99	1.06	22.3	16.5	27.9	13.6	20.0	16.9	14.7	17.9
NaI	3.03	0.734	0.89	23.8	17.4	31.3 (13.7)	14.4 (11.9)	20.9 (8.79)	17.7	15.4	18.8
KF	6.56	1.25	1.46	23.3	17.1	30.2	12.0	24.4	18.2	14.0	20.2
KCl	4.05	0.629	0.66	22.2	16.3	28.4 (18.4)	10.0 (7.7)	26.9 (8.8)	18.5	12.6	21.5
KBr	3.46	0.515	0.56	22.2	16.3	28.8 (18.2)	9.7 (7.3)	27.3 (9.6)	18.5	12.6	21.5
KI	2.75	0.369	0.45	21.9	15.9	29.8	9.0 (7.4)	28.1 (10.7)	18.6	12.2	21.7
RbF	5.52	0.925	1.40								
RbCl	3.63	0.465	0.62	27	20	38	12	35	23	15	27
RbBr	3.14	0.383	0.48	32	23	42	12	45	28	17	34
RbI	2.56	0.280	0.36	40	29	38	15.5 (12.6)	69 (19.7)	36	22	43

columns. Discounting the rubidium salts for which the data are poor, the constancy in values is noteable. However, before this is construed as strong support for a dislocation model of melting, we must note that the bulk modulus (in the next column) and, by selecting the softest modulus for each crystal, Young's modulus show a similar though not so marked constancy. Therefore, rather than committing ourselves to a particular structural defect, a more powerful approach may be made to melting by considering the melt as an arbitrarily strained crystal.

4.2 Elastic Strain Formulation of Melting.

The total melt strain may be resolved into six independent strains: one dilatation and five shear strains which are in fact the eigenvectors of the elastic modulus reduced matrix. These strains together with the three separate eigenvalues of the matrix are

$$\left.\begin{aligned} \delta &= \epsilon_{11} + \epsilon_{22} + \epsilon_{33} \\ e_1 &= (2\epsilon_{33} - \epsilon_{11} - \epsilon_{22})/\sqrt{3} \\ e_2 &= \epsilon_{11} - \epsilon_{22} \end{aligned}\right\} \quad \begin{aligned} \beta &= \tfrac{1}{3}(c_{11} + 2c_{12}) \\ \mu' &= \tfrac{1}{2}(c_{11} - c_{12}) \end{aligned} \qquad (4.3)$$

$$\left.\begin{aligned} e_3 &= 2\epsilon_{12} \\ e_4 &= 2\epsilon_{23} \\ e_5 &= 2\epsilon_{31} \end{aligned}\right\} \quad \mu = c_{44}$$

The ϵ_{ij} are the components of the strain tensor, the dilatation δ is a simple volume change while e_1 and e_2 are shears on $\{110\}$ planes and e_3, e_4 and e_5 are shears on $\{100\}$ planes. Since the melt cannot sustain a macroscopic shear the e_i are local shears which average to zero in time and space. The eigenvalues are the bulk modulus, β , the $\{110\}$ shear modulus, μ', and the $\{100\}$ shear modulus, μ . In their proper tensor forms μ' is μ transformed through a rotation of $\pi/4$. The magnitudes of the three groups of strains are chosen such that, provided the moduli may be considered to be constant, the strain energy density W is given by

$$W = \tfrac{1}{2}\beta\delta^2 + \tfrac{1}{2}\mu'(e_1^2 + e_2^2) + \tfrac{1}{2}\mu(e_3^2 + e_4^2 + e_5^2) \qquad (4.4)$$

The enthalpy of melting is therefore

$$\Delta H_m = (1/\rho_1 V) \int_V W dV = (1/2\rho_1)\left\{\beta \hat{\delta}^2 + \mu'(\hat{e}_1^2 + \hat{e}_2^2) + \mu(\hat{e}_3^2 + \hat{e}_4^2 + \hat{e}_5^2)\right\} \quad (4.5)$$

The capped strains, thus $\hat{e}_i$, denote rms values. We shall see in §4.3 that the moduli may not be considered to be constant throughout the melting process and appropriate modifications will be made. The volume change on melting is simply

$$\Delta V/V = (1/V) \int_V \delta \, dV = \bar{\delta} \quad , \quad (4.6)$$

where $\bar{\delta}$ is the simple mean dilatation. Dividing through eqn. (4.5) by ΔH_m we have an equation where the mean square strains have coefficients $\beta/\rho_l \Delta H_m$, $\mu'/\rho_l \Delta H_m$ and $\mu/\rho_l \Delta H_m$. When converted back to tensor notation, the first of these is invariant under transformations and we have seen in Table 4.2 that β correlates well with $\rho_l \Delta H_m$ such that $\beta/\rho_l \Delta H_m \sim 30$. It is of course more realistic to use the values of the moduli [1-7] at T_m and where these are available values of $\beta/\rho_l \Delta H_m$ are given in brackets. These are more scattered in value but this is probably due to the rather unreliable data. The two shear coefficients are orientation dependent and we have to be sure that the crystal is softest in $\{100\}$ and $\{110\}$ shear since any two shear moduli, such that one equals the other transformed through a $\pi/4$ rotation, could serve as independent moduli in our formulation. Listed below are some low index slip systems with the appropriate shear moduli:

1 L. Hunter and S. Siegel, loc. cit.

2 F.D. Enck, loc. cit.

3 O.D. Slagle and H.A. McKinstry, J. Appl. Phys. 38, 437 (1967).

4 S.P. Nikanorov and A.V. Stepanov, Sov. Phys. Sol. St. 3, 2579 (1961).

5 P. Antonov, B. Kardashev and S. Nikanorov, ibid. 9, 527 (1967).

6 B. Karashev and S. Nikanorov, ibid. 9, 747 (1967).

7 R.F.S. Hearmon, loc. cit.

$\langle 010 \rangle \{100\}$: c_{44} , $\frac{1}{2}(c_{11} - c_{12})$

$\langle 011 \rangle \{100\}$: c_{44} , $\frac{1}{2}(c_{11} - c_{12})$

$\langle 110 \rangle \{110\}$: $\frac{1}{2}(c_{11} - c_{12})$, c_{44}

$\langle 001 \rangle \{110\}$: c_{44} , $\frac{1}{4}(c_{11} - c_{12} + 2c_{44})$

$\langle 111 \rangle \{110\}$: $\frac{1}{3}(c_{11} - c_{12} + c_{44})$, $\frac{1}{12}(c_{11} - c_{12}) + \frac{10}{12} c_{44}$

$\langle 110 \rangle \{111\}$: $\frac{1}{3}(c_{11} - c_{12} + c_{44})$, c_{44}

$\langle 112 \rangle \{111\}$: $\frac{1}{3}(c_{11} - c_{12} + c_{44})$, c_{44}

Each of the moduli divided by $\rho_l \Delta H_m$ are included in Table 4.2 and indeed μ and μ' sum to the lowest values of any of the combinations. Of these, the softest modulus at room temperature is μ' for the lithium group and μ for the remainder. These are seen to correlate fairly well with $\rho_l \Delta H_m$ with $\mu(\text{softest}) / \rho_l \Delta H_m \sim 12.5$ and the complementary shear modulus μ for lithium halides and μ' for the remainder, averages to about 24 times $\rho' \Delta H_m$ with a similar degree of correlation. At the melting point, $\{110\}$ shear is softer than $\{100\}$ for sodium as well as lithium halides and again, provided one takes the softest shear moduli excluding LiF and RbI, correlation with $\rho_l \Delta H_m$ is reasonable with $\mu(\text{softest})/\rho_l \Delta H_m \sim 7.7$ for the 6 salts and the harder complementary shear moduli average to $\sim 10.3\ \rho_l \Delta H_m$. This means that the rms strains in eqn. (4.5) will be in approximately similar proportions for all the alkali halides, with due allowance for which is the softest shear plane.

The change in vibrational entropy may be calculated from the strain induced shift in the $6N_\circ$ normal mode frequencies ν_i by using the formula[1]

$$\Delta S_{vib} = k \sum^{6N_\circ} \ln \left(\frac{\nu_i + \Delta \nu_i}{\nu_i} \right) = k \sum^{6N_\circ} \frac{\Delta \nu_i}{\nu_i} \qquad (4.7)$$

1 N.F. Mott and R.W. Gurney, Electronic Processes in Ionic Crystals (Clarendon Press, Oxford, 1940), p. 31.

The frequency change due to the dilatation may be connected to that strain using the Gruneisen parameter[1], g in the equation

$$\Delta\nu_i / \nu_i = - g\delta \quad , \tag{4.8}$$

or more accurately

$$\Delta\nu_i / \nu_i = \exp(- g\delta) - 1 \quad , \tag{4.9}$$

while the change due to shear is a smaller second order effect which may be described by

$$\sum_k \Delta\nu_{ik} / \nu_{ik} = - {}^3/_2 \; g_s(j) \; e_j^2 \tag{4.10}$$

Here the k summation is over the x,y and z modes. In Appendix A we determine g and $g_s(j)$ by considering nearest neighbour interactions of the Born-Mayer kind[2]. We show that

$$g = g_s(j) = (\gamma^2 - 2\gamma - 2)/6(\gamma - 2) \quad j = 3,4,5 \tag{4.11}$$

and

$$g_s(j) = - (\gamma^3 - 3\gamma^2 - 2\gamma - 2)/12(\gamma - 2) \quad j = 1,2 \tag{4.12}$$

In these equations $\gamma = a/2\rho_B$ where a is the cation-cation distance and ρ_B the Born-Mayer characteristic repulsion distance which for the alkali halides is close to 3×10^{-11}m. g is usually calculated from the Gruneisen relationship

$$\alpha_V V = g\chi C_V \; . \tag{4.13}$$

Values of g thus obtained[3] are listed in Table 4.3 together with values[4] of ρ and thence g calculated from eqn. (4.11), and $g_s(1)$ from eqn. (4.12). The theoretical g values are in reasonable agreement with experimental values except for the

1 E. Gruneisen, in Handb. der Physik, X, ed. by S. Flugge (Springer-Verlag, Berlin, 1926).

2 M. Born and K. Huang, Dynamical Theory of Crystal Lattices (Clarendon Press, Oxford, 1954) p.

3 J.C. Slater, Introduction to Chemical Physics, (McGraw-Hill, N.Y., 1940).

4 M.P. Tosi in Solid State Physics 16, 52 (1964) ed. by F. Seitz and D. Turnbull (Academic Press, N.Y.).

Salt	g expt.	$\rho_s/10^{-11}$ m.	g eqn.(4.11)	$g_s(1)$ eqn.(4.12)
LiF	1.34	2.99	1.05	-2.71
LiCl	1.52	3.42	1.19	-3.60
LiBr	1.70	3.53	1.24	-3.93
LiI	2.05	4.30	1.10	-2.97
NaF	1.51	3.30	1.10	-3.00
NaCl	1.63	3.17	1.43	-5.40
NaBr	1.56	3.40	1.41	-5.22
NaI	1.68	3.86	1.34	-4.67
KF	1.45	3.38	1.26	-4.07
KCl	1.60	3.37	1.51	-6.06
KBr	1.68	3.35	1.59	-6.78
KI	1.63	3.55	1.61	-6.97
RbBr	1.37	3.35	1.67	-7.45
RbI	1.41	3.37	1.77	-8.50

Table 4.3 Experimental and theoretical values of the Gruneisen parameter g and the shear frequency modulating coefficient $g_s(1)$. Values of g are from Slater loc. cit. and values of ρ_s are from Tosi loc. cit.

lithium salts where next nearest neighbour interactions are important and consequently we may expect the values of $g_s(j)$, $j=1,2$ to be reasonably close to the actual values at least for NaCl through to RbBr. The resulting total vibration entropy is

$$\Delta S_{vib} = 2\eta R\left[1 - \exp(-g\bar{\delta})\right] + 3R\sum_{j=1}^{5} g_s(j)\hat{e}_j^2 \qquad (4.14)$$

where as for ΔH_m we have averaged over the volume V assuming δ to be uniformly distributed and we have replaced the factor 3 for the x,y and z modes by η in recognition of the possibility that, let us say, a linear defect with $\eta = 2$ may be operative. In addition to the vibrational entropy there is the communal entropy 2R arising from the fluidity of the melt which allows freedom of access of each ion to any point within the melt volume and there is the entropy $R\ \ln(V_l^*/V_s^*)$ due to the isothermal expansion of the free volume V_s^* of the solid to V_l^* for the liquid. The free volumes are calculated as functions of dilatation δ in Appendix B using the Born-Mayer potential for nearest neighbour overlap repulsions in a cell model. We show that

$$V_l^*/V_s^* = \sqrt{1+\delta}\left(\frac{\gamma - 2}{\gamma' - 2}\right)^{3/2} \exp\left[3/2\ (\gamma' - \gamma)\right] \qquad (4.15)$$

where $\gamma' = (1+\delta)^{1/3}\gamma$. Inclusion of next nearest neighbour repulsions results in negligible changes in ΔS in all except the lithium salts. Gathering all the terms together we obtain

$$\Delta S_m = R\left\{2 + \ln\left(V_l^*/V_s^*\right) + 2\eta\left[1 - \exp(-g\bar{\delta})\right] + 3\sum_{1}^{5} g_s(j)\hat{e}_j^2\right\} \qquad (4.16)$$

The principal assumption in this formulation is that melt properties are simple extrapolations with respect to strain of solid properties and at first sight this would seem unreasonable in view of the complexity and irregularity of the liquid state and in the light of cautions presented in § 2 regarding modelling liquids on solids. The point at which this assumption is most critical is in the evaluation of the change in free volume given by eqn. (4.15). This calculation gives the change in free volume of the solid due to a dilatation arising e.g. from a decrease in external pressure and

we have applied this to the melting expansion with no reference to the variability and average decrease in co-ordination number. To refine the present model one would wish to relate the co-ordination number to the shear strains e_j and recalculate the free volume and the frequency modulating coefficients g and $g_s(j)$ as functions of δ and the e_j. This will not be done here but we shall see that in at least some instances it is quite sufficient to formulate properties related to melting as functions of dilatation only, in a solid like lattice. To substantiate this, we shall present some simple but remarkable observations.

4.3 The Dilatation Dependence of Elastic Moduli.

Most physical properties of a substance will undergo discontinuous changes as functions of temperature when the substance passes from solid to liquid. If, however, a physical property is examined as a function of an extensive variable such as volume, which itself undergoes a discontinuous change on melting, it is not obvious that that property will be discontinuous. In particular fig. 4.1 shows the isothermal bulk modulus for NaF, NaCl, NaI, KCl and KBr, as a function of the dilatation of the solid lattice due to thermal expansion. The temperature dependent adiabatic bulk moduli for the crystals are obtained from references 5 and 7 on p.44 and the thermal expansions from 1,2 and 3 below. Isothermal bulk moduli may be calculated from the adiabatic values using the relation:

$$\beta_{is} = \beta_{ad} - \alpha_V^2 VT\, \beta_{ad}^2 / C_p \qquad (4.17)$$

The temperature dependence of C_p is obtained from JANAF Thermochemical Tables[4], and the isothermal bulk moduli for the melts from Bockris and Richards[5]. NaCl, KCl and KBr were the only salts for which full, reliable data was avail-

1 F.D. Enck and J.G. Dommel, J.Appl. Phys. 36, 839 (1965).
2 F.D. Enck,D.G.Engle and K.I.Marks,J.Appl.Phys.33,2070(1962).
3 K.K. Srivastava and H.D. Merchant, J.Phys. Chem. Solids 34, 2069 (1973).
4 D. Stull and H. Prophet,JANAF Thermochemical Tables NSRDS - NBS 37 (1971).
5 J. Bockris and N.E. Richards,Proc.Roy.Soc. A241,44 (1957).

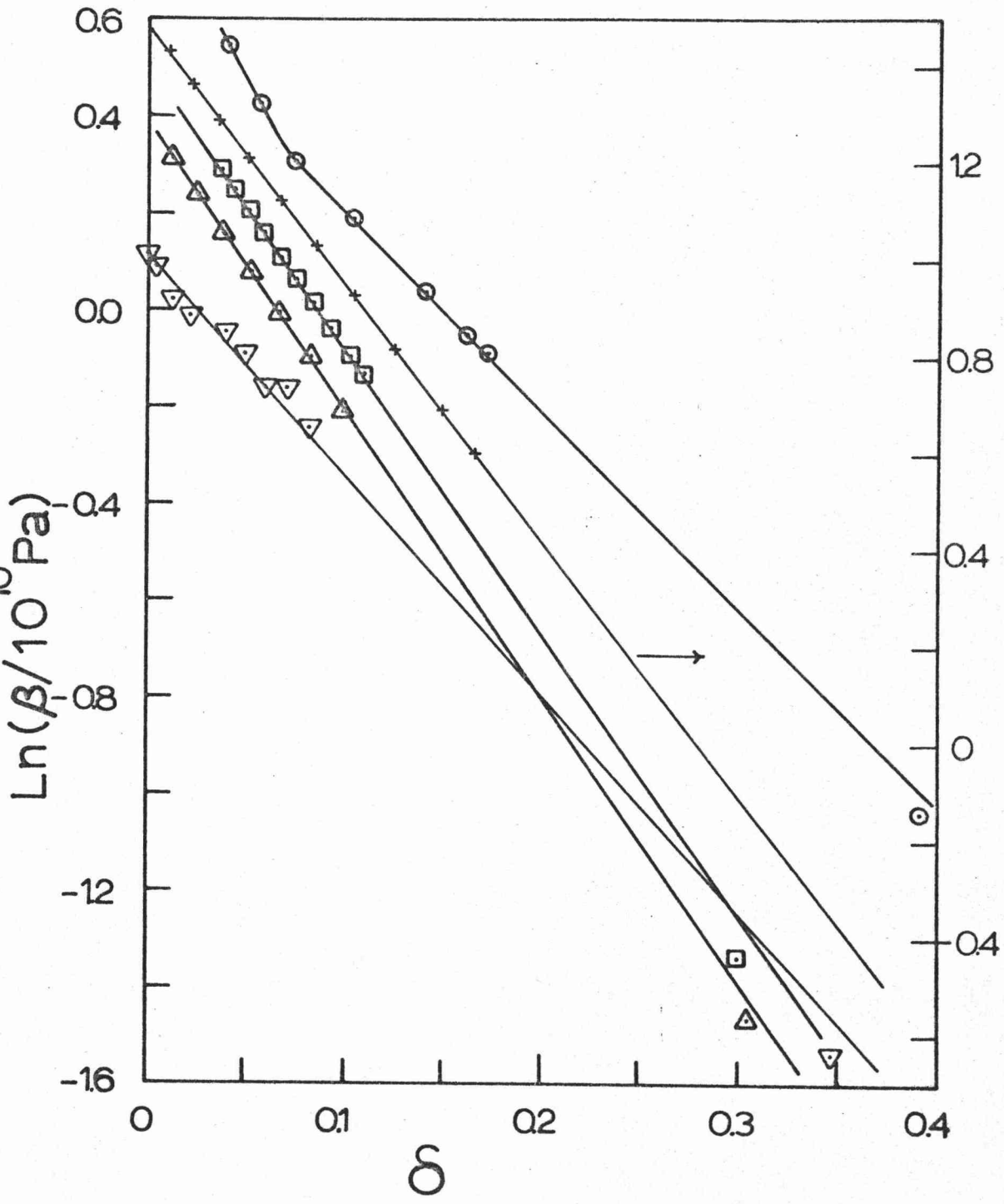

Fig. 4.1 The isothermal bulk modulus, β as a function of dilatation for alkali halides up to their melting points and in their melts (the single points to the extreme right) + : NaF ; ⊙ : NaCl ; ⊡ : KCl ; △ : KBr ; ▽ : KI. β is not available for the melt of NaF.

able although we are able to include NaF and NaI. The last point in each group is either at or close to T_m. Clearly for all crystals the isothermal bulk modulus has the form $\beta = \beta_o \exp(-g_\beta \delta)$ where g_β appears to be three times the Gruneisen constant. This should be compared with eqn. (4.9) and the implied expression for the force constants $f = fo \exp(-2g\delta)$. Interestingly for NaCl, NaI, KCl and KBr the bulk modulus for the melt just above T_m nearly fits the extrapolated line. (The small discrepancy between point and line may be explicable in terms of a small second order shear contribution). We may therefore imagine the bulk modulus to be a simple continuously variable function of dilatation through the melting expansion and the question arises as to whether other properties may be treated in the same way without reference to the disordered structure of the melt. The most immediate implication is that where we have assumed the elastic moduli to be constant during melting in formulating equation (4.4) for the strain energy density, we must admit rather large changes in the moduli. Fig. 4.1, however, has shown that we may safely integrate through the melting expansion. Thus the dilatation strain energy becomes

$$W_\delta = \int_{\delta_m^s}^{\delta_m^l} \beta\,\delta\,d\delta = \beta_o \int_{\delta_m^s}^{\delta_m^l} \delta \exp(-g_\beta \delta)\, d\delta$$

$$= (g_\beta)^{-2} \left\{ (1 + g_\beta \delta_m^s)\, \beta_m^s - (1 + g_\beta \delta_m^l)\, \beta_m^l \right\} \qquad (4.18)$$

δ_m^s e.g. denotes the value of δ in the solid at the melting point. Values of g_β, β_o and $W_\delta / \rho_l \Delta H_m$ calculated from fig. 4.1 are listed in Table 4.4 and evidently the expansion on melting contributes only about one third the enthalpy of melting. Therefore the local shear which takes place on melting, manifesting itself as a change in co-ordination number must contribute the remaining two thirds. To calculate the shear contribution we plot ln c_{44} against dilatation in fig. 4.2 and extrapolate the high temperature linear regions to obtain the local $\{100\}$ shear moduli marked by solid points. The isothermal value of c_{44} is the same as the adiabatic value and consequently we have complete results

Salt	g_β^-	$\frac{\beta_o}{10^{10}\text{Pa}}$	$\frac{w_\delta}{\rho \Delta H_m}$	g_μ	$\frac{\mu_o}{10^{10}\text{Pa}}$	$\frac{\mu_\ell}{10^{10}\text{Pa}}$	$\frac{w_e}{\rho \Delta H_m}$	$g_{\mu'}$	$\frac{\mu_o'}{10^{10}\text{Pa}}$	$\frac{\mu_\ell'}{10^{10}\text{Pa}}$	$\frac{w_{e'}}{\rho \Delta H_m}$	$\frac{\mu_\ell V_\ell}{2RT}$
LiF				2.13	6.16			7.26	3.02	.107		.823
NaF	5.26	4.54	.237	1.38	2.69	1.50	$8.55\sum_3^5 \hat{e}_i^2$	4.45	3.59	.549 (.219)	$4.05\sum_1^2 \hat{e}_i^2$	5.55 (2.21)
NaCl	4.11	1.85	.372	1.54	1.24	.676	$7.58\sum_3^5 \hat{e}_i^2$	4.75	1.34	.209 (.087)	$5.23\sum_1^2 \hat{e}_i^2$	4.40 (1.84)
NaI	4.75	1.13	.346	2.01	.784	.390	$10.8\sum_3^5 \hat{e}_i^2$	8.63	1.24	.062	$3.92\sum_1^2 \hat{e}_i^2$	2.2
KCl	5.84	1.66	.294	1.88	.621	.354	$7.23\sum_3^5 \hat{e}_i^2$	9.26	1.67	.103	$5.95\sum_1^2 \hat{e}_i^2$	2.90
KBr	5.92	1.47	.331	2.95	.530	.215	$6.90\sum_3^5 \hat{e}_i^2$	10.8	1.51	.056	$5.38\sum_1^2 \hat{e}_i^2$	1.87
KI				1.79	.371	.223		6.96	1.07	.147 (.055)		6.28 (2.35)
RbI				2.34	.300	.280		13.6	1.36	.059		2.82
CsBr				8.83	.749	.108		2.41	1.16	.683		4.85
CsI				9.30	.628	.083		2.56	.905	.517		4.55

Table 4.4 Values of parameters describing the dilatation dependence of β, μ and μ' together with contributions to the enthalpy of melting from dilatation, (100) shear and (110) shear. The last column shows the activation exponent for maximum shear. For discussion see the text.

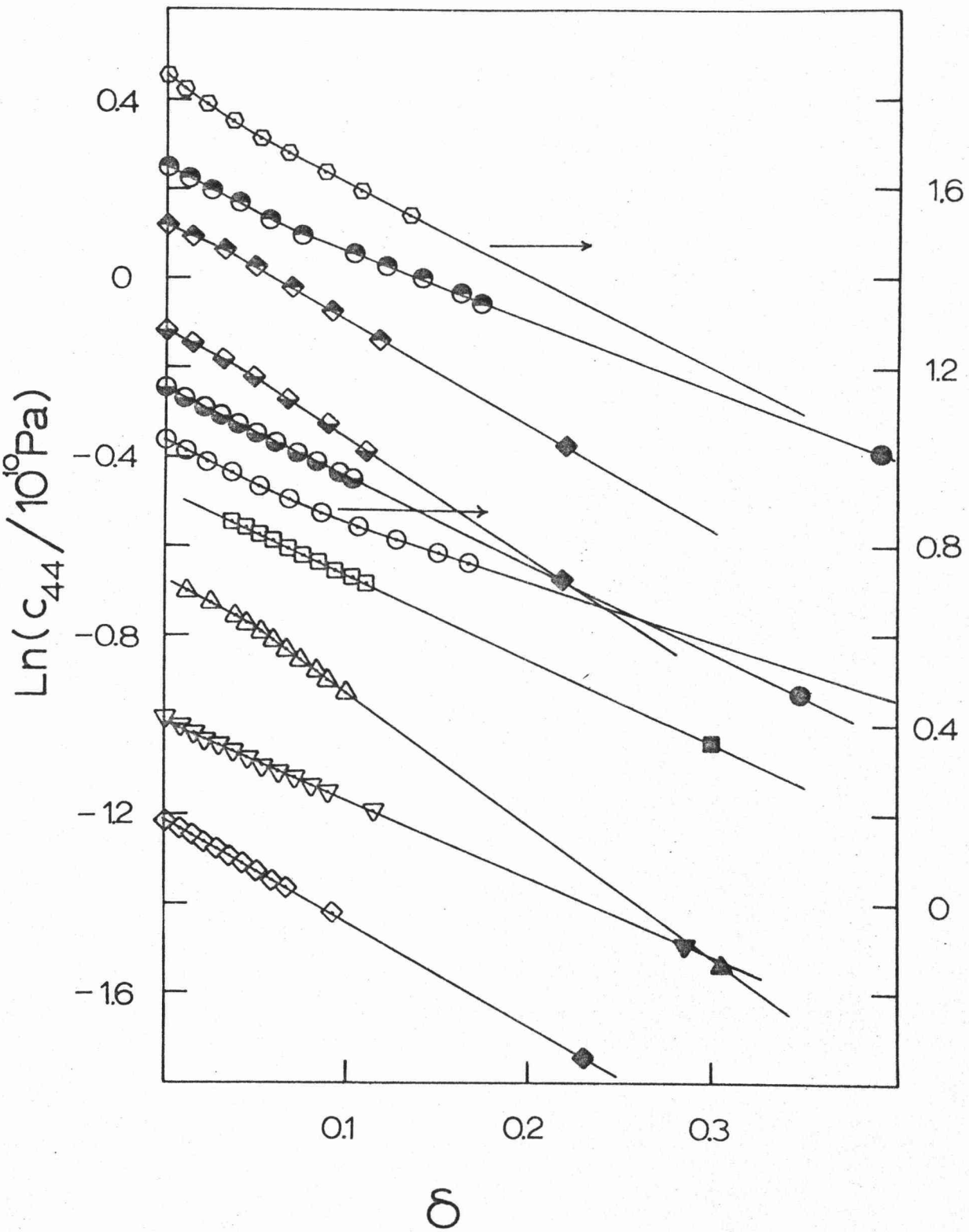

Fig. 4.2 The shear modulus c_{44} as a function of dilatation in the solid and in the melt. The solid points are the predicted effective shear moduli for the melts. ⊙ : LiF ; ⊙ : NaF ; ◓: NaCl ◓ : NaI ; ⊡ : KCl ; △ :KBr ; ▽ :KI ; ◇ :RbI ; ◆ : CsBr ; ◆ : CsI. The modulus for CsBr and CsI is $\frac{1}{2}(c_{11} - c_{12})$.

here for a greater number of salts. Thermal expansion data was obtained from ref. 3 p.49. Some of the salts have two linear regions and consequently we can say that at high temperature the dilatation dependence is of the form

$$\mu = \mu_o \exp (- g_\mu \delta), \qquad (4.19)$$

and the values of g_μ , μ_o and the effective shear modulus c_{44}^1 for the melt are listed in Table 4.4. To calculate the $\{100\}$ shear strain energy it is necessary to select a path of integration for the differentials. There are two extreme virtual processes which might be considered. At the dilatation of the solid at the melting point the shear may appear with energy $\frac{1}{2} \mu^s (e_1^2 - e_s^2)$ and subsequently the dilatation appear adding a term $(\mu^1 - \mu^s) e_1^2$, or on the other hand the dilatation may first appear with energy $(\mu^1 - \mu^s) e_s^2$ and then the shear with a further energy $\frac{1}{2} \mu^1 (e_1^2 - e_s^2)$. Here e denotes any one of the e_j, j = 3, 4 or 5, and we have assumed the moduli depend only on dilatation and not shear. It is more likely, however, that an intermediate path will be followed whereby the dilatation and shear increase hand in hand. Moreover, from symmetry considerations, the dilatation must be an even function of the shear, consequently we assume $e^2 = C\delta$ and obtain for the shear energy density

$$W_e = \int_{e_s}^{e_1} \mu e de = C\mu_o \int_{\delta_m^s}^{\delta_m^1} e^{-g_\mu \delta} d\delta$$

$$= C g_\mu^{-1} (\mu_s - \mu_1)$$

$$= (g_\mu \delta_m)^{-1} (\mu_s - \mu_1)(e_1^2 - e_s^2). \qquad (4.20)$$

If we assume the dilatation is uniformly distributed then the mean energy is given by replacing e_1 and e_s by their rms values. The total mean shear energy from strains e_3, e_4 and e_5 is given by summing the mean square shears in (4.20) and if we set $\hat{e}_{jm}^2 = \hat{e}_j^2 - \hat{e}_{js}^2$ we obtain

$$\overline{W}_e = (g_\mu \delta_m)^{-1} (\mu_s - \mu_1) \sum_{j=3}^{5} \hat{e}_{jm}^{\,2} \qquad (4.21)$$

The next listing in Table 4.4 gives the fractional contribution $\overline{W}_e/\rho_l \Delta H_m$ to the enthalpy of melting as a function of the as yet undetermined sum of the mean square $\{100\}$ shear strains, $\sum_3^5 \hat{e}_{jm}^{\,2}$. We have included the data for CsBr and CsI because of an interesting development we shall refer to soon. We emphasize at this point that μ' for these salts behaves similarly to μ for the rock-salt alkali halides and μ similarly to μ'. This is very evident in the table. The common feature shown in column 4 (and column 8 for CsBr and CsI) is that g_μ lies between 1.5 and 3 and consequently μ varies with dilatation only slowly.

Finally, we wish to examine the behaviour of the other shear strains e_1 and e_2 and the dilatation dependence of $\mu' = \frac{1}{2}(c_{11} - c_{12})$ and here perhaps the most significant feature appears. Fig. 4.3 is a direct plot of μ' against δ (μ for CsBr and CsI) and it is apparent that the curves extrapolated to the dilatation of the melt at T_m probably cut the δ axis there. We have therefore taken the liberty of plotting the points $\mu'(\delta = \delta_m^1) = 0$ and constructing smooth curves through the sets of data points for each salt. The resultant curves in every single case show that this shear modulus vanishes at the melting point but on the melt side rather than the solid side as Born's instability theory assumes. Some adjustment in δ_m^1 was necessary in the case of CsBr and CsI. The fractional change in volume on melting, δ_m, in CsBr is 26.8% and in CsI, 28.5% whereas in CsCl it is only 10.5%. However, at ~ 750 K CsCl changes to the rock salt structure with an expansion of 16.5%. It has therefore been suggested[1] that CsBr and CsI experience this transition on melting so that the observed melting expansion comprises a sum of the bcc to fcc expansion and the real melting expansion. We have therefore, for want of more accurate numbers, subtracted the 16.5% expansion seen in CsCl from the observed melting expansions and used the new dilatations in fig. 4.3. The

1 J.W. Johnson, P.A. Agron and M.A. Bredig, J. Am. Chem. Soc. 77, 2734 (1955).

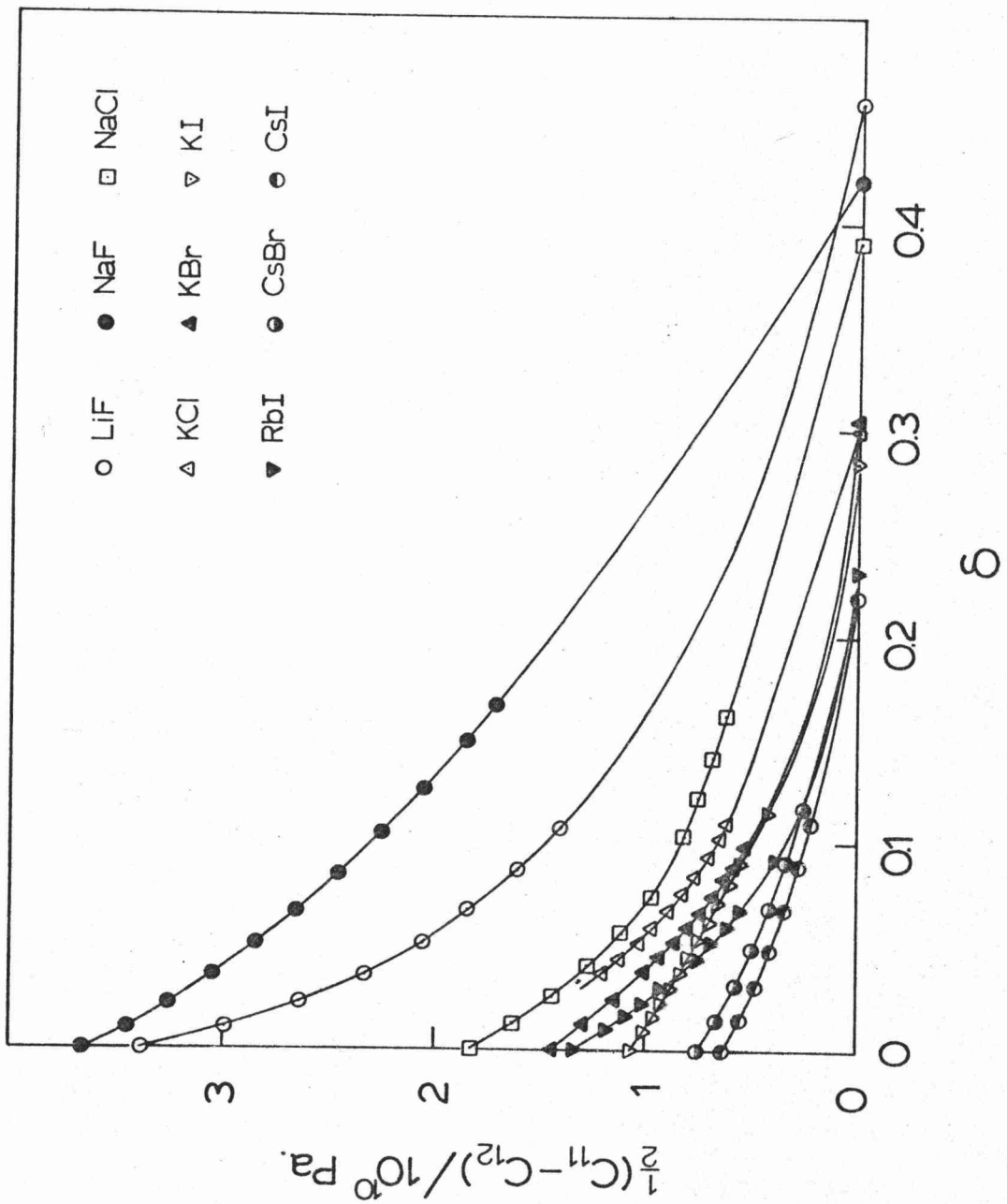

Fig. 4.3 The shear modulus $\frac{1}{2}(c_{11} - c_{12})$ as a function of dilatation in the solid and in the melt. The modulus appears to vanish at the melt side of the melting point. The modulus for CsBr and CsI is c_{44}.

result is that both curves extrapolate to zero at these points thus emphasizing the generality of this result. If $\ln(\mu')$ is plotted against δ, straight lines result so that

$$\mu' = \mu'_o \exp(-g_{\mu'} \delta), \qquad (4.22)$$

and the values of μ'_o and $g_{\mu'}$ are listed in Table 4.4. If there is no departure from this form, μ' will be close but not equal to zero at δ_m^1 and the extrapolated values of μ'_1 are also listed in the table. The average shear energy density arising from $\{110\}$ shear is given by an expression similar to eqn. (4.21), namely

$$\bar{W}_{e'} = (g_{\mu'} \delta_m)^{-1} (\mu'_s - \mu'_1) \sum_1^2 \hat{e}_{jm}^2 \qquad (4.23)$$

and the fractional contribution $\bar{W}_{e'} / \rho_1 \Delta H_m$ to the enthalpy of melting is listed in the second to last column in Table 4.4. Now, since the three contributions $\bar{W}_\delta / \rho_1 \Delta H_m$, $\bar{W}_e / \rho_1 \Delta H_m$ and $\bar{W}_{e'} / \rho_1 \Delta H_m$ sum to unity, we have for NaCl

$$5.23 \sum_1^2 \hat{e}_{im}^2 + 7.58 \sum_3^5 \hat{e}_{im}^2 = 0.628 \qquad (4.24)$$

and similar obvious equations for NaF, NaI, KCl and KBr also hold.

4.4 A Shear Instability Hypothesis for Melting.

We have shown that the elastic moduli may be considered to be continuous functions of dilatation only, and most importantly that one of the shear moduli vanishes at the liquid side of the melting point i.e. when $\delta = \delta_m^1$. Born's theory of melting may therefore be reformulated in a manner which avoids the objections raised in the review in §2.2. Firstly, if μ' is plotted against temperature it is still finite and large at the melting point, where its macroscopic value discontinuously falls to zero. On this basis alone the instability theory could be rejected except that now we see that the most useful variable is dilatation rather than temperature and provided the expansion on melting is viewed as a virtual process μ' falls continuously to zero. Furthermore, the theory now becomes a two phase theory in that the solid at the melting point has dilatation δ_m^s and the melt at T_m is described by the same parameters and formulae as the solid except that the dilatation is δ_m^1. In Born's theory,

solid and liquid at the melting point are identical, with μ or μ' equal to zero i.e. his melting transition is not first order. With our model, the discontinuity of the transition may be deduced rather simply. Supposing that the δ dependence of the shear modulus μ' is as shown in fig. 4.3. If the lattice is expanded continuously the energy of the lattice is continuously increased and this may be continued until vanishes. Just before this point, the free energy has some well defined value and when $\mu' = 0$ the onset of fluidity will cause the molar entropy to increase by an amount equal to the communal entropy 2R, and the free energy therefore to decrease. We may thus move back along the curve decreasing the dilatation and hence the elastic internal energy to locate a point at which the virtual solid-free energy equals the free energy at $\delta = \delta_m^l$. (The shift will also involve a change in vibrational entropy so the elastic energy must be decreased by more than 2RT). This point is of course $\delta = \delta_m^s$ and the solid may transform isothermally with heat absorbtion from $\delta = \delta_m^s$ to $\delta = \delta_m^l$. Another strength of the model is that if melting is seen to be a continuous expansion from δ_m^s to δ_m^l the free energy just below δ_m^l is greater than at δ_m^l by 2RT per mole. Consequently, there is a nucleation barrier of this magnitude and melting will tend to nucleate preferentially at surfaces and strained sites to avoid this barrier. The model therefore naturally leads to heterogeneous melting.

It would, therefore, be worthwhile to re-examine Born's melting theory in terms of this modified criterion for melting to see how the quantitative predictions are altered. We only go as far as transposing his elastic modulus μ as a function of temperature to a function of dilatation for atmospheric pressure. This is shown in fig. 4.4. and is similar in form to the curves in fig. 4.3. The value of g_μ obtained from a semi-logarithmic plot of Born's μ is 8.4 which is of similar magnitude to $g_{\mu'}$ for most salts in Table 4.4 and to g_μ for CsBr and CsI.

The fact that μ' is of the form of eqn. (4.22) means that μ' is close to but not equal to zero at $\delta = \delta_m^l$. Indeed μ' does not need to vanish for shear flow to take place spontaneously,

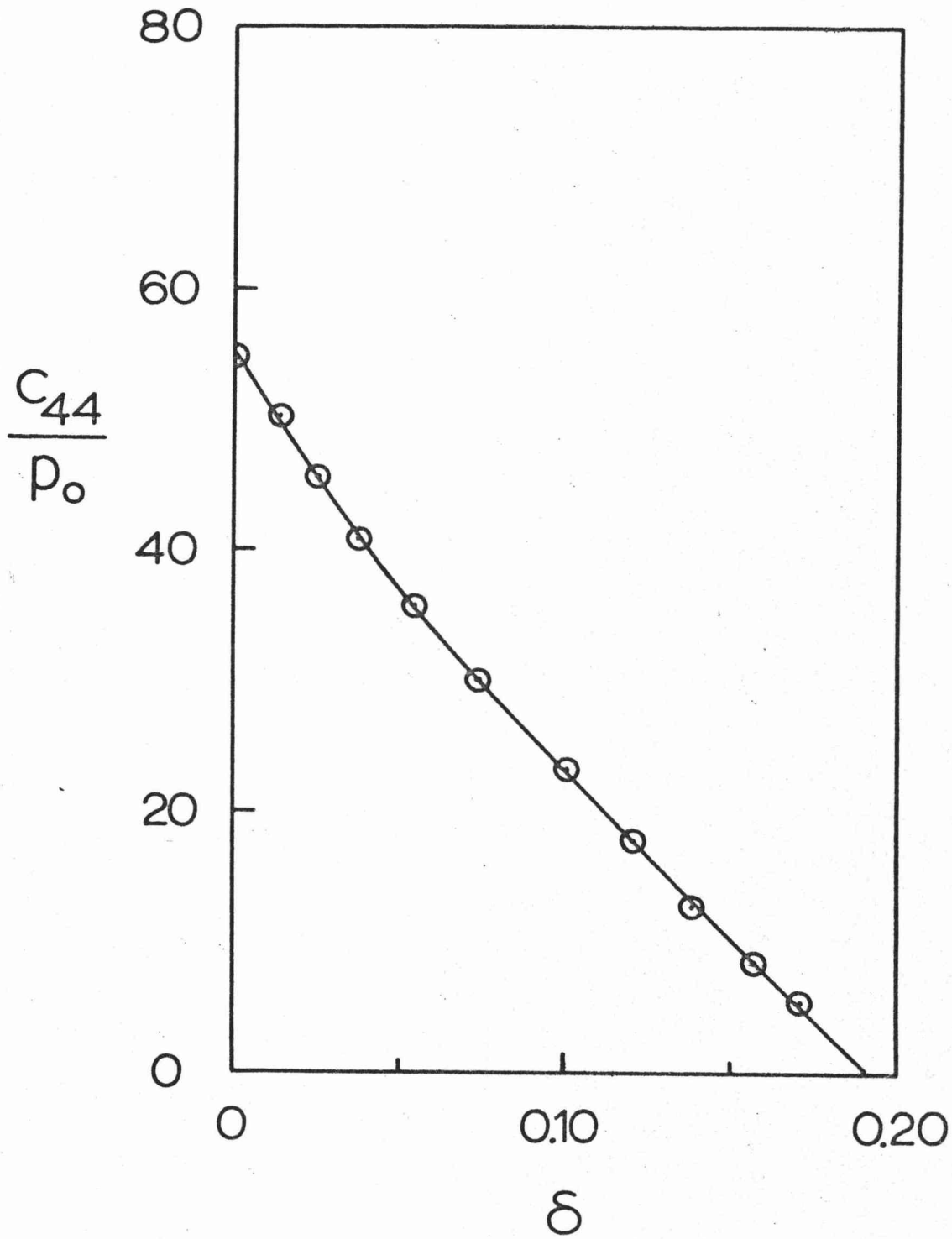

Fig. 4.4 Born's theoretical values of the shear modulus c_{44} replotted versus dilatation. p_o is given by u/V_o where V_o is the atomic volume and u is the dissociation energy of an isolated atom pair. The form of this curve should be compared with that of the experimental curves shown in fig. 4.3.

it needs only to become small enough that the shear energy for maximum local shear is comparable to the thermal energy. Now the shear energy per mole is $\frac{1}{2}\mu_1'\hat{e}_1^2 V_1$ and the maximum shear is $e_1 = 1$ where an anion is at point of riding over a cation. The proportion of ions at any instant in this state of maximum shear, i.e. which are flowing, is $\exp(-\mu_1' V_1/2RT_m)$. Values of the exponent are listed in the last column of the table and there is a fairly wide variation which is greatly amplified via the exponential function. It became clear to us, however, that there were inconsistencies between the reported thermal expansions[1], volume expansions on melting[2] and densities of the melts.[3] Where there was disagreement, we assumed it was in the thermal expansion data (which in many instances applied only up to 100 to 200 K below T_m) and calculated the molar volume and dilatation of the solid at the melting point from the melt density and melting expansion. This altered the values of many of the parameters in Table 4.4 and we have included new estimates of μ_1' and $\mu_1' V_1/2RT$ in brackets in the appropriate columns. The significant point is that, except in the cases of LiF, CsBr and CsI, $\mu_1 V_1/2RT$ is approximately, and averages to, 2.3. As a consequence, about 1/10 of all ions at any instant are in the process of passing through maximum shear. The fact that CsBr and CsI have larger values of $\mu_1' V_1/2RT$ is undoubtedly due to our inability to determine the operative volume expansions in the melting of these salts.

A cursory examination of the temperature dependence of the elastic constants of metals[4] suggests that the same shear instability hypothesis we have proposed here may also apply with them and it will be very interesting to see how

1 K.K. Srivastava and H.D. Merchant, loc. cit.

2 H. Schinke and F. Sauerwald, Z. Anorg. Chem. 287, 313 (1956).

3 G.J. Janz et al, NSRDS - NBS 15 (1968).

4 R.F.S. Hearmon, loc. cit.

general our hypothesis is. The fact that we can proceed as far as we have with often inaccurate and incomplete data suggests that great value could be obtained from further precise measurements of both elastic constants and volume expansion right up to and through the melting point for a wide range of single crystalline materials.

4.5 Calculation of the Strains $\hat{e}_i$ in the Melt.

By equating the strain energy density with the enthalpy of melting, we obtain eqn. (4.24) for NaCl and similar equations for the other alkali halides. The sums of $\{110\}$ mean square strains $\sum_1^2 \hat{e}_i^2$ and $\{100\}$ mean square strains $\sum_3^5 \hat{e}_i^2$ may be determined separately by evaluating the entropy of melting expressed in eqn. (4.16). In Table 4.5 the melting entropies are compared with the sum ΔS of the first three terms of eqn. (4.16) for $\eta=2$ and $\eta=3$. In both cases ΔS exceeds ΔS_m and consequently the net shear contribution to the entropy must be negative. This is of course possible since Table 4.3 shows $g_s(1)$ and $g_s(2)$ to be negative and approximately three times the magnitude of $g_s(3)$, $g_s(4)$ and $g_s(5)$. By including the shear terms and equating the total theoretical expression for ΔS_m with the observed valueswe obtain e.g. for NaCl with $\eta=2$

$$-5.40 \sum_1^2 \hat{e}_{im}^2 + 1.63 \sum_3^5 \hat{e}_{im}^2 = -0.407 \qquad (4.25)$$

Let us denote $(\sum_1^2 \hat{e}_{im}^2)^{\frac{1}{2}}$ by $\hat{e}_{110}$ and $(\sum_3^5 \hat{e}_{im}^2)^{\frac{1}{2}}$ by $\hat{e}_{100}$, then by combining eqns. (4.25) and (4.24) we find $\hat{e}_{110} = 0.289$ and $\hat{e}_{100} = 0.163$. These values and those calculated for the other five salts for which full data is available, are also listed in Table 4.5 for $\eta=2$. The ratio $\hat{e}_{100}/\hat{e}_{110}$ of $\{100\}$ shear strain to $\{110\}$ shear strain is listed for $\eta=2$ and $\eta=3$.

One self consistent interpretation of these results becomes apparent. The closest set of values of ΔS to ΔS_m is for $\eta=2$, which implies a local two-dimensional strain, in particular, that δ is of the form $\epsilon_{11} + \epsilon_{22}$. This is suggestive of a local linear disorder such as that due to arrays of dislocations. In Appendix F we present equations

Salt	$\Delta S_m/R$ (expt)	$\Delta S/R$ ($\eta=2$)	$\Delta S/R$ ($\eta=3$)	$\hat{e}_{100}$ ($\eta=2$)	$\hat{e}_{110}$ ($\eta=2$)	$\hat{e}_{100}/\hat{e}_{110}$		
						($\eta=2$)	($\eta=3$)	dislocation
LiF	2.91	4.20	4.85					
LiCl	2.70	4.21	4.87					
LiBr	2.58	4.23	4.91					
LiI	2.38							
NaF	3.16	4.23	4.91	.163	.364	.448	-	.696
NaCl	3.16	4.38	5.05	.163	.289	.565	.129	.600
NaBr	3.08	4.11	4.70					
NaI	3.04	3.81	4.35	.190	.260	.729	.481	.680
KF	2.89	3.53	3.97					
KCl	3.03	3.74	4.22	.232	.231	1.01	.692	1.12
KBr	3.05	3.75	4.24	.242	.222	1.09	.788	1.22
KI	3.03	3.68	4.14	.311	.232	1.34	1.08	1.34
RbF	2.73							
RbCl	3.06							
RbBr	2.73	3.32	3.66					
RbI	1.64	3.31	3.63					

Table 4.5: Melting entropies obtained from experiment and from the first three terms in eqn. (4.16) for $\eta=2$ and $\eta=3$ together with values of the rms shear strain required for equality of the total theoretical value of ΔS_m (eqn. 4.16) with the experimental value. The values of $\hat{e}_{100}/\hat{e}_{110}$ for $\eta=2$ and $\eta=3$ are given together with the value of that ratio, calculated from elastic constants at T_m, for an edge dislocation. Agreement is good with the $\eta=2$ value which is consistent with the two dimensional dilatation $(\epsilon_{11}+\epsilon_{22})$ in the core of an edge dislocation. This suggests the applicability of a dislocation theory of melting.

for the stresses about an isolated edge dislocation calculated from isotropic elasticity. Using μ and μ' we may calculate the rms shear strains from these and the ratio of $\{100\}$ to $\{110\}$ shear strain is

$$\hat{e}_{100}/\hat{e}_{110} = (\mu'/\mu)\left[1 + \tfrac{2}{3}(1-2\nu)^2\right]^{-\frac{1}{2}}, \qquad (4.26)$$

where ν is Poisson's ratio. The expression for $\hat{e}_{100}/\hat{e}_{110}$ for an edge dislocation is evaluated and presented alongside the values for $\eta=2$ and $\eta=3$ in Table 4.5 and indeed the agreement with the values for $\eta=2$ is remarkably good. On the other hand there is no agreement with the values obtained for $\eta=3$. The only salt for which the shear strain ratio for $\eta=2$ is not very close to the ratio for an edge dislocation is NaF and referring to Table 4.3 we note that for this salt our estimate of g from eqn. (4.11) is much less than the experimental value. Consequently the value of $g_s(1)$ estimated from eqn.(4.12) is probably also too low. Comparing the value of $g_s(1)$ in column 4 with the values for other salts suggests this is probably the case. If $g_s(1)$ were increased, $\hat{e}_{110}$ would decrease possibly giving better agreement for the shear strain ratios. Strictly the ratio $\hat{e}_{100}/\hat{e}_{110}$ for an edge dislocation should be calculated using the anisotropic elasticity theory of dislocations[1] however the equations become so awkwardly large that we have not done this. We conclude then that the local dilatations are probably of the form $\delta = \epsilon_{11} + \epsilon_{22}$, thus strongly suggesting the appearance of dislocation-like two dimensional strains in the melt. Furthermore, the ratios of $\{100\}$ to $\{110\}$ shear strain for the six alkali halides for which we have data are in agreement with the shear strain ratios for edge dislocations. Both these results suggest that the melt may be satisfactorily modelled in terms of arrays of dislocations.

1 J.W. Steeds, Anisotropic Elasticity Theory of Dislocations (Clarendon Press, Oxford, 1973) p.76.

In summary we have found it useful to describe the disordered state of the melt in terms of a set of independent dilatation and shear strains from which both the enthalpy and entropy of melting for 6 alkali halides can be well characterised. The enthalpy is determined from the separate strain energies and the entropy from the dependence of vibration frequencies on dilatation and (as a second order effect) on shear strain. The values of these strains suggest that the local disorder in the melt is similar to that near dislocations. By examining the dilatation dependence of the elastic constants we showed that there is a continuity through the melting expansion and liquid elastic properties could be considered as extrapolations with respect to dilatation of solid properties. In particular, the melting point is determined by the fact that the shear modulus $\frac{1}{2}(c_{11}-c_{12})$ for the rock-salt alkali halides and c_{44} for the caesium halides becomes sufficiently small on the liquid side of the melting point that a substantial proportion ($\sim\frac{1}{10}$) of all ions are in a state of shear flow. This model explains both the first order and the nucleation character of melting.

5 EXPERIMENTAL TECHNIQUE

Our experimental measurements near the melting temperature were, in the main, of electrical conductivity and differential thermometry under various conditions of ambient gas, heating rates, crystal type, orientation, and preparation. Other complementary information was obtained from visible changes and scanning electron microscopy.

5.1 Specimens.

Four kinds of alkali halides were studied: LiF, NaCl, NaBr and KCl. Each kind was investigated using differential thermometry, however, in only NaCl and KCl was the electrical conductivity extensively examined. All specimens were cleaved or sawn from highest purity single crystal optical blanks procured from Harshaw Chemical Company (Cleveland, Ohio). Wherever possible, specimens were fresh cleaved immediately prior to experimentation, however, to study the orientation dependence of surface conductivity we found we could not satisfactorily cleave faces of higher index than $\{100\}$. $\{110\}$, $\{111\}$ and $\{112\}$ faces were therefore prepared by sawing to the approximately correct orientation using a diamond wire (0.2 mm diameter) saw. They were then microtomed and polished, working down to 0.05 μm alumina grit in ethane-diol. Microtoming tended to produce a fine mosaic of small pits on the surfaces due to cracking and this could be largely eliminated by moistening the blade with ethane diol. The concentration of divalent impurities in the specimens as determined from the position of the extrinsic/intrinsic "knee" in the conductivity curves was generally less than 5 p.p.m.

5.2 Specimen Electrodes.

The electrical conductivity was measured using a number of electrode systems the basic configuration being that of the standard parallel plate capacitor, for rectangular prism crystals, with and without guard rings. In an effort to completely eliminate surface conduction, and because very close to T_m the conductance for the parallel plate system exceeded the limits for the conductance bridges, platinum

wire electrodes were inserted into crystals at right angles to each other and guard rings were affixed around the crystal edges. Measurements of surface conduction alone were made using a silver print earth ring painted concentrically around a silver print disc electrode on the crystal surface. The three electrode configurations are shown in fig. 5.1.

5.2.1 Parallel Plate Electrodes.

Conventional specimens were fresh cleaved to typical dimensions of 10 mm x 10 mm x 3.5 mm. These were plated over the whole of their large surfaces by careful painting using GC silver conducting print no. 21-2 (Hydrometals, Rockford, Illinois 61101) and were attached to the electrode leads by platinum wires with a dab of silver paint. The guard electrode was painted as a fine line along the middle of the smaller faces as shown in fig. 5.1a.

For an ideal parallel plate capacitor, the geometrical relationship between the electrical conductivity σ and the conductance G is

$$G = \sigma A/t \quad , \qquad (5.1)$$

where A is area of one of the plates and t is the separation of the plates. However, for specimens with the above dimensions fringing effects are significant, and we calculate these as follows. For a semi-infinite pair of parallel plates, if x denotes distance from an edge into the capacitor and parallel to a plate, then the field strength at $x/t = 1.0$ is 1.016 times the ideal field strength, and between that point and the edge, the flux is increased by 31.1% above the ideal.[1] Thus to first order, A in equation (5.1) must be increased by 0.311 times the perimeter area running from $x/t = 1.0$ to the edge, so that

$$G = \sigma\{A/t + 0.622\ (\lambda_1 + \lambda_2 - 2t)\}. \qquad (5.2)$$

λ_1 and λ_2 are the lengths of the large face. This edge correction neglects the second order corner correction which however is as small as the measurement errors. For the

1 E. Weber, Electromagnetic Fields 1 (Wiley,N.Y. 1950)p.337.

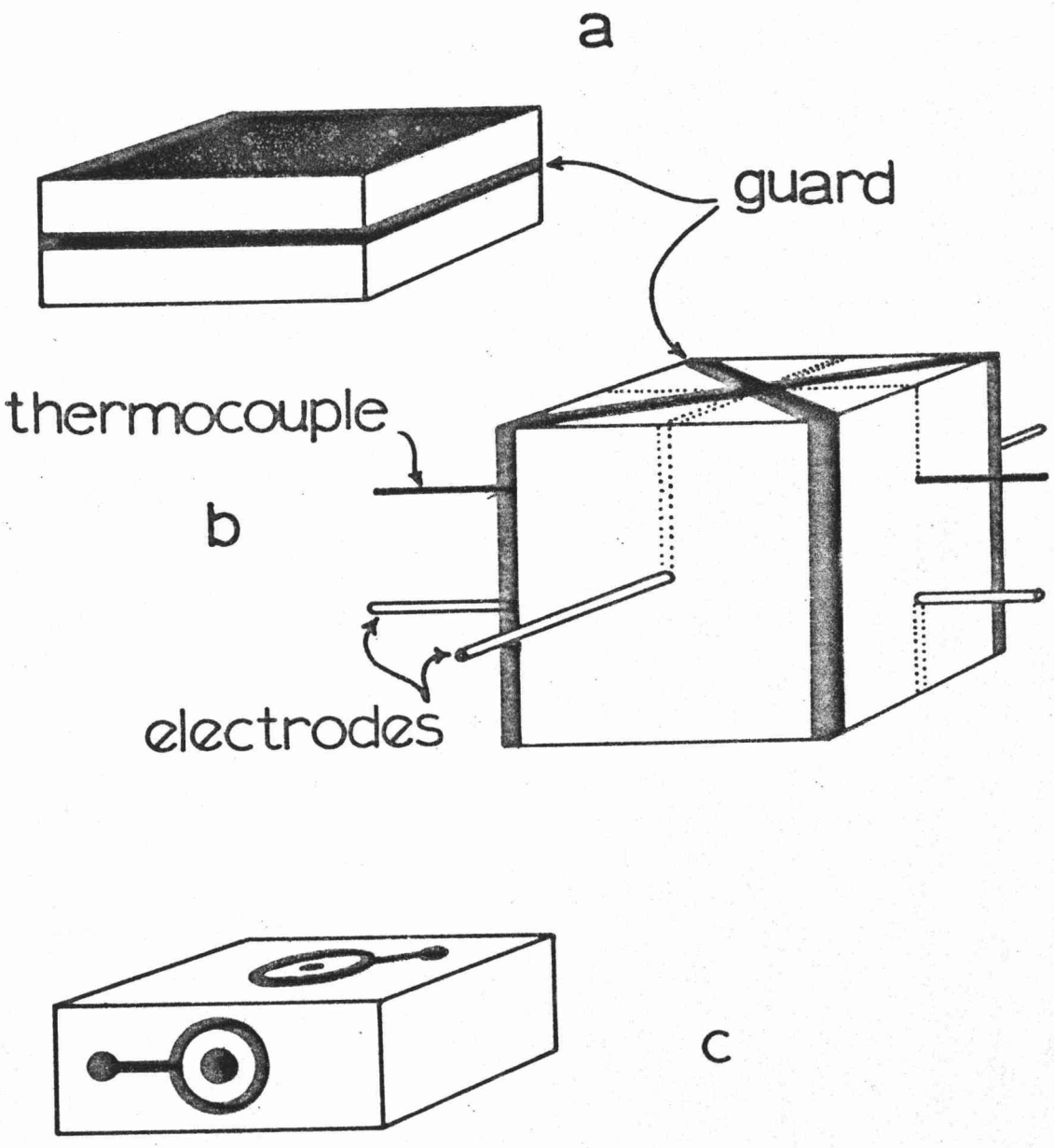

Fig. 5.1 Various electrode systems used for measuring ionic conductance (a) standard parrallel plate capacitor with guard ring (b) crossed inserted wires with guard ring and inserted thermocouple (c) concentric rings of silver conducting paint for measuring surface conductance.

typical dimensions noted above the correction is seen to be as large as 30% which means that all defect entropies obtained from conductivity experiments which neglect fringing will be systematically in error, and this error is of the same sign as that introduced by not suppressing surface conduction.

Near the melting point heat absorbtion by the specimen becomes sufficiently great that temperature differentials between specimen and specimen chamber develop, giving spurious results unless the thermocouple junction is placed within the specimen. This is, of course, not possible with the conventional specimens and the specimens were therefore mounted on a slab of the same material with a Pt - Pt/13% Rh thermocouple inserted from the side. The largest faces of the specimen and slab were horizontal. The thermocouple insertion technique is described in the next section.

5.2.2. Inserted Platinum Wire Electrodes.

While accurate measurements of σ may be effected using the parallel plate system, a number of problems became apparent when operating within a degree or so of T_m: (i) differential thermal analysis required the thermocouple to be inserted in the specimen itself and no additional slabs to be present in the chamber; (ii) evaporation and melting cause the geometrical factor A/t to decrease with time; as noted above (iii) a more effective means of blocking surface conduction was required and (iv) the value of G rose above the working limits of the conductance bridges. The most appropriate solution to these problems we were able to develop was to use platinum wire electrodes inserted into the crystals.

The rig in which this operation was performed is shown in fig. 5.2. Cube specimens of 1 cm edge are placed on a counterbalanced pivoted platform with an upthrust of about 5 gm wt. against a taut 0.3 mm diameter platinum wire which is supported parallel to the surface of the specimen. A current from a voltage controlled source is passed through the wire and increased slowly until, when the wire is a dull red heat, for most of the alkali halides, the crystal

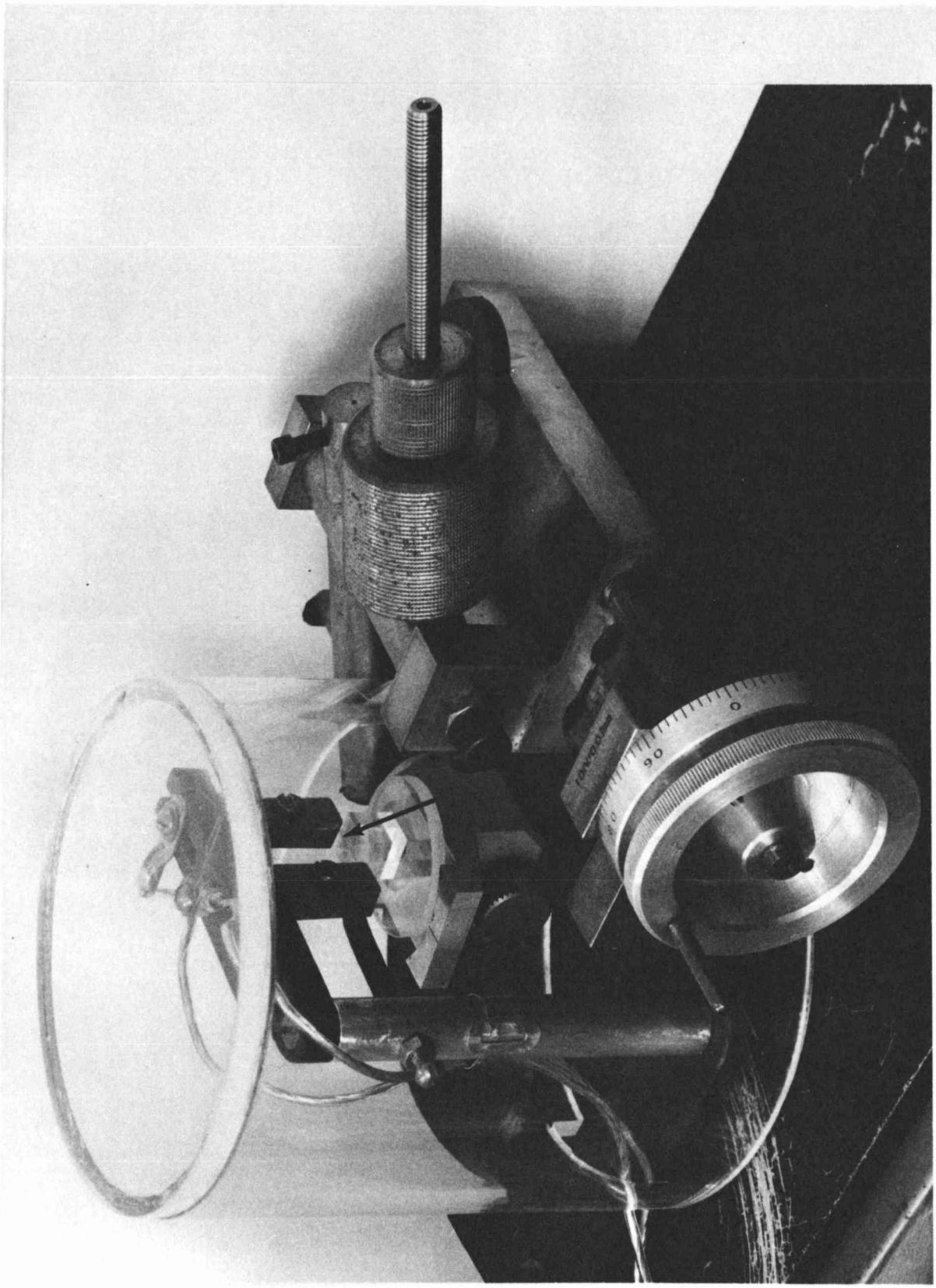

Fig. 5.2 Rig for inserting a wire electrode (arrowed) into specimens.

immediately adjacent to the wire melts and the wire slowly sinks to the required depth. (This depth must always exceed 2 mm otherwise the crystal will crack on cooling). The platinum wire is pulled to ~20 gm wt. tension by a light spring so as to prevent slight buckling of the wire when heating, and the mounting posts are sited 2-3 mm beyond the edge of the crystal. A larger gap would allow the free portion of wire to overheat and cause vaporisation and bubbles to form about the wire near the edge of the crystal. The whole procedure is carried out in an inert atmosphere of He. The thermocouple wires and junction may be inserted into the crystal using the same technique provided the junction bead is small, preferably no larger than the wire diameter. The result is that for NaCl, NaBr and KCl one can regularly insert wires which are bubble-free and have only a very thin sheath of crystal around the leading edge which has been melted and is therefore probably polycrystalline. Photographs obtained from the optical microscope suggest this sheath is less than 5 μm in thickness. Figs. 5.3 and 5.4 show typical optical microscope pictures of wires near the crystal edge as seen through the crystal, firstly for a careful insertion and secondly when the wire was allowed to overheat. In the former, except at the very edge, no bubbles are evident and the crystal looks undisturbed along the length of the wire; in the second numerous bubbles have formed around the wire. The track of the wire as seen on the side of the crystal is shown in fig. 5.5 and it is evident there that little more of the crystal than the width of the wire is disturbed by the procedure. After an experiment at high temperature near T_m, this track was no longer distinguishable suggesting that a substantial amount of grain growth had taken place in the polycrystalline region.

Two platinum wires are thus inserted perpandicular to each other from opposite faces to a separation ~2.0 - 2.5mm a little below the centre of the crystal and the thermocouple is inserted above. In this way, the conduction is confined to the region near the centre of the wires where they cross and is therefore unaffected by the presence of the thermo-

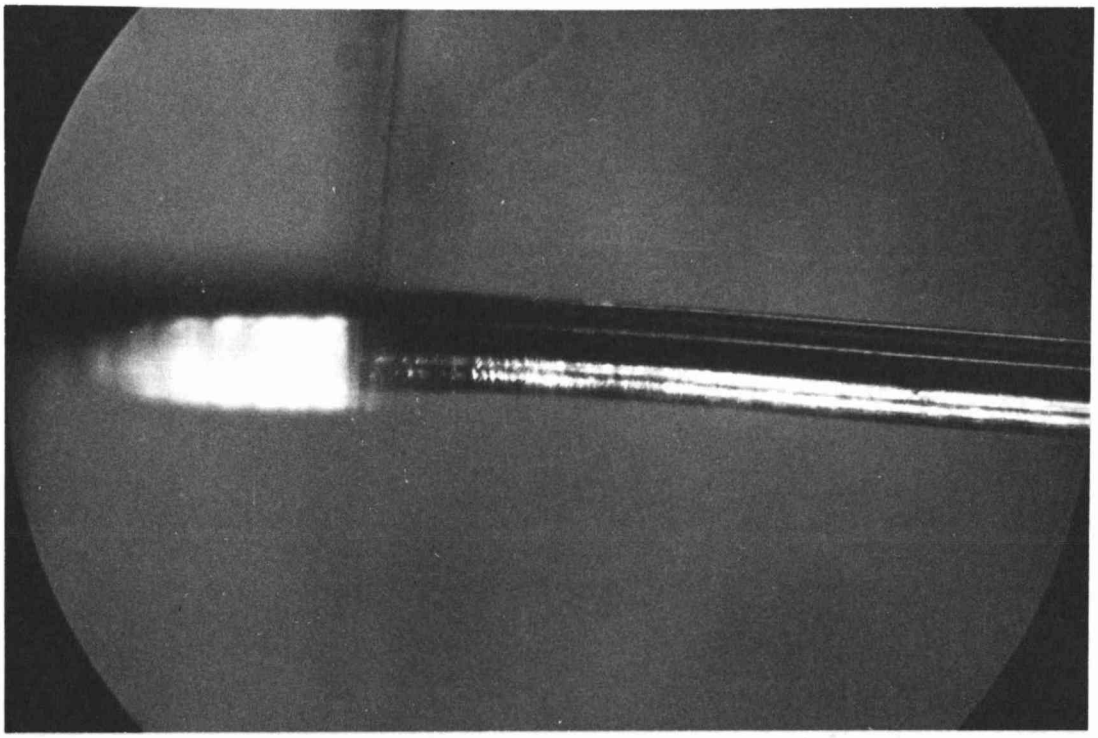

Fig. 5.3 Optical microscope photograph of a carefully inserted electrode near the edge of an NaCl crystal viewed through the crystal. Magnification = 50x.

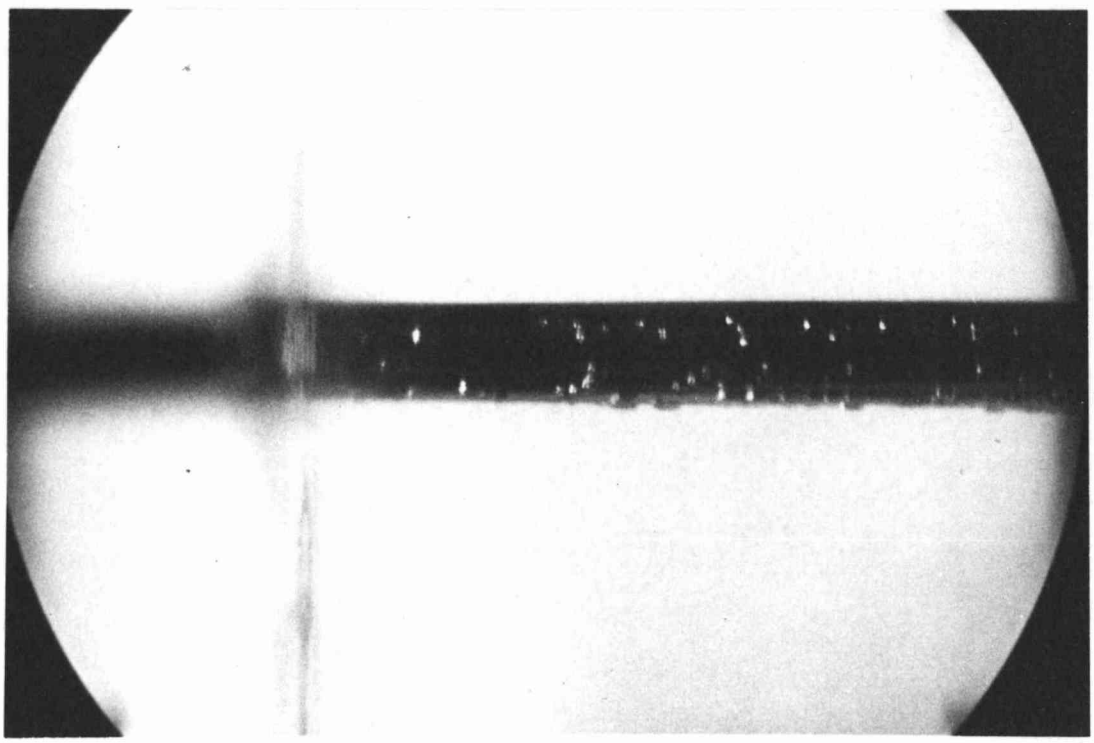

Fig. 5.4 An inserted electrode which was allowed to overheat. Bubbles have formed around the wire surface. KCl , 50x.

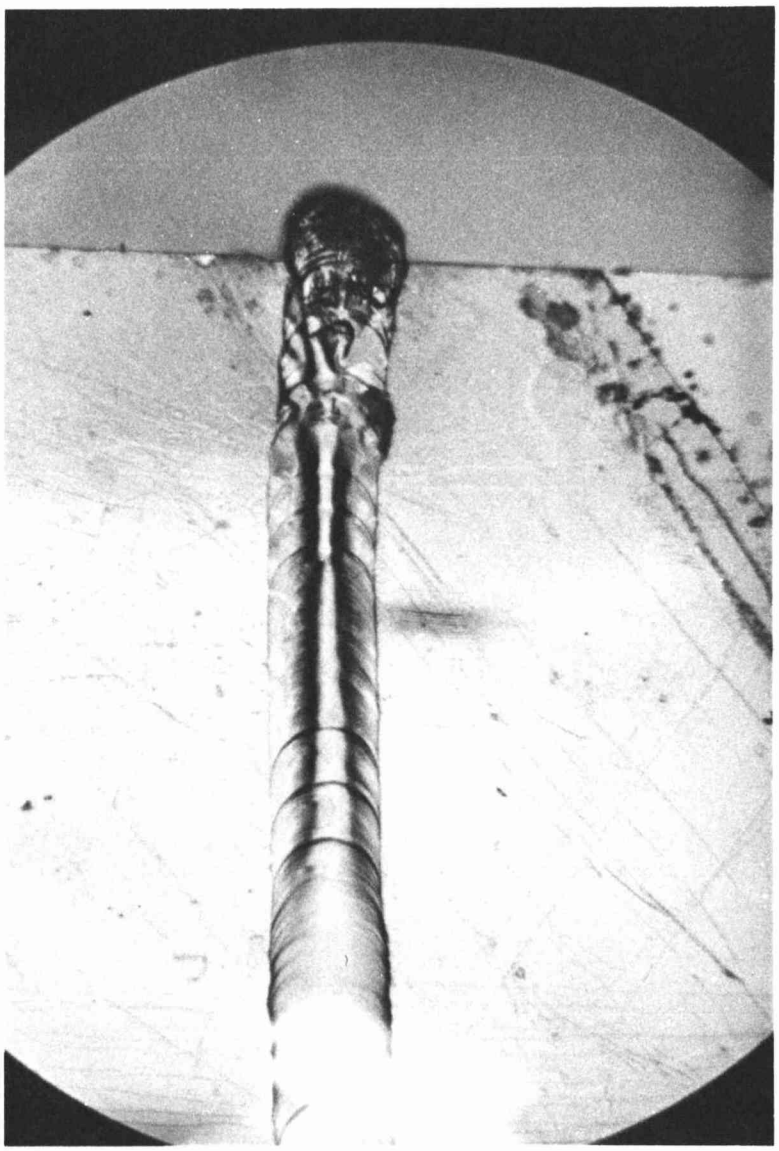

Fig. 5.5 The heated electrode track on the surface of a KCl specimen. Magnification = 50x.

couple and by loss of crystal due to vaporisation and melting. The absolute value of conductance is also lower than for the parallel plate system and the path for surface conduction is very much longer. In addition a silver print guard electrode was painted as shown in fig. 5.1 on the four vertical edges and as a cross on the top and bottom sides so that the two electrodes were electrically isolated via the surface path.

As a check that the inserted electrode technique gives valid results we prepared a specimen with parallel wires inserted 3 mm apart and painted silver print guard rings around each end of one wire. The electrostatics of this electrode system are readily soluble and it can be shown[1] that

$$G = \sigma \pi \lambda / \ln \left[D/d + \sqrt{(D/d)^2 - 1} \right] , \qquad (5.3)$$

where λ is the length of wire in the crystal, D is the separation of the two wires and d their diameter. This equation holds only for $\lambda \gg D, d$ where fringing at the ends may be neglected. For a finite rod[2]

$$G = \sigma \pi \lambda / \ln \left\{ \left[\sqrt{1 + (2D/\lambda)^2} - 1 \right] \lambda^2 / Dd \right\} , \qquad (5.4)$$

and for the present specimen the fringing correction was found to be only 2.6%.

Values of σ thus obtained are compared in fig. 5.6 with values obtained by the conventional parallel plate system for a specimen annealed overnight at 975 K. Typical of all specimens the conductivity of the parallel wire specimen at low temperatures has a negligible surface contribution which however increases markedly above the conductivity "knee" until it reaches and remains at a constant multiple ($\sim$2.3) of the bulk conductivity. The measured conductivity is less by a factor of 4.3 than the expected conductivity and is increased only a little by prolonged annealing at high temperature. It is not until the temperature is raised just into the anomalous premelting region

1 E. Weber, ibid., p.119.

2 ibid., p.114.

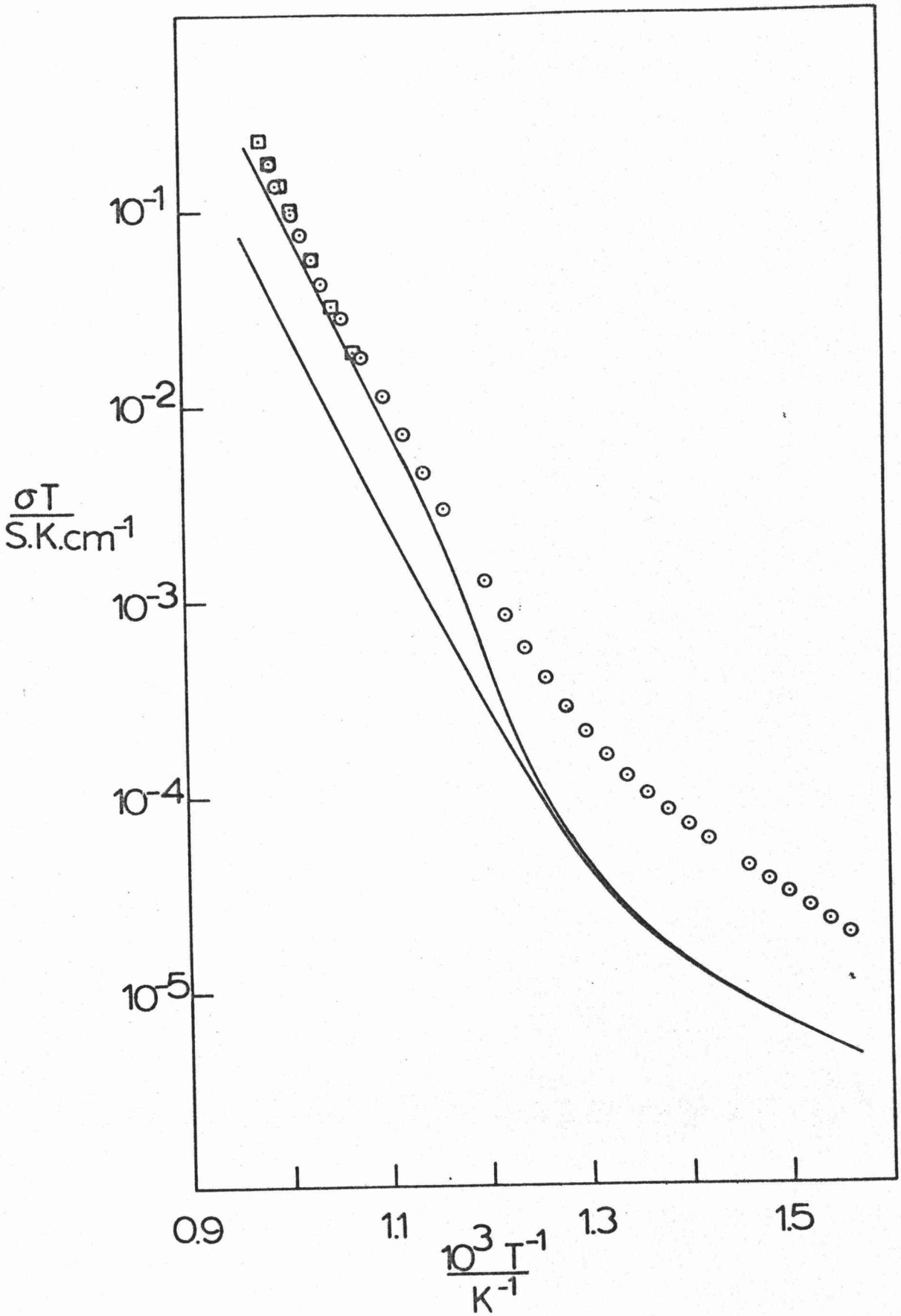

Fig. 5.6 Ahhrenius plot of the ionic conductivity of NaCl specimens. ⊙ well annealed parallel plate specimen with guard ring and fringing correction. Solid line, first heating of a specimen with parallel wire electrodes and a guard ring. The upper solid line is allowing surface conduction, the lower is suppressing surface conduction. On entering the premelting region and cooling the conductance (⊡) comes into agreement with that obtained with the standard system.

that agreement is obtained and this remains after subsequent entries into the premelting region. The squares in fig. 5.6 show a cooling curve after the first entry and the agreement with the parallel plate bulk conductance fully justifies the use of inserted wires. The annealing in the premelting region is presumed to be due to the escape of bubbles from the electrode wires.

5.3 Specimen Mounting Rig.

All specimens were mounted in the rig shown in fig.5.7 the skeleton of which was assembled from stainless steel threaded rods and annular rings. Four baffle discs which neatly fitted the furnace bore were located at different points along the rig to reduce convective flow within the furnace and thus assist in eliminating temperature gradients. Leads to the specimen were passed down eight alumina tubes into the specimen chamber, these leads comprising: two platinum and one platinum/13% rhodium thermopure Johnson and Mathey thermocouple leads and five high purity silver wires. This allowed the use of one absolute and one differential thermocouple and the silver leads provided for a number of simultaneous guarded conductance measurements.

In an effort to reduce specimen vaporisation, the specimen was enclosed in a chamber shown in fig. 5.8 comprising a fused quartz tube capped top and bottom by stainless steel discs.

The specimen platform was supported by a slender 1 mm diameter rod in order to ensure heat transfer to the specimen was radiative rather than conductive via the platform and its support. This was in fact demonstrated by the absence of preferential melting at the base of the crystal. Both fused quartz and stainless steel platforms were used. Specimens were separated from the platform by fused quartz, mica, slabs of the same specimen material, or placed directly on the platform. No significant effects were observed resulting from direct contact between the specimen and the stainless steel platform. All stainless steel used was nickel/chromium 316, and the furnace and rig were well baked out under vacuum at

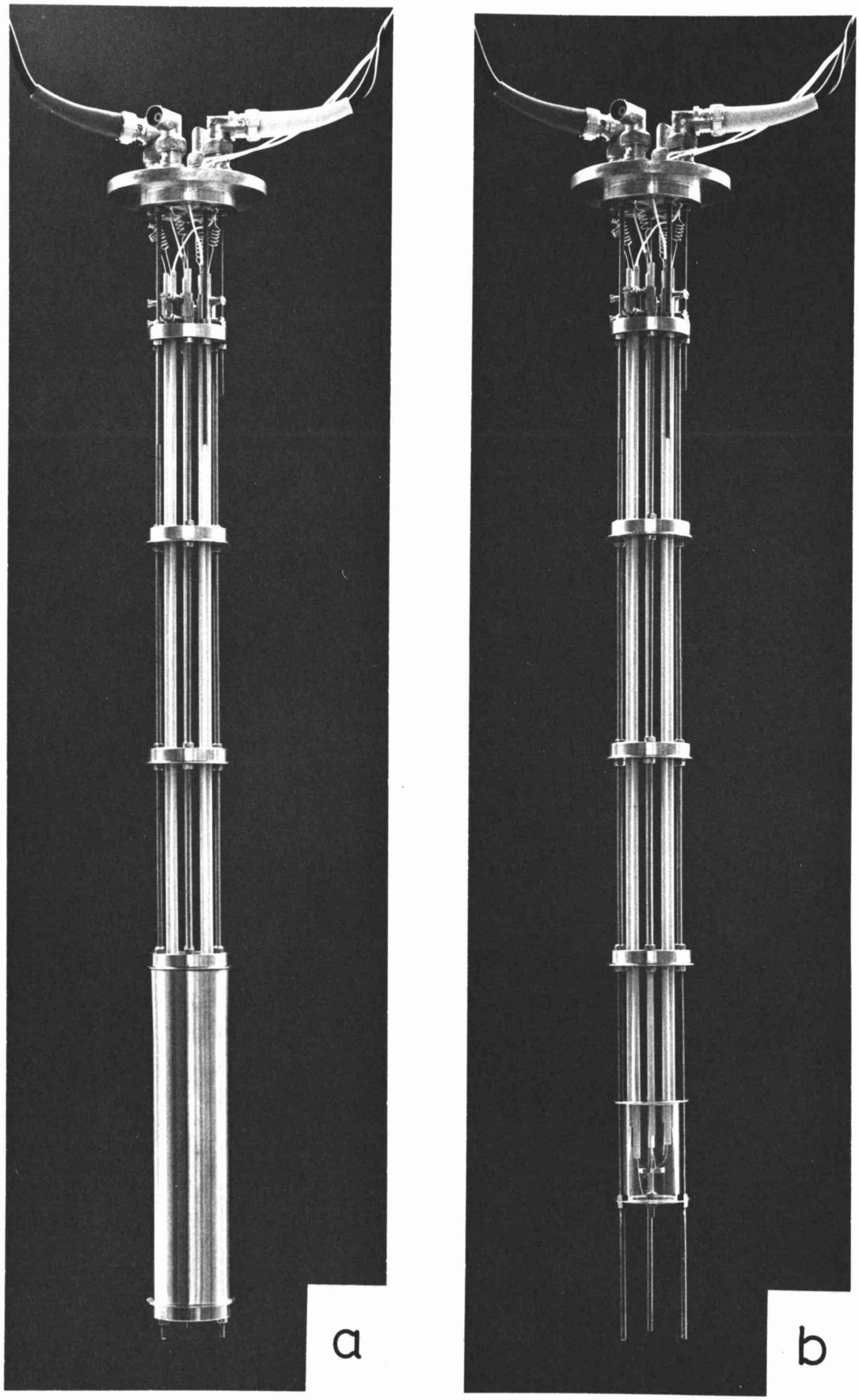

Fig. 5.7 Specimen mounting rig (a) fully assembled (b) showing inner specimen chamber.

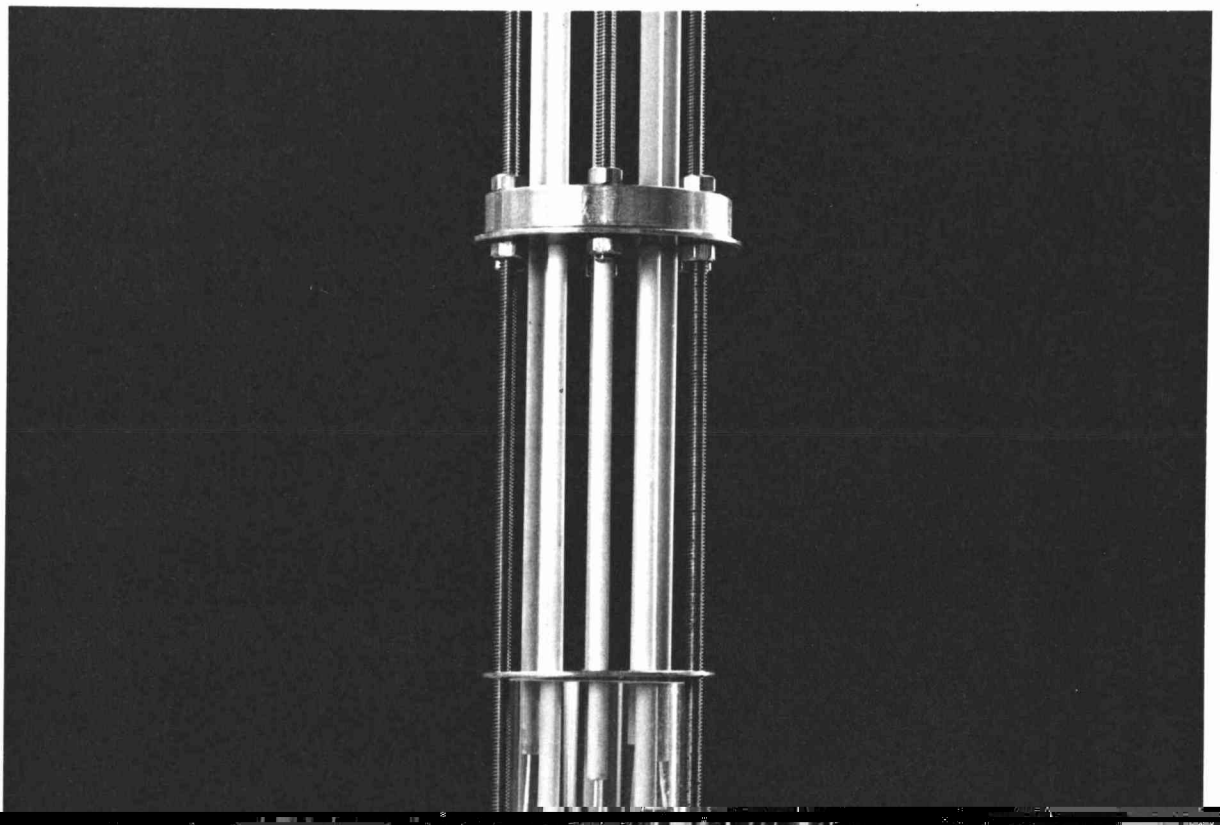

~1125 K before experimentation.

5.4 Furnace and Vacuum System.

The conductance rig was suspended down a furnace tube which has a working temperature range of 300 K to 1250 K and may be pumped down to 10^{-3} Pa using an oil diffusion pump or up to 3×10^{5} Pa (~3 atm). The temperature gradient was adjusted to be a minimum in the region of the specimen at the appropriate melting point to be studied and under static conditions the gradient was measured to be no greater than 0.25 K/cm and usually less than 0.1 K/cm. The temperature was maintained by a proportional controller and the set temperature could be continuously altered at a constant rate by means of a stepping motor and gear-box which rotated the control potentiometer. The rate could be continuously altered by varying the frequency of the drive voltage to the stepping motor. Short term temperature control was accurate to within .01 K and long term drift was of no consequence as virtually all experiments were performed at heating or cooling rates of 50 K/h. Only in a few experiments on rate dependence were faster rates of 100 and 300 K/h used.

Electrical leads were passed out of the vacuum system through low vapour pressure silicone rubber bungs. The wires were inserted by thrusting a hyperdermic needle, wiped in vacuum grease, through the bung, feeding a wire through the needle capillary then extracting the needle. Thermocouple voltages were measured using a Tinsley vernier potentiometer which allowed voltage readings to within 0.5 μV, and the thermocouples were calibrated against the melting points of NaCl and KCl agreeing to within 1.0 K of the values reported in NBS thermochemical tables.[1] NBS thermocouple reference tables[2] based on the International Practical Temperature Scale of 1968 were used to calculate temperatures

1 D.R. Stull and H. Prophet, JANAF Thermochemical Tables NSRDS - NBS 37 (1971).

2 R.L. Powell et al., NBS Monograph 125 (1974).

from the thermocouple voltages.

5.5 Experimental Procedure.

The general procedure for an experimental run was to raise the temperature from room temperature at a rate of 100 K/h under a vacuum of $\sim 3 \times 10^{-3}$ Pa to 600 K then leave overnight under vacuum to remove all volatiles, particularly water and organic materials in the silver print. Then, to minimise sublimation at high temperature, a high purity inert gas (usually He although sometimes Ar or N_2) was introduced to a pressure of 8×10^4 Pa (~ 0.8 atm.) and the temperature was raised at a rate of 100 K/h to ~ 50 K below the experimentation range and usually held for an anneal of ~ 6 h before experiments commenced.

The premelting experiments were carried out by approaching the melting point at a constant furnace heating rate of 50 K/h and measuring the specimen temperature and conductivity, intermittently allowing surface conduction, then suppressing surface conduction. In the conductivity experiments, when the temperature was within 0.25 K of the melting point the temperature was lowered rapidly back to $\sim$ 10 K below T_m, then raised again and the process repeated. When differential thermometry alone was performed the specimen was heated right to T_m. T_m was measured as the temperature, when, at a constant furnace heating rate, the specimen temperature did not detectably increase in two or more minutes i.e. the specimen temperature increased by less than 0.04 K, if at all, in two minutes. This temperature is the level of the heating curve plateaux shown e.g. in fig.6.8.

5.6 Equipment for the Measurement of Electrical Conductivity.

Electrical conductivity was measured initially using a Wayne-Kerr B221 manual conductance/capacitance bridge, however, as values of G changed so rapidly in the anomalous premelting region that manual balancing of the bridge was difficult, and since high precision was not needed, a simple potential divider circuit was constructed and used. The use of three such circuits enabled the simultaneous measurement of 3 conductances in different crystals or on different surfaces. Later in the course of the work a Wayne-Kerr B331 auto-balance bridge became available which enabled continuous

accurate recording of specimen conductance and capacitance.

The potential divider circuit and its interfacing with other instruments is shown in fig. 5.9. A constant 10 V rms was supplied by a Wayne-Kerr audio-frequency signal generator to a resistance, selected to be large with respect to the specimen so as to apply a constant current to the specimen. The specimen voltage was measured by a Hewlett-Packard 400 E ac - voltmeter, while the component of that voltage in phase with the voltage supplied by the signal generator was monitored on an ORTEC phase sensitive detector. All voltages were continuously recorded on a Rikadenki KA-61 six-pen recorder and all channels could be 'pipped' to mark temperature readings from the potentiometer. The specimen guard ring was held at precisely the same voltage as the 'live' electrode by using a voltage follower, power boosted to cope with the high specimen conductance close to T_m. The low pass filter between the operational amplifier and the power booster is introduced to damp a high frequency instability resonance. Finally, we note that both the signal generator voltage and frequency could be readily altered although most measurements were at a frequency of 1592 Hz where, in general, polarisation effects do not appear.

5.7 Superheating Experiments.

With the understanding that melting is a heterogeneous process which must be nucleated, we attempted to superheat an NaCl crystal. There appear to be three possible courses of action in such an endeavour:

(i) To heat the specimen internally. This has been used by Haykin and Benet[1] to superheat by 2 K the interior of tin single crystals by passing an electric current through tin rods which are placed in a stream of cool air to ensure the interior temperature always exceeds the surface temperature.

(ii) To use a heating rate so high that the interfacial velocity is sufficiently slow that the crystal interior superheats before it is reached by the s-l interface. We have

1 S.E. Haykin and N.P. Benet, loc. cit.

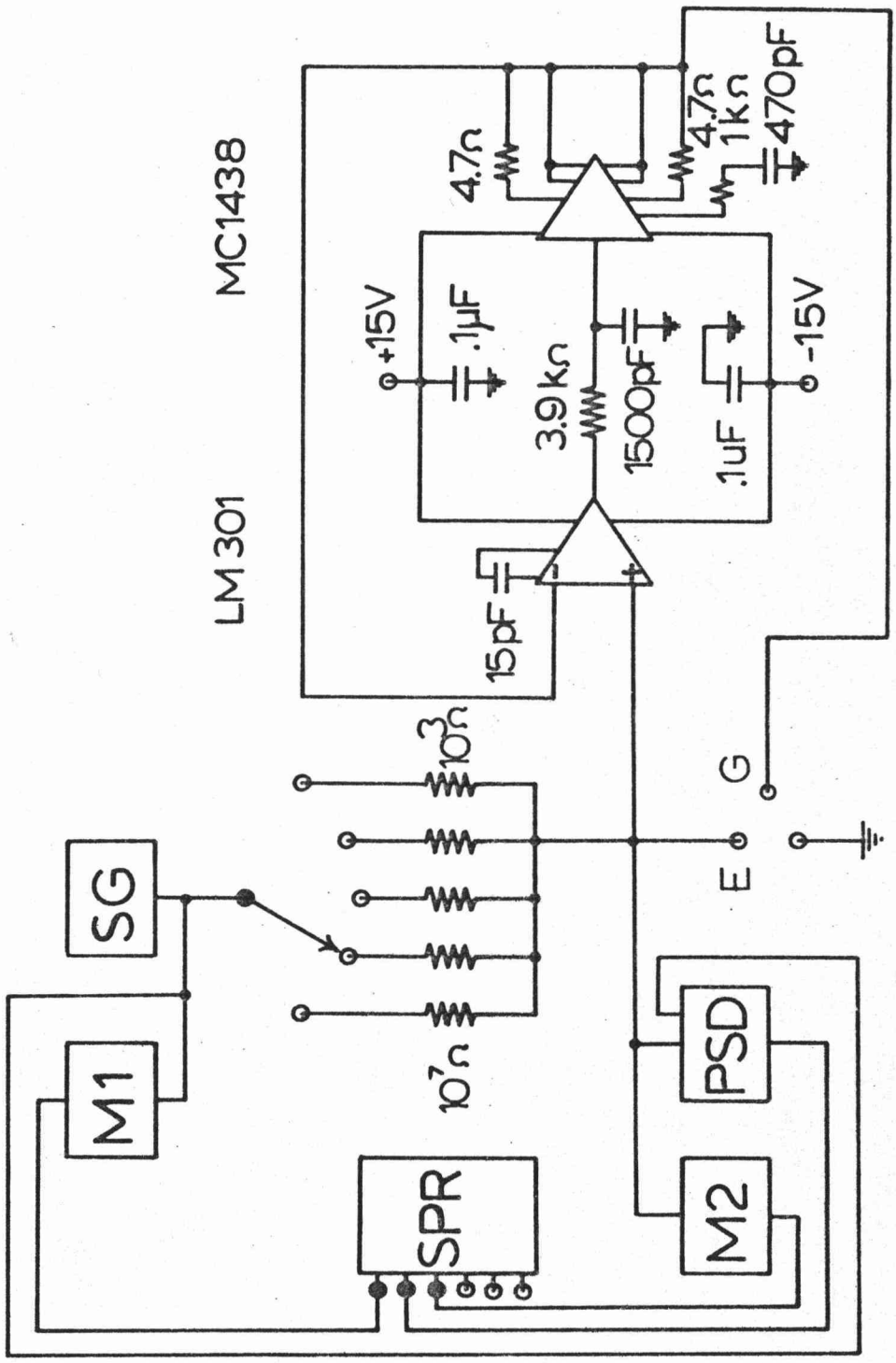

Fig. 5.9 Circuit for measuring electrical conductance and its interfacing with other instruments. E denotes the electrodes and G the guard ring which is controlled by a power boosted voltage follower. SG denotes a signal generator, M1 and M2 a.c. voltmeters, SPR a six pen recorder and PSD a phase sensitive detector.

already referred to the work of Ainslie et al and Cormia et al in superheating quartz and phosphorus pentoxide in this manner by up to 300 K and 50 K respectively. If a crystal is superheated by $\Delta_m T$ K, the s-l interface velocity U is given by[1]

$$U = \Delta H_m \quad \Delta_m T / 3\pi \lambda_o^2 \eta_m N_o T_m \qquad (5.5)$$

where λ_o is the 'jump' distance, η_m the viscosity of the melt and N_o is Avogadro's number. For a superheat of only 0.1 K in NaCl, U = 4.1 mm. sec^{-1} which is just too fast to allow superheating of 10 mm cube specimens at a maximum heating rate of 300 K/h.

(iii) To grow a coherent layer of a higher melting point crystal over the entire surface of the specimen and heat the composite.

We attempted to use the first technique by grinding NaCl 20 mm x 10 mm x 10 mm single crystals to cylinders of radius 9.5 mm and, after washing and drying, applying two silver paint electrodes diametrically opposite each other along 17 mm of the length. By applying an alternating voltage between the electrodes the interior of the crystal can be heated because of the concentration of the field lines at the axis. The uncoated area subtends an angle of 2α at the axis of the cylinder and we selected the optimum angle α to ensure that the power dissipation was maximised at the axis. The electrostatics of the specimen are solved in Appendix C, and in fig. C3 the power density P is plotted against position along the $\theta = 0$ and $\theta = \pi/2$ axes. Only for values of α close to $\pi/6$ does P maximise at the axis and we therefore prepared our specimens with $\alpha = \pi/6$ to ensure that the maximum temperature within the specimen was along the axis. The power supply used for the specimens was a Sullivan Beat Frequency Oscillator with a maximum output of 13 watts. An accurately calibrated 10Ω resistance was placed in series with the specimen in order that by measuring the voltage drop over it the current through the specimen could be monitored. The total voltage drop over specimen and 10Ω

1 D. Turnbull and M. Cohen, in Modern Aspects of the Vitreous State 1 ed. by J.D. Mackenzie(Butterworth,London,1960)p.38.

resistance was also measured, thus allowing the specimen conductance and the power dissipated to be calculated. The voltages were measured on Hewlett-Packard 400 E ac voltmeters and the frequency of all measurements was 1592 Hz.

Two specimens with silver paint electrodes were employed. The first, for the purpose of calibration had inserted a Pt/Pt:13% Rh thermocouple prepared from 0.1 mm wire with the junction at the centre of the crystal. The specimen was mounted in the furnace which was raised to 1020 K and held at that temperature while the ac voltage was applied across the specimen. The axial temperature increment was thus determined as a function of applied voltage and this process was repeated at 1040 K, 1050 K and again at 1060 K. The second specimen in which the actual attempt at superheating was to be performed had no thermocouple as this would provide a nucleation site for internal melting. With the essentially voltage-controlled supply to the specimen we have an unstable situation with respect to melting in that any small amount of melting which may arise increases the conductance and hence the heat dissipation,with the result that, a rapidly increasing amount of melting occurs. This is, however, what we want since this is the only index of melting for the specimen with no thermocouple. If the source were current-controlled the system would be stable with respect to melting and there would be no well defined index of melting.

In an attempt to maintain the surfaces at approximately furnace temperature and thus prevent surface melting, we prepared a superheating rig, shown in fig. 5.10, comprising two solid pure graphite arc anular prisms - the electrodes, separated by two fired pyrophilite arc anular prisms which act as insulators, assist to keep the specimen surface at the furnace temperature and help suppress vaporisation. The graphite and pyrophilite components are rounded on their outer edges and sit in a conical pyrophilite seat such that they lean onto the specimen as shown in the figure. Constructed in this way, the fully assembled rig was very stable and remained intact after gentle shaking about. The results of these experiments are presented in the next chapter.

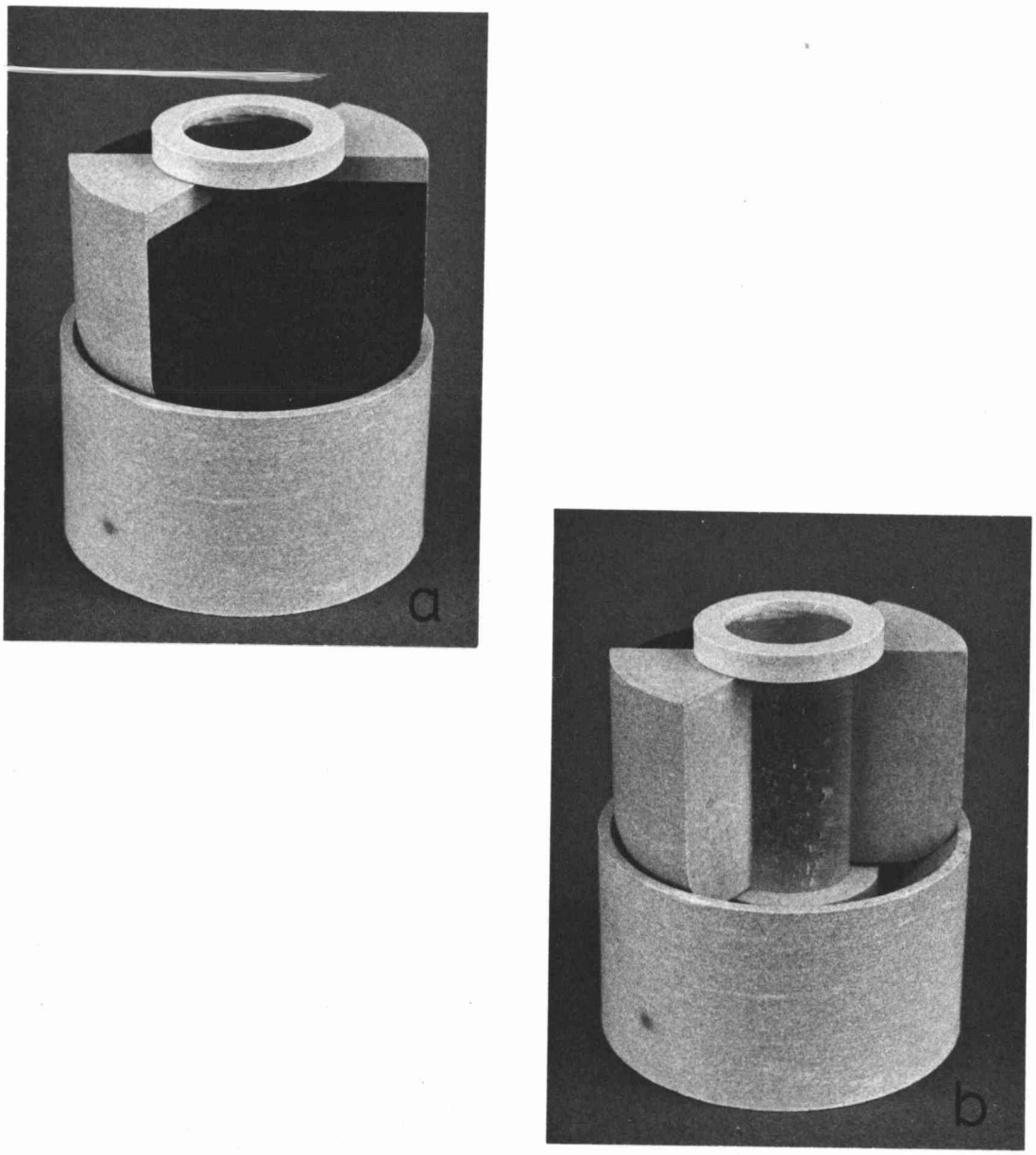

Fig. 5.10 Superheating rig comprising two graphite electrodes and two pyrophilite spacers mounted on a pyrophilite base (a) fully assembled (b) one electrode removed exposing the cylindrical specimen and showing the curved lower edges of the components which tilt against the specimen on the conical surface of the base. The two pyrophilite rings are to reduce surface conduction around the top or base of the crystal.

6 EXPERIMENTAL RESULTS

6.1 Premelting Conductivity and Heat Absorbtion.

In agreement with Allnatt and Sime[1] we find the conductance of the alkali halides we studied, rose rapidly towards the molten salt conductance within about 6 K of the melting point. Fig. 6.1 shows an Ahhrenius plot of the apparent conductivity of KCl for three successive entries into the anomalous region, determined using a specimen with crossed wire electrodes. The rise is independent of voltage amplitude, has an apparent activation energy of ~ 300 eV and appears as though it will intercept the molten salt conductivity at the melting point. However, plotting σ rather than G assumes that it is the bulk conductivity which increases and this, we shall see, is incorrect. Temperature measurements for this specimen were made with a thermocouple mounted tightly in the specimen platform, and attempts to proceed closer to the melting point resulted in the conductance appearing to level off at about the highest point shown in fig. 6.1. This is because, while the temperature of the specimen chamber including the platform continues to rise, the specimen temperature begins to lag behind due to an absorbtion of heat.

The temperature increase with time is shown in fig. 6.2 for an NaCl crystal with an inserted thermocouple when the furnace temperature is raised at a constant rate of 50 K/h. Below 1065 K the temperature is quite linear with time and evidently beginning at 1068.7 K an increasing rate of heat absorbtion occurs. The straight line above the curve is the calculated temperature of the specimen chamber, and the temperature differential ΔT between chamber and specimen will be used later to analyse this heat absorbtion.

The conductance of this same specimen in the vicinity of T_m is shown in fig. 6.3. The bulk conductance for the first

1 A.R. Allnatt and S.J. Sime, Trans. Faraday Soc. 67, 674 (1971).

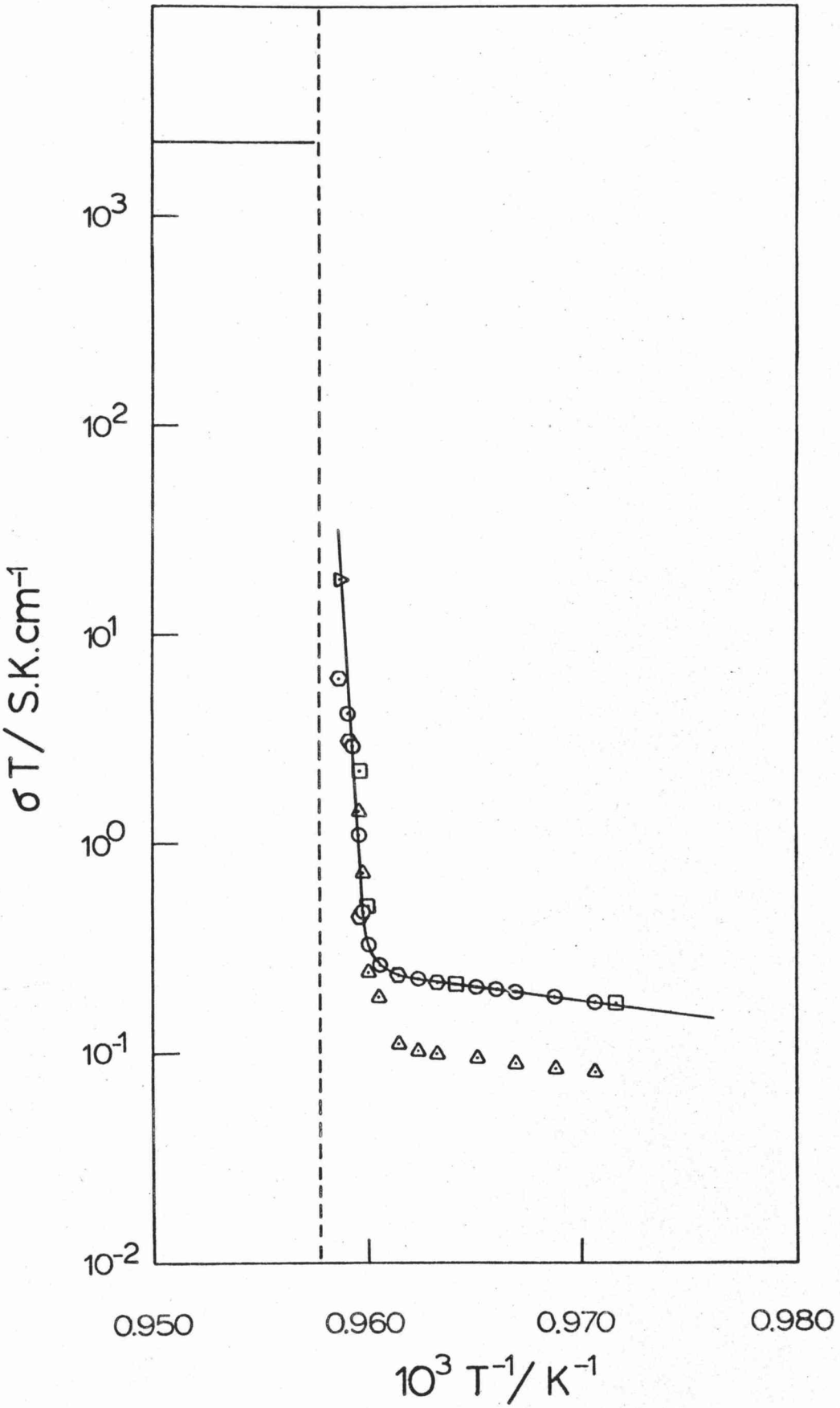

Fig. 6.1 Ahhrenius plot of the conductivity of KCl using inserted crossed wires electrodes. △ : rising first time; ⊙ : rising second time; ⊡ : falling second time; ⊙: rising third time and ▷ : falling third time. The dashed line shows the melting point T_m and the solid line beyond T_m is the conductivity of the melt.

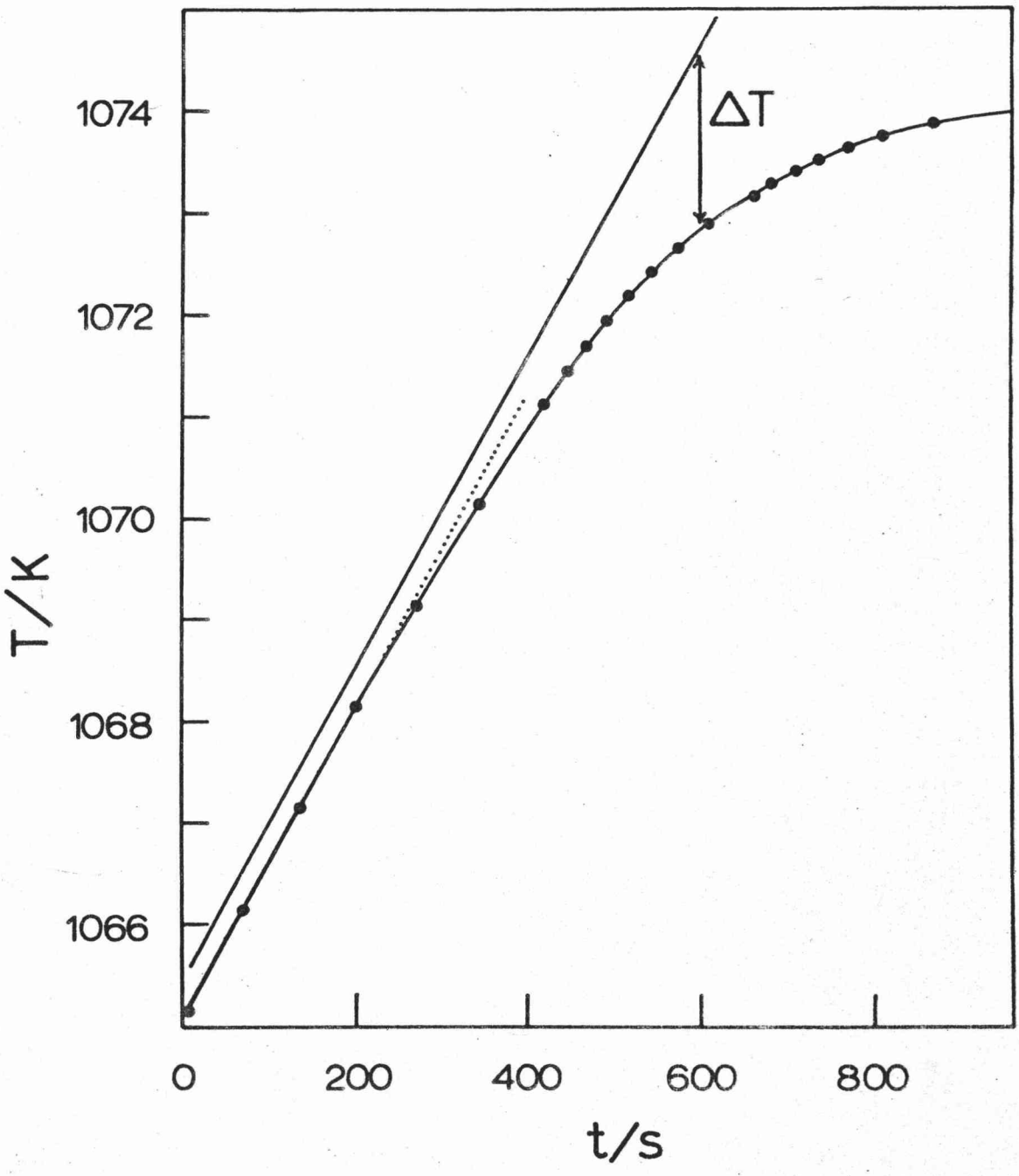

Fig. 6.2 Specimen temperature as a function of time for a constant furnace heating rate for a 1 cm cube NaCl specimen. The straight solid line is the calculated temperature of the specimen chamber.

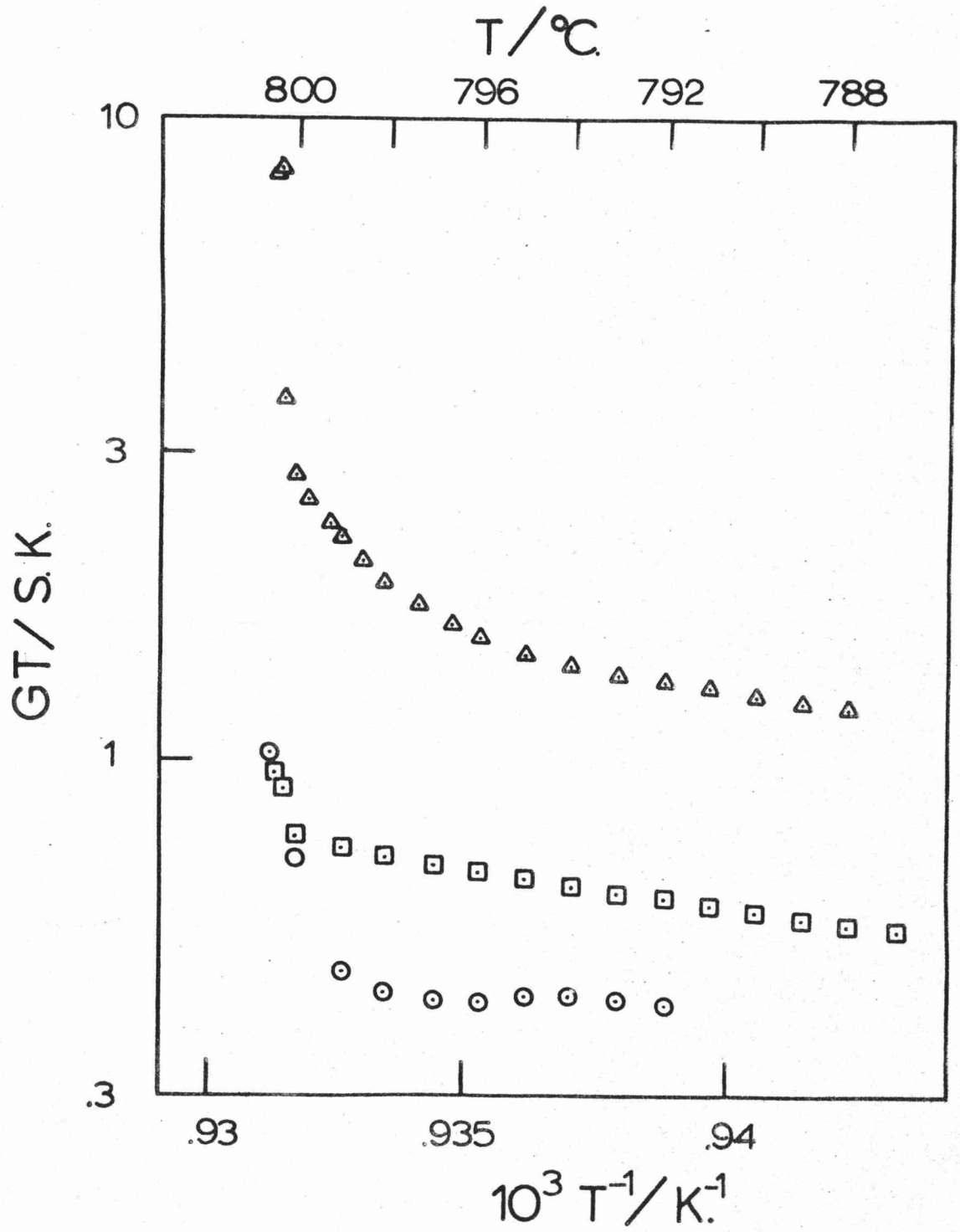

Fig. 6.3 Ahhrenius plot of the conductance of the same specimen described in fig. 6.2. ⊙ : first rise suppressing surface conduction; ⊡ : a typical subsequent rise suppressing surface conduction; △ : a typical subsequent rise allowing surface conduction. The rise in surface conduction coincides with the commencement of the heat absorbtion shown in fig. 6.2.

rise is denoted by circles, and typical of many experiments, is irregular and lower than on subsequent entries. This is due to the presence of bubbles on the electrodes, which disappear with annealing in the premelting region. The triangles show the subsequent conduction when the voltage follower is disconnected from the guard electrode, that is, when surface conduction is allowed. Interestingly, the premelting rise commences earlier, and at the same temperature as the heat absorbtion does. On the other hand, when surface conduction is suppressed no premelting is evident up to within half a degree of the melting point and the small rise which does occur there is largely attributable to inability to completely suppress surface conduction. We measured the melting point to be 1073.99 K. The retention of normal bulk solid properties up to the melting point agrees with the similar conclusions of Hunter and Siegel[1] based on ultrasonic measurement of elastic constants of NaCl near T_m.

The absorbtion of heat and rise in surface conductivity cannot be explained in terms of there being a temperature gradient over the specimen, such that the surface encountered the normal melting temperature before the interior. For the premelting range here is 5 K and a differential thermocouple placed in a similar specimen, with one juction in the middle and the other junction half protruding from a face, showed a temperature difference $\sim$ 0.08 K between surface and interior up to $\sim$ 0.1 K below T_m. Thereafter, the temperature differential rose rapidly.

Fig. 6.3 also shows the important contribution of surface conduction below the premelting region, which, as was emphasised in §5, persists throughout the intrinsic region. The conductivity of a guarded NaCl crystal allowing for fringing effects, which was shown in fig. 5.6, may be regarded as our best lower temperature conductivity results, and in the intrinsic region these are consistently lower than other reported date for NaCl because of these two corrections. For example, the very careful and thorough work

1 L. Hunter and S. Siegel, loc. cit.

of Allnatt, Pantelis and Sime[1] shows values of σ greater than ours by a factor ~ 2.0. Nadler and Rossel[2] have already drawn attention to the need for guard rings in the measurement of electrical conductivity in alkali halides, although they do not report the benefits quantitatively.

The guard configuration we have used with parallel plate electrodes (shown as 'a' in fig. 5.1) is by no means the best configuration. A superior method is used by Kao, Giles and Calderwood[3]. This involves polishing out a flat-bottomed recess in the specimen, plating the bottom of the recess and the underside of the crystal and applying the guard ring to the proud rim. In this configuration the guard has a negligible effect on the capacitance of the specimen. If configuration a is used with the potential divider circuit, the capacitance is modified by the guard ring since the guard is held at the same potential as the live electrode. For this reason, this electrode configuration was used only with the Wayne-Kerr B331 auto-balance as this keeps the guard neutral, and consequently the guard ring does not alter the specimen capacitance.

Returning now to the premelting results, it seems clear since the heat absorbtion and sudden rise in surface conductivity appear at precisely the same temperature, that the heat absorbtion is associated with some phenomenon occurring at the surface. In the light of comments in § 2 on premature surface melting and in § 3 on sublimation, three possibilities suggest themselves. (i) The melting point may be depressed due to the presence of impurities. (ii) A skin of melt is forming prematurely on the crystal surface (after the ideas presented by Tamman and Stranski), which increases in thickness as T_m is approached, until at T_m, in equilibrium it contains the whole specimen. (iii) The sublimation rate increases rapidly in the premelting region as found by Ewing

1 A.R. Allnatt, P. Pantelis and S.J. Sime, J. Phys C-Sol. St. Phys.

2 G. Nadler and J. Rossel, Phys. Stat. Solid. A 18, 711 (1973).

3 K.C. Kao, L.J. Giles and J.H. Calderwood, J.Appl. Phys. 39, 3955 (1968).

and Stern at the melting point. The effect may of course arise from all these phenomena or from any of many subtle variants which will be considered in chapter 7.

6.2 Physical Changes in the Premelting Region.

In an attempt to distinguish between the possible causes, we examined some of the physical alterations which took place at the beginning of premelting. Fig. 6.4 shows a 0.2 mm slot which was cut into the upper face of a 1 cm cube NaCl single crystal using a diamond wire saw. The crystal was washed in 25% water 75% ethanol to remove the dust. The upper picture shows the slot immediately before heating in the furnace, the bottom picture shows the same slot after entering 0.5 K into the premelting region and reversing. The slot has filled. This is suggestive of melting, although it is not conclusive evidence, as the slot might fill by sublimation and redeposition. More decisive information was obtained by simply placing a platinum wire on the top surface of the crystal. The side view, shown in fig. 6.5 of this surface after entering the premelting region and cooling, reveals two ridges which had climbed up around the base of the wire. This is strongly suggestive of a capilliary effect with melt on the surface. The base of the valley between the ridges is at the same level as the rest of the surface whereas if sublimation were the only effect the reduced vaporisation rate under the wire would leave the wire supported above the level of the surface on a ridge. Fig. 6.6 shows a view of the ridges from above.

One might suppose that no melting has taken place and the capilliary lowering of surface energy has occurred by plastic flow in the solid. However, Herring[1] in discussing the possibility of surface tension induced plastic flow in sintering, shows that this kind of behaviour is unlikely. The surfaces in fig. 6.4, 5 and 6 all show marked dimpling and "puddling" and particularly the last shows distinct signs of flow. Presumably the dimples result from preferential melting or vaporization at points where dislocations

1 C. Herring, in the Physics of Powder Metallurgy, ed. by W.E. Kingston (McGraw-Hill, N.Y., 1951) p. 170.

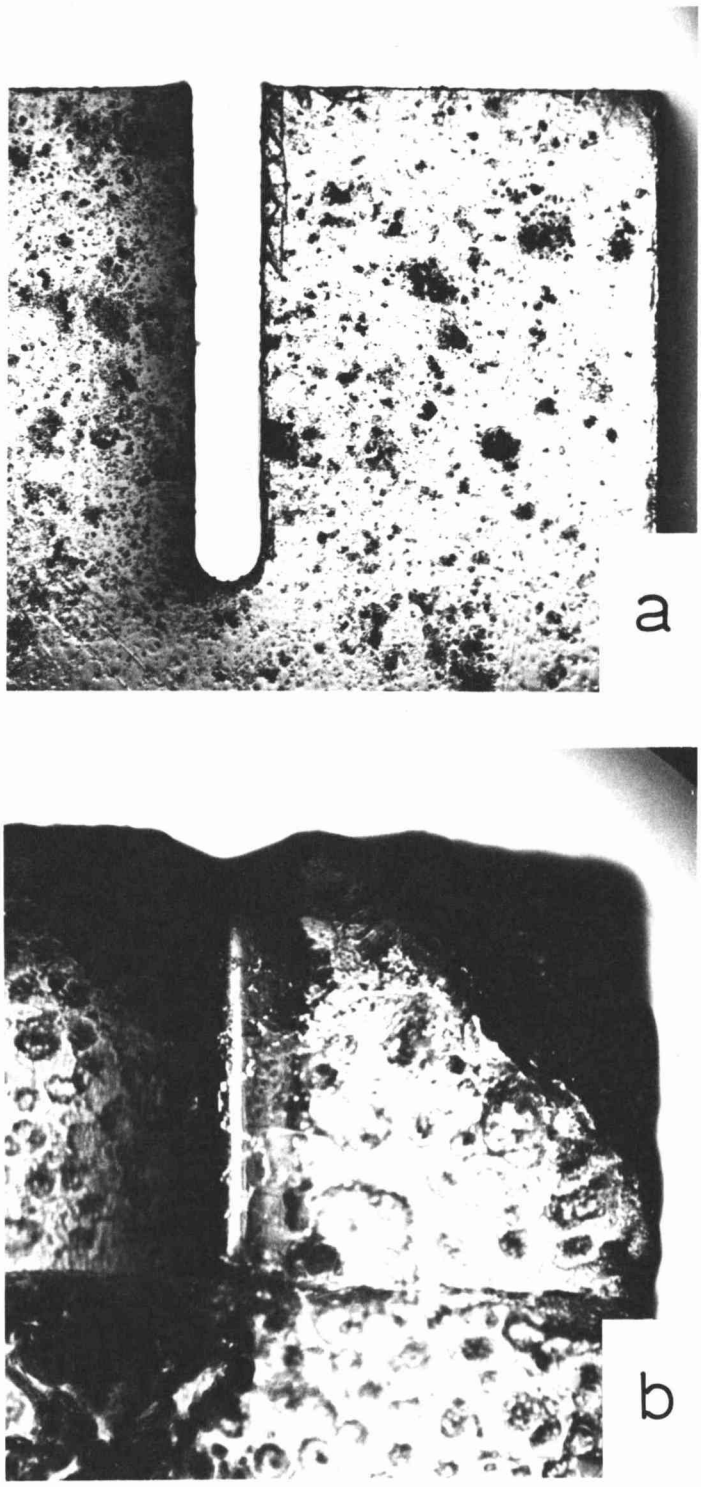

Fig. 6.4 A 0.2 mm slot cut into the upper face of an NaCl single crystal (a) after washing (b) after entering 0.5 K into the premelting region then cooling rapidly. The slot has filled. Vaporisation pits about dislocations are very evident.

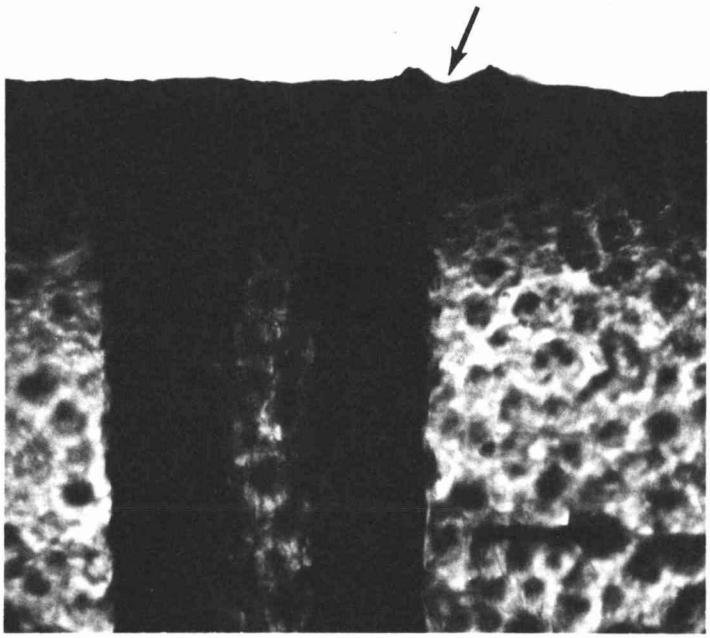

Fig. 6.5 Side view of surface on which a platinum wire was placed. After an entry of 0.5 K into the premelting region the surface had climbed up round the sides of the wire where indicated by the arrow. Mag. = 50 x.

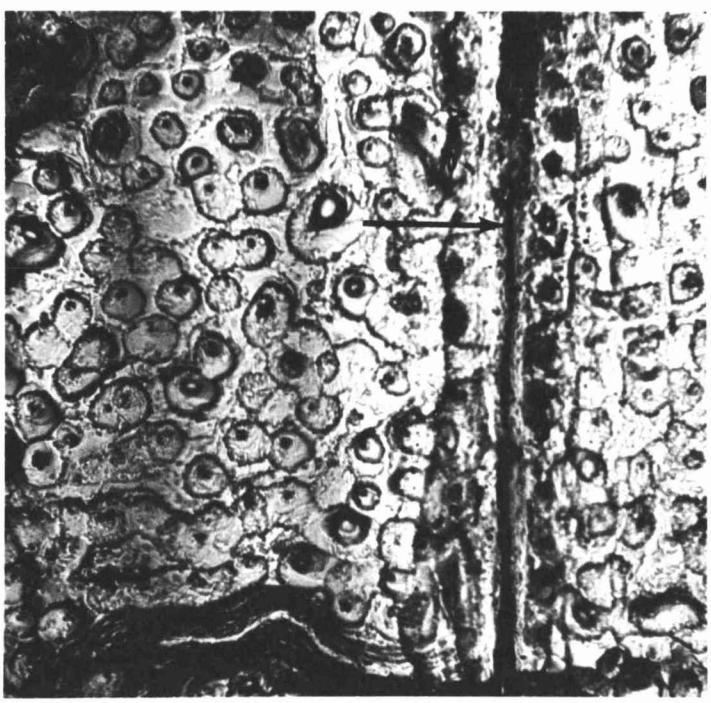

Fig. 6.6 Top view of the channel formed where the platinum wire was placed indicated by the arrow. Vaporisation pits about dislocations are very distinct. Magnification = 50 x.

meet the surface. We shall discuss these dimples and puddles in the next chapter but note here that the dimples are ~ 60 μm in diameter and the curvature of their walls $\sim$ 10 μm in radius.

We conclude then that the surface effect is melting or a combination of melting and vaporization but not vaporization alone.

6.3 The Effect of Ambient Gas.

Various possible causes of surface melting will be discussed in §7 but as it seemed that impurity depression of melting point was the most likely candidate, some experiments were performed to examine this possibility. Possible sources of impurities are: (i) trace impurities in the crystals as supplied; (ii) organic material from preparation, washing and silver painting; (iii) silver from painted electrodes, and from vapour from the silver leads entering the specimen chamber, (iv) ambient gas, including also metal vapour subliming from the stainless steel or silicon from the silica. The first three possibilities may be dismissed for the following reasons: (i) Typical analyses by the specimen suppliers suggest that trace impurities are present in proportions of 20 ppm or less, and the position of the "knee" in the conductivity curves, suggests that the amount of divalent impurity in solution was $\sim$1-5 ppm. (ii) None of the crystals discussed in this section were touched by the fingers and they were raised slowly under vacuum to 600 K and annealed there to remove volatiles. (iii) Subsequent to premelting experiments, analyses by arc emission spectrography and by energy dispersive analysis of X-rays (EDAX) from scanning electron microscopy failed to locate any silver (down to, respectively, 10 ppm and 500 ppm) on unpainted surfaces and in the interior of specimens.

To examine the effect of the last group, namely ambient gas, metal and silicon oxide vapours, one 1 cm cube NaCl crystal with thermocouple only was raised under a vacuum of 2×10^{-2} Pa from 970 K to 1050 K at 300 K/h, then to the melting point at 100 K/h. The resulting heat absorbtion

curve shown in fig. 6.7 is very irregular in the anomalous region, but the smoothed curve is still very similar to the curve in fig. 6.2 obtained for an ambient He pressure of 8×10^4 Pa. We may conclude from this that ambient gas and vapour provide no major contribution to at least the premelting heat absorbtion. The irregular rise and fall in thermocouple voltages for a specimen in vacuo arises from a non-uniform heat absorbtion, which suggests that vapour must have been bubbling off the crystal. This may be due to the small bubbles around the thermocouple wire escaping intermittently.

Although EDAX from scanning electron microscopy detected no silicon, nickel, chromium or iron, some manganese was apparent on many of the crystal surfaces in proportions $\sim 10^{-4}$ to 10^{-3} which would be sufficient for a displacement in melting temperature of 0.03 to 0.3 K. Local concentrations might be greater so that if the melt could sustain a concentration up to 1.4×10^{-2} we have here a possible explanation of the premelting. One difficulty with this proposition is that the Mn derives from the 316 stainless steel (which contains up to 2% Mn) yet Allnatt and Sime used a conductivity rig constructed solely from fused silica and platinum. Furthermore, arc emission spectrographic analysis of the crystal bulk subsequent to an experiment place the Mn content at less than 0.002% while Si, Ni and Al, although more abundant were still in proportions as low as 0.02%, 0.02% and 0.01% respectively.

Further experiments on the effect of ambient gas were performed by increasing the helium gas pressure and by pumping down to 3×10^{-3} Pa, then introducing argon or nitrogen. The results as a whole were not entirely consistent but the general trend was that for changes which would decrease the solubility of ambient gas the surface melting temperature was shifted closer to the bulk melting temperature. E.g. by decreasing the helium pressure from 2.7×10^5 Pa to 8×10^4 Pa the onset of premelting shifted closer to T_m by 0.5 K; changing to argon at 8×10^4 Pa the shift was a

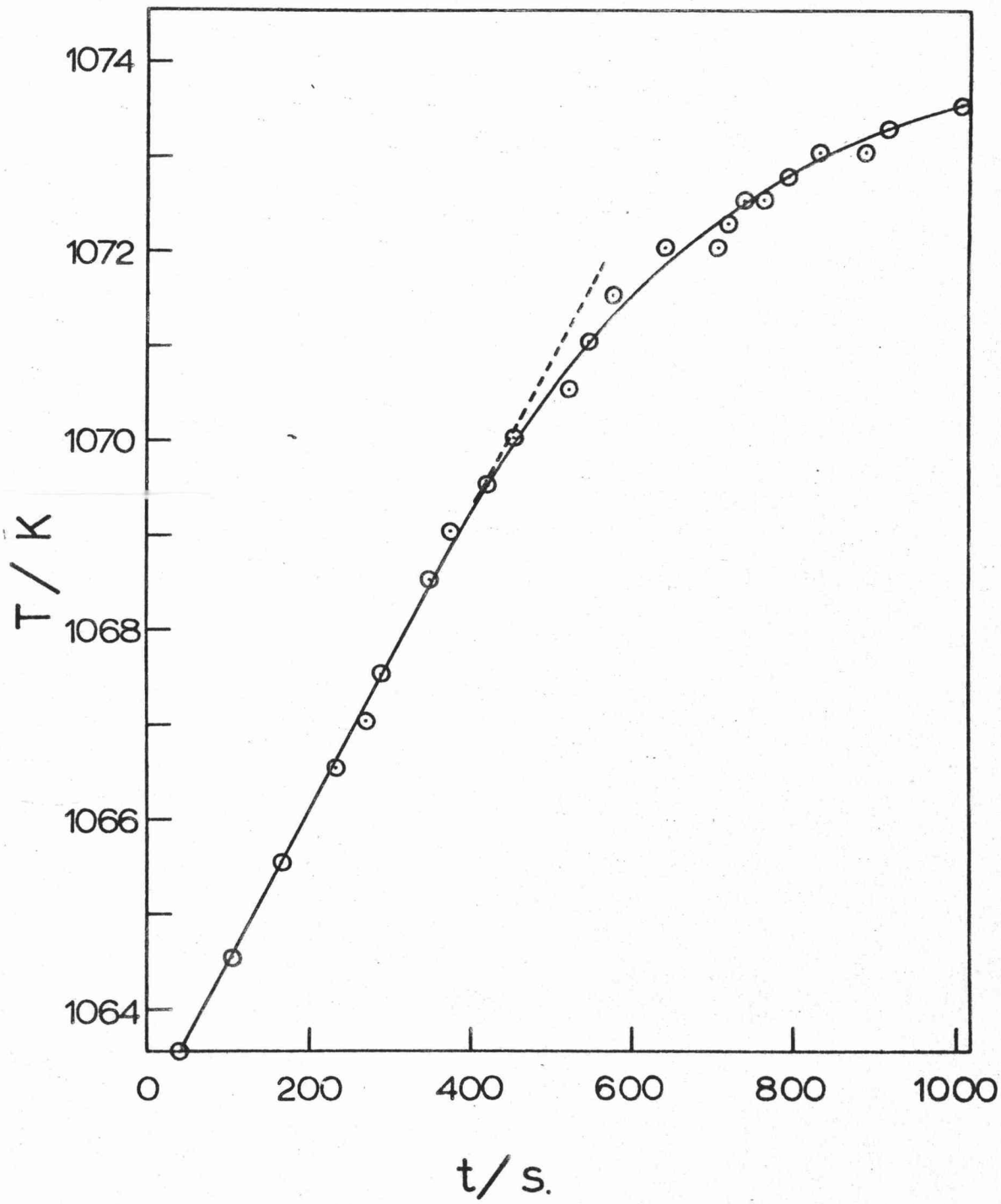

Fig. 6.7 Heating curve for a 1 cm cube NaCl specimen in an ambient vacuum of 2×10^{-2} Pa.

further 0.15 K and changing to nitrogen at 8×10^4 Pa the shift was a further 0.3 K. The effective radii of He, Ar and N_2 are .122 nm, .192 nm and .200 nm so that the solubilities should decrease in that order. There does, therefore, appear to be a small contributing effect due to ambient gas although the last two results (i.e. for changing to Ar then to N_2) are explicable in terms of reduced sublimation rates, and the results for different pressures were not wholly consistent. Further study is necessary to fully clarify the question of ambient gas.

In another experiment, the lower temperature conductivity of a parallel plate specimen with guard ring was examined under a vacuum of 3×10^{-3} Pa, to see whether the surface conduction there might be attributable to, or at least affected by, ambient gas. The conductivity curve showed the same development of surface conduction above the extrinsic/intrinsic 'knee' exhibited by specimens in gas. The temperature was held at $10^3/T = 1.2\ K^{-1}$ and nitrogen introduced, pumped down to 3×10^{-3} Pa and argon introduced, then finally helium, and no significant changes in surface conductance with gas were observed.

6.4 Melting Temperatures

The heat absorbtion was studied in a number of crystals with a thermocouple, only, inserted. Lithium fluoride was a problem in that the melting point was just too high to successfully insert the thermocouple by the means described in §5, and we eventually drilled a fine hole through a specimen to accommodate the thermocouple. The melting points for the four alkali halides studied, obtained from the levels of the plateaux in the heating curves are given in Table 6.1 and compared firstly with values reported in the 1971 NBS Thermochemical Tables.[1] The errors quoted are the random errors observed rather than absolute errors. Since the

1 D.R. Stull and H. Prophet, loc, cit.

reported values were measured prior to the introduction of the 1968 International Practical Temperature Scale (IPTS 68) they should be reduced by the appropriate amount to compare with our values. The corrected values are given in brackets.

Crystal	LiF	NaCl	NaBr	KCl
Observed T_m/K	1118.3±.1	1073.99±.1	1017.2±.1	1044.15±.1
Reported T_m/K	1121.3[1] (1120.5) 1118.2[2]	1073.8[1] (1073.1)	1020[1] (1019.5) 1013.5[3]	1044[1] (1043.4) 1044.4[4]

Table 6.1 Melting points of alkali halides obtained in this work, as reported in JANAF Thermochemical Tables NBS 37 (1971), and as reported elsewhere.

Underneath these are othermeasured values (corrected to the IPTS 68 scale) which show that our values are reasonable. Absolute errors are seen to be at least of the order of 1 K.

6.5 Heating Rate Dependence

The effect of varying the heating rate for NaCl is shown in fig. 6.8 and the premelting region appears to be narrowed and the height of the plateau raised for faster heating rates. In fact the melting temperatures for heating rates of 100 K/h (a) and 50 K/h (b) are 1073.96 K while that for 300 K/h (c) is 1074.06 K. A more interesting effect is observed when heating at the fast rates if the whole specimen is allowed to melt. This effect is shown in fig. 6.9 for KCl where the temperature remains fixed at T_m during melting, then, as the last portion of the crystal melts the temperature drops by ~0.18 K, even though the temperature differential between specimen and chamber is 24.5 K. When melting is

1 ibid.

2 H. Flood, V. Fykse and S. Urnes, Z. Elektrochem. 59, 364 (1955).

3 M. Blanc, Compt. Rend. 246, 570 (1958).

4 J.W. Johnson and M.A. Bredig, J. Phys. Chem. 62, 604 (1958).

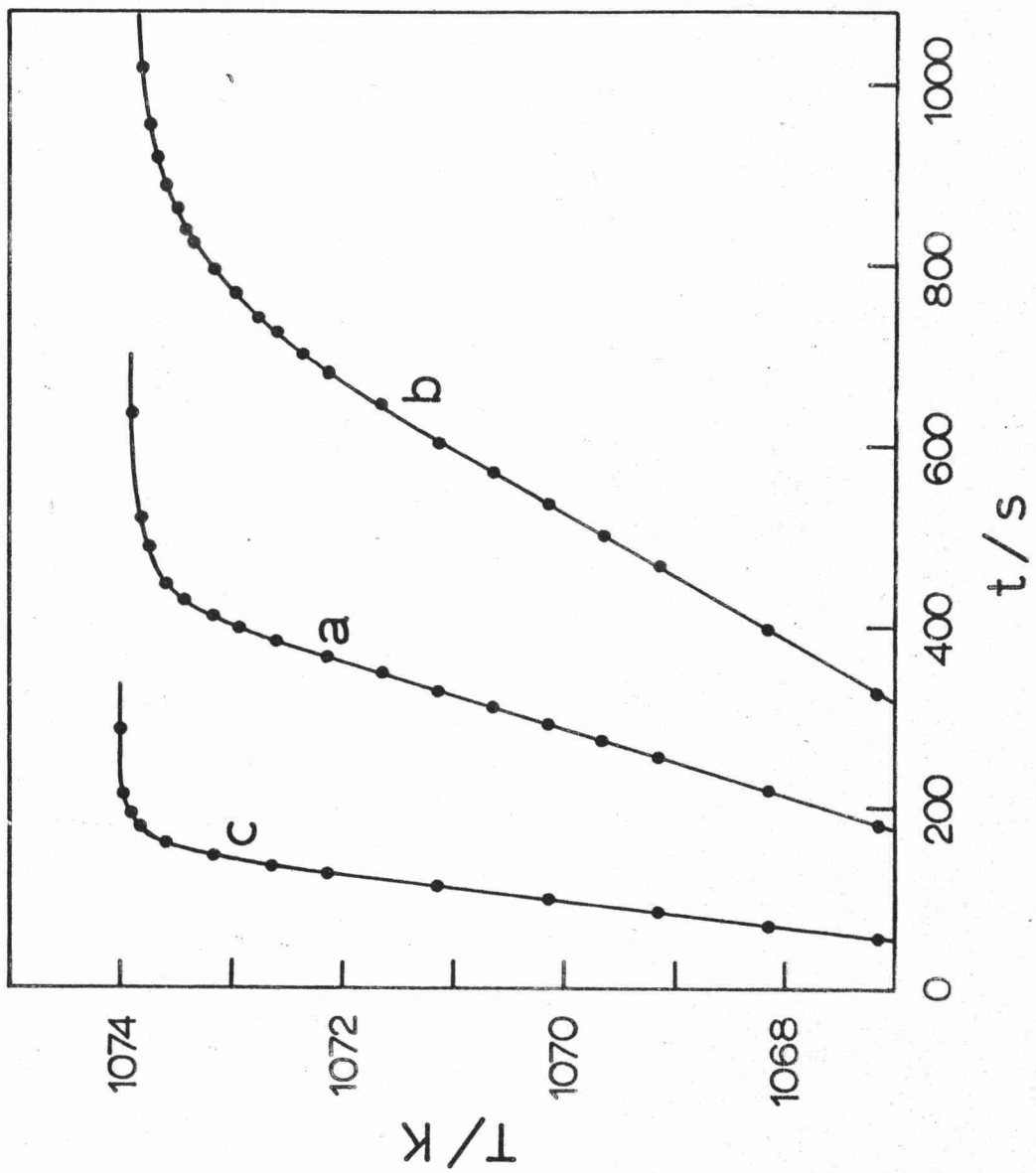

Fig. 6.8 NaCl heating curves for a range of heating rates (a) 100 K/h (b) 50 K/h and (c) 300 K/h.

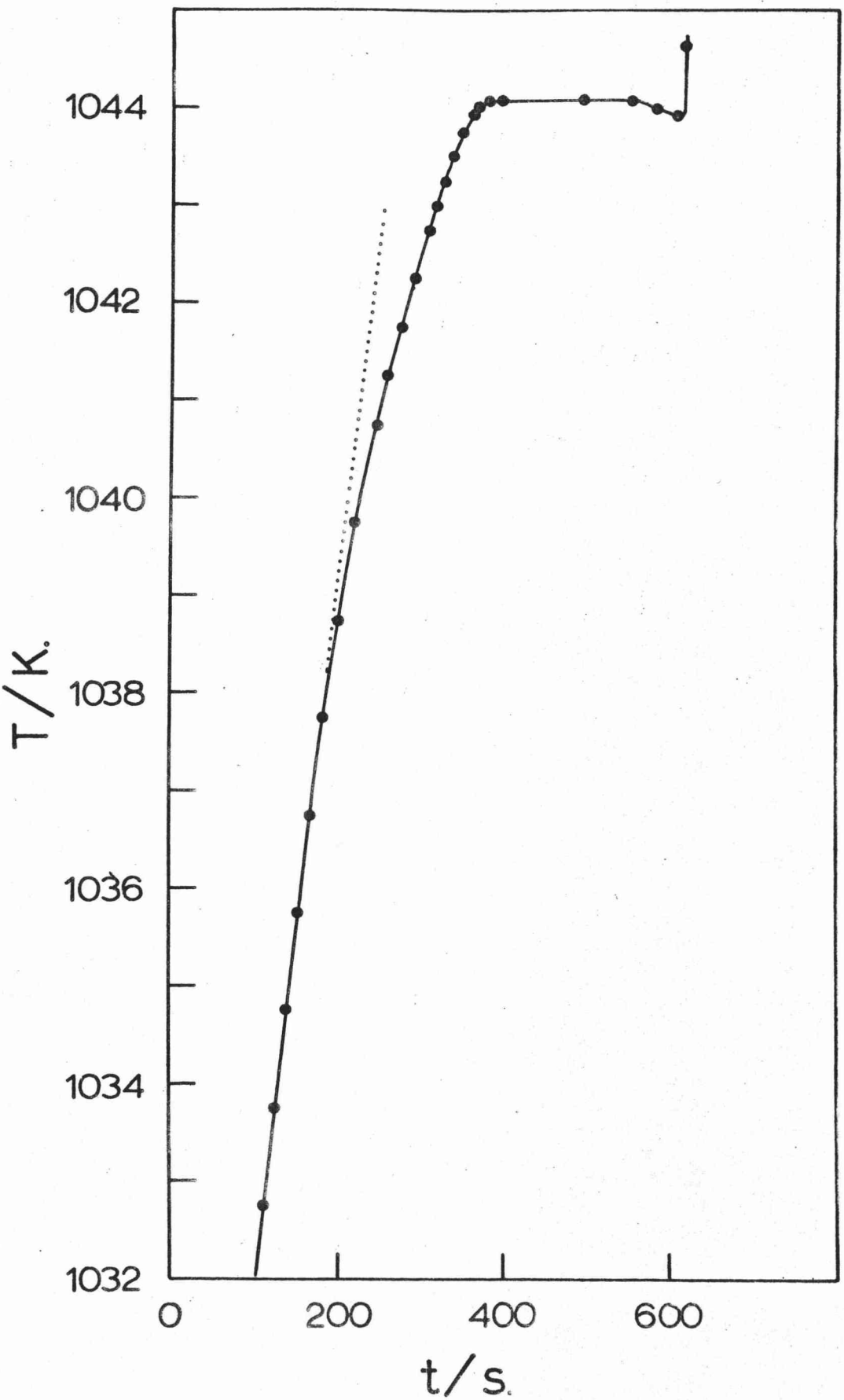

Fig. 6.9 Heating curve for KCl at 300 K/h. A drop of 0.18 K occurs prior to melting.

complete the temperature rises rapidly. The drop might be considered to be due to the melt around the thermocouple junction drawing a small current. It may be due to the solid-liquid interface drawing impurites, such as helium or manganese, after it and hence being cooler than the maximum allowable temperature - the melting temperature. Or, it might be that at this fast heating rate, the interior of the crystal is superheated by $\sim 0{,}18$ K. This was shown to be unlikely in § 5.7. With regard to the first of these possibilities: the presence of the melt about the thermocouple junction is equivalent to a resistance in parallel with the potentiometer. This does not alter the absolute thermocouple voltage but only the galvonometer sensitivity. Moreover, the absorbtion of heat (~ 30 mW) by the thermocouple in driving a current through the melt is exactly offset by the joule heating within the melt.

We conclude then, that the small drop in temperature occurs when the thermocouple junction is encountered by the s-l interface, which has moved from the specimen exterior and is consequently contaminated from ambient gas and therefore at a temperature lower than T_m. This is consistent with the small effect of ambient gas discussed in § 6.3 and the small increase in T_m at the fastest heating rate.

6.6 Thickness of the Premelting Surface Layer.

The results from the differential thermal analysis experiments are best summarized by putting the depth of apparent surface melting in a functional form. To do this we analyse the heat balance between radiant arrival of heat, specific heat and melting enthalpy for a given depth, τ of surface melt. The following equation readily results

$$4Ae\,\sigma_B\,T^3\Delta T = \left\{ mC_s + \rho_l A \left[\Delta H_m + (C_l - C_s)T\right]\frac{d\tau}{dT} \right\} \frac{dT}{dt} \qquad (6.1)$$

If the heat absorbtion is rather by vaporisation, the evaporated thickness may be determined simply by replacing ΔH_m, in this equation, by ΔH_v and setting $C_l = 0$.

The term on the left hand side is the Stefan-Botzmann law expanded to first order in ΔT, for the rate of arrival of radiant energy. A is the specimen surface area, e the emissivity and σ_B is the Stefan-Boltzmann constant. The right hand side terms are, in order, the heat absorbtion via the specific heat, C_s of the solid, via the enthalpy of melting ΔH_m, and finally a small correction due to the replacement of a layer of solid by a thickness τ of melt with specific heat C_l. m is the specimen mass, ρ_l the density of the melt and t is time in seconds. We assume the emissivity to be unity i.e. the specimen is a black body receptor since any transmitted radiation will be re-radiated by the walls of the chamber toward the specimen very many times. ΔH_m, ρ_l, C_l and C_s are listed in Table 4.1 and m and A were measured prior to an experiment so that by measuring T and $\frac{d\tau}{dT}$ from heat absorbtion curves such as in figs. 6.2 and 6.8, $\frac{d\tau}{dT}$ may be calculated. It should be emphasized that all curves examined were as smooth as that shown in fig. 6.2 and often had a greater density of data points. The effective temperature of the specimen chamber shown as the straight line above the heating curve in fig. 6.2 is obtained from the value of ΔT in the linear region below the commencement of surface melting. This is calculated from eqn. (6.1) for $\frac{d\tau}{dT} = 0$ i.e. from

$$4 A \sigma_B T^3 \Delta T_{lin} = mC_s \frac{dT}{dt} \qquad (6.2)$$

The variation in T^3 over 10 K is negligible and consequently the heating curve below the premelting region is quite linear.

We found for all specimens except KCl that logarithmic plots of $\frac{d\tau}{dT}$ against $T_m - T$ gave straight lines within 1 to 1.5 K of T_m with gradients of -2. We therefore show in fig. 6.10 values of $\frac{d\tau}{dT}$ as a function of $(T_m - T)^{-2}$ for NaCl, NaBr and LiF in He at 8×10^4 Pa for a heating rate of 50 K/h, and for NaCl heated at 57 K/h in a vacuum of 2×10^{-2} Pa. In each case the linear dependence is very good. Another point lies off-scale but precisely on the extrapolated line

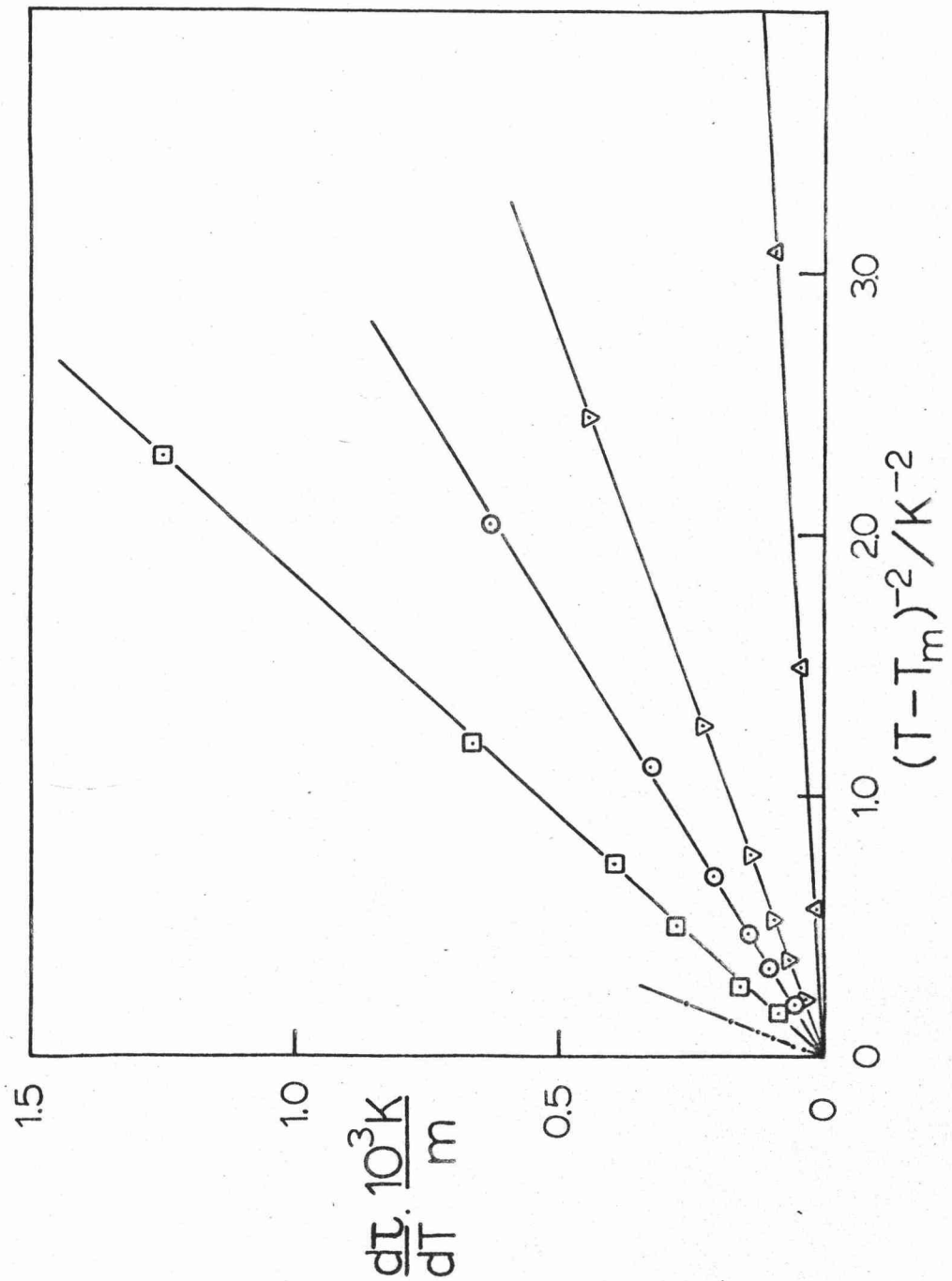

Fig. 6.10 Temperature rate of change of the apparent depth of melting versus $(\Delta_m T)^{-2}$. • : LiF ; △ : NaCl ; ⊙ : NaCl in vacuum; ⊡ : NaBr at 50 K/h ; ▽ : NaBr at 300 K/h.

for NaCl in He, and other data for faster heating rates not plotted in fig. 6.10 because the gradients are too small show exactly the same functional dependence. It appears then that LiF, NaCl and NaBr, irrespective of heating rate and gas pressure, melt to a depth τ at a given distance $\Delta_m T = T_m - T$ from the melting point such that

$$\frac{d\tau}{dT} = S_1 (\Delta_m T)^{-2} , \qquad (6.3)$$

or, by integration

$$\tau = S_1 (\Delta_m T)^{-1} . \qquad (6.4)$$

The values of S_1 given by the slopes of the lines in fig. 6.10 and other such lines not plotted there are summarized in Table 6.2. While the functional form is very reproducible, the value of S_1 is not, as may be seen by the first two items in the Table. However, there does appear

Crystal	Gas	Heating Rate K/h	S_1 m.K.	S_2 m
NaCl	He	50	1.1×10^{-4}	-
NaCl	He	50	3.01×10^{-5}	-
NaCl	He	100	6.83×10^{-6}	-
NaCl	He	300	4.98×10^{-6}	-
NaCl	Vacuum	57	3.03×10^{-4}	-
LiF	He	50	1.28×10^{-3}	-
NaBr	He	50	5.44×10^{-4}	-
NaBr	He	300	1.82×10^{-4}	-
KCl	He	50	-	3.12×10^{-5}
KCl	He	50	-	1.26×10^{-4}

Table 6.2 Values of the constants S_1 and S_2 appearing in equations (6.4) and (6.6) for a range of crystals and experimental conditions.

to be a definite trend that the faster the heating rate the smaller the value of S_1.

KCl shows a rather different behaviour as shown in fig. 6.11. For this crystal the functional dependence is

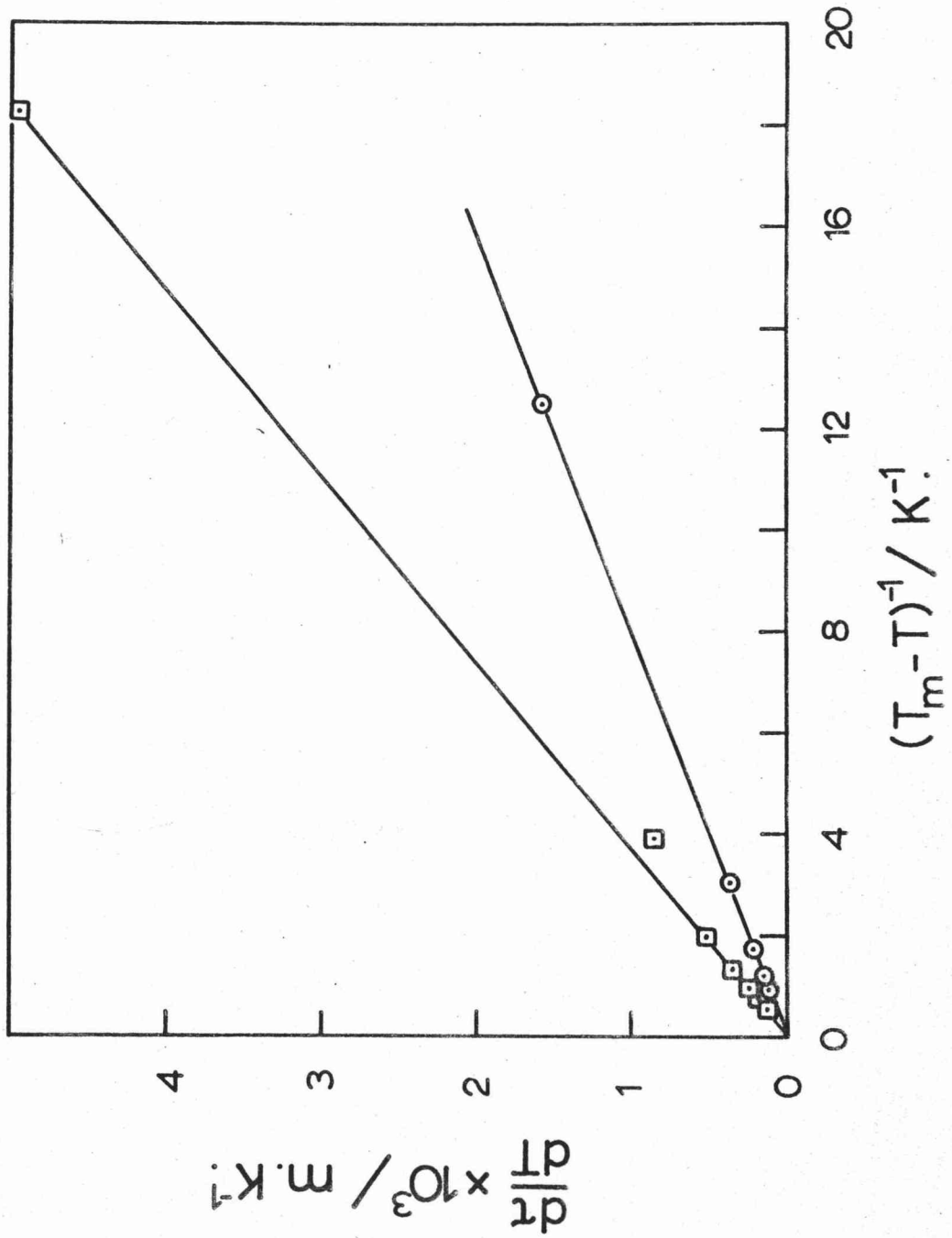

Fig. 6.11 Temperature rate of change of the apparent depth of melting versus $(\Delta_m T)^{-1}$ for two 1 cm cube KCl specimens heated at 50 K/h.

given by

$$\frac{d\tau}{dT} = S_2(\Delta_m T)^{-1} \qquad (6.5)$$

or, by integration

$$\tau = S_2 \ln\left\{\frac{\Delta_m T_{sm}}{\Delta_m T}\right\} \qquad (6.6)$$

where $\Delta_m T_{sm} = T_m - T_{sm}$ and T_{sm} is the temperature at which τ first becomes non-zero, i.e. the surface melting temperature. Values of S_2 calculated from two separate experiments are included in Table 6.2 . The dependence of S_1 and probably S_2 on heating rate indicates that the observed volume of specimen melted at any temperature is not the equilibrium volume, suggesting that there is a kinetic effect present. The important question is whether it is the supply of heat or the kinetics of the heat absorbtion which is the rate-limiting step. Equations (6.4) and (6.6) were satisfied only within 1 to 1.5 K of T_m. For the earlier 3 to 4 K of the premelting region values of τ were higher than is given by these equations. We emphasize that these equations describe a heat absorbtion equivalent to a bulk surface melting with values of $\tau \sim 0.1$ to 1.0 mm within 0.1 K of T_m.

6.7 Deformation Dependence

Many experimental studies of the surface conductivity alone were carried out under varying conditions using the concentric ring electrode configuration sketched in fig.5.1c. The first of these was to study the effect of deformation. Allnatt and Sime reported no discernible effect on the premelting rise in conductivity due to 5% compression, although we have noted that for one deformed specimen the first rise was half as steep as the second rise. This suggests an annealing of the dislocation arrays and shows the inappropriateness of using simple compression to study deformation dependence at high temperature. What is more suitable is to use a deformation which introduces stable arrays of dislocations which must remain present to maintain the deformed geometry of the crystal.

To do this we bent a 40 mm x 3 mm ⟨100⟩ NaCl single crystal very slowly at a temperature of 800 K in a three

point bending rig[1] so as to generate a single kink in the specimen with inner radius ~ 15 mm and outer radius ~19 mm. The excess of dislocations of one sign over those of the other, required to accommodate a bend of radius r, has a density n_d given by[2]

$$n_d = (br)^{-1} \qquad (6.7)$$

where b is the Burgers vector of the dislocation, in this case $a/\sqrt{2}$. This gives a dislocation density of 1.5×10^{11} lines/m^2. Etch pit studies[3] show that, surprisingly, only near the neutral axis does the total dislocation density agree with that given by eqn. (6.7), and near the surface, n_d is about three times the value.

The straight ends of the specimen were cleaved off, leaving a specimen length ~15 mm and ring electrodes were placed at the kink on the convex surface and on the surface normal to the kink axis. The latter surface is the one cut by the dislocations which accommodate the bend. Another pair of ring electrodes were placed on a surface well away from the kink where there was no visible deformation. The three surface conductances, normalised at 1013 K are shown in fig. 6.12 and these reveal a very definite deformation dependence. The surface cut by the dislocations shows a rise in surface conductivity at 1036 K, well below the melting point, the convex surface at 1044 K and the deformation-free surface at 1054 K. In the last case, electrode contact was poor and the irregularity just before the premelting rise appeared intermittently at lower temperatures throughout the approach to melting.

The sequence of surface melting in the three regions is just as one would expect from considerations of the increase

1 L.R. Greenbank, W.H. Robinson and P.H. Sutter, J. Phys. E3, 949 (1970).

2 J.F. Nye, Acta. Met. 1, 153 (1953).

3 R.W. Whitworth, Phil. Mag. 10, 801 (1964).

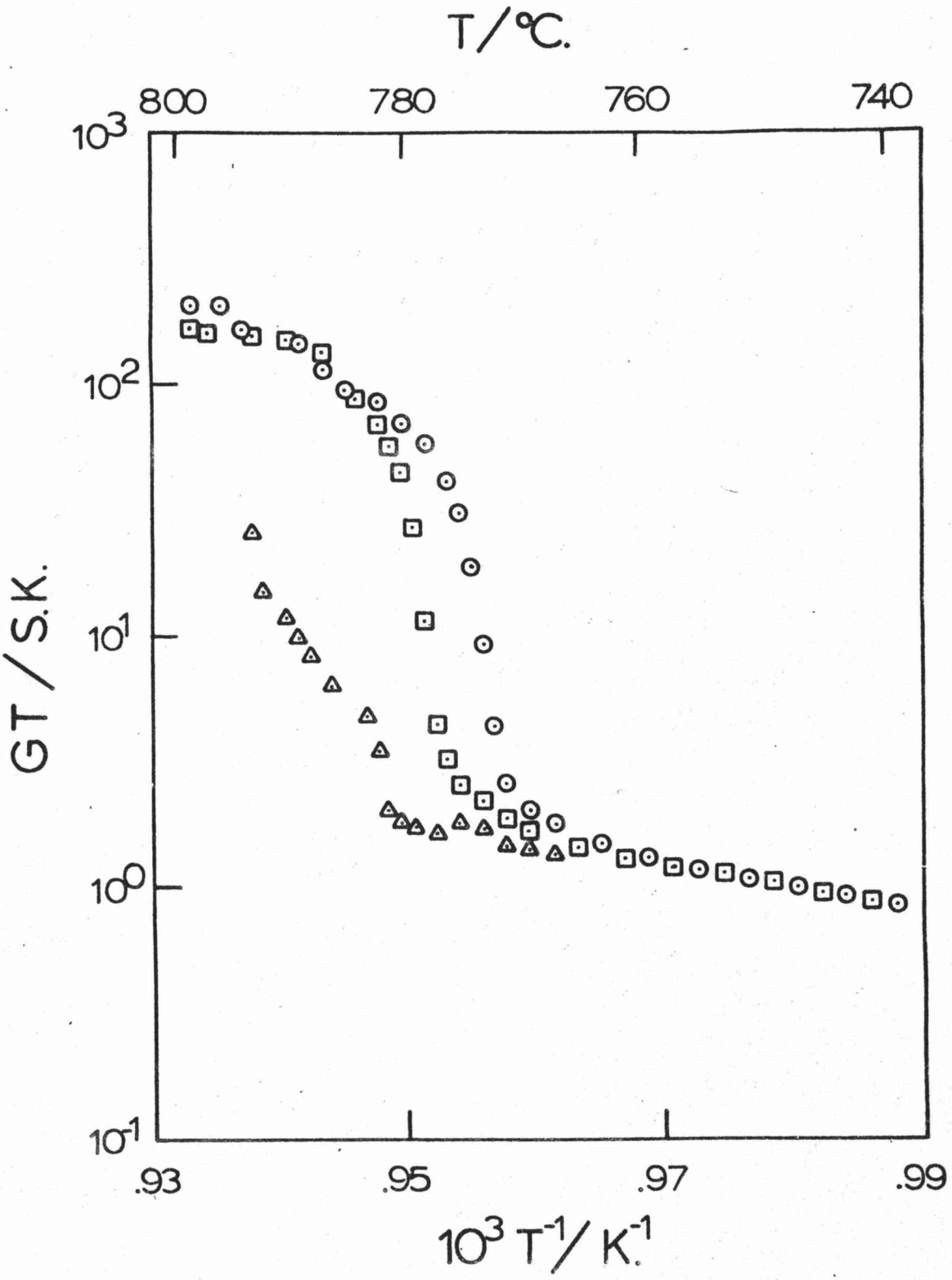

Fig. 6.12 Ahhrenius plot of the surface conductances of different regions of a bent NaCl single crystal. ⊙ : surface normal to the axis of the bend; ⊡ : convex surface and △ : surface in an undeformed region.

in free energy of the solid due to the strain energy of the dislocations. It does not, of course, necessarily mean that a dislocation mechanism of melting is implicated. Ideally, the convex surface should not be cut by dislocations but the fact that surface melting begins there intermediate between the other two faces suggests that many dislocations do pass in and out of this face presumably in the form of long arcs.

We may supplement these results by the observation that abraded (400 grit) surfaces commence melting up to 20 K before cleaved and washed faces, and cleaved faces marginally, by up to 1 K, before washed faces. The faces which were washed, were done so in 25% water and 75% ethanol and quickly dried by soaking up water droplets with absorbent tissue paper in a stream of warm dry air. This leaves a few very small crystallites on scattered regions of the surface, however the electrodes were placed over an area which was smooth and clear. The obvious explanation of the results is that abrasion produces severe deformation at, and just below, the surface with a consequent elevation of the free energy of the local solid and therefore a lowering of the surface melting temperature. On the other hand, washing presumably relieves surface stresses which resulted from cleavage, with the result that the surface melting temperature is higher.

6.8 Orientation Dependence

The variation with surface orientation of the temperature T_{sm} of the rapid rise in surface conductivity was examined for a number of KCl specimens. Values of T_{sm} for $\{100\}$, $\{110\}$, $\{111\}$ and $\{121\}$ surfaces in He and under a vacuum of 2×10^{-2} Pa are plotted in fig. 6.13 against, for want of a better parameter, the surface packing density. The figure also contains diagrams of the structure of $\{100\}$, $\{110\}$ and $\{111\}$ surfaces. The order of surface melting is $\{111\}$, $\{110\}$, $\{112\}$ then $\{100\}$. The surfaces other than $\{100\}$ will be by no means smooth on the atomic scale, and even though much surface annealing will have taken place during heating it is difficult to separate out effects due to deformation from the microtoming and polishing, nevertheless,

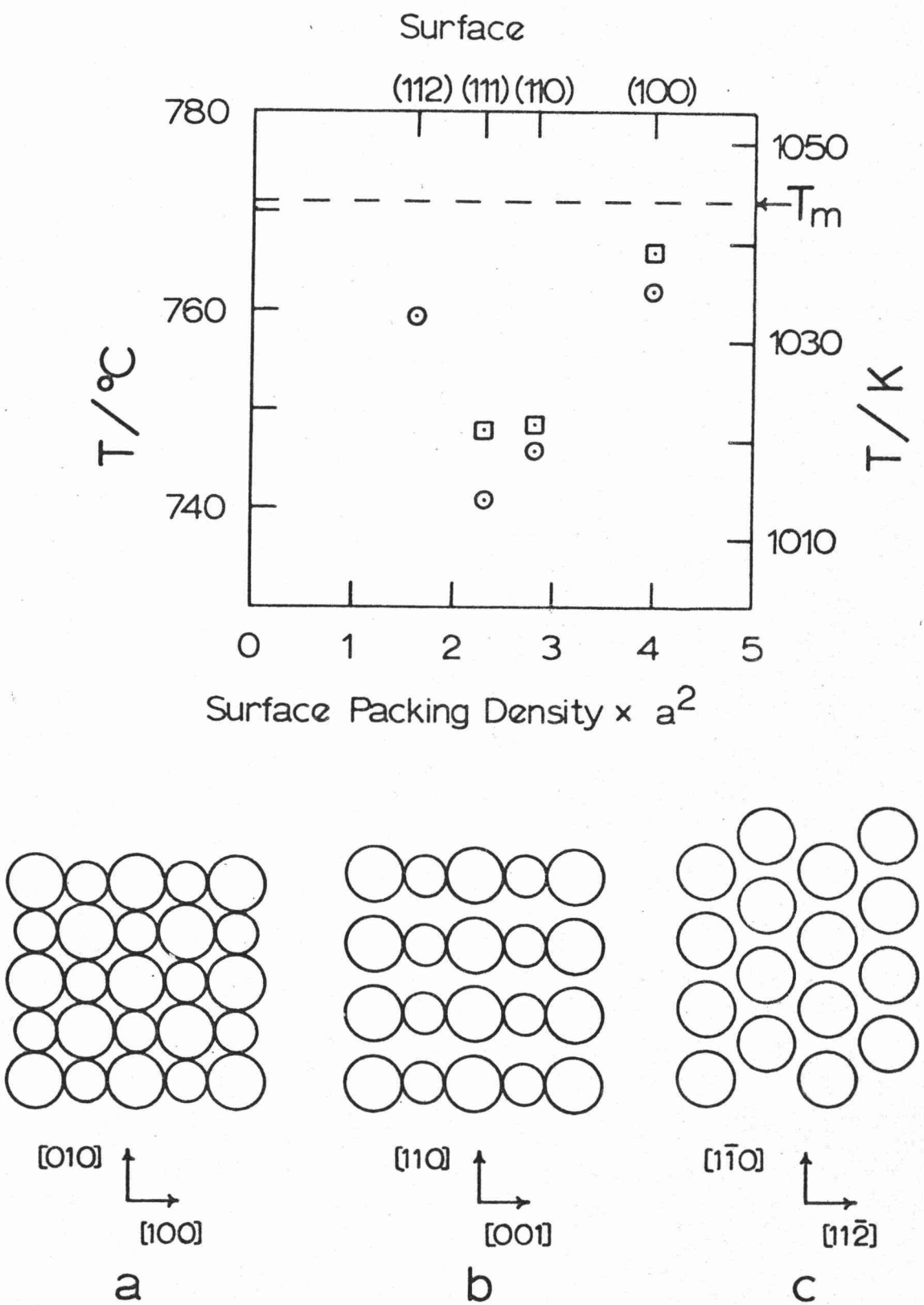

Fig. 6.13 Temperature of the anomalous rise in surface conductivity for a KCl specimen on (100),(110),(111) and (112) surfaces. ⊡ : vacuum of 2×10^{-2} Pa and ⊙ : helium at 8×10^{4} Pa. The structures of the (a) (100), (b) (110), (c) (111) surfaces are also shown. Large circles denote anions, and small circles denote cations.

apart from the {112} surface, the surfaces do follow the order of surface melting proposed by Stranski (as discussed in § 2.2). Because of the physical impossibility of obtaining atomically smooth faces except by cleaving, it is not surprising that a higher index face such as the {112} does not fit into this scheme. In the scanning electron microscope this surface (after an experiment) appears to consist of an array of ⟨100⟩ oriented steps and ledges very much resembling pillars lying obliquely on the surface (see fig. 6.14). In fact all surfaces other than {100} are likely to facet to {100} steps and ledges and it is possible that on the atomic scale we are not observing surface melting of true {110} and {111} faces at all. If these faces are true, then one might also expect that any given surface with index higher than {100} should exhibit an anisotropy in its melting, such that melt-like properties should occur earlier in the less dense packed directions.

To examine this possibility, the surface conductivity of a KCl crystal was measured on a {110} surface in two directions: the closest packed direction ⟨001⟩ and perpandicular to this, the direction ⟨110⟩ (see fig. 6.13). This is a demanding test since on naive geometrical considerations it might be considered that the surface channels in the ⟨001⟩ direction would assist an earlier premelting rise in conductivity in the ⟨001⟩ direction. The conductance curves are shown in fig. 6.15 and quite consistently the conductance rises 4 K earlier in the ⟨110⟩ than in the ⟨001⟩ direction. This is remarkably consistent with Stranski's ideas as well as those of Burton, Cabrera and Frank, and Jackson which were discussed in § 2.4. For all of these higher index surfaces the rapid rises in surface conductivity were not accompanied by a detectable heat absorbtion. Rather, this occurred as for the ⟨100⟩ specimens later at ~ 5 K below T_m. Because the lower limit of detection of heat absorbtion corresponds to melting to a depth of 1 μm, this means that if the rise in surface conduction for crystals other than {100} is due to surface melting, the equivalent depth of melt over the surface is less than 1 μm.

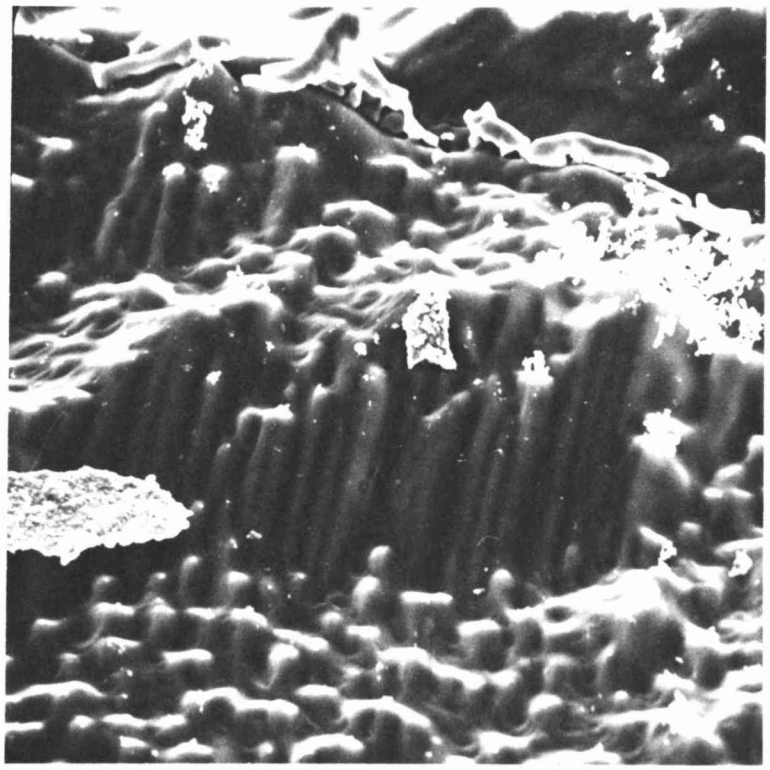

Fig. 6.14 Scanning electron micrograph of a (112) surface which has been taken up to its surface melting transition. The surface has facetted to (100) ledges with rounded edges. Magnification = 560 x. The debris on the surface is dust from sawing the sample from the specimen.

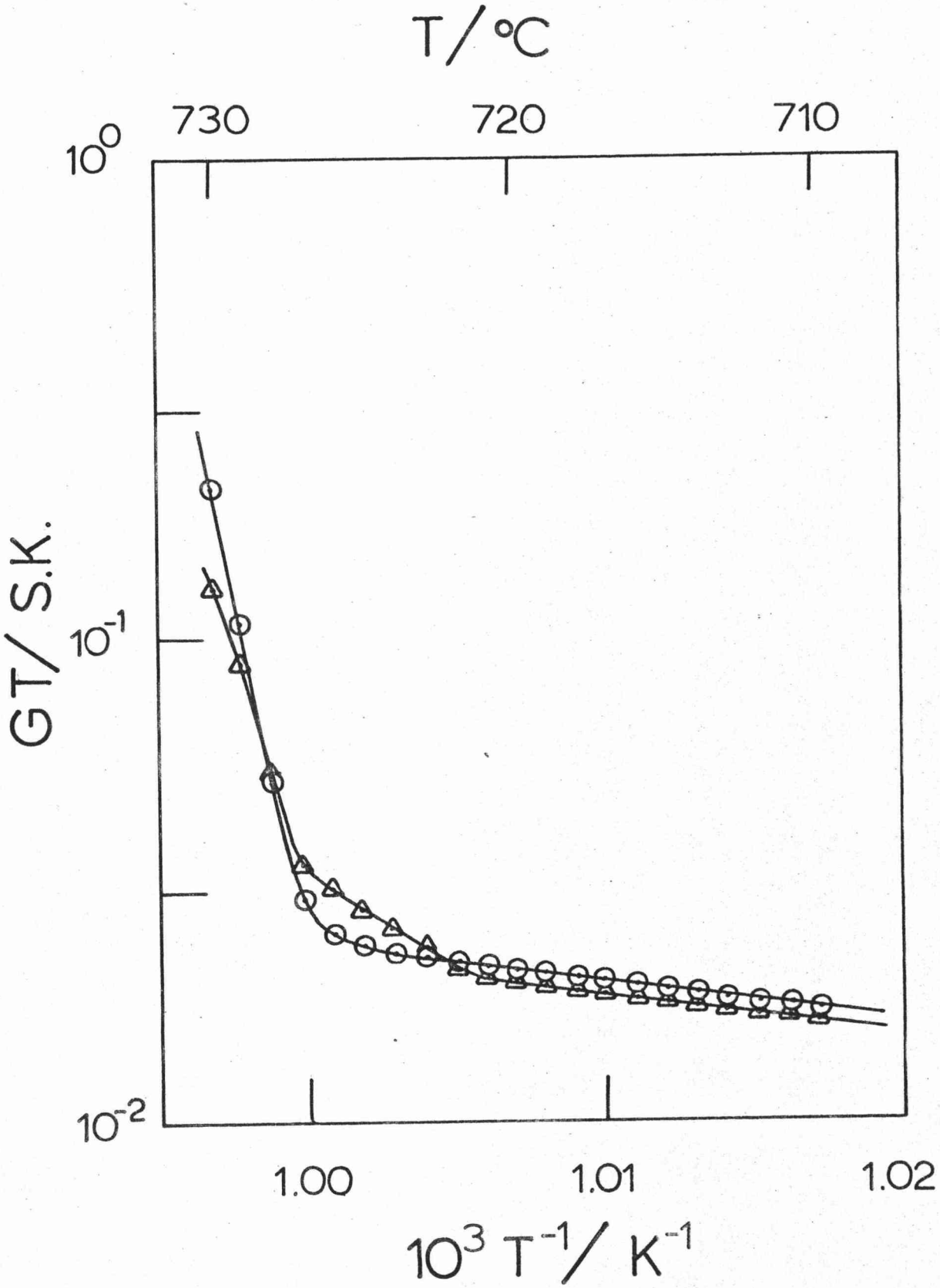

Fig. 6.15 Anisotropy of the anomalous rise in ionic conductivity for a KCl {110} surface.
⊙ : ⟨100⟩ direction; △ : ⟨110⟩ direction.

6.9 Surface Features

The surface features revealed by the scanning electron microscope distinguish markedly between melting, premelting and the conditions at temperatures below the premelting region. Fig. 6.16 shows the surface of a KCl crystal which was raised at 100 K/h to 1020 K then cooled i.e. the specimen did not enter the premelting region. Many thermal etch pits due to preferential sublimation from dislocations cutting the surface are apparent, but apart from these and a few cleavage steps, the surfaces are flat and featureless. Figs. 6.4 to 6.6 showed surfaces of an NaCl crystal which just entered the premelting region and then was cooled rapidly. The etch pits are still apparent there, but the edges of these are rounded and the surface has a 'puddled' appearance. On the other hand, when the surface has encountered the bulk melting point, the etch pits disappear and the surface acquires long, smoothly rounded ledges and flow patterns, a typical example of which is shown in fig. 6.17. Clearly, then, the premelting surface is distinct from the melting surface in that in the former, the single crystalline defects extend right to the surface. This is consistent with the view which has been emerging and which we shall develop in chapter 7, that in the premelting region, shallow intrinsic surface melting occurs on the atomic scale with an accompanying high vaporisation rate. Dislocation thermal etch-pits would therefore persist in this region. On the other hand, when the surface has encountered the bulk melting point, crystalline defects such as dislocations become 'buried' beneath the isotropic melt layer.

When the previously melted surface is annealed just below the premelting region, crystalline features appear again as shown in fig. 6.18. This is due partly to the single crystal growing into the polycrystalline previously melted layer, and partly to the stripping off of this layer due to vaporisation. This figure shows the rounded edge of

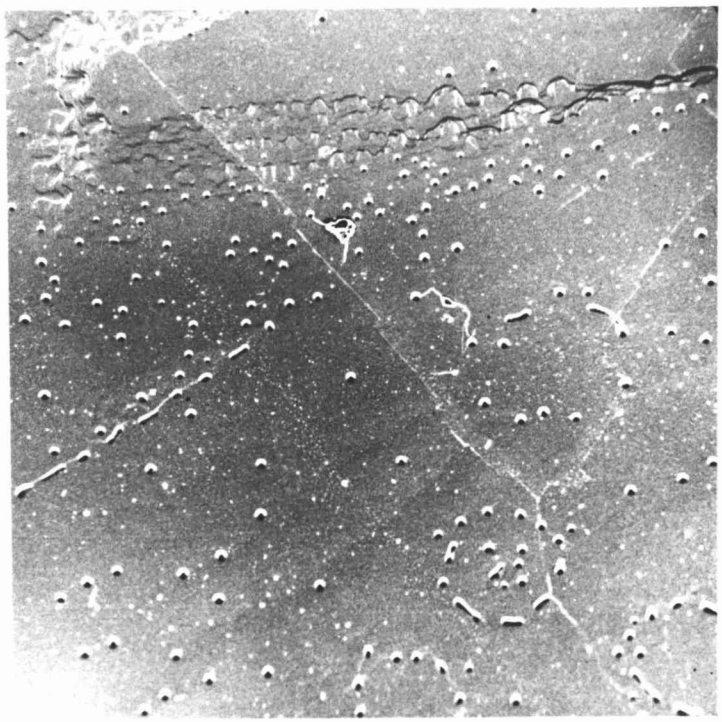

Fig. 6.16 Scanning electron micrograph of a (100) surface of a KCl crystal which had been raised to just below the premelting region. The surface has remained flat apart from the appearance of thermal etch pits. The pits are often grouped in rings. Magnification = 60 x.

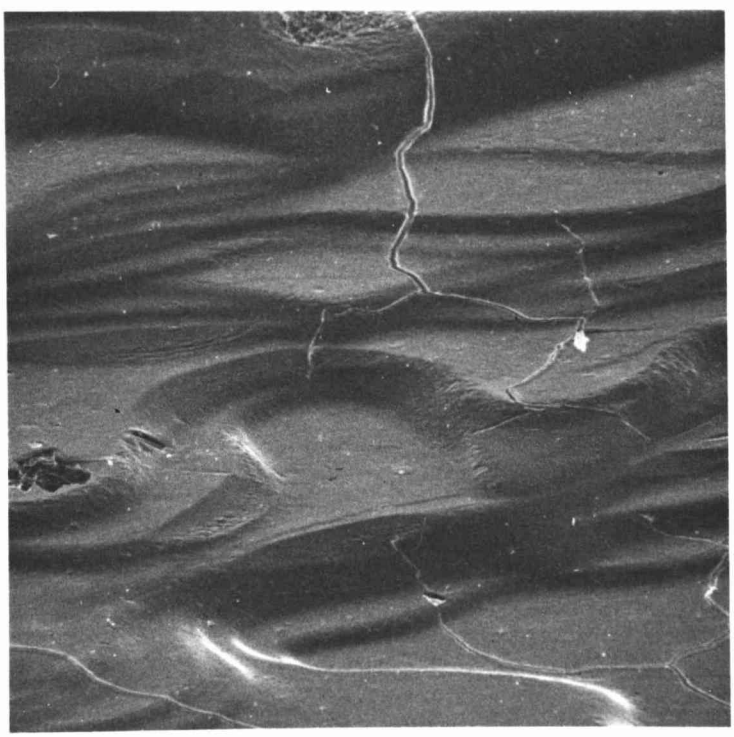

Fig. 6.17 Scanning electron micrograph of an NaCl surface which has just reached the bulk melting point. Magnification = 430 x.

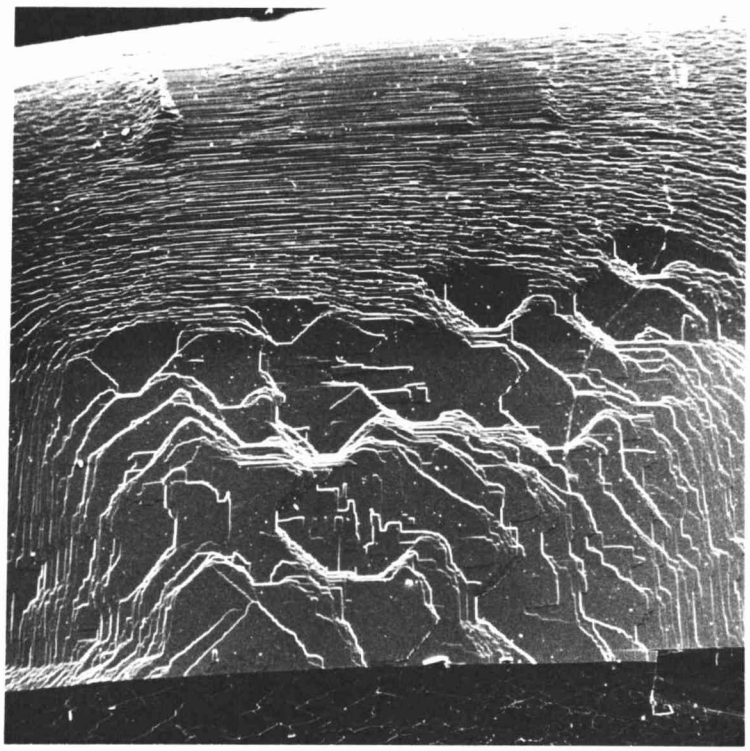

Fig. 6.18 The refacetting of a KCl single crystal (100) surface which had been taken to the bulk melting point then cooled and annealed for 20 mins. at ~1020 K. The (100) ledges run closer together at the rounded edge. Magnification = 33 x.

a KCl specimen and the surface comprises facetted ledges and steps, the steps coming closer together at the edge to accommodate the bend.

6.10 Superheating Experiment

The attempt at superheating a cylindrical NaCl specimen was unsuccessful, even though the calibration runs gave completely satisfactory results. Fig. 6.19 shows the heating transients due to the application of a range of applied voltages from 5 V rms to 12 V rms at just one of the base furnace temperatures, 1060 K. In each case, the specimen axial temperature rose according to the standard exponential form of

$$\Delta T = \Delta T_{ss} \left\{ 1 - \exp(-t/\Theta) \right\} \qquad (6.8)$$

where ΔT_{ss} is the steady state temperature increment and Θ is the time constant. In all cases Θ was not a simple function of temperature and applied voltage but ranged from ~ 40 s to 50 s. Accordingly, after ~ 3 minutes we could be sure that the specimen without an internal thermocouple would have reached its steady state value. Values of ΔT_{ss} are shown in fig. 6.20 plotted against σV_o^2 for a range of base temperatures from 1020 K to 1060 K, and the relationship is linear, as we may deduce from eqn. (C 10). The straight line is

$$\Delta T_{ss} = 1.37\, \sigma V_o^2 \ (\mathrm{K.m.W^{-1}}). \qquad (6.9)$$

However, when we attempted the actual superheating experiment, we could get little closer than 5 K below T_m before joule heating in the high conductance surface region caused melting there, and the subsequent increase in conductance caused further heating and a resultant divergence in melting. The use of the superheating rig shown in fig. 5.10 failed to give much improvement and the electrode contact was poor.

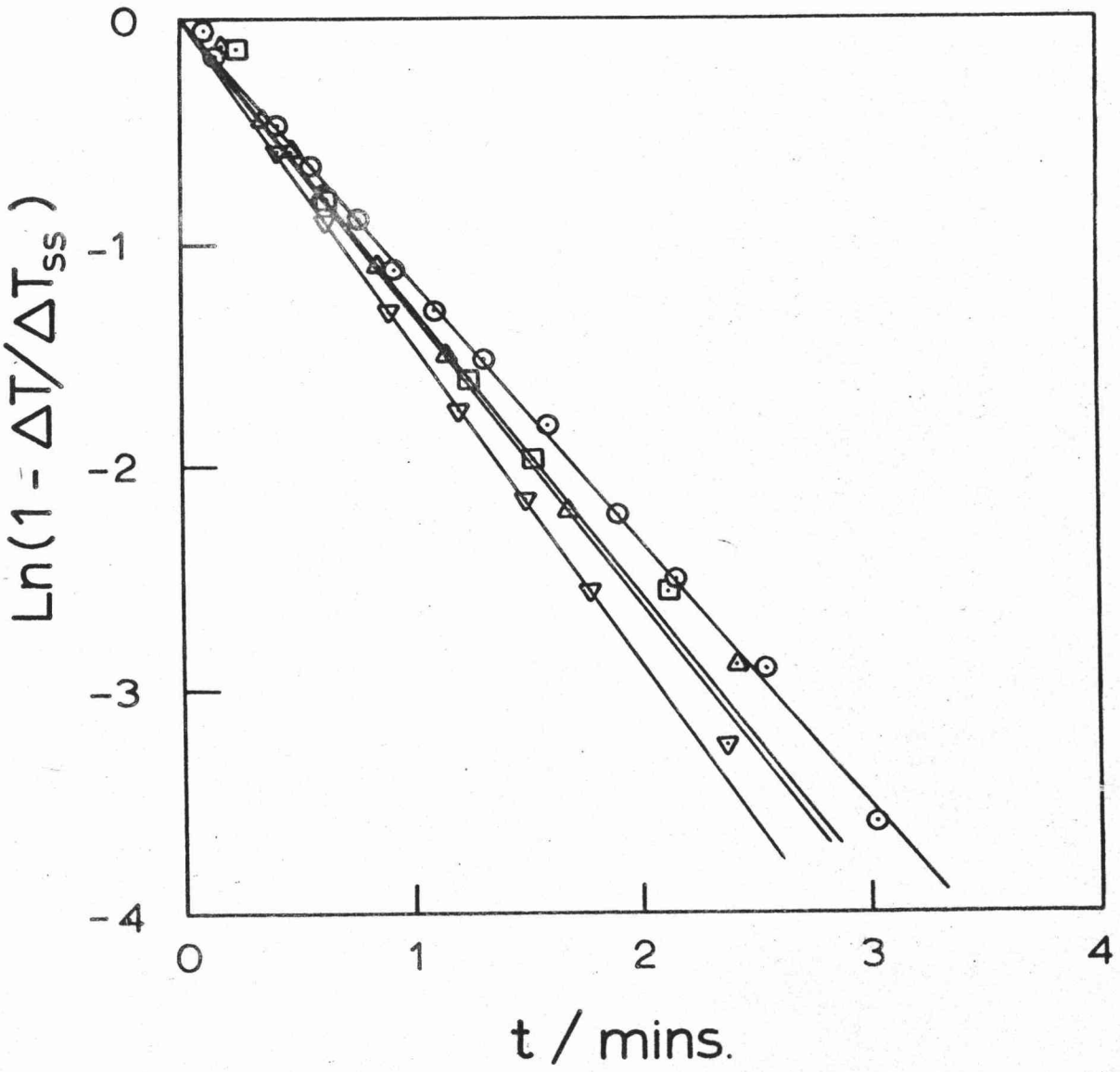

Fig. 6.19 Joule heating transients in a superheating experiment for a range of applied voltages. △ : 5V ; ⊡ : 7V ; ⊙ : 10V ; ▽ : 12V.

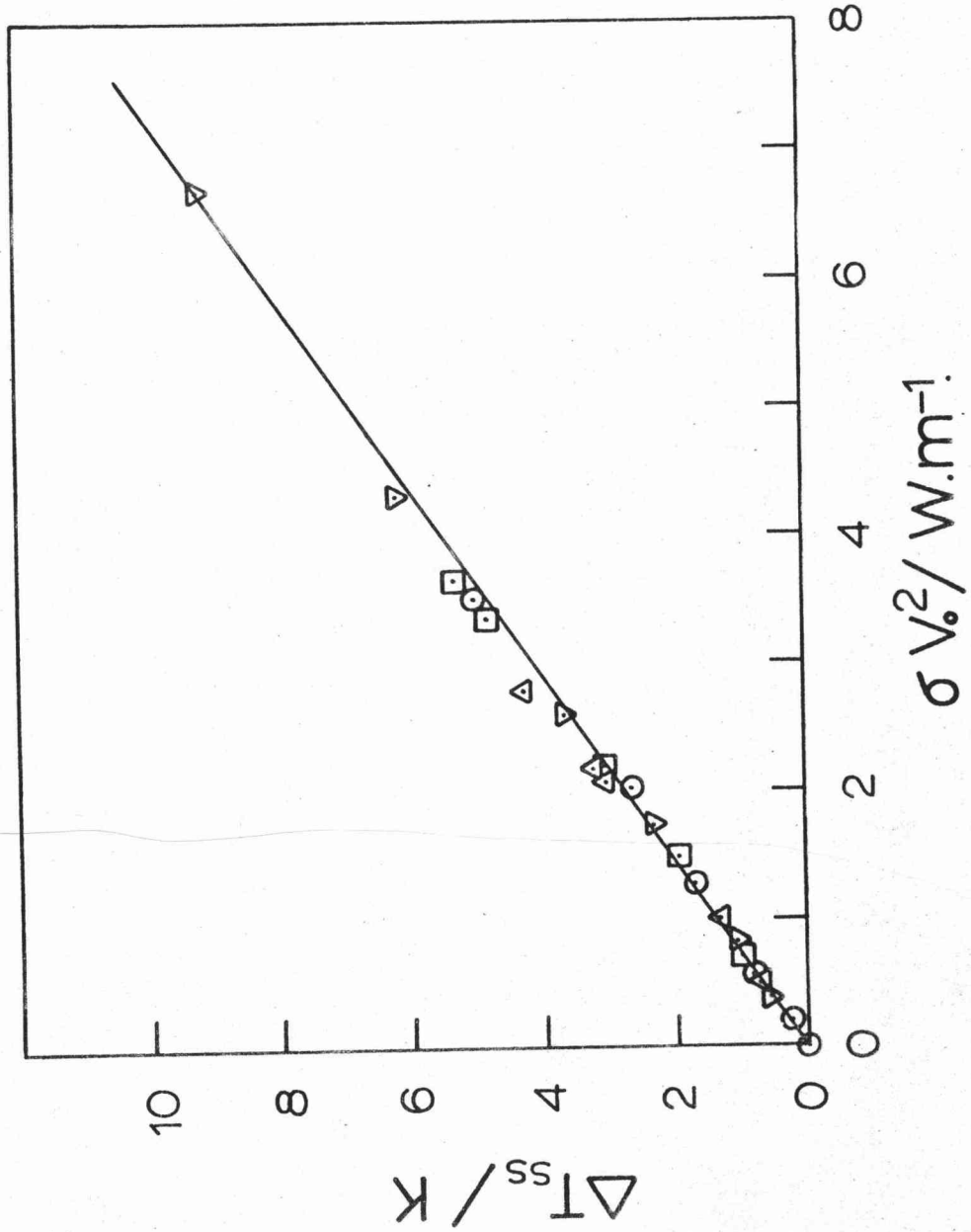

Fig. 6.20 Steady state temperature increments versus σV_o^2 for a range of furnace temperatures. ⊙ : 1020 K; ⊡ : 1040 K; ▽ : 1050 K and △ : 1060 K.

7 DISCUSSION

In this chapter we attempt to explain at least qualitatively the experimental results we have presented in § 6 and to develop the implications of our explanation with a view to further clarification of the processes and mechanisms involved in melting. We begin by examining the various possible causes of the premelting heat absorbtion, then discuss in detail the roles of vaporisation and premature surface melting. We introduce a dislocation theory for intrinsic surface melting, then develop this to discuss the movement of the s-l interface from the surface into the crystal interior.

Our principal experimental result is that there is no bulk premelting rise in conductivity up to within at least 0.5 K of the melting point, and while we are unable to distinguish between bulk and surface heat absorbtion, it seems likely that the heat absorbtion also is at the surface only. We proceed therefore under the assumption that no premelting of any kind is occuring within the crystal bulk. Thus, no bulk theory of premelting finds application to the alkali halides we have studied. These include for example the possibility of a diffuse transition involving the disordering of the cation sublattice as suggested in § 3, or Robinson's[1] analysis of the premelting conductivity reported by Allnatt and Sime in terms of pipe diffusion along thermally formed dislocations. Firstly, we shall discuss a number of possible surface-related processes which might contribute to an enhanced surface conduction together with an absorbtion of heat.

7.1 Possible Mechanisms of Surface Heat Absorbtion and Surface Conductivity.

It was suggested in § 6 that two possible basic processes might account for our premelting results: premature surface melting and sublimation, and because of the capilliary creep of the specimen surface around a platinum wire (§ 6.2, p.91), the conclusion was that the active

1 W.H. Robinson, J. Appl. Phys., in press.

process was the first or, more likely, both together, but not sublimation alone. Surface melting in turn might be attributable to a number of causes including the intrinsic excess-free energy of a surface, exposure to internal impurities, or external impurities such as the ambient gas or metal vapour, melting along edges and at corners, melting in the neighbourhood of where a dislocation cuts a surface, melting of the curved portions of a rumpled or dimpled surface or, finally, the excess-free energy of a surface arising from the Debye-Hückel charge cloud beneath the surface which, in turn, arises from the preferential formation of cation vacancies at surfaces. Each of these will be considered in turn, while sublimation or vaporisation will be examined separately in the next section.

7.1.1 Stranski's Surface Melting.

The first of these: surface melting due to the intrinsic excess-free energy of a surface as proposed by Tammann and Stranski explains, as we have seen, our observed sequence of melting of low index surfaces. The immediate obstacle, however, is that we have suggested in §2.2.2 (p.12) that the surface quasi-melt occupies between 3 and 5 ion spacings depending on surface orientation whereas we are observing heat absorbtion consistent with the melting of from 1 μm at $\sim$5 K below T_m, to in excess of 100 μm within 0.25 K of T_m (see §6.6, p. 106). This process alone is not therefore at all able to account for our results.

7.1.2 External Impurities.

External impurites impinging on the crystal surfaces may cause a lowering of melting point and the diffusion of such impurities after the s-l interface may be shown to give two regimes of $\tau \propto \Delta_m T^{-1}$ and $\tau \propto -\ln \Delta_m T$ depending on the mobility of the impurity. Nevertheless, it would seem that there is just not enough impurity present in the melt for this process to be tenable. Let us examine this in more detail. For a given impurity present in the melt in mole fraction x the greatest depression of melting point occurs when the impurity is soluble only in the melt and not in the solid. For this case, Raoult's law gives

$$\Delta_m T_R = RT_m^2 \kappa / M\Delta H_m . \qquad (7.1)$$

There is little experimental data available on the solubilities of inert gases in alkali halide melts, however Blander et al[1] have estimated solubilities by assuming the energy of a molecule in the melt is given by the continuum surface-free energy of a spherical cavity, and thus obtain

$$\ln(C_d/C_g) = - 4\pi r^2 N_o \gamma_1 \qquad (7.2)$$

where r is the radius of the molecule, C_g is the concentration, P/RT, of gas molecules in the gas and C_d is the concentration, $\rho_1 \kappa / M$, of gas molecules dissolved in the melt. ρ_1 is the density of the melt. The melting point depression is thus given by

$$\Delta_m T = (PT_m / \rho_1 \Delta H_m) \exp(-4\pi r^2 \gamma_1 / kT_m) . \qquad (7.3)$$

Now, at the highest pressure of He used in any of the present experiments, namely 2.74×10^5 Pa with NaCl, the shift in melting point is calculated to be only 0.093 K. Lee and Johnson[2] have obtained a more reasonable expression for gas solubilities in melts, which are in good agreement with experiment, and for inert gases in alkali halides solubilities are about two to three times these given by eqn. (7.2). We might expect therefore that ambient gas in our experiments has an effect on melting point to a maximum extent of about 0.2 K. The shifts in T_{sm} with changing gas and gas pressure reported in §6 were of this order of magnitude and these are plotted in fig. 7.1 against values of $\Delta_m T$ obtained from eqn. (7.3) multiplied by 2.5. If the observed shifts are reliable, they are still a little too large to be accounted for by gas solubility in the melt, particularly in view of the fact that inert gases are soluble also in the solid alkali halides[3] which means that $\Delta_m T$ is smaller than is

1 M. Blander, W.R. Grimes, N.V. Smith and G.M. Watson, J. Phys. Chem., 63, 1164 (1959).

2 A.K.K. Lee and E.F. Johnson, I and E.C. Fundamentals 8, 726 (1969).

3 N.N. Alekseenko, P.V. Volobuev and P.E. Suetin, Sov. Phys. Solid State 14, 2073 (1973).

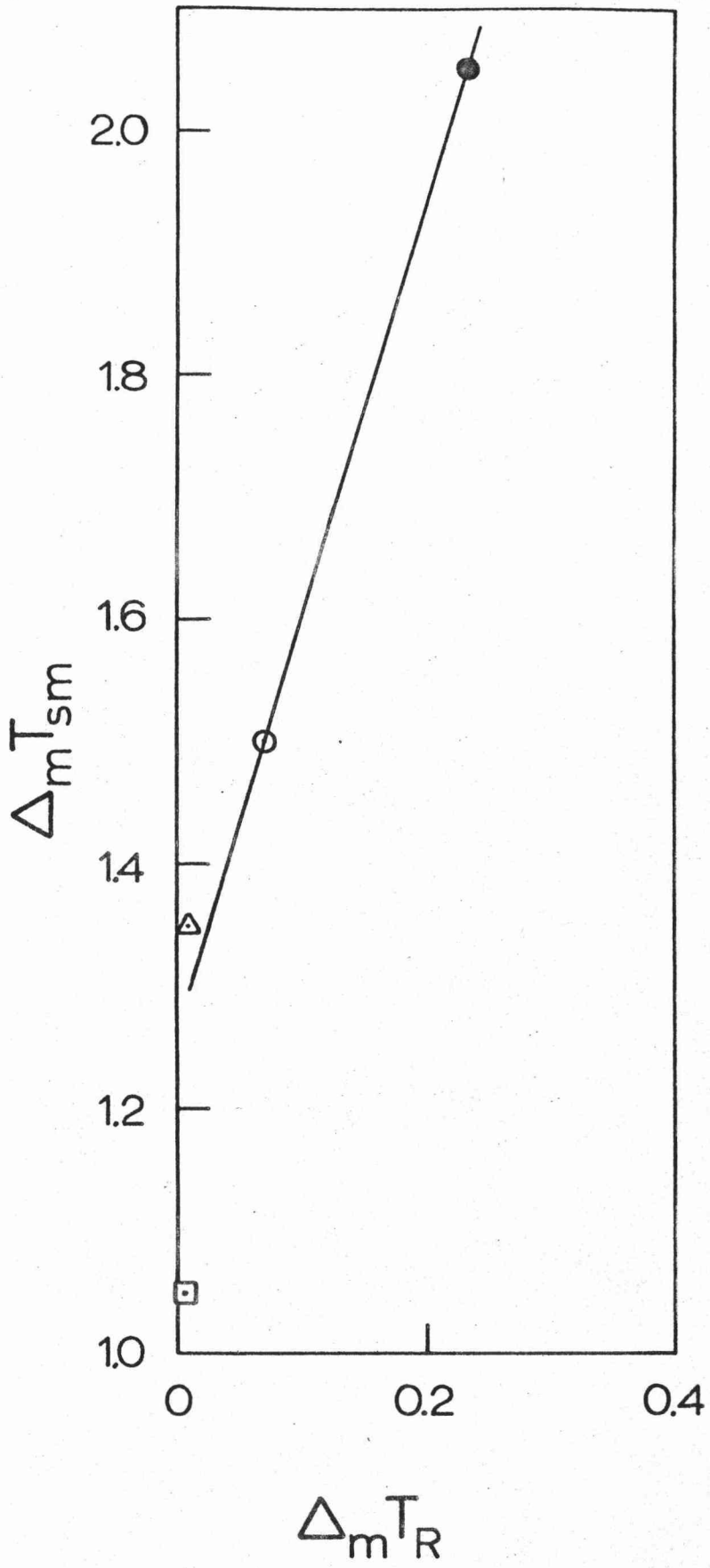

Fig. 7.1 The shift in the apparent surface melting temperature versus the shift given by Raoult's law for a gas dissolved in the melt. ● : He, 2.7 x 10^5 Pa; ⊙: He, 0.8 x 10^5 Pa; △: Ar, 0.8 x 10^5 Pa and ⊡ : N_2, 0.8 x 10^5 Pa.

given by eqn. (7.1). Unfortunately, however, nothing very conclusive can be drawn here as the errors in reproducibility for this experiment were about as large as the shifts observed. At least the shifts are in the correct sequence as suggested by eqn. (7.3) but they are also largely consistent with suppressed evaporation due to ambient gas. What is certain, is that the absolute value of $T_m - T_{sm} \sim 5$ K is too large to be accounted for by the effect of ambient gas.

The same applies for any metal vapour which might deposit on the specimen. For $\Delta_m T = 5$ K in NaCl, eqn. (7.1) suggests $\varkappa = 1.4 \times 10^{-2}$, one or two orders of magnitude higher than the concentration of Mn observed on the crystal surface by EDAX after an experiment. Within the crystal bulk, spectrographic analysis revealed the following mole fractions of impurity: Si, 2×10^{-4}; Ni, 2×10^{-4} and Al, 1×10^{-4}. If this impurity is segregated in the solid but soluble in the melt, and moreover, if the total impurity content at any time is dissolved in the melt, then from Raoult's law for a given value of $\Delta_m T$ the thickness of surface melting is

$$\tau = vRT_m^2 \varkappa / A \, \Delta H_m \, \Delta_m T \qquad (7.4)$$

where v is the total crystal volume and A the total surface area. Thus, at any temperature there is a non-zero melt thickness and this increases inversely with $\Delta_m T$, as found for NaCl, NaBr and LiF. For the first entry in Table 6.2 $vRT_m^2 \varkappa / A \, \Delta H_m = 1.1 \times 10^{-4}$ m.K^{-1} giving $\varkappa = 1.9 \times 10^{-4}$ close to, and in fact less than, the impurity levels noted above. The cause of the premelting may thus appear explained except that the total impurity content of the solid is required to be dissolved in the melt, whereas analysis after an experiment showed a uniform distribution of the impurity, thus requiring a mole fraction two orders of magnitude higher to explain the results. Moreover, these impurities are soluble in the solid at high temperatures.

7.1.3 Melting at the Edges of Steps.

A small contribution to surface conductivity and

heat absorbtion arises due to premature melting of corners and edges on the steps and ledges on surfaces which are present in abundance at the atomic level, and certainly such regions are important in the nucleation of melting. The theory for the depression of melting point at corners and edges is worked out in Appendix D, and it is shown that in the case of an edge, a cylindrical s-l interface appears, the radius of which increases hyperbolically with $\Delta_m T$ as T_m is approached, and the interface moves progressively into the lattice. A similar result occurs if the surface is rumpled or dimpled from a previous approach to melting as is shown in fig. 6.6. However, even in the extreme where the total surface has its maximum density of rumples and edges, the actual average depth of surface melting would be $\sim r_{sl}$ which is about half the melting radii for spherical particles and these are shown in Table D1 of Appendix D to lie between .02 and .03 μm. Again, the predicted extent of melting is far too small to account for our observed heat absorbtion. For the surface dimples referred to in figs. 6.4, 5 and 6 the edge curvature were noted to be $\sim 10\mu$mwhich, using the melting point depression constants in Table D1, gives a melting point there only .016 K below T_m.

7.1.4 Melting where a Dislocation cuts the Surface.

The effect of deformation on the surface melting temperature as shown in fig. 6.12 for a kinked specimen suggests that the large density of dislocation cores is sufficient to raise the free energy of the solid and cause premature melting. The energy per unit length of a dislocation comprises an elastic part, U_e and a core part U_c given, for an edge dislocation, by[1]

$$U = U_e + U_c = b^2\mu/4\pi(1-\nu)\ \ln(R_c/r_o) + b^2\mu\xi/4\pi(1-\nu) \qquad (7.5)$$

where $b = a/\sqrt{2}$ is the Burgers vector of the dislocation, ν is Poisson's ratio, r_o the radius of the core, R_c the cut-off radius being half the average separation of dislocation cores and ξ is an experimental constant of the order of unity. (We find in § 7.3, $\xi = 0.752$ for NaCl). The

1 J.P. Hirth and J. Lothe, Theory of Dislocations (McGraw-Hill, N.Y., 1968) p.78.

distributed energy density is therefore $n_d(U_e + U_c)$, where n_d is the dislocation density. Therefore, the shift in melting point is

$$\Delta_m T = T_m n_d (U_e + U_c) / \rho_s \Delta H_m \qquad (7.6)$$

Using the estimated value of $n_d = 1.5 \times 10^{11}$ lines/m^2 and Hunter and Siegel's elastic constants for NaCl at T_m we obtain a very low value of $\Delta_m T = 2 \times 10^{-4}$K. Clearly then, any effect arising from the dislocations introduced by bending must occur at the cores rather than via the average distributed energy density.

Two effects are possible at the cores: the cores may melt, even within the crystal bulk, or the region where the dislocation cuts the surface may melt causing a melt dimple much in the same way that a thermal etch pit forms at the exit of a dislocation. These questions are examined in Appendix E and it is shown that while the core does not melt, a broad shallow melt dimple does appear at the dislocation exit, the radius of which increases as $(\Delta_m T)^{-\frac{1}{2}}$ and the volume of which increases as $(\Delta_m T)^{-4/3}$. The radii, depths and volumes for a range of values of $\Delta_m T$ are given in Table E1 and again it is apparent that the quantity melted is far too small to account for our results. Taking the extreme case of $\Delta_m T = 0.05$ K for a dislocation density of 1.5×10^{11} lines/m^2 the equivalent uniform depth of melting over the whole crystal surface would be 3×10^{-13}m ! It is, by the way, notable that the melt pit radius at this value of $\Delta_m T$ is as large as 100 times its Burgers vector.

Similarly, the Debye-Hückel charge cloud beneath the crystal surfaces is incapable of producing the extent of surface melting necessary to explain our results. The width of the charge cloud at T_m is ~ 4 nm[1] and only a part of this could contribute to any appreciable surface melting.

1 W.H. Robinson, J.L. Tallon and P.H. Sutter, Phil. Mag., in press.

We conclude therefore that premature surface melting cannot, on its own, explain the very substantial heat absorbtion which occurs within 5 K of the melting point, and consequently we are left with the only remaining possibility that both surface melting and vaporisation (rather than sublimation) are occurring.

7.2 Vaporisation.

We shall now develop what we believe is the operative mechanism of premelting in the alkali halides. Sublimation and vaporisation studies by Ewing and Stern[1] have been briefly referred to in §3. These showed in the case of metallic silver and lithium fluoride a continuous Ahhrenius behaviour in vaporisation rate with no change in passing from solid to melt. In marked contrast for NaCl, KBr and CsI the vaporisation flux begins to level out starting about 100 K below their respective melting points. At and beyond the melting point the flux rises rapidly. A schematic of the vaporisation curve is shown in the top right hand corner of fig. 7.8,p.137. We propose that due to all of the

adsorbed surface state, the second a desorbtion step to the vapour. We suggest that the levelling off of the flux as a function of temperature, which commences about 100 K below T_m, arises from the facetting of the $\{100\}$ faces. At lower temperatures the desorbtion step is rate controlling, however, at higher temperatures where the maximum flux is as large as 50 mg. cm^{-2}. min^{-1}., the activation step for singular surfaces will almost certainly become rate controlling and the flux will increase less with further temperature increase. The same applies to vaporisation from vicinal surfaces, and in these, vaporisation will be confined to the steps on ledges. Thus for singular and vicinal surfaces the vaporisation sites are not formed fast enough, and the flux is therefore less than what it might have been. When surface melting begins near T_m, the appearance of irregular atomic cavities across the whole surface introduces a large number of further vaporisation sites and the flux climbs with further increase in temperature.

We have seen in § 2.4 that the $\{100\}$ faces of many of the alkali halides are either singular or vicinal and consequently their vaporisation near their melting points is saturated, or nearly so. Thus there is a nearly constant rate of heat absorbtion which appears only as a nearly constant temperature differential between specimen and chamber. Accordingly, for a constant heating rate the specimen temperature increases linearly until when surface melting commences the vaporisation rate begins to climb and the specimen temperature to lag increasingly further behind the chamber temperature, as we have observed. Surfaces which are non-singular in the neighbourhood of the melting point are so atomically rough that vaporisation continues freely and thus in the case of metallic silver, which is non-facetting,[1] there is no anomalous behaviour.

There is, of course, a problem with LiF that no vaporisation anomaly was observed by Ewing and Stern, yet we observed a distinct premelting effect. One likely explanation arises. According to Table 2.1 LiF is borderline, but

1 D. Woodruffe, The Solid-Liquid Interface (Cambridge University Press, 1973.

probably should have non-singular {100} surfaces. It may be that under vacuum (as in Ewing and Stern's experiments) it is non-facetting and in gas it is facetting. This is certainly so in the case of metals[1] which thermally facet in the presence of adsorbed gases but, in general, do not in the absence of an adsorbate since for them $\alpha < 2$. On the other hand, MgO which has the same structure as the rock salt type alkali halides has been found to facet under vacuum on {100} planes[2] and this is because the value of α at the facetting temperature of 1400 K is as large as 4.43.

As a test of our hypothesis we had searched for a premelting heat absorbtion in a crystal with {110}, {111} and {112} faces and with no {100} faces exposed. None of these faces according to Table 2.2 are facetting and consequently the crystal should evaporate freely and experience no premelting heat absorbtion. In fact it had been observed in the experiments on surface conductivity of higher index faces that these evaporated far more quickly than {100} faces. However, as noted in §6.8 the heat absorbtion for these crystals is still present within 5 to 6 K of the melting point, and there is no trace of heat absorbtion at the surface melting transition which occurs up to 30 K below T_m for these crystals, as might have been expected. This, doubtless, arises from the fact that the {110}, {111} and {112} faces do not long remain such but quickly transform to arrays of obliquely oriented {100} steps and ledges as shown e.g. in fig. 6.14, so that while the vaporisation rate is higher than for a single cleaved {100} surface, the facetting on the ledges still contribute to the premelting rise in vaporisation rate and subsequent heat absorbtion.

A more distinct example of the facetting of surfaces of higher index than {100} is shown in fig. 7.2. This is a view of a portion of a KCl crystal which had just melted, run

1 J.J. Lander in: 'Progress in Solid State Chemistry 1, 26 (1965).

2 V.E. Henrich, Surface Sci. 57, 385 (1976).

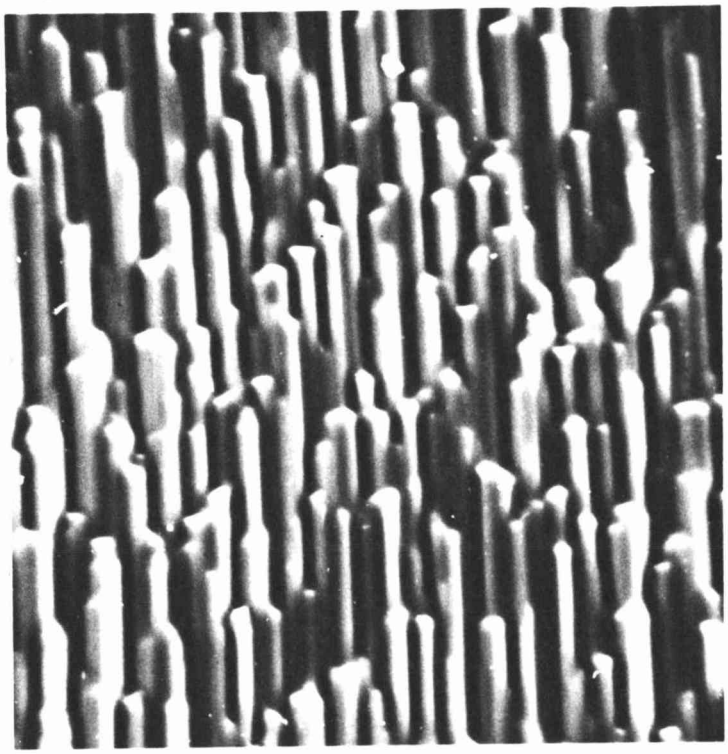

Fig. 7.2 Thermal facetting of a plane oriented ~ 40° to the {100} plane. Mag. = 560 x.

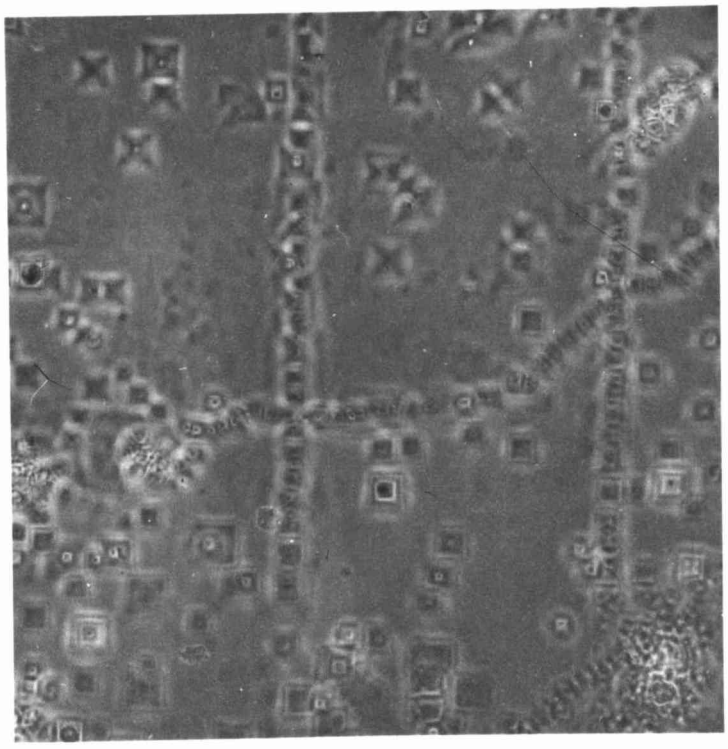

Fig. 7.3 Chemically etched {100} surface of a KCl crystal. The pits are distinctly rectangular. Dislocation density = 1.8×10^9 m^{-2}, mag. = 250 x.

down the side of the crystal and crystallised in a wedge-shaped block at the foot of the crystal with an incline of about 40°. With annealing, the block appears to have recrystallised as a coherent extension of the single crystal and the inclined surface has facetted to form an array of long {100} steps. Accordingly, the apparent surface melting of higher index faces may be due to premature melting on the edges of these exposed ledges rather than Stranski's surface melting of ideal loose packed surfaces.

A more critical test would be to look for premelting effects in LiBr, LiI or RbI which according to Table 2.2 should have no facetting faces and therefore, according to our hypothesis, no premelting rise in vaporisation rate. It is perhaps also significant to note here that in the extremely careful demonstration of the lack of premelting phenomena in Gallium by Wenzl and Mair[1], Gallium is characterised by a very high boiling point relative to its melting point (T_m = 302.91 K, $T_b \sim$ 1870 K) and consequently has a low vapour pressure at its melting point and is therefore unlikely to be affected by any changes in vaporisation rate there.

7.2.2 Thermal Etch Pits

Before we proceed to examine the vaporisation heat absorbtion quantitatively, there are some features in the vaporisation pits about dislocations shown in fig. 6.16 which are worthy of discussion. This particular KCl specimen had been raised at 100 K/h to 1020 K and had not entered the premelting region. The pits are evidently quite circular and these may be compared with pits obtained by chemical etching at room temperature shown in fig. 7.3[2]. These are rectangular in perimeter due to the elastic anisotropy at room temperature whereas the circular shape of the high temperature pits reflects the nearly isotropic conditions which obtain near the melting point. The pits are as large as 30 μm in diameter and, interestingly, often appear grouped in rings, one of which may be seen in fig. 6.16 and is reproduced at higher magnification and at a more oblique angle in fig.7.4.

1 H. Wenzl and G. Mair, loc. cit.

2 W.H. Robinson, Ph.D. Thesis, University of Illinois,unpubd.

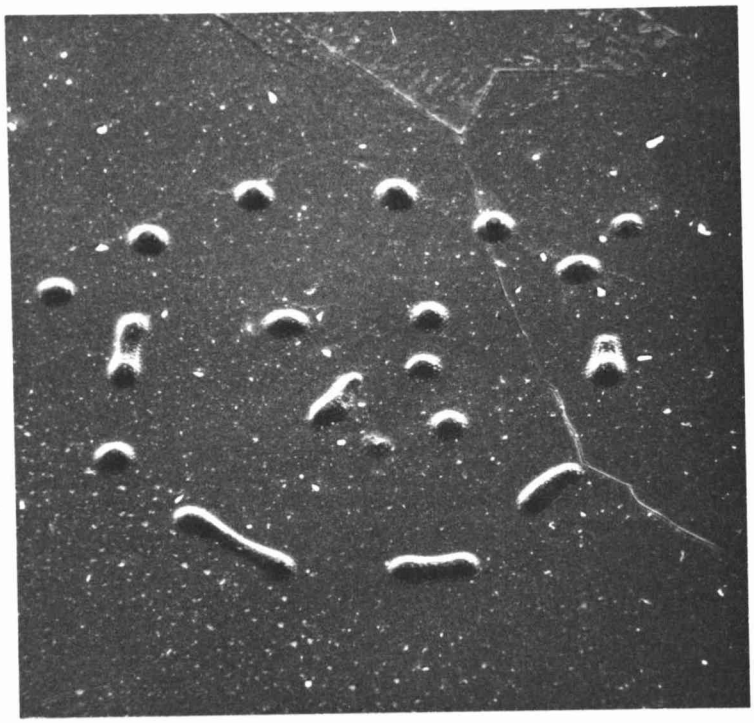

Fig. 7.4 Scanning electron micrograph of the ring of thermal etch pits shown in fig. 6.16. Magnification = 240 x.

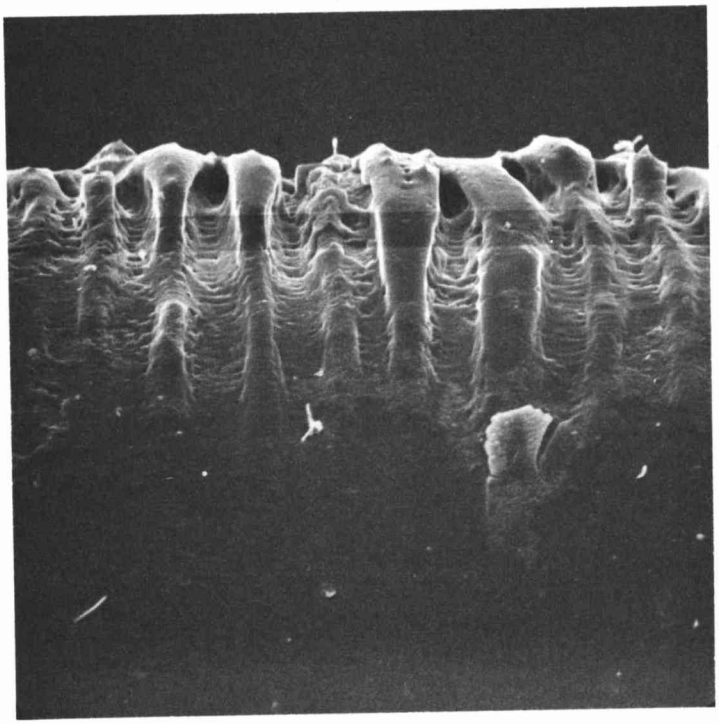

Fig. 7.5 Scanning electron micrograph after washing of the concave surface of a <100> NaCl rod kinked to ~ 17 mm radius. Magnification = 2000 x.

Holt[1] has shown that a uniform distribution of dislocations tends to redistribute to form stable cells of dislocations with diameter given by

$$d = 20\, n_d^{-\frac{1}{2}}. \qquad (7.8)$$

For a typical well-annealed dislocation density of $2 \times 10^9\ m^{-2}$, d is 4.5×10^{-4}m, while the typical ring diameter we have observed for pits in KCl is 2.8×10^{-4}m. in good agreement with this figure. The rings are therefore probably stable cells as described by Holt.

7.2.3 Evaporation from Deformed Regions

Near the melting point in the anomalous vaporisation region the vaporisation flux from a facetting surface which has been deformed must be greatly enhanced due to the abundance of vaporisation sites. It is well known that if a metal whisker is bent plastically it dissolves in nitric acid very rapidly at the bend.[2] We have found similar results for NaCl. Fig. 7.5 shows the concave edge of a bent NaCl single crystal which had been placed in 25% water 75% ethanol for 20 secs. Attack is very severe in the highly deformed regions whereas in other undeformed parts of the crystal attack was barely discernable. Similar results must occur for vaporisation. The high surface conductance near T_m which develops for bent crystals, as shown in fig. 6.12, must arise from the enhanced vaporisation and an associated diffuse surface region. This will be discussed in § 7.5.

7.2.4 Calculation of the Vaporisation flux

The heat absorbtion by vaporisation may be analysed using eqn. (6.1) with ΔH_m replaced by ΔH_s and by setting $C_1 = 0$. The increment in vaporisation flux, ΔJ is thus obtained using the relation

$$\Delta J = \rho \frac{dT}{dt} \cdot \frac{d\tau}{dT} \qquad (7.9)$$

The base flux J_p on the flux plateau (shown schematically in fig. 7.8) below the melting point may be calculated from the temperature differential ΔT between the specimen chamber

1 D.L. Holt, J.Appl. Phys. 41, 3197 (1970).
2 J.F. Green and A.A. Woolf, Research 11, 38 (1958).

and the specimen when the temperature is constant using the relation

$$4Ae\sigma_B T^3 \Delta T = J_p \Delta H_s A \qquad (7.10)$$

Unfortunately, the value of ΔT was not known precisely for all the specimens examined. In §6.6, ΔT was calculated below the premelting region neglecting vaporisation and consequently the actual values are higher than that shown e.g. in fig. 6.2. However ΔT was measured for the NaCl specimens at constant temperature to be 2.1 K which is consistent with a vaporisation flux of 0.85 mg. $cm.^{-2}$ $min.^{-1}$ Ewing and Stern measure the free vaporisation flux for NaCl in vacuo to be ~ 52 mg.$cm.^{-2}min.^{-1}$. just below the melting point. The difference of course is due to the confined space about our specimen and the presence of ambient gas, both of which reduce J. The total flux, $J=J_p+\Delta J$ for NaCl is presented in an Ahhrenius plot in fig. 7.6 for a number of specimens and heating rates. The static value of ΔT for a NaCl specimen under a vacuum of 2×10^{-2}Pa was about 10 K giving the expected higher vaporisation rates shown also in fig. 7.6. The dashed line shows the vaporisation curve above T_m obtained by Ewing and Stern in vacuo displaced downwards by a constant factor to allow for the reduced value of J in our experiments. This serves to illustrate that our estimated flux obtained over a narrow temperature range is not inconsistent with the relative changes in flux they observed at higher and lower temperatures. Figs. 7.7, 7.8 and 7.9 contain the flux curves obtained in the same way for LiF, NaBr and KCl except that in the absence of exact data the base flux for ambient He was assumed to be the same as for NaCl, namely 0.85 mg. cm^{-2}. $min.^{-1}$ The asymptotic straight line regions have the effective activation energies H_{eff} shown in Table 7.1.

The inset curve in the top right hand corner of fig. 7.8 is a schematic diagram of the full vaporisation curve sketched from Ewing and Stern's paper and the box about the 'knee' in the curve shows the region of our study in relation

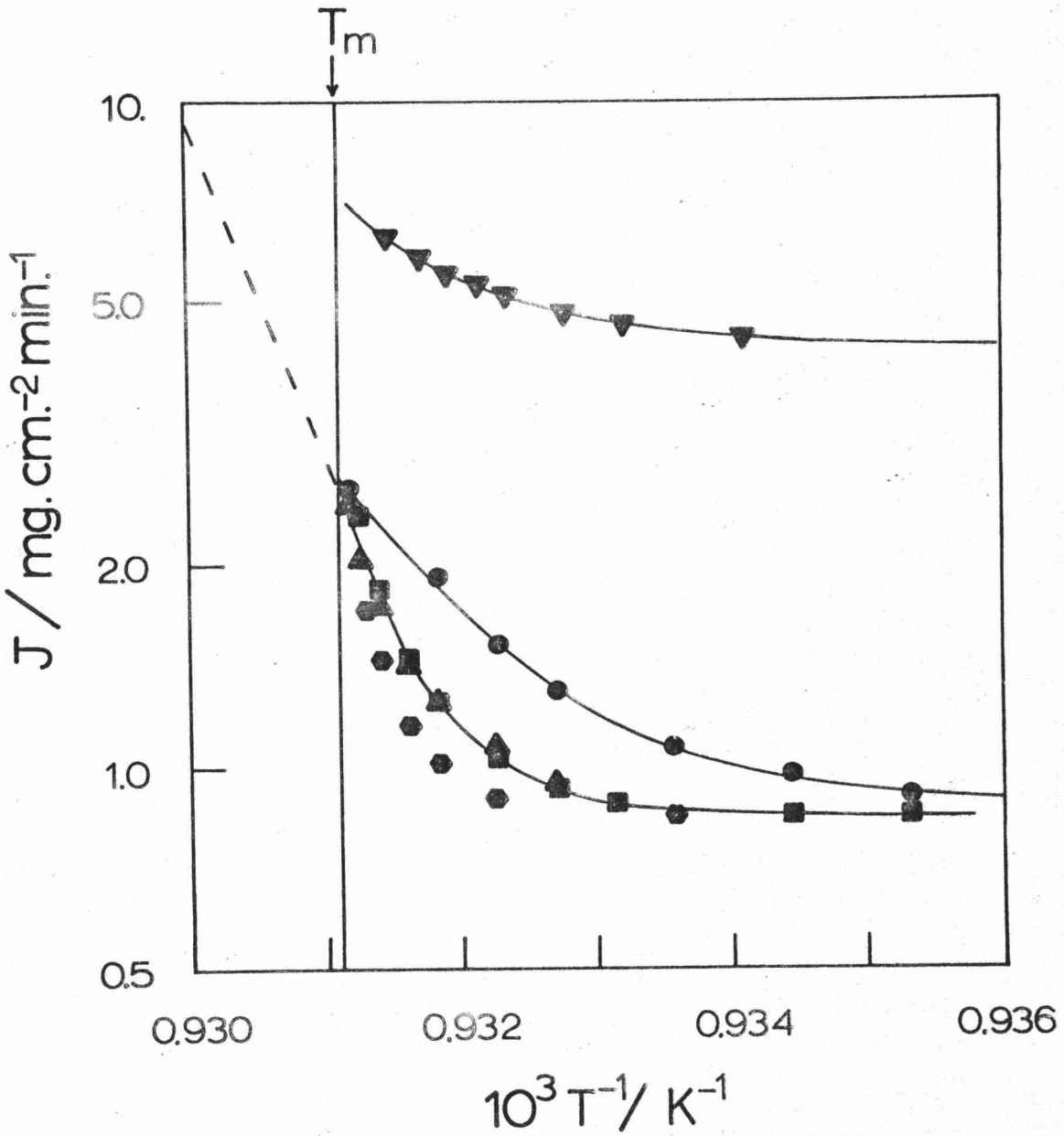

Fig. 7.6 Ahhrenius plot of the calculated vaporisation flux J for NaCl as determined from heat absorbtion near T_m. Tha dashed line shows the gradient obtained by Ewing and Stern for free vaporisation in vacuo. ● : 50 K/h ; ■ : another specimen at 50 K/h ; ▲ : at 100 K/h ; ⬢ : at 300 K/h and ▼ : another specimen at 57 K/h in a vacuum of 2 x 10^{-2} Pa.

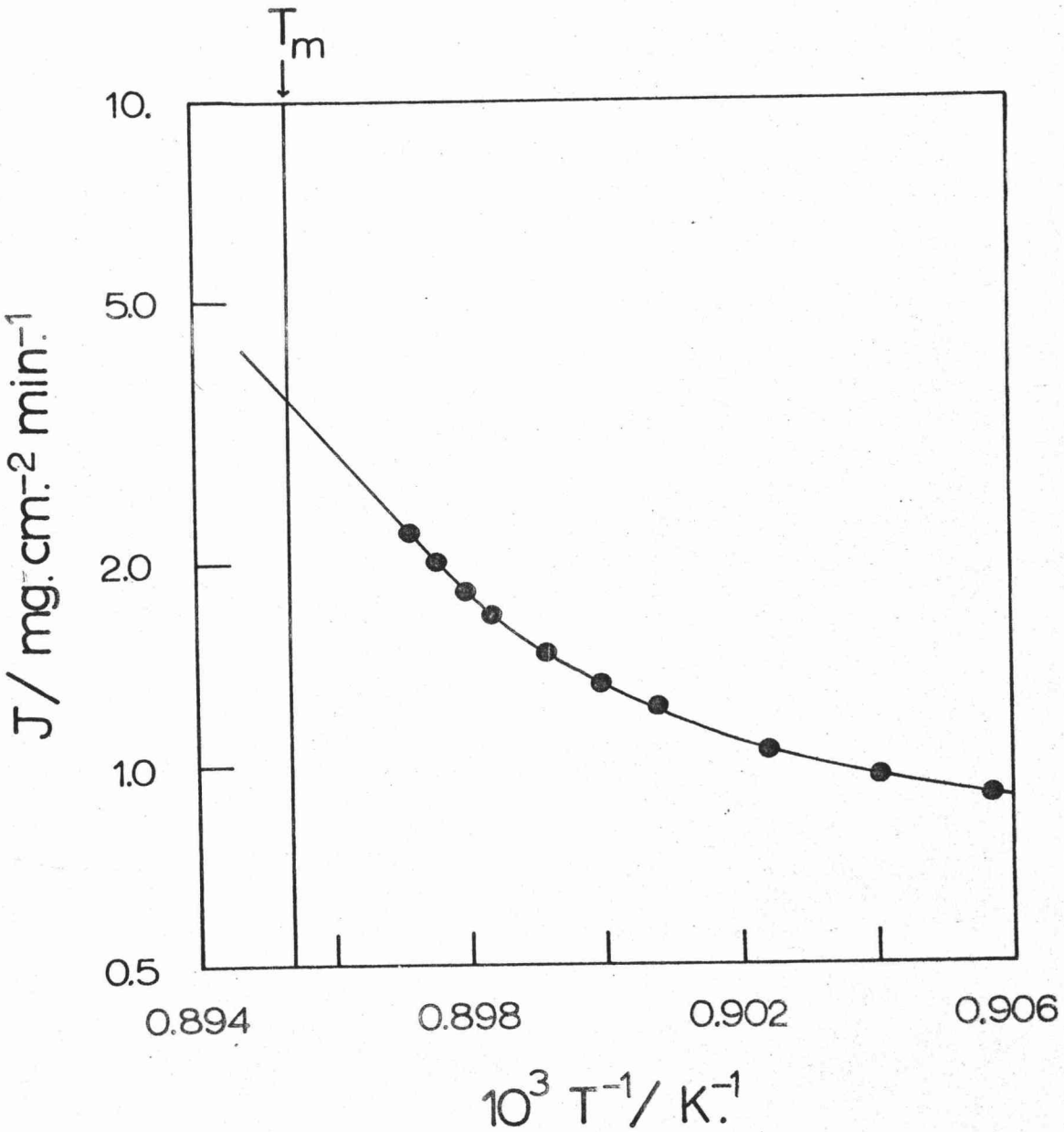

Fig. 7.7 Calculated vaporisation flux for LiF at a heating rate of 50 K/h.

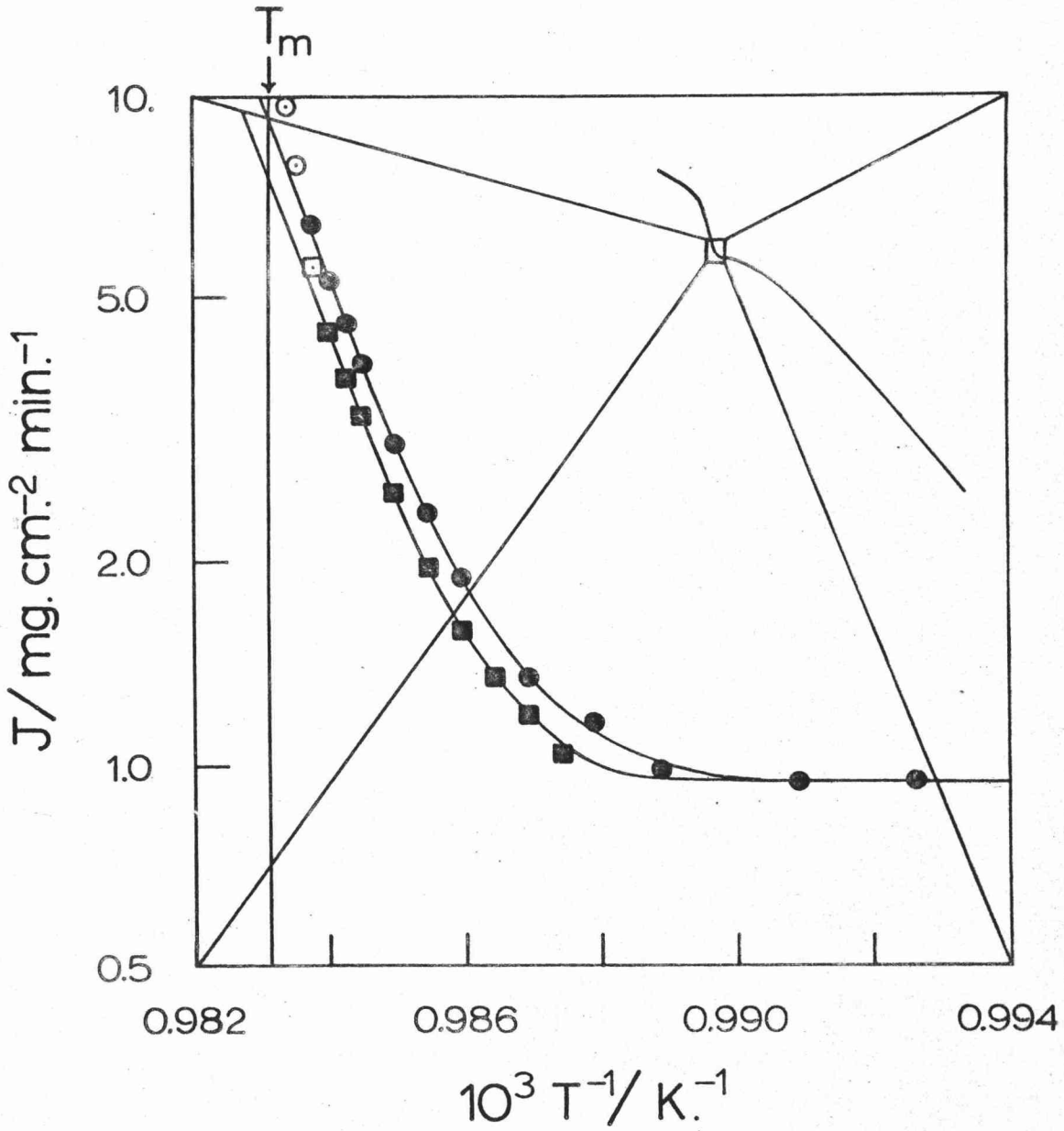

Fig. 7.8 Calculated vaporisation flux for NaBr. ■ : heating at 50 K/h and ● : at 300 K/h. The curve in the right hand corner is a schematic diagram of the full vaporisation curve from 800 K to 1200 K for NaCl, KBr and CsI obtained by Ewing and Stern. The box shows the region of our study in relation to the full vaporisation curve.

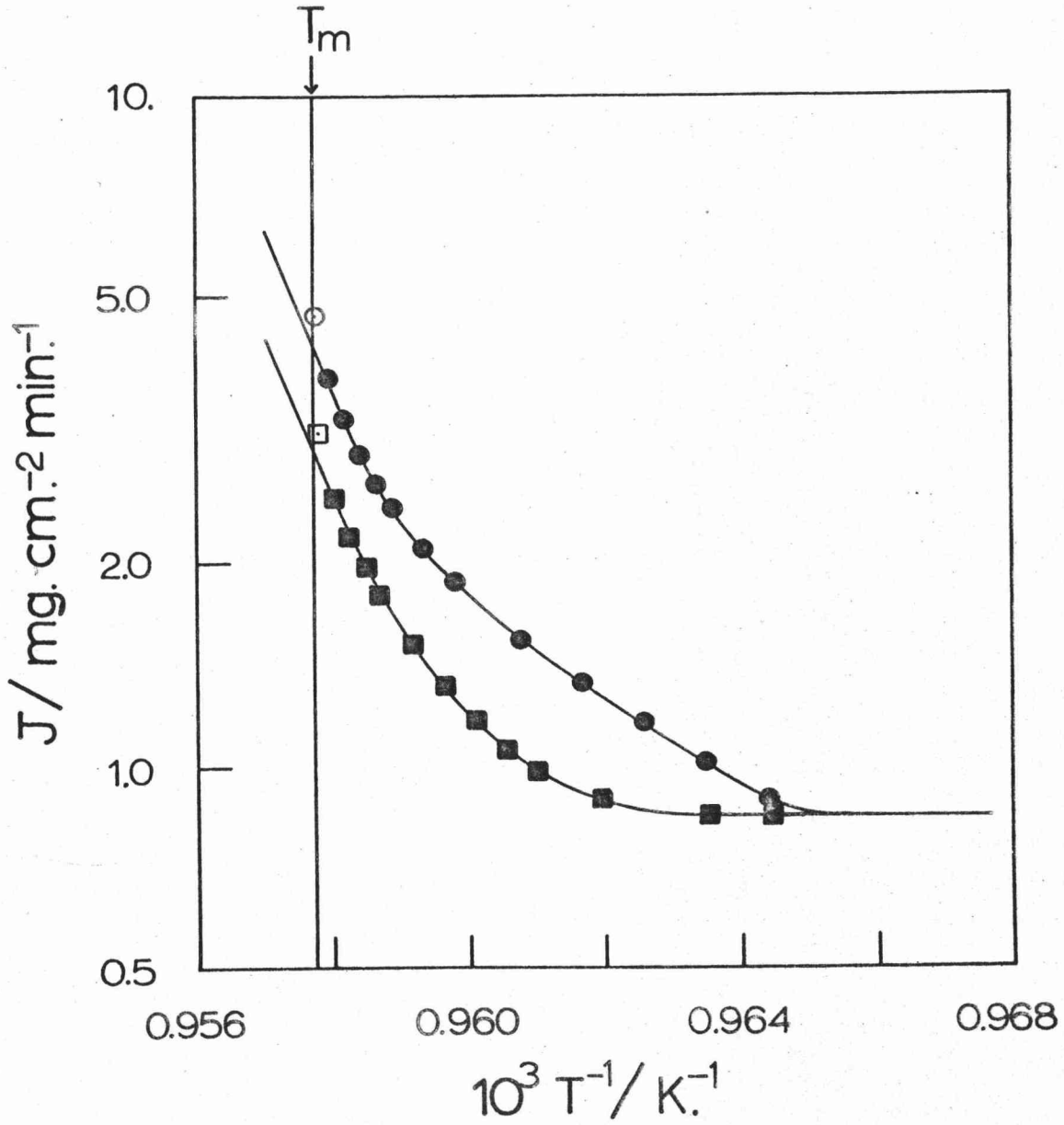

Fig. 7.9 Calculated vaporisation flux for KCl for two separate specimens heated at 50 K/h.

to the full vaporisation curve. There appears to be no distinction between the flux curves for KCl and those for LiF, NaCl and NaBr. We have no likely explanation other than surmise for the $(\Delta_m T)^{-2}$ and $(\Delta_m T)^{-1}$ dependence of $\frac{d\tau}{dT}$ established in §6 nor for the distinction between KCl and the three other salts. It appears, though, that as the vaporisation process continues smoothly through the melting point, the occurrence of a $(\Delta_m T)^{-n}$ dependence, which describes a critical type of behaviour, is inconsistent.

Salt	H_{eff}
LiF	22
NaCl	99
NaBr	55
KCl	45

Table 7.1: Effective activation energies for vaporisation at the melting point.

This dependence occurs only close to T_m and probably arises from macroscopic melting due to impurities and heat transport through the specimen platform. In fact, close to T_m, the apparent vaporisation rate climbs rapidly in the case of NaBr and KCl (shown as open circles and squares in figs. 7.6 and 7.7) and presumably this is really macroscopic melting. In the absence of any further available data, particularly vaporisation studies near the melting point under ambient gas conditions, we cannot proceed with any further elucidation of the premelting vaporisation.

In summary, we have proposed that in LiF, NaCl, NaBr and KCl facetting below and near the melting point causes the vaporisation flux to saturate due to the limited number of vaporisation sites available, then at ~ 5 K below T_m atomic scale premature melting on surfaces, corners and edges of ledges and where dislocations cut surfaces, provides a continuously increasing density of vaporisation sites, the consequent enhanced flux providing an absorbtion of heat. The associated enhanced conductivity will be discussed in § 7.5.

7.3 Surface Melting

Premature melting of surfaces is to be expected, not only on the basis of considerations of surface free energy, but also on account of the enhanced mean square vibrational displacements of surface atoms. Such enhanced displacements have now been demonstrated for a wide range of crystals[1] and since the Debye temperature is inversely proportional to the rms displacements, simple application of the Lindemann relation predicts a reduced melting temperature for surface atoms.

The premature melting of a surface means that, in principle, melting is not a discontinuous process, but rather, at any given temperature there is a skin of melt of finite depth and as the temperature rises, so the melt thickness increases, until at T_m, the equilibrium depth is infinite. The appearance of a discontiniuty arises due to the extreme narrowness of the intrinsic skin of melt just below T_m. In practise, the appearance of the thinnest possible skin of melt is discontinuous due to the non-zero width of the first ionic layer.

7.3.1 LEED Studies of Surface Melting.

Goodman and Somorjai[2] have investigated the melting of lead, bismuth and tin using Low-Energy Electron Diffraction (LEED) and find that there is no loss of diffraction features until the melting point is encountered thus demonstrating the absence of any premature surface melting. In the case of tin, loss of diffraction features did occur within 6 to 8 K of the melting point due to an effective surface melting arising from surface contamination (even at ultra-high vacuum pressures of 1.3×10^{-6} Pa). This could be eliminated by cleaning the surface by ion bombardment.

1 G.A. Somorjai, Principles of Surface Chemistry (Prentice-Hall, New Jersey, 1972) p.97.

2 R.M. Goodman and G.A. Somorjai, J. Chem. Phys. 52, 6325 (1970).

This suggests that ambient gas may be the cause of atomic dimension surface melting in the alkali halides. Gas solubility in the outermost ion layer is likely to be much higher than that given for the bulk by eqn. (7.2) and might readily give a 5 K shift in melting point at the surface. Moreover, solubilities in the $\{110\}$ surface would be greater and in the $\{111\}$ surface greater still, consistent with our observed order of surface melting. The surface cleaning effect due to vaporisation is of no assistance in diminishing this effect, since, for a vaporisation rate of 0.85 mg. $cm.^{-2}$ $min.^{-1}$, every second something like 260 layers of crystal are stripped off, whereas for an ambient He pressure of one atmosphere the equivalent of 3.2×10^{8} layers of He impinge on the crystal. The persistence of the premelting effect in a vacuum of 2×10^{-2} Pa however, appears to discount the importance of the gas, for at this pressure the flux of He is at the most 64 layers per second and would in fact be less due to the helium in the specimen chamber being driven out by the specimen vapour. Furthermore, the "sticking probability" of a He atom to the specimen surface is likely to be rather less than 1. On the other hand, the flux from the specimen in vacuo has risen to 1240 layers per second so that under these conditions the specimen surface will be kept clean by the vaporisation. Intrinsic surface melting due to excess surface free energy must therefore still be considered the most likely candidate for the surface melting. We observe that Goodman and Somorjai do not detail how, or in fact whether at all, they distinguished between the bulk melting point and the surface melting point. The one case where it is obvious from their results that the former does not exceed the latter is with Bismuth which on account of its volume contraction on melting probably does not exhibit premelting anyway. Thus we shall proceed to examine this intrinsic surface melting further.

7.3.2 Existing Theories of Surface Melting.

We have referred in §2.4 to three distinct theories of surface melting namely, the statistical thermodynamic

two-dimensional co-operative theory of Burton, Cabrera and Frank; Stranski's equilibrium form model using the ideas of surface wettability; and Gurney's vacancy model. None of these however can be successfully applied as they were developed, to the alkali halides. In the first of these, the multi-level solution is approximate only, and the critical temperature for surface disordering greatly exceeds the melting point. Specifically, the critical temperature is given by

$$kT_c/\phi \approx 0.63, \qquad (7.11)$$

where ϕ is the inter-ionic potential. We may estimate ϕ as $1/6$ of the binding energy per ion, which, since for NaCl the binding energy is 182.8 kcal. mol^{-1}, T_c = 4900 K! The situation is worse with the remaining two theories in that neither of them may be used quantitatively , and rather than developing these theories to the point where they may be used quantitatively, we have chosen, particularly in the light of developments in §4, to introduce a fourth, more simple, approach: a dislocation model of surface melting.

7.3.3 Rationale for a Dislocation Model of Surface Melting.

It is known that a two dimensional crystal of any given atom has an equilibrium lattice spacing different from that in the three dimensional crystal of that atom[1]. E.g. in the case of NaCl it is estimated that the difference is ~ 9%. If then we think of a crystal surface as a two dimensional lattice monolayer placed on a crystalline substrate, we can see there will be a tendancy for that monolayer to have a lattice spacing intermediate between that for the substrate and that for the isolated 2-D lattice. The tendancy to misfit may be accommodated in one of two ways. The monolayer (and the substrate) spacings may be elastically compressed or extended uniformly over the entire surface so that the monolayer and substrate remain in coherent contact. Or, the average spacing of the monolayer may be nearly unchanged by a number of adjacent atoms lying in the substrate surface

1 G.C. Benson and R.S. Yun in the Solid-Gas Interface ed. by E.A. Flood (Marcel Dekker, Inc., N.Y., 1967).

potential wells, and periodically, one or two atoms riding up and over, in a region of misfit, the substrate potential wells as shown in fig. 7.10.

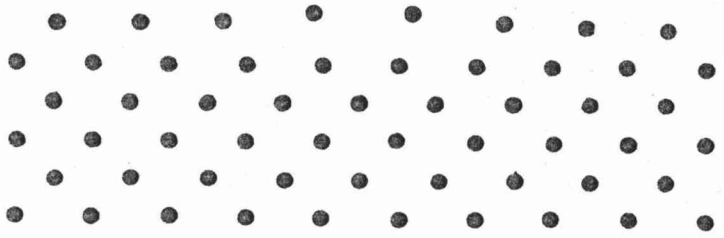

Fig. 7.10 Schematic diagram showing the periodic riding up of surface atoms over the adjacent inner atoms thus forming a surface dislocation.

Furthermore, if the process of placing the ideal 2-D lattice on its own substrate is visualised, it can be seen that the riding up will occur in rows where the misfit of the ideal lattices is a maximum. What we are describing is essentially the periodic absence of a row of atoms in the surface, or, in fact, a periodic array of edge dislocations lying in the surface such as to maintain the different natural lattice spacing of the outermost atom layer. This array will run in two directions at right angles so that total array will form a grid or lattice on the surface. At low temperatures the uniform elastic extension will prevail yielding a facetted surface, however at higher temperatures the dislocation array may become favoured and we propose to identify this transition with surface melting or disordering. The high surface mobility would then be attributable to "pipe diffusion" or more correctly "channel diffusion" along the surface dislocation cores.

Strictly regular arrays of displaced surface atoms have been observed by LEED on gold and platinum[1] {100} faces, and these are caused by the outer layer of atoms relaxing to a

1 A.E. Morgan and G.A. Somorjai, J.Chem. Phys. 51, 3309 (1969).

hexagonal close packing when the inner layers are those of a fcc lattice. Such a surface structure could be resolved into a two dimensional array of dislocations. We are, of course, not necessarily proposing a strictly regular array of surface dislocations although this is one possibility. In a different context, Herring[1] has previously suggested that crystals may possess an array of edge dislocations beneath their surfaces in order to partially relieve the surface tension, and Frank and van der Merwe[2] examined the theory of one dimensional dislocations with applications to monolayers on crystalline substrates, and to the edge row on a ledge on a growing crystal. We shall use an approach which is rather different from these two.

7.3.4 Formulation of the Dislocation Theory.

An array of edge dislocations just under the surface of a crystal has a stress field approximately equivalent to that due to the array and an image array of opposite sign dislocations just above the surface, as illustrated in fig.7.11.

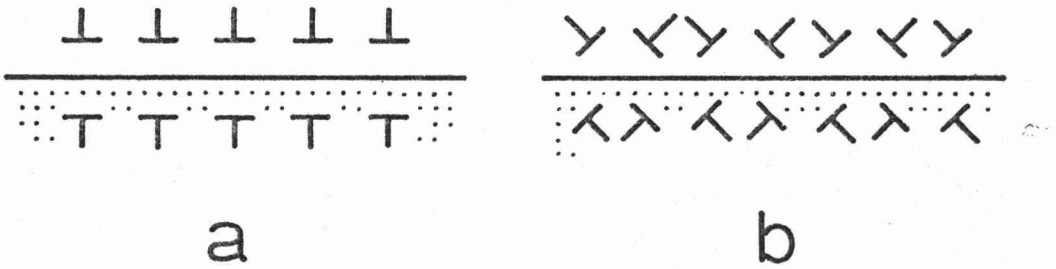

Fig. 7.11 Arrays of surface dislocations showing the image arrays above the surface.
(a) Burgers vector parallel to the surface
(b) inclined at $\pi/4$ to the surface.

The calculation of the stress fields of such arrays is a standard problem[3] and it can be shown that, in the limit as the distance of the array below the surface approaches zero, the long range stress field vanishes. We need therefore to

1 C. Herring in The Physics of Powder Metallurgy ed. by W.E. Kingston (McGraw-Hill, N.Y., 1951) p. 166.

2 F.C. Frank and J.H. van der Merwe, Proc. Roy. Soc. A198, 205 (1949).

3 J.P.Hirth and J.Lothe, Theory of Dislocations (McGraw-Hill N.Y., 1968) p.669.

consider only the core energy of a surface dislocation. When a surface dislocation is formed, a complete row of ions is removed from the surface and must be distributed over the crystal surface in the form of adsorbed ion pairs and because these are highly mobile they will have a communal or configurational entropy, $S_{conf.}$. There will also be an entropy S_{ie} due to the isothermal expansion of the lattice. At the surface, the effect of an array of dislocations is to change the surface from a solid-vapour interface to a solid-liquid interface plus a liquid-vapour interface. The change in surface free energy is $\sim (\gamma_l + \gamma_{sl} - \gamma_s)$, and we emphasise that γ_s is the surface free energy rather than the surface tension, which for a solid is not equal to γ_s. For each dislocation this change appears over an area $\underline{\hat{n}}.\underline{b}$ per unit length of dislocation, where $\underline{\hat{n}}$ is the unit vector in the surface plane normal to the dislocation line. The change in Gibbs function is therefore $\underline{\hat{n}}.\underline{b}\{\gamma_l + \gamma_{sl} - \gamma_s\}$ and the total change in Gibbs function is

$$\Delta G = U_c^s - \Gamma_p U_{am} + \underline{\hat{n}}.\underline{b}\{\gamma_l + \gamma_{sl} - \gamma_s\} - T\{S_c^s + S_{conf} + S_{ie}\} \qquad (7.12)$$

Here $U_c^s = \xi \mu_s b^2/4\,(1-\nu)$ is the core energy per unit length of dislocation for the operative slip system, s, S_c is the core entropy, U_{am} is the binding energy of an adsorbed monomer or ion-pair and Γ_p is the number of planes cut perpandicularly by the dislocation per unit length of dislocation. The surface melting temperature, T_{sm}, at which surface dislocations spontaneously appear, is that temperature at which ΔG vanishes, namely

$$T_{sm} = \frac{U_c^s - \Gamma_p U_{am} + \underline{\hat{n}}.\underline{b}\{\gamma_l + \gamma_{sl} - \gamma_s\}}{S_c^s + S_{conf} + S_{ie}} \qquad (7.13)$$

Now a simple calculation of S_{conf} shows that at any temperature there exists a surface dislocation density, however small, at which T_{sm} equals that temperature, and as temperature increases the dislocation density increases. That is,

the transition is a broad non-first order transition.

7.3.5 Aggregation of Ion-Pairs on the Surface.

Surface melting will be continuous, or non-first order, only if the ion-pairs released on the surface remain free and isolated. However, if enough ion-pairs can come together for two dimensional nucleation to occur, a monolayer island will grow, acting as a sink for all ion-pairs. Thus, surface dislocations may form on this island rather than under the island. If this is the case, the terms arising from the ion-pairs may be eliminated. To examine this point, we define γ_δ as the step free energy, then the free energy of an island of n ion-pairs is

$$G = - n\Lambda\gamma_s + \Sigma\sqrt{n\Lambda}\ \gamma_\delta \qquad (7.14)$$

where Σ is a shape factor equal to 4 for a square and $2\sqrt{\pi}$ for a circle, and $\Lambda = (1/2)a^2$ is the ion-pair area. The critical number n* for continuous growth is given when $\left.\frac{\partial G}{\partial n}\right|_{n^*}$ vanishes. This occurs when

$$n^* = \left\{ \frac{\Sigma\ \gamma_\delta}{2\gamma_s\sqrt{\Lambda}} \right\}^2 \qquad (7.15)$$

and

$$G^* = \tfrac{1}{2}\Sigma^2\ \frac{\gamma_\delta^2}{\gamma_s} \qquad (7.16)$$

If there are N ion-pairs released by the formation of surface dislocations, the total possible number of critical islands we could form is N/n^*. The equilibrium number, Υ of islands of critical size is therefore

$$\Upsilon = (N/n^*)\ \exp\left[- G^*/kT\right] \qquad (7.17)$$

But we need only one critical island to form which will act as a sink for all the ion-pairs. The critical number of ion-pairs for the formation of the critical nucleus is therefore

$$N^* = n^*\ \exp(G^*/kT) \qquad (7.18)$$

Benson and Yun[1] calculate the surface enthalpy and entropy

1 G.C. Benson and R.S. Yun in the Solid-Gas Interface ed. by E.A. Flood (Marcel Dekker, Inc., N.Y., 1967).

for a NaCl {100} surface to be h_s = 0.276 J. m^{-2} and $s_s = 8.4 \times 10^{-5}$ J. m^{-2} K^{-1} which at 1070 K gives a surface free energy, γ_s = 0.186 J. m^{-2} Expressed as energy per surface ion-pair this is 0.186 $\Lambda = 2.96 \times 10^{-20}$ J/ion-pair. In order to estimate the step free energy γ_δ we assume that the step energy is greater than the surface energy in the same proportion as the reduction in neighbours. In moving an ion from the bulk to the surface, nearest neighbours plus next nearest neighbours drop from 18 to 13, and a further decrease to 10 results on transfer to an edge. This provides an estimate for $\gamma_\delta \approx (8/5)\gamma_s = 4.74 \times 10^{-20}$ J/ion pair $= 8.41 \times 10^{-11}$ J/m, and using eqns. (7.15) and (7.18) we find for a square island $n^* = 5$ and $N^* = 4.5 \times 10^9$. This means a total of ~ 250 surface dislocations (i.e. N^*/Γ_p x width of crystal) are sufficient for the nucleation of islands from the released ion-pairs. Considering that the ion-pairs are generated in localised regions, i.e. along the cores, the critical nucleus of 5 ion-pairs will probably be achieved with a far smaller number, N*. Therefore, in view of the fact that we are talking of a dislocation array 10^6 to 10^7 in number across a 1 cm square surface, accumulation of ion-pairs into islands will occur readily and we need not consider the ion-pair surface binding energy U_{am} and its configurational entropy, S_{conf}.

7.3.6 The Relative Change in Melting Point at the Surface.

By removing U_{am} and S_{conf}, eqn. (7.13) reduces to

$$T_{sm} = \left\{U_c^s + \underline{\hat{n}}.\underline{b}\,[\gamma_1 + \gamma_{s1} - \gamma_s]\right\} / \,(S_c^s + S_{ie}). \qquad (7.19)$$

For a dislocation model of melting, the bulk melting temperature is given simply by

$$T_m = U_c^m / \,(S_c^m + S_{ie}), \qquad (7.20)$$

where the superscript, m denotes the slip system of the dislocations involved in the melting process. For the rocksalt alkali-halides, m would denote the slip system

$\langle 110 \rangle \{110\}$ as will be shown in § 7.4. By combining eqns. (7.19) and (7.20) we obtain for the relative shift in surface melting temperature

$$\Delta_m T_{sm}/T_m = \hat{\underline{n}}.\underline{b}\ (\gamma_s - \gamma_1 - \gamma_{s1})(S_c^m + S_{ie})/U_c^m (S_c^s + S_{ie})$$

$$+ 1 - U_c^s (S_c^m + S_{ie})/U_c^m (S_c^s + S_{ie}), \qquad (7.21)$$

so that, if the dislocations participating in the surface melting have the same slip system as those participating in the bulk melting, the shift in melting point is

$$\Delta_m T_{sm}/T_m = \hat{\underline{n}}.\underline{b}\ (\gamma_s - \gamma_1 - \gamma_{s1})/U_c^m. \qquad (7.22)$$

Thus we concur with Tamman and Stranski that if $\gamma_s = \gamma_1 + \gamma_{s1}$ there is no premature surface melting.

Huntington, Dickey and Thomson[1] have computed the core energy of a $\langle 110 \rangle \{110\}$ dislocation in NaCl by calculating the detailed ionic interactions and they obtain $U_c = 2.19 \times 10^{-10}$ J. m.$^{-1}$ at a temperature of 80 K. The expression for $\mu/(1-\nu)$ in terms of the elastic modui for elastic anisotropy is given by eqn. (4.1) and using the elastic constant data of Hunter and Siegel for NaCl we find this energy implies a value for ξ of 0.752, which is quite reasonable. Reversing this procedure, by assuming ξ remains constant we may now calculate U_c at the melting point and obtain $U_c = 1.05 \times 10^{-10}$ J. m.$^{-1}$ (i.e. about the same as our estimated surface step energy for the same temperature). Values of $\gamma_1 = 0.114$ J. m.$^{-1}$ and $\gamma_{s1} = 0.0841$ J. m.$^{-1}$ are listed in Table 4.2 giving $\gamma_s - \gamma_1 - \gamma_{s1} = -0.012$ J. m.$^{-1}$ Finally, since the core energy is lower and as we shall see in Appendix F, the entropy is higher, $\langle 110 \rangle \{110\}$ dislocations would be favoured over $\langle 110 \rangle \{100\}$ or $\langle 100 \rangle \{100\}$ dislocations, so that under a $\{100\}$ surface, the orientation of the dislocations would be as shown in fig. 7.11 b and $\hat{\underline{n}}.\underline{b} = \frac{1}{\sqrt{2}\sqrt{2}}\, a = .282$ nm. Thus, for a $\{100\}$ surface

1 H.B. Huntington, J.E. Dickey and R.M. Thomson, Phys. Rev. 100, 1117 (1955).

$$\Delta_m T_{sm} = -1074 \times 2.82 \times 10^{-10} \times 0.012/1.05 \times 10^{-10} \text{ K}$$
$$= -38 \text{ K.} \qquad (7.23)$$

This value is more of the magnitude of $\Delta_m T_{sm}$ found for $\{110\}$ and $\{111\}$ surfaces and is of the wrong sign since, here, $\gamma_s < \gamma_l + \gamma_{sl}$. This arises from the experimental inaccuracies in measuring γ_s, γ_l and γ_{sl} and all that can be said is that γ_s is close to $\gamma_l + \gamma_{sl}$ in value, but the individual uncertainties are sufficiently great that large errors exist in the difference, $\gamma_s - (\gamma_l + \gamma_{sl})$. Our value of $\Delta_m T_{sm} = 5.5$ K suggests that $\gamma_s - \gamma_l - \gamma_{sl} = 1.8 \times 10^{-3}$ J. m.$^{-2}$ i.e. accepting the values for γ_l and γ_{sl}, $\gamma_s(T_m) = 0.191$ J. m.$^{-2}$

7.3.7 Anisotropy of $\{110\}$ Surface Melting.

The $\{110\}$ surface plane is anisotropic and we have to consider the formation of two different sets of dislocations at right angles to each other. The simplest are those dislocation lines running in a $\langle 100 \rangle$ direction with Burgers vectors in the $\langle 110 \rangle$ direction. These are the normal $\langle 110 \rangle \{110\}$ slip dislocations and therefore will be oriented with Burgers vector parallel to the surface as shown in fig. 7.11a. The relative shift in melting point is given again by eqn. (7.22) and here $\hat{\underline{n}}.\underline{b} = (1/\sqrt{2})a = .413$ nm, that is

$$\Delta_m T_{sm}/T_m = 3.94 \ (\gamma_s - \gamma_l - \gamma_{sl}) \qquad (7.24)$$

γ_s and γ_{sl} will differ from the $\{100\}$ case due to their orientation dependence and γ_l of course is not orientation dependent. Benson and Yun[1] give the solid surface energy E_s for a $\{110\}$ surface as .354 J. m.$^{-2}$, i.e. much larger than for a $\{100\}$ surface, but the value for γ_{sl} for a $\{110\}$ interface is not available. Fig. 6.15 shows a value of T_{sm} = 1000 K for the $\langle 100 \rangle$ direction on a $\{110\}$ surface i.e. $\Delta_m T_{sm}/T_m = 0.0421$ which suggests $\gamma_s - \gamma_l - \gamma_{sl} = 0.0107$ J. m.$^{-2}$ for a $\{110\}$ surface. (These are tentative assignments only, because we believe that this surface is probably not ideal but rather comprises $\{100\}$ facetted ledges, and the apparent surface melting giving enhanced conductivity is partly due

1 G.C. Benson and R.S. Yun, Loc. cit.

to premature edge melting).

The array of dislocations at right angles to this array under the $\{110\}$ surface could be a simple array as in fig. 7.11a in which case they would be $\langle 100\rangle$ $\{110\}$ dislocations. For these, $\hat{\underline{n}}.\underline{b}$ = a and consequently the core energy is twice that for $\langle 110\rangle$ $\{110\}$ dislocations and, furthermore, we show in Appendix F that the core shear vibrational entropy is negative and large, which precludes $\langle 100\rangle$ $\{110\}$ edge dislocations from any role in either surface or bulk melting. The only possibility then is an array of $\langle 110\rangle\{110\}$ dislocations which zig-zag along under the surface first toward the surface in steps of length a. More specifically for the surface melting of a $(\bar{1}10)$ surface, the zig-zagged arrays would be equal and evenly distributed numbers of $[0\bar{1}\bar{1}](01\bar{1})$ and $[0\bar{1}1](011)$ dislocations running in the $[100]$ direction and similarly of $[\bar{1}01](101)$ and $[101](10\bar{1})$ dislocations running in the $[010]$ direction. These arrays resolve to the equivalent of $[00\bar{1}](\bar{1}10)$ dislocations, but for each, $\hat{\underline{n}}.\underline{b} = \frac{1}{\sqrt{2}\sqrt{2}}$ a and consequently eqn. (7.22) becomes for NaCl

$$\Delta_m T_{sm}/T = 2.79\ (\gamma_s - \gamma_l - \gamma_{sl}) \qquad (7.25)$$

Furthermore, the values here of γ_s and γ_{sl} for the $[110]$ direction on the $(\bar{1}10)$ surface will differ from those values in eqn. (7.24) for the $[001]$ direction on the same surface. Because the former direction has a lower packing density, it is to be expected that γ_s will be higher and γ_{sl} will be lower than for the latter. Such considerations led us to measure the temperatures at which the conductivity in $\langle 100\rangle$ and $\langle 110\rangle$ directions on a $\{110\}$ KCl surface began to climb sharply below the melting point. The results were presented in fig. 6.15. Surface melting in the $\langle 110\rangle$ direction began at 994 K, 6 K below that in the $\langle 100\rangle$ direction, which suggests that $\{\gamma_s - \gamma_l - \gamma_{sl}\}$ in eqn. (7.24) equals 0.0171 J. m.$^{-2}$ Again, these assignments are only tentative.

We now move on to considering the application of the

dislocation model to bulk melting and the movement of the s-l interface from the surface into the bulk.

7.4 Bulk melting and the progression of the s-l interface.

7.4.1 The Melting Temperature.

We shall first examine the quantitative features of our simple dislocation theory of melting. The dislocation core energy provides a contribution to the enthalpy of the dislocated lattice equal to

$$\Delta H = \frac{\xi \mu_e b^2}{4\pi} \cdot n_d V_1 = U_c n_d V_1 \qquad (7.26)$$

and if we presume that in the melt dislocations are packed in three dimensions to their greatest density i.e. their cores are just touching, then $n_d = 3(2r_o)^{-2}$ where r_o is the core radius. Eqn. (7.26) becomes

$$\Delta H = \tfrac{3}{4} U_c V_1 r_o^{-2} \qquad (7.27)$$

The dislocation cores possess a volume expansion ϑ per unit length and so that fractional volume change on melting is given by

$$\Delta V_m / V_s = \tfrac{3}{4}\vartheta r_o^{-2} \qquad (7.28)$$

This volume change contributes $2\eta\vartheta gR$ per unit length of dislocation to the vibrational entropy, where η is a factor which is two or three according to whether the dilatation in the core is of the form $\epsilon_{11} + \epsilon_{22}$ or $\epsilon_{11} + \epsilon_{22} + \epsilon_{33}$. In addition, there is a shear contribution to the entropy which is calculated for the elastic field about an isolated edge dislocation in Appendix F. For a $\langle 110 \rangle \{110\}$ edge dislocation, under the assumption of isotropic elasticity, this is

$$\Delta S_{shear} = \frac{3\ R\ U(edge)}{2\ \mu_e}\left\{\left[1 + \tfrac{2}{3}(1-2\nu)^2\right] g_s(3)\left(\frac{\mu_e}{\bar{\mu}}\right)^2 + g_s(1)\left(\frac{\mu_e}{\bar{\mu}'}\right)^2\right\} \qquad (7.29)$$

We assume that the shear entropy of the core is given simply by replacing the elastic energy U(edge) in eqn.(7.29)

by the core energy U_c. In addition to vibrational entropy, there is the change in entropy due to the isothermal expansion ϑ per unit length of dislocation. For this, we require the change in free volume of the core ions. We have not calculated this, instead, we have simply used equation (B5) from Appendix B for the relative change in free volume as a function of a uniform dilatation. The last remaining contribution is the communal entropy, 2 R. The total change in entropy is therefore

$$\Delta S = \tfrac{3}{4} r_o^{-2} \left[2\eta g R\vartheta + \frac{3RU_c}{2\mu_e} \left\{ \left[1 + \tfrac{2}{3}(1-2\nu)^2\right] g_s(3) \left(\frac{\mu_e}{\mu}\right)^2 + g_s(1) \left(\frac{\mu_e}{\mu'}\right)^2 \right\} \right] + R \ln(V_1^*/V_s^*) + 2R \quad . \qquad (7.30)$$

Spontaneous generation of dislocations occurs at the melting point when $\Delta G = \Delta H - T\Delta S$ vanishes, and the melting temperature is therefore given by

$$T_d = \frac{\Delta H}{\Delta S} \qquad (7.31)$$

We proceed with the calculation under the assumption that ξ for all the alkali halides is equal to the value found for NaCl, namely $\xi = 0.752$. Accordingly, using the elastic constants at the melting point, we may calculate U_c and from ΔH_m we may deduce r_o from eqn. (7.27). This in turn allows ϑ to be determined from eqn. (7.28) and finally the dilatation entropy and thence the total entropy is calculated.

The results are tabulated in Table 7.2 and we note that the core radius is about one half the lattice spacing and the volume expansion of the core, for one ion-pair length, is from $\frac{1}{4}$ to $\frac{1}{3}$ the ion-pair volume. The only exception in the values of r_o is that for RbI which is higher than the others by a factor of about $\sqrt{2}$. The reason for this appears to be that the measured values of ΔS_m and ΔH_m are about $\frac{1}{2}$ the values that would be expected. This may be seen most clearly by comparing the value of ΔS_m for RbI in Table 4.1 with all the values for the other alkali halides. These are all close to 3.0 R while, for RbI, $\Delta S_m = 1.64$ R. The experimental value listed may thus be in error by a factor of

Salt	$U_c/10^{-10}$ J.m^{-1}	$\nu(T_m)$	r_o/nm	r_o/a	$4\vartheta a^{-2}$	$T_d(\eta)$ / K	T_d/K $\eta=2$	T_d/K $\eta=3$	T_m/K
LiF	1.027	.203	.178	.42	.282	$\frac{2.71 \times 10^4}{6.5\eta-12.2+7.4+16.6}$	1084	859	1121
NaF	1.486	.153	.237	.49	.354	$\frac{3.33 \times 10^4}{6.9\eta-3.2+7.3+16.6}$	966	805	1269
NaCl	1.059	.335	.291	.50	.331	$\frac{2.82 \times 10^4}{6.8\eta-16.6+8.6+16.6}$	1269	972	1074
NaI	.878	.235	.359	.53	.281	$\frac{2.36 \times 10^4}{5.2\eta-7.3+6.1+16.6}$	911	758	933
KCl	.950	.294	.336	.52	.245	$\frac{2.63 \times 10^4}{4.6\eta-7.1+6.4+16.6}$	1047	884	1044
KBr	.905	.269	.357	.52	.242	$\frac{2.55 \times 10^4}{4.6\eta-5.8+6.5+16.6}$	958	816	1007
KI	.651	.060	.345	.47	.190	$\frac{2.40 \times 10^4}{4.3\eta-4.1+6.4+16.6}$	873	755	954
RbI	.796	.315	.557	.74	.368	$\frac{1.25 \times 10^4}{3.0\eta-3.6+5.4+16.6}$	513	457	915

Table 7.2 Values of various parameters obtained by fitting the enthalpy of melting and the volume change on melting to a dislocation theory of melting. U_c is the dislocation core energy, ν the Poisson's ratio, and r_o the core radius. Values of r_o/a reveal that the core radius is approximately one half the lattice parameter. The volume expansion, ϑ per unit length of the core is shown as a fraction $4\vartheta a^{-2}$ of the ion-pair volume. The next column shows the various contributions to eqn. (7.31) for T_d and this is followed by the calculated values for $\eta=2$ and $\eta=3$, and the actual melting temperature, T_m. Agreement between T_d and T_m is best for $\eta=2$.

two. Eqn. (7.27) would then imply that r_o was too high by a factor of $\sqrt{2}$, while eqn. (7.31) suggests that T_d would be too low by a factor of $\frac{1}{2}$. This is in fact the case.

The various contributions to eqn. (7.31) for T_d are given in the sixth column where the denominator, in order, contains first the dilatation vibrational entropy, then the shear vibrational entropy, the entropy due to the isothermal expansion and finally the communal entropy, 2 R. The units here are J/mole. Evidently all contributions are significant. The values of T_d agree best with the values of T_m for $\eta = 2$, as we found in § 4.5 for our generalised elastic strain theory of melting, and this presents a strong internal consistency in this dislocation theory of melting, in that $\eta = 2$ suggests the kind of local two dimensional strain one would expect for a dislocation model to be valid. The values of T_m are remarkably good considering the crudeness of the model and the dependence on $g_s(1)$, and V_l^*/V_s^* which we have estimated only approximately in Appendices A and B.

For $\langle 100 \rangle \{100\}$ dislocations $g_s(3)$ and $g_s(1)$ should be interchanged in eqn. (7.29) thus making ΔS_{shear} a little more negative. ΔS_{shear} for $\langle 100 \rangle \{110\}$ dislocations is also determined in Appendix F and shown to be large and negative. Moreover, since the Burgers vectors of both these dislocations are a, while that for $\langle 110 \rangle \{110\}$ dislocations is $a/\sqrt{2}$, the elastic energies of both dislocations are about a factor of two greater than the energy of $\langle 110 \rangle \{110\}$ dislocations. Accordingly, neither dislocation is able to participate in bulk melting.

7.4.2 Displacement of the Surface Dislocations between T_{sm} and T_m.

If the temperature is raised above the surface melting temperature the surface dislocations may glide into the interior, driven by the interfacial tension as shown in fig. 7.12. If a dislocation array is displaced inwards to a depth τ below the surface, the elastic energy increases until the Gibbs function vanishes again. The array at the

surface is equivalent to two such arrays back to back in the interior separated by a distance 2τ .

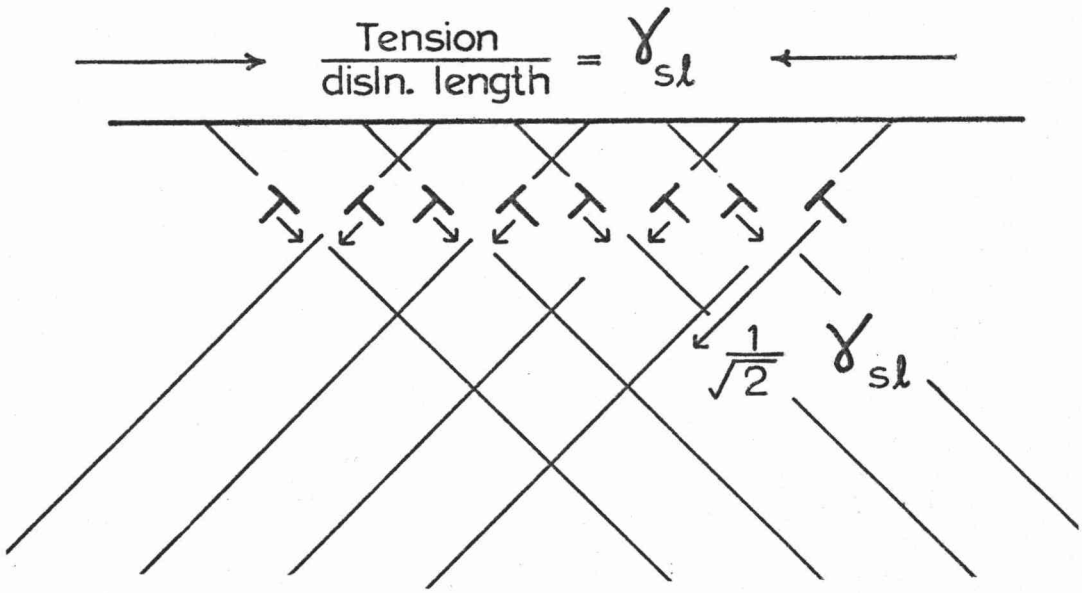

Fig. 7.12 Schematic diagram of a surface array of edge dislocations showing their glide planes and the shear stress on these planes arising from the interfacial tension.

The energy of such a double array may be determined by considering the interaction energy of a single dislocation with a single array when placed 2τ away from it, i.e. the work done in displacing the dislocation from a distance $2r_o$ to 2τ . This displacement may only be achieved by climb and the climb force on an edge dislocation is $\sigma_{11}b$, where σ_{11} is one of the stress components of the array. Hirth and Lothe[1] give the stress σ_{11} due to an array of dislocations of the form shown in fig. 7.11a as

$$\sigma_{11} = \frac{\mu b}{4r_o(1-\nu)} \cdot \frac{2\pi X[\cosh(2\pi X).\cos(2\pi Y)-1]}{[\cosh(2\pi X) - \cos(2\pi Y)]^2} \qquad (7.32)$$

where $X = x/2r_o$ and $Y = y/2r_o$. The elastic energy per unit length of dislocation is therefore

$$U_e = \int_{2r_o}^{2\tau} \sigma_{11}\, b\, dx$$

$$= \frac{\mu b^2}{2\pi(1-\nu)} \left\{ .0136 + \ln[2\sinh(\pi\tau/r_o)] - (\pi\tau/r_o)\coth(\pi\tau/r_o) \right\} \qquad (7.33)$$

1 J.P. Hirth and J. Lothe, loc.cit.p.671.

and since $\tau > r_o$

$$U_e \approx 2U_c\xi^{-1} \left\{ .0136-(1 + 2\pi\tau/r_o)\exp(-2\pi\tau/r_o) \right\} . \quad (7.34)$$

For an array under a $\{100\}$ surface as shown in fig.7.11b

$$U_e = 2U_c\xi^{-1} \left\{ .0647 + \ln[2\sinh(\pi\tau/\sqrt{2}r_o)] - (\pi\tau/\sqrt{2}r_o)\coth(\pi\tau/\sqrt{2}r_o) \right\} \quad (7.35)$$

Therefore the Gibbs function is

$$\Delta G = U_c + U_e - \underline{\hat{n}}.\underline{b} \ (\gamma_s - \gamma_l - \gamma_{sl}) - T(S_c + S_{ie}) , \quad (7.36)$$

where we have not included the communal entropy as there is none. At the melting point the depth to which the array has glided is given by the equality

$$U_e = \underline{\hat{n}}.\underline{b} \ (\gamma_s - \gamma_l - \gamma_{sl}) = U_c \ \Delta_m T_{sm}/T_m. \quad (7.37)$$

For $\langle 100 \rangle$ NaCl crystals $\Delta_m T_{sm}$ = 5.5 K giving $\tau_m = 1.008r_o$ i.e. the array has barely glided at all before bulk melting occurs. On the other hand, for melting in the $\langle 100 \rangle$ direction on a $\{110\}$ surface $\Delta_m T_{sm}/T_m = 0.0421$ the array must climb (rather than glide) to $\tau_m > 2r_o$ and still not enough elastic energy appears. Consequently, the climb must be accompanied by the formation of fresh dislocations or additional displacements of ions in the cores so as to provide greater internal energy.

7.4.3 Progression of the s-l Interface at T_m.

Once the melting point is encountered, melting may proceed into the crystal by the continued glide of the surface dislocations, leaving behind them trails of dislocation pairs. The dislocations are driven on by the interfacial tension. Fig. 7.13 shows the process by which a gliding edge dislocation may generate a pair of dislocations in its path. As the dislocation moves from its position in a to its adjacent position, the ionic displacements are such as to favour the connecting up of the row marked by dashes

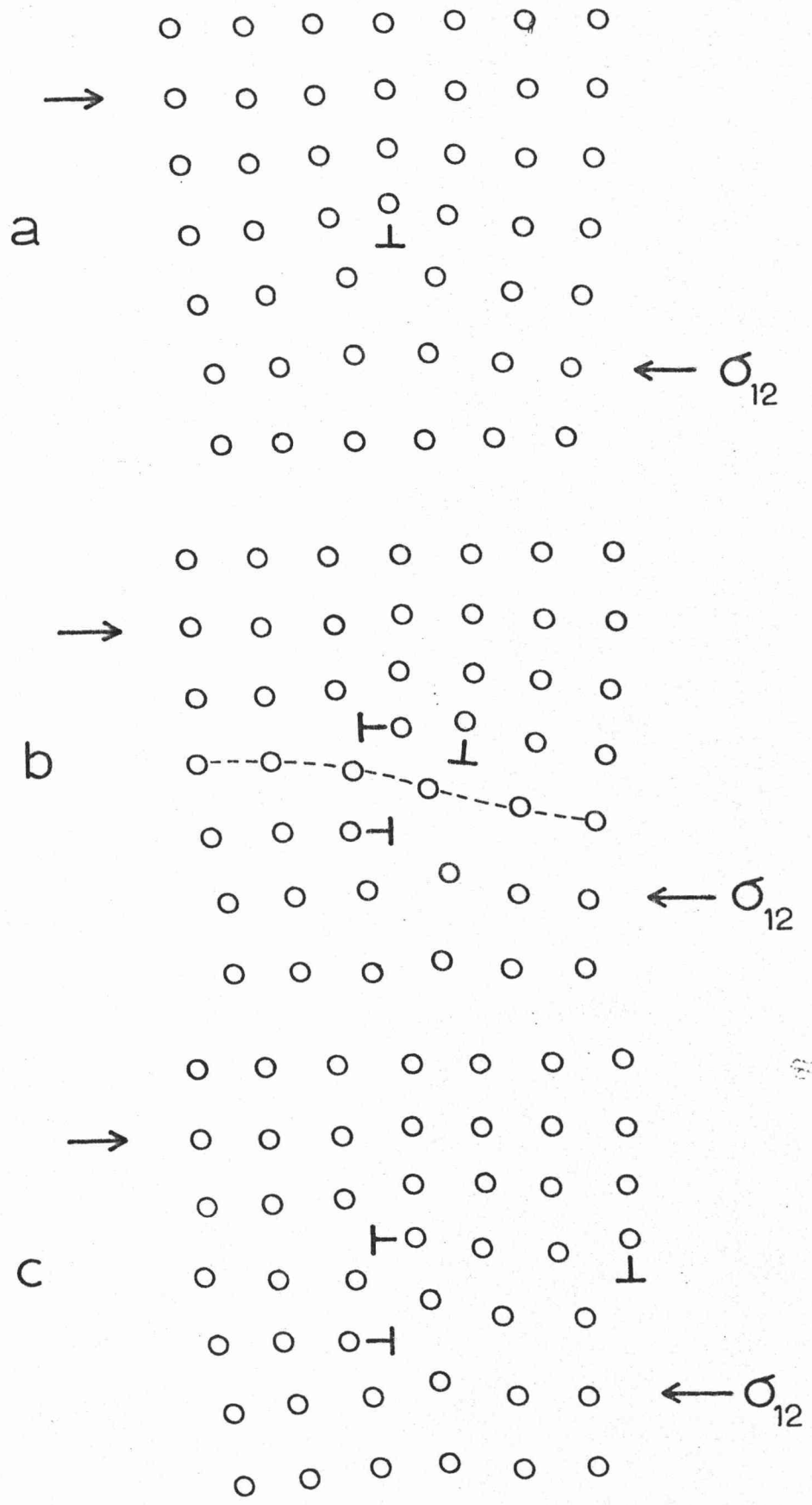

Fig. 7.13 The generation of a pair of opposite dislocations at T_m by the glide of a parent dislocation.

in b, thus forming a pair of opposite sign dislocations. The process may continue at close intervals such that a dense packed array of dislocations is left behind the leading dislocations, much as melt is left behind the moving s-l interface.

7.4.4 The Velocity of the s-l Interface.

If the surface in fig. 7.12 is now imagined to be the s-l interface with tension γ_{sl} (we shall neglect the distinction between interfacial free energy and interfacial tension), the shear force per unit length of dislocation driving each dislocation down their glide planes is $\frac{1}{\sqrt{2}}\gamma_{sl}$. This force is acting over the width of the interface which we suppose to be two dislocation core diameters. In Table 7.2 r_o is about a/2 so that the width of the interface is about 2a. The shear stress is therefore $\gamma_{sl}/2\sqrt{2}a = 5.09 \times 10^7$ N. m^{-2}. This is a large shear stress and according to the temperature and stress dependence of dislocation velocities measured by Gilman and Johnston[1] the interface dislocations should glide under this stress at speeds approaching the shear velocity of sound in the specimen, $\sqrt{4c_{44}/\rho_s}$. Using the values of c_{44} and ρ_s near T_m we find a shear velocity $\sim 4.4 \times 10^3$ m.sec^{-1}. Typically, however, interface velocities of the order of only 10^{-5} to 10^{-4} m.$sec.^{-1}$ are often observed. This is because the leading dislocations may only proceed as quickly as dislocation pairs can be generated in their path, so as to partially shield the long range stress field of the interface dislocations. Pair generation clearly requires activation and will therefore be the rate limiting process. If the effective activation free energy for pair production is G_{eff} the interface velocity will be lower by a factor $\exp(-G_{eff}/kT)$ giving the following relationship.

$$4.4 \times 10^3 \exp(-G_{eff}/kT_m) = 10^{-5} \text{ to } 10^{-4} \qquad (7.38)$$

1 J.J. Gilman and W.G. Johnston in Solid State Physics 13, ed. by F. Seitz and D. Turnbull (Academic Press, N.Y., 1962) p. 174.

This requires G_{eff} = 1.6 to 1.8 eV which are quite reasonable values. In comparison the free energy of formation of a cation-anion vacancy pair for the alkali halides is about 1.5 to 1.7 eV.[1]

7.4.5 The s-l Interfacial Energy.

Kotzé and Kulmann-Wilsdorf[2] have suggested that γ_{sl} is approximately equal to $\frac{1}{2}$ the energy of a single bulk subgrain-boundary since this is equivalent to two s-l interfaces placed back to back. The energy per unit area of such a subgrain-boundary is $U_c/2r_o$ plus the long range elastic term. Now eqn. (7.35) with $\tau = \infty$ gives the energy of two subgrain-boundaries at infinite separation. Thus the total interface energy γ_d should be

$$\gamma_d = U_c/4r_o + U_e/8r_o$$

$$= U_c/4r_o \left\{1 + .0647\ \xi^{-1}\right\} \qquad (7.39)$$

For the six alkali halides for which we have both the elastic data (Table 7.2) and the interfacial free energy data (Table 4.1) we plot γ_d versus γ_{sl} in fig. 7.14. In all cases, except LiF, agreement is very good. Turnbull[3] has noted a close relationship between γ_{sl} and ΔH_m for the metals. Defining the molar interfacial energy as

$$\gamma_M = N_o^{\frac{1}{3}}\ V_s^{\frac{2}{3}}\ \gamma_{sl} \qquad (7.40)$$

he finds experimentally

$$\gamma_M = 0.45\ \ \Delta H_m \qquad (7.41)$$

Fig. 7.15 shows γ_M plotted against ΔH_m for the alkali halides and a similar relationship holds, although with some degree of scatter, with the constant of proportionality between 0.25 and 0.29. Now by combining eqns. (7.27), (7.39) and (7.40) we obtain

1 A.D. Franklin in Point Defects in Solids ed. by J.H. Crawford and L.M. Slifkin (Plenum, N.Y., 1972) p. 76.

2 I.A. Kotzé and D. Kulmann-Wilsdorf, Phil. Mag. 23, 1133 (1971).

3 D. Turnbull, J. Appl. Phys. 21, 1022 (1950).

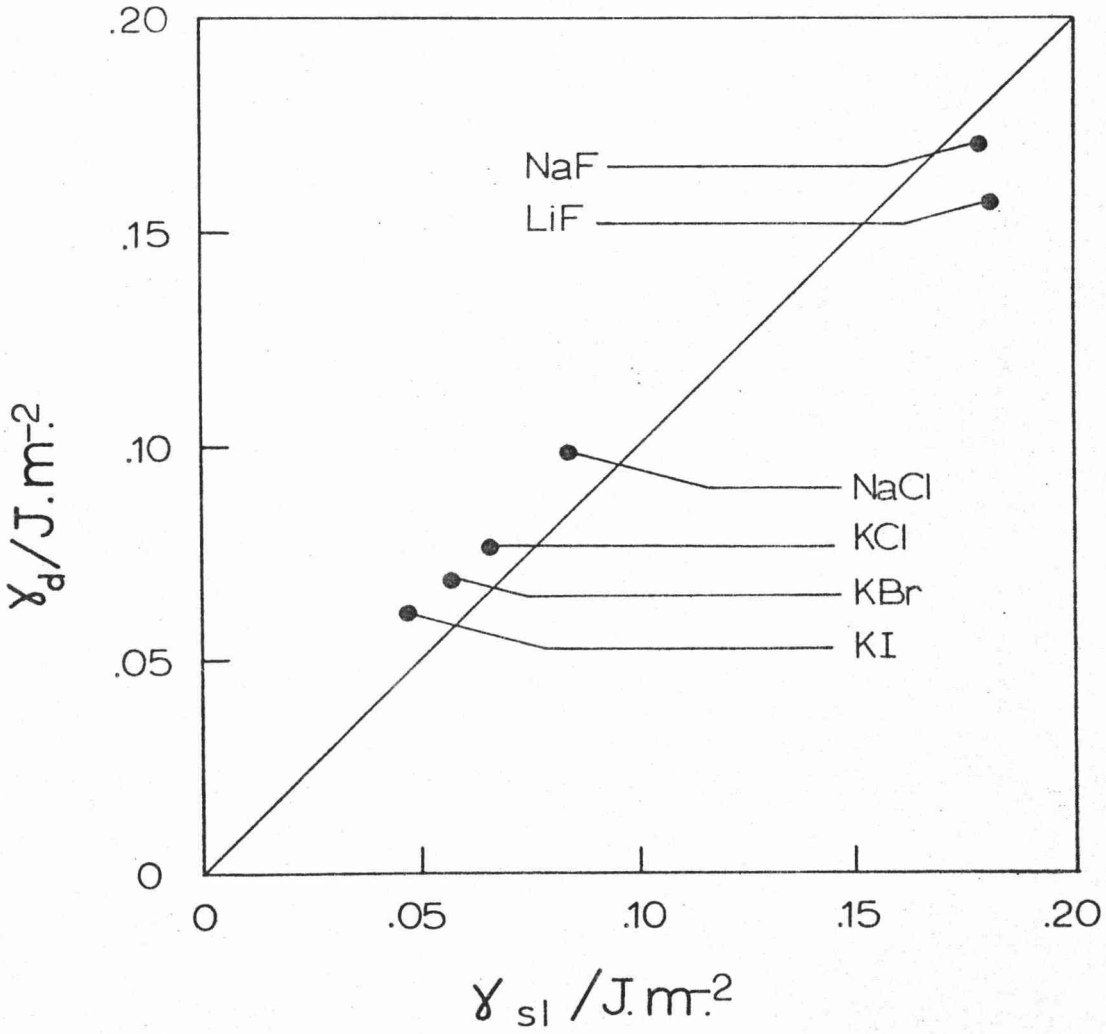

Fig. 7.14 The solid-liquid interfacial energy estimated as one half the energy of a sub-grain boundary plotted against the actual interfacial energy.

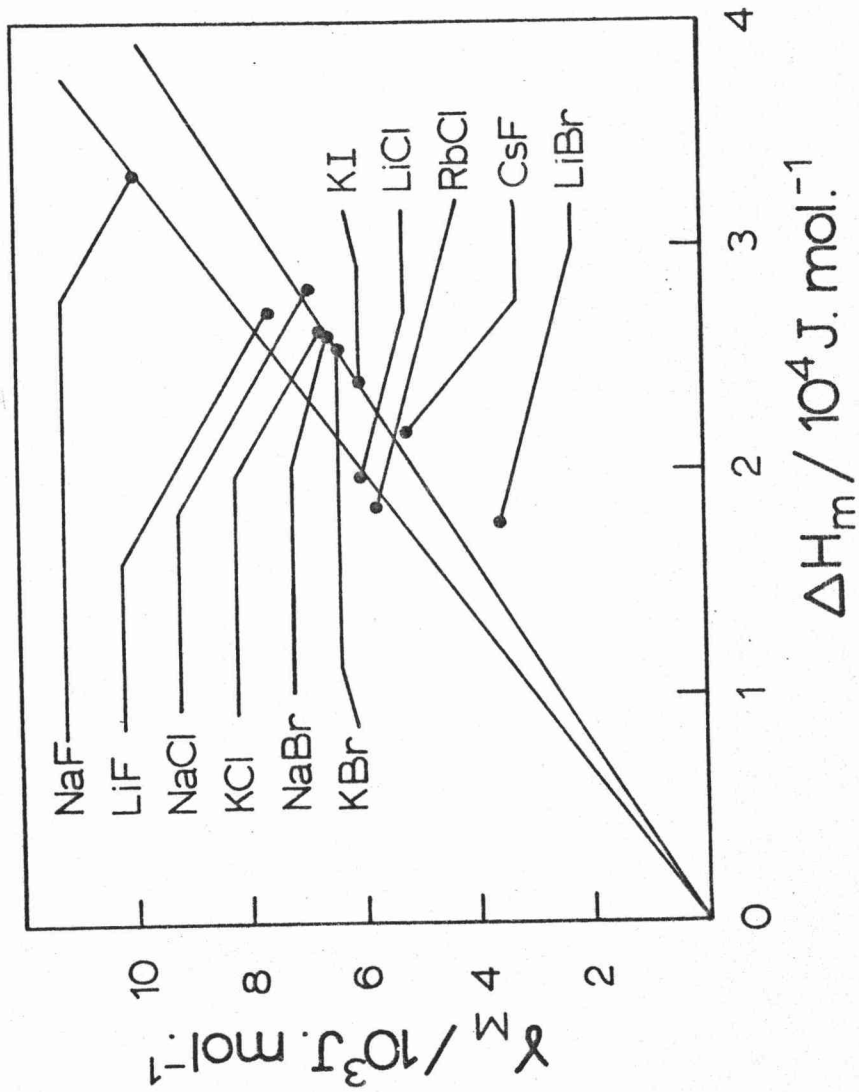

Fig. 7.15 The molar solid-liquid interfacial energy plotted against the enthalpy of melting. γ_M lies between 0.25 and 0.29 ΔH_m.

$$\gamma_M = \tfrac{1}{3}\, 4^{\frac{1}{3}} \left\{1 + .0647\ \xi^{-1}\right\} (r_o/a)\ \Delta H_m \qquad (7.42)$$

So that, since $r_o/a = 0.5$ and $\xi = 0.752$ for all alkali halides, we obtain the constant of proportionality ~ 0.29 in agreement with the observed value.

7.4.6 Superheating and the Homogeneous Nucleation of Dislocation Loops.

In the interior of an internally heated perfect crystal no interface dislocations are present and consequently nucleation of positive/negative pairs of dislocations by dislocation glide as shown in fig. 7.13 is not possible. Instead, small dislocation loops will continually appear by thermal fluctuation and collapse again. At a critical superheating, loops of critical size may be formed which will then continue to elongate stably until they reach other loops or surfaces. This then is the dislocation model of homogeneous nucleation of melting and the process depicted in fig. 7.13 is the dislocation model of heterogeneous nucleation of melting.

We have, in the last two sections, (§7.3 and §7.4) extended the approach of Kulmann-Wilsdorf to a dislocation model of melting. In particular, we have included the entropy due to shear modulation of the vibration frequencies and that due to the isothermal expansion, with the result that melting temperatures can be well characterised for the alkali halides. The elastic energy and the shear entropy excludes $\langle 100\rangle\{100\}$ and $\langle 100\rangle\{110\}$ dislocations from any possible role in melting and favours $\langle 110\rangle\{110\}$ dislocations. The model can be applied to the premature melting of surfaces although its application is limited due to lack of accurate data (and in many cases, any data at all) for the solid-vapour, liquid-vapour and solid-liquid interfaces, particularly for higher index s-v and s-l interfaces.

As the temperature is raised above the surface melting temperature towards T_m the surface dislocation arrays are displaced inwards, only marginally under $\{100\}$ surfaces and

by about one ion spacing under $\{110\}$ surfaces, until at T_m the individual dislocations may glide into the lattice leaving wakes of closely packed positive and negative dislocation pairs in their paths. The s-l interfacial energy, given by one half the energy of a single planar array of dislocations agrees well with values obtained from homogeneous nucleation of supercooled melts. Thus, although the dislocation model of the melt may be only a crude physical description of the actual liquid state, it has considerable appeal in terms of both its predictive success and its simplicity.

Some of the features developed and discussed here also have an important bearing on the understanding of mechanical properties at lower temperatures which are quite unrelated to melting, particularly the shear contributions to the entropy and the free energy of dislocations.

7.5 The Apparent Bulk Surface Melting.

We close this chapter with a brief discussion of a number of effects which find their most ready explanation in terms of a bulk surface melting in the premelting region but which must be explained in terms of enhanced vaporisation or more generally in terms of any process other than bulk surface melting. These include the $\tau \propto \Delta_m T^{-1}$ relationship obtained for NaCl, NaBr and LiF; the magnitude of the premelting electrical conductivity; the appearance of 'puddling' on the surface in the premelting region and the changes in elastic constants observed by Hunter and Siegel, Enck, and Slagle and McKinstry.

7.5.1 The Thickness, τ of the Premelting Layer.

While the $\tau \propto \Delta_m T^{-1}$ relationship has a simple explanation in impurity depression of melting point, we have found this to be untenable due to the low impurity concentration. A simple explanation related to vaporisation is not evident nor is the distinction of KCl in its $\tau \propto \ln(\Delta_m T)$ relationship readily explicable. We have seen that KCl differs from LiF, NaCl and NaBr in that it is nearly isotropic and we may note that these three salts have ion radius ratios of

r^+/r^- = 0.51, 0.55 and 0.51 respectively, while KCl has r^+/r^- = 0.78. However, the distinction may not relate to fundamental ionic processes since the derived vaporisation rate (which is proportional to the product $\frac{d\tau}{dT} \cdot \frac{dT}{dt}$) for KCl appears to be no different numerically from NaBr and in form from LiF and NaCl. The difference in τ or $\frac{d\tau}{dT}$ between KCl and the three other salts may therefore arise simply from the detailed heat transfer to the specimen, contained in the term $\frac{dT}{dt}$.

7.5.2 Premelting Changes in Elastic Constants.

The rapid changes in elastic constants observed close to the melting point which were discussed in § 3, pp 33 and 34, might also be interpreted in terms of a bulk surface melting. For, depending on whether the resonant frequency of the specimen was greater or less than that of the total ultrasonic composite oscillator so surface melting might increase or decrease the apparent elastic constant being measured. However, since bulk surface melting cannot be rationalised, we must suppose that the changes in elastic constants near T_m are due to plastic flow or deformation. Indeed, these crystals are highly plastic near T_m, the results of Hunter and Siegel, Enck, and Slagle and McKinstry are not consistent among each other near T_m and the changes there are not reproducible but involve permanent displacements[1], thus strongly suggesting the occurrence of plastic flow.

7.5.3 Premelting Surface Features

The 'puddling' which occurs on the crystal surfaces when the crystal enters the premelting region as shown in fig. 6.6, p. 93, certainly gives the appearance of substantial surface melting to a depth of .1 mm to .5 mm. However, as we have noted, the same surface tension effects might be achieved by plastic flow, limited flow in the extremely thin intrinsic surface melt layer, or more likely still by sublimation and redeposition. Furthermore, we noted in § 6.9, p.114 that the melting and premelting surface features are very different. When a surface is freely subliming there will be a diffuse region above the crystal in which the bond

1 L Hunter and S. Siegel, loc. cit.

between molecule and crystal is tenuous and consequently a very high surface mobility is possible, which may allow sufficient mass transport for surface tension effects to occur. Our hypothesis is that in the premelting region the surface is sheathed in a very thin intrinsic melt layer and it is at the same time vaporising. Consequently, moving outwards from the crystal there is likely to be a continuous transition from true solid to liquid to vapour, with enhanced mobilities throughout and increasing in magnitude with the progression outwards. At the same time, mass density decreases with the progression so that at some position intermediate between true solid and true vapour, there will be a region of maximum possible mass transfer.

7.5.4 Premelting Electrical Conductivity:

Similar arguments apply to the apparent electrical conductivity also. If the premelting rise in conductivity were due to conduction in a layer of surface melt covering the crystal then melt thicknesses of the order of those given by eqns. (6.3) and (6.4) i.e. 1 μm to 100 μm are necessary to explain the magnitude of the surface conduction. However, with an intrinsic melt thickness of the order of (1.0 to 1.5) nm, mobilities of the order of 10^3 times those in bulk melt must be assumed to explain the premelting conductivity. In the diffuse surface region such mobilities may be possible. Indeed, if from the extrinsic/intrinsic 'knee' in the conductivity curve up to T_m surface conduction by highly mobile surface adatoms produces a significant contribution to the overall specimen conductance, then an even greater effect may be expected when the surface is disordered and rapidly vaporising. With the progression from true solid through liquid to true vapour, as well as there being a decrease in mass density, the ions become increasingly bound as ion-pairs and so unable to contribute to electrical conduction. Consequently, again there will be some intermediate region between solid and vapour of maximum possible conductivity. Typical measurements of the electrical conductivity of ionic melts are performed in apparatus in which there is no free

surface path between the electrodes, and therefore this high mobility effect would not be apparent. Elementary experimentation, however, could readily demonstrate the existence (or non-existence) of this effect.

Many such questions relating to a wide range of behaviour have been raised throughout this work. Because available experimental data is limited both in extent and accuracy, a certain degree of surmise has been necessary throughout which suggests a number of obvious discriminatory experiments which should be carried out in the future. These and possible useful areas of theoretical research will be outlined in the next chapter and the salient features of this present work will be summarised.

8 CONCLUSIONS AND FURTHER WORK

8.1 Conclusions

We have in this work drawn attention to the need for describing melting as a heterogeneous process which commences in localised regions and spreads through a crystalline material by the progression of a solid-liquid interface. The experiments we have described have emphasized the importance of surfaces in the nucleation of melting and we have developed a generalised elastic strain theory as well as a particular dislocation theory of melting both of which implicate the nucleation aspects of melting. At intervals throughout this work we have presented summaries of sections of discussion and analysis. The main summaries are: on p.27 of theories of melting; on p.64 of our instability hypothesis for melting and elastic strain theory of melting; on p.139 of the relationship between vaporisation saturation and facetting and between premelting vaporisation and surface melting; on p.162 of the dislocation theory of melting developed herein. We shall now recount the more significant conclusions which have been established in this work.

(i) Theories of melting are summarised according to their categories in Table 2.2, p.28. The only theories of melting which have the potential of universal success are those which formulate the distinctive features of the melt, namely, fluidity, coherence, lack of long range order and variability in co-ordination. However, the mathematical complexities involved in such a formulation are so great that theories which model on the solid or gas phases remain attractive. The most successful of these are the Dislocation theory, and the theory of Significant Structures.

(ii) A wide range of premelting effects have been reported, including anomalies in specific heat, thermal expansion, thermal conductivity, atomic diffusion, and in the case of alkali-halides in electrical conductivity, elastic moduli and vaporisation flux. Some of these find a ready explanation in impurity depression of melting point, however, many appear to be intrinsic effects. In the case of binary systems

some premelting behaviour may be attributable to a diffuse transition involving the disordering of one sublattice premature to melting.

(iii) For the alkali-halides, the room temperature values of Young's modulus, E, the bulk modulus, β, and the two shear moduli, μ and μ' all correlate well with the solid density times the enthalpy of melting provided that the softest modulus is selected within each group. One is therefore not justified in using any one correlation to justify a particular theory of melting. Values obtained are E (softest) = $35.5\rho\Delta H_m$, $\beta = 30.3\rho\Delta H_m$, μ(softest) = $12.5\rho\Delta H_m$ and μ'(harder) = $24\rho\Delta H_m$. The correlation for the moduli at T_m is poorer but this is probably due to the greater uncertainty in the high temperature data.

(iv) We have shown that a number of properties may be considered to be continuous with respect to dilatation through the melting expansion. These are the elastic moduli $\beta = \frac{1}{3}(c_{11} + 2c_{12})$, $\mu = c_{44}$ and $\mu' = \frac{1}{2}(c_{11} - c_{12})$; and indirectly, the free volume, V^* and the vibration frequency spectrum, ν_i.

(v) The shear modulus, μ' for the rock salt type alkali halides and μ for CsBr and CsI vanishes at the end of the melting expansion, so that Born's instability theory of melting is essentially correct except that the shear modulus is zero (or nearly so) at the dilatation of the liquid at the melting point, rather than of the solid, as Born proposed. This hypothesis naturally requires melting to be a first order transition and explains the nucleation and growth character of melting.

(vi) Assuming that β, μ, μ', V^* and the ν_i are all continuous functions of dilatation up to and through the melting point, allows the enthalpies and entropies of melting of a number of alkali halides to be well characterised. The vibrational entropy due to shear strain is shown to make an important contribution to the total entropy. Local two dimensional strains in the melt appear to apply for the six salts for which data is available, namely NaF, NaCl, NaI, KCl, KBr and KI. This is assumed to intimate local

dislocation-like structures in the melts of the alkali-halides. Furthermore, the ratio of {100} to {110} shear strain predicted by the theory agrees well with the ratio which occurs for edge dislocations.

(vii) We find that surface conduction in the alkali-halides makes a large contribution to the total specimen conductance at all temperatures above the extrinsic/intrinsic 'knee' in the conductivity curve. All measurements above this point must therefore employ guard rings and where guard rings have not been used in the past, computed vacancy data is in error.

(viii) We find that "fringing effects" with specimens having standard parallel plate electrodes introduce errors in conductance of up to 30%. Fringing must therefore be taken into account when extracting the conductivity, σ from the conductance, G.

(ix) We have developed a technique for inserting heated platinum electrodes and thermocouples into single crystal alkali-halide specimens by allowing the wire to melt a narrow pathway to the crystal interior. This avoids spurious temperature measurements when the specimen is absorbing heat more rapidly than its environment, and by inserting the electrodes at right angles to each other the electrical interaction may be confined to a small region in the crystal interior unaffected by changes in the external geometry of the specimen due to evaporation or melting on the surfaces.

(x) Melting temperatures obtained are: LiF, 1118.3 K; NaCl, 1073.99 K; NaBr, 1017.2 K; and KCl, 1044.15 K. NBS thermocouple tables based on the International Practical Temperature Scale of 1968 were used to convert the thermal voltages to temperatures. These melting temperatures compare with the following values listed in NBS Thermochemical Tables: LiF, 1120.5 K; NaCl, 1073.1 K; NaBr, 1019.5 K; and KCl, 1043.4 K. Other reported values are listed in Table 6.1, p.98.

(xi) Our experiments reveal that there is no premelting

rise in the bulk electrical conductivity in LiF, NaCl, NaBr and KCl to within at least 0.5 K of the melting point and that previously reported premelting rises in conductivity are due to rapid increases in the surface conductivity. For ⟨100⟩ crystals this premelting rise occurs at ~ 5 K below the melting point and is accompanied by a substantial heat absorbtion. The thickness of the surface layer in which the heat absorbtion occurs is as large as 0.1 mm or higher within 0.1 K of T_m. Higher index surfaces become highly conducting on their surfaces at lower temperatures and in the following order: {111}, {110}, {112} then {100}. The third of these is considered to be spurious. The {110} surface becomes highly conducting in the ⟨110⟩ direction first then at a temperature ~ 6 K higher, in the ⟨100⟩ direction. For these higher index surfaces the heat absorbtion does not accompany the rise in surface conductivity but always occurs ~ 5 K below T_m. Deformation causes the premelting rise in surface conduction to occur at a lower temperature. Ambient gas at one atmosphere pressure gives a calculated and observed depression of melting point of about 0.2 K. The surface features in the premelting region are distinct from both those below the premelting region and those at the melting point. The features suggest that vaporisation is more significant in premelting than surface melting.

(xii) We interpret these results in terms of a premature melting of the crystal surfaces possibly due to the intrinsic excess surface free energy as proposed by Stranski, and the order of surface melting and the anisotropy of the {110} face is consistent with the ideas Stranski has developed. We cannot altogether discount the possibility of an effect from surface contamination or the intrinsic melting of edges on terraced surfaces. Whatever the cause, we propose that the surface melting is to a depth of only atomic dimensions and that the substantial heat absorbtion which occurs at ~ 5 K below T_m is due to a rapidly increasing vaporisation rate as has been observed for some alkali-halides elsewhere. We suggest that at temperatures below the premelting region vaporisation saturates due to facetting of {100} surfaces, then

with the advent of surface melting, the vaporisation flux commences to rise again rapidly, manifesting itself as an increasing rate of heat absorbtion by the crystal.

(xiii) A dislocation model of surface melting, bulk melting and the progression of the solid-liquid interface from the surface into the bulk was developed. This allowed melting temperatures and the solid-liquid interfacial energies for LiF, NaF, NaCl, NaI, KCl, KBr, KI and RbI to be predicted remarkably successfully. The theory again confirms the occurrence of local two dimensional strains in the melt.

The implications that arise from the ideas developed in this work are many and we therefore wish to collect together a number of proposals for what we consider to be useful further experimental and theoretical work.

8.2 Further Work

(i) It would be extremely fruitful to measure the elastic constants and thermal expansion as functions of temperature for more alkali-halides and indeed for existing measurements to be repeated with greater accuracy in order to examine more fully the dilatation dependence of the bulk and shear moduli, and to check the generality of the vanishing of one of the shear moduli at $\delta = \delta_m^l$. There is a wide range of data on thermal expansion and elastic constants of metals at high temperatures and our hypotheses could be checked immediately with these, Thermal expansion needs to be measured right up to the melting point, and the volume change on melting simultaneously measured, in order to obtain a consistent set of data on thermal expansion, volume change on melting, and the melt density. Dilatometric measurements of $\Delta V_m/V$ for the alkali halides are not consistent with values obtained using the Clausius-Clapeyron equation. The volume changes therefore need to be re-examined with a view to establishing this consistency. It would also be useful to

measure the isothermal bulk modulus β of the alkali fluorides to check on the continuity of β as a function of δ through the melting expansion.

(ii) It is necessary to perform a more accurate lattice dynamics computation of the shear frequency modulating coefficients $g_s(j)$ and the free volume V* as a function of crystal dilatation. Experimental values of $g_s(j)$ might be extracted from the binding entropy of a vacancy pair or an impurity-vacancy pair which could be determined from measurements and analysis of ionic conductivity. We have also suggested that it is possible to relate the local shear strains e_j to the apparent co-ordination number. When this is done a more realistic generalised strain model of the melt may be formulated which takes into account variability in co-ordination.

(iii) We have proposed that much information could be derived from Monte-Carlo or molecular dynamics computer studies of semi-infinite lattices. The premature melting at surfaces could thus be studied for different surface orientations as well as the progression of the s-l interface into the lattice at the melting point. Instantaneous configurations of the surface layers could be examined for the presence of dislocation arrays close to T_m, could demonstrate facetting of surfaces, and such studies may even demonstrate the existence of vaporisation and the vaporisation anomaly which exists in some alkali halides. One might also search existing Monte Carlo configurations of the bulk melt near T_m for possible local two dimensional strains.

(iv) More study could be applied to the equilibrium shape of alkali halides at high temperatures and the phenomenon of thermal facetting. It would be useful to develop better experimental techniques for the preparation of higher index faces particularly the $\{110\}$ face. Certainly the orientation dependence and anisotropy of surface melting needs to be re-examined using faces which are not sawn and polished. We note that Gilman[1] found he could not satisfactorily cleave $\{100\}$ planes in LiF crystals which had been deformed, due to

1 J.J. Gilman, J. Appl. Phys. 32, 738 (1961).

cracks running off in ⟨110⟩ directions. This could be used to advantage. Perhaps a specimen, notched with a {110} slot to localise the glide bands, after compression may cleave readily along the glide band giving a reasonable surface after annealing. Perhaps a {110} plane may be cleaved more readily by simultaneously ultrasonically vibrating a ⟨110⟩ crystal. Low energy electron diffraction studies of a range of alkali halides within a few degrees of their melting points would be particularly useful. The possibility of surface melting and the existence of a diffuse surface region close to T_m could thus readily be investigated, provided there was some accurate method of distinguishing between surface melting and bulk melting.

(v) We have suggested that the conductivity of the surface of an alkali-halide melt greatly exceeds the bulk conductivity due to the surface being diffuse. Conductance measurements of melts, which distinguish between bulk and surface conduction should be performed in order to test this proposal.

(vi) Our last proposals relate to vaporisation. It would be useful to perform simultaneous measurements of vaporisation rates and premelting experiments such as described in the present work in order to establish conclusively the connection we have postulated here. It needs e.g. to be established that the rise in vaporisation flux occurs ~ 5 K below T_m rather than at T_m. We have suggested that the vaporisation of LiBr, LiI and RbI should show

LiF, LiCl, KF, RbF and RbBr, develop the vaporisation anomaly and hence the premelting effect due to facetting in ambient gas conditions, whereas in vacuo they are non-facetting. This would be a critical test for the ideas developed in this work.

APPENDIX A

Calculation of the Shear Frequency Modulation Parameters, $g_s(i)$

Since the normal mode lattice frequencies ν_i vary as the square root of the atomic force constants f_{kk} then

$$\Delta\nu_{i_k} / \nu_{i_k} = \tfrac{1}{2} \Delta f_{kk} / f \; ; \quad k = x, y, z \qquad (A1)$$

where i_k runs over the 2N k-modes. f is the force constant for the unstrained lattice and is the same for the x,y and z directions and f_{kk} are the diagonal elements of the dynamical matrix. If U is the lattice potential seen by an isolated ion then the restoring force matrix elements are given by the second partial derivatives of U, or summing over the x,y and z directions:

$$\sum_k f_{kk} = \nabla^2 U \qquad (A2)$$

We see from Laplace's equation that the electrostatic part of U does not contribute. The remaining potential terms are confined to the Born-Mayer overlap repulsion potentials for nearest neighbours with no great loss of accuracy. The repulsion potential is written as $A_B \exp(-r/\rho_B)$ where[1] $A = 3.38 \times 10^{-19} \exp\left[(r^+ + r^-)/\rho_B\right]$ and r^+ and r^- are the cation and anion radii respectively. Simple differentiation yields:

$$\sum_k f_{kk} = A_B \rho_B^{-1} \sum_{1=1}^{6} \exp\left[-r(1)/\rho_B\right]\left[\rho_B^{-1} - 2r(1)^{-1}\right], \qquad (A3)$$

where 1 runs over the six nearest neighbours. For the unstrained lattice

$$f = \tfrac{1}{3} \sum_k f_{kk}^{o} = 8 A_B a^{-2} \gamma e^{-\gamma} (\gamma - 2), \qquad (A4)$$

where a is the cation-cation lattice parameter and $\gamma = a/2\rho_B$. Now if the lattice is dilated all the r(1) become $a/2 + \Delta r$. Working to first order in Δr and noting that the dilatation strain $\delta = 6\,\Delta r/a$ we obtain

$$\Delta\nu_i / \nu_i = - \frac{\gamma^2 - 2\gamma - 2}{6(\gamma - 2)} \delta = - g \delta \; . \qquad (A5)$$

1 M.P. Tosi, in Solid State Physics, 16, 52 (1964), ed. by F. Seitz and D. Turnbull (Academic Press, N.Y.).

The so called Gruneisen parameter[1] g thus has the expression

$$g = (\gamma^2 - 2\gamma - 2)/6(\gamma - 2). \qquad (A6)$$

For a shear strain e_3 on a $\{100\}$ plane $r(1) = (a/2)\sqrt{1 + e_3^2}$ and $r(2) = r(3) = a/2$ giving for $j = 3$ (and also $j = 4,5$)

$$\sum_k \Delta\nu_{i_k} / \nu_{i_k} = (3/2)\, g_s(j)\, e_j^2 \ , \qquad (A7)$$

where $g_s(j)$ may be called the shear frequency modulating parameter and for e_3, e_4 and e_5 we find it equals the Gruneisen parameter i.e.

$$g_s(j) = g \qquad j = 3, 4, 5 \ . \qquad (A8)$$

For the shear strain e_2 on the $\{110\}$ plane

$r(1) = (a/2\sqrt{2})\sqrt{1 + (1 + e_2)^2}$, $r(2) = (a/2\sqrt{2})\sqrt{1 + (1 - e_2)^2}$

and $r(3) = a/2$. Again the first order term vanishes and we obtain an expression of the form of (A3), which also applies for e_1, with

$$g_s(j) = -(\gamma^3 - 3\gamma^2 - 2\gamma - 2)/12(\gamma-2); j=1,2. \qquad (A9)$$

We have defined the $g_s(j)$ in (A7) such that they are the average for the x,y and z modes. Finally we note that the $g_s(j)$ for $j = 1,2$ are negative and therefore shear on the $\{110\}$ plane reduces the vibrational entropy while for $j = 3,4,5$ $g_s(j)$ are positive so that $\{100\}$ shear increases vibrational entropy.

1 E. Gruneisen, in Handb. der Physik, X, ed. by S. Flugge (Springer-Verlag, Berlin, 1926).

APPENDIX B

Calculation of free volume as a function of dilatation

The free volume of the solid is defined as

$$V^* = \int \exp\left[-\phi/kT\right] dV \qquad (B1)$$

the integral being over one atomic cell and ϕ being the potential within the cell relative to the value at the centre of the cell. We assume that the nearest neighbours remain fixed at the equilibrium positions. The free volume given by (B1) is essentially a weighted integral of the volume of an atomic cell so that away from the centre of the cell ϕ is large due to strong repulsion and the contribution to the integral is small. We shall therefore expand ϕ to second order in r, the distance from the centre of the cell, and assume that when r is large enough for higher order terms to be important the contribution to the integral is negligible. By symmetry the first order term is zero and due to Laplace's equation there is no second order electrostatic component in ϕ so that we are left solely with the Born-Mayer terms. Summing these up to second order we obtain

$$\phi = A_B\gamma(\gamma-2)\, e^{-\gamma}\,(2r/a)^2 = \psi\,(2r/a)^2 \qquad (B2)$$

The boundaries of the cell are $x = \pm a/4$, $y = \pm a/4$ and $z = \pm a/4$ giving

$$\begin{aligned} V^* &= \int \exp\left[-\frac{\psi}{kT}\left(\frac{2r}{a}\right)^2\right] dV, \\ &= 8\int_0^{a/4} \exp\left[-\frac{\psi}{kT}\left(\frac{2x}{a}\right)^2\right] dx \int_0^{a/4} \exp\left[-\frac{\psi}{kT}\left(\frac{2y}{a}\right)^2\right] dy \int_0^{a/4} \exp\left[-\frac{\psi}{kT}\left(\frac{2z}{a}\right)^2\right] dz \\ &= \left(\frac{a}{2}\sqrt{\frac{\pi kT}{\psi}}\right)^3 \left[\operatorname{erf}\left(\tfrac{1}{2}\sqrt{\frac{\psi}{kT}}\right)\right]^3 . \end{aligned} \qquad (B3)$$

erf( ) denotes the normal error function[1] and since $\frac{1}{2}\sqrt{\frac{\psi}{kT}} \sim 4$ the value of the function here is very close to 1. According we have

$$V^* = \left\{\left(\frac{a}{2}\right)^2 \frac{\pi kT}{A_B\gamma(\gamma-2)e^{-\gamma}}\right\}^{3/2} . \qquad (B4)$$

1 M. Abramowitz and I.A. Stegun, Handbook of Mathematical Functions, NBS AMS 55 (1964), p. 231.

If the lattice is dilated such that the new lattice parameter a' is given by $a' = (1+\delta)^{1/3} a$ and $\gamma' = (1+\delta)^{1/3} \gamma$ then

$$\frac{V'^*}{V^*} = \sqrt{1+\delta} \left(\frac{\gamma-2}{\gamma'-2}\right)^{3/2} \exp\left[\tfrac{3}{2}(\gamma'-\gamma)\right] . \qquad \text{(B5)}$$

We now suppose that the melting process may be approximately described by such a dilatation so that the ratio of free volumes is replaced by V_l^* / V_s^* , and moreover, if we assume the dilatation is nearly uniformly distributed the δ in (B5) may be replaced by $\bar{\delta}$.

APPENDIX C

Electrostatic analysis of the internally heated cylindrical crystal.

Fig. C1 shows the electrode geometry of the cylindrical crystal used in an attempt to superheat the crystal interior by internal Joule heating supplementary to external furnace heating. The general solution to Laplace's equation for the crystal is[1]

$$V(r,\theta)/V_o = \sum_{-\infty}^{\infty} \Phi_m \left(\frac{r}{a}\right)^m \cos m\theta + \sum_{-\infty}^{\infty} \phi_m \left(\frac{r}{a}\right)^m \sin m\theta \qquad (C1)$$

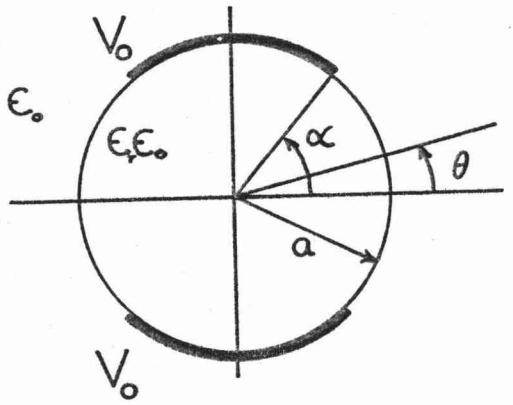

Fig. C1: The electrode geometry for the cylindrical specimen. The usual (r,θ,z) cylindrical coordinates are used, the specimen radius is a and the unplated surface subtends an angle of 2α at the centre.

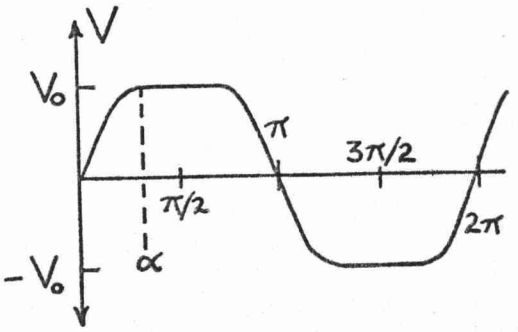

Fig. C2: Schematic diagram of the potential profile around the crystal perimeter.

At $r=a$ the potential profile is as shown in fig. C2 and Φ_m and ϕ_m are the fourier coefficients of this curve. Considerations of the symmetry of the potential curve require that $\Phi_m = 0$ for all values of m and $\phi_m = 0$ for all even m. Therefore the general solution becomes

$$\left.\begin{aligned} &\text{Crystal interior, } r \le a : \quad V(r,\theta)/V_o = \sum_{\text{odd } m>0} \phi_m \left(\frac{r}{a}\right)^m \sin m\theta \\ &\text{Crystal exterior, } r \ge a : \quad V(r,\theta)/V_o = \sum_{\text{odd } m>0} \phi_m \left(\frac{a}{r}\right)^m \sin m\theta \end{aligned}\right\} (C2)$$

Because at $r=a$ V is constant from $\theta=\alpha$ to $\theta=\pi/2$ the integral of V at $r=a$ from α to $\pi/2$ should equal $(\pi/2 - \alpha)V_o$.

1 W. Panovsky and M. Phillips (Addison - Wesley, 1962) p. 74.

Thus

$$\sum_{\text{odd } m} m^{-1} \phi_m \cos m\alpha = \pi/2 - \alpha \ . \qquad \text{(C3)}$$

The energy density of an electrostatic field is $\frac{1}{2} \epsilon_r \epsilon_o E^2$ where ϵ_r is the dielectric constant ϵ_o the vacuum permittivity and E the local electric field intensity given by $-\nabla V$. By evaluating E and integrating the energy density over the interior and exterior of the crystal one finds that the total electrostatic energy is

$$U = \tfrac{1}{2} \pi (1+\epsilon_r) \epsilon_o V_o^2 \sum_{\text{odd } m} m \phi_m^2 \ . \qquad \text{(C4)}$$

The constants ϕ_m may now be evaluated by minimising this energy subject to the constraint given by eqn. (C3) by the method of Lagrange multipliers. The result is

$$\phi_m = -\lambda \tfrac{1}{4} \pi (1+\epsilon_r) \epsilon_o V_o^2 \ , \qquad \text{(C5)}$$

where λ is the Lagrange multiplier arising from the minimisation and is given by

$$\lambda \sum_{\text{odd } m} \tfrac{1}{2} m^{-3} \cos^2 m\alpha = -(\pi/2 - \alpha) \ . \qquad \text{(C6)}$$

λ must be evaluated by numerical summation for each value of α considered. The surface charge density S is obtained from the boundary form of Gauss's law [1]

$$S = \hat{\underset{\sim}{n}} \cdot (\underset{\sim}{D}_{out} - \underset{\sim}{D}_{in}) \ , \qquad \text{(C7)}$$

where $\hat{\underset{\sim}{n}}$ is the unit normal to the surface, $\underset{\sim}{D}_{out}$ is the electric displacement out of the boundary, and $\underset{\sim}{D}_{in}$ the electric displacement into the boundary. Applying this to the crystal perimeter we obtain

$$S = (1+\epsilon_r) \epsilon_o V_o \sum_{\text{odd } n} n a^{-1} \phi_n \sin n\theta \ . \qquad \text{(C8)}$$

The total charge q on one electrode is given by integrating S over the electrode area from $\theta = \alpha$ to $\theta = \pi - \alpha$ and the capacitance, C per unit length is given by dividing the charge by $2V_o$ the potential between the electrodes. Thus

$$C = (1+\epsilon_r) \epsilon_o \sum_{\text{odd } n} \phi_n \cos n\alpha \ . \qquad \text{(C9)}$$

The Joule heating or power dissipation per unit volume, P equals $\sigma \underset{\sim}{E} \cdot \underset{\sim}{E}$ where σ is the electrical conductivity. In terms of the coefficients ϕ_n this gives

$$P = \sigma V_o^2 \sum_{\text{odd } n} \sum_{\text{odd } m} \phi_n \phi_m nm \, a^{-2} \left(\frac{r}{a}\right)^{n+m-2} \cos[(n-m)\theta] \ . \qquad \text{(C10)}$$

1 Ibid. p. 31.

Again, except for some special values of θ P must be evaluated by numerical summation. Fig. C3 shows a plot of P along the $\theta = 0$ and $\theta = \pi/2$ axes for a range of values of α. At the two extremes $\alpha = 0$ and $\alpha = \pi/4$ the maximum value of P occurs near r = a on the $\theta = 0$ axis for the former and on the $\theta = \pi/2$ axis for the latter. Both of these cases are unacceptable. The optimum condition is for $\alpha = \pi/6$ where the maximum in P occurs along the axis of the crystal.

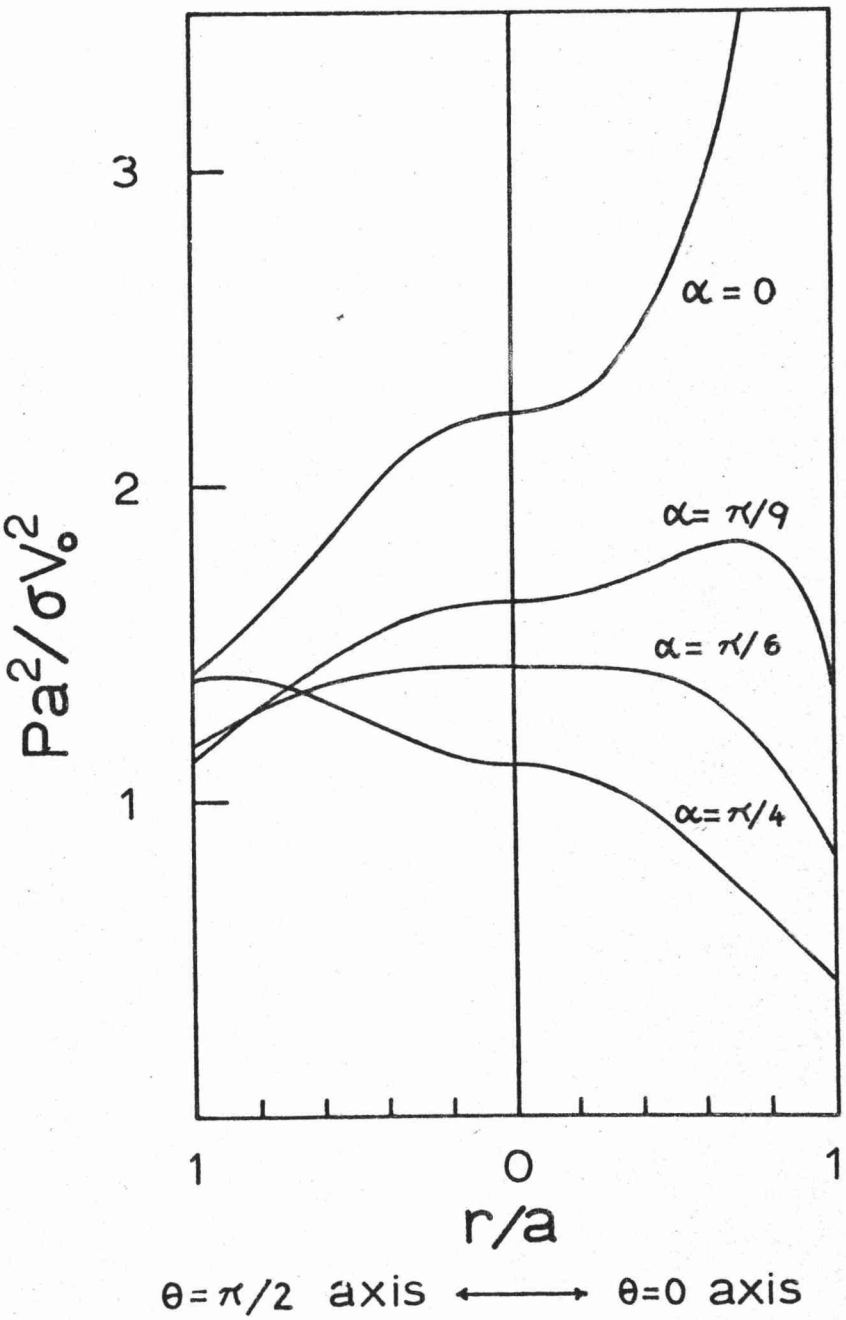

Fig. C3 Reduced power density as a function of position along the $\theta = 0$ and $\theta = \pi/2$ axes for a range of values of α.

APPENDIX D

Premature melting of spherical particles and corners and edges of crystal ledges.

The depression of melting point in small spherical particles has been formulated by a number of people[1-3] beginning with Pavlov in (1909). Here we shall use the approach of Reiss and Wilson[2] and apply it to the melting at corners and edges of crystals. The increment in chemical potential of the solid caused by lowering the temperature a small amount from T_m to T' and by increasing the pressure by ΔP, provided the entropy S_s and molar volume V_s of the solid remains constant, is

$$\Delta\mu_s = -S_s(T-T_m) + V_s \Delta P \quad , \tag{D1}$$

and a similar expression holds for the liquid. Now, according to Kelvin's equation, the pressure increase ΔP over a curved interface with principal radii of curvature ρ_1 and ρ_2 is given by

$$\Delta P = \gamma(\rho_1^{-1} + \rho_2^{-1}) \tag{D2}$$

where γ is the interfacial tension. In the case of a spherical particle of radius r with a negligibly thin surface layer of melt, $\rho_1 = \rho_2 = r$ and

$$\Delta\mu_s = S_s \Delta_m T + 2V_s(\gamma_\ell + \gamma_{s\ell}) r^{-1} \quad , \tag{D3}$$

and

$$\Delta\mu_\ell = S_\ell \Delta_m T + 2V_\ell \gamma_\ell r^{-1} \tag{D4}$$

At the equilibrium melting point the chemical potentials of the solid and liquid phases are equal so that shift in melting point is given by

$$\Delta_m T = (2T_m/\rho_s \Delta H_m r)(\gamma_{s\ell} - \delta_m \gamma_\ell) \quad , \tag{D5}$$

1 P. Pavlov, Z. physik. Chem. 65, 1 (1909).

2 H. Reiss and I.B. Wilson, J. Colloid Sci. 3, 551 (1948).

3 C.R.M. Wronski, Brit. J. Appl. Phys. 18, 1731 (1967).

where C is a constant, ΔH_m is in J kg^{-1} and ρ_s is the density of the solid. In their equivalent formula Reiss and Wilson mistakenly assume that $\gamma_s = \gamma_\ell + \gamma_{s\ell}$ and have in place of the second brackets $(\gamma_s - \frac{V_\ell}{V_s}\gamma_\ell)$. Using the values of γ_s, $\gamma_{s\ell}$, ΔH_m and $\rho_s(T_m)$ listed in Table 4.1, we have evaluated the constant C and the values of r for a depression in melting point of 5 K for a number of alkali halides. These are listed in Table D1.

Salt	$C/\mu m.K.$	$r(\Delta_m T = 5K)/\mu m$
LiF	.102	.021
LiBr	.110	.022
NaF	.163	.033
NaCl	.127	.026
NaBr	.135	.027
KCl	.159	.032
KBr	.160	.032
KI	.161	.032
RbCl	.139	.028

Table D1. Values of the melting point depression constant for small particles and the particle radii for a depression of 5 K.

It is a straightforward matter now to apply these ideas to the melting of edges and corners. In the case of edges there is only one principal radius for the liquid surface and the s-l interface and these are shown in fig. D1.

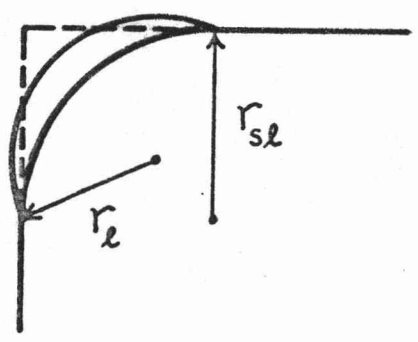

Fig. D 1. Principal radii for the liquid surface and the s-l interface in the premature melting of an edge.

If there is no other surface melting the melt on the corner may not flow down the side as there $r_{s\ell} = \infty$ and the melt would crystallise. If $r_\ell = \eta_e r_{s\ell}$, where $\eta_e < 1$ and may be

determined readily enough from the geometry in Fig. D 1 then

$$\Delta_m T = (T_m / \rho_s \Delta H_m r_{s\ell})(\gamma_{s\ell} - \delta_m \gamma_\ell / \eta_e) . \qquad (D\ 6)$$

If the surface has a thin skin of melt arising from the excess strain energy at and near the surface then the melt at the corner may slowly flow down the side or due to enhanced vaporisation from the melt it may evaporate off, in which case $\eta_e = 1$ thus allowing $r_{s\ell}$ to be a little greater for a given $\Delta_m T$.

One might expect edge melting to commence at the corners where the surface free energy is greater still. At the corners the s-l interface and the liquid surface will be segments of spheres and at each point there are two principal radii of curvature. Accordingly $\Delta_m T$ is given by an expression 2 x that in equ. (D 6) with η_e replaced by η_c where η_c is the corner geometrical factor defined in the same way as η_e. Thus at a given temperature $r_{s\ell}$ for corners will be twice that for edges. Nevertheless because of the shear length of edges the corner effect will be negligible. We emphasise that these are not just the extreme corners and edges which delineate the boundaries of the crystal but the edges of ledges which on the microscopic scale are in abundance. These may contribute extensively to the surface conductivity within 50 K of T_m, but probably not markedly to the heat absorbtion as the radii in Table D 1 are about 3% of our observed total apparent depth of melting over the entire surface when $\Delta_m T \sim 5K$.

APPENDIX E

Pit Melting and Evaporation where a Dislocation Cuts a Surface.

The evaporation problem has been treated in part by Frank[1] and we shall use his notation to examine the melting problem. In the vicinity of the melting point it is conceivable that the cores of all dislocations, whether in the crystal interior or near the surface, may melt due to the excess strain energy there. If this is the case, the s-l interface will have the shape of a funnel at the surface. If, on the other hand, the core does not melt we will assume with Frank that the strain energy density is constant in the core and here the s-l interface is an inverted bell-shape. Whichever the case, we have to consider both principal radii of curvatuve of the s-l interface and these are shown with the co-ordinate system used, in fig. E 1. The strain energy density about a screw dislocation is[2] $\mu b^2/8\pi r^2$ where b is the Burgers vector and μ the appropriate shear modulus for the dislocation; while that for an edge dislocation is[3] $\mu b^2 [\sin^2(\theta) (1-2\nu) + \cos^2(\theta)]/8\pi r^2(1-\nu)^2$. Clearly in the former case the cross section of the interface will be symmetric while in the latter the cross section is not symmetric and because of this complication we restrict the following to screw dislocations.

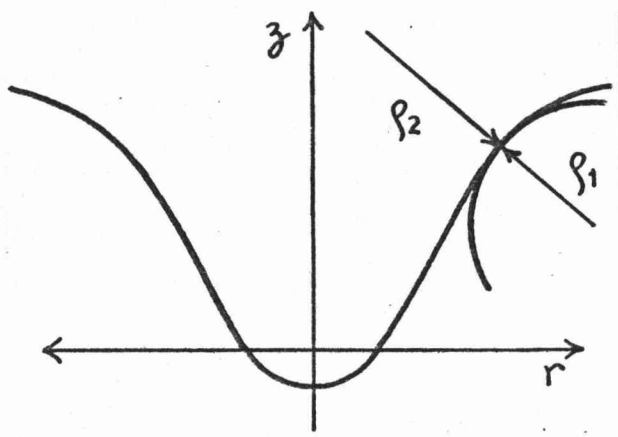

Fig. E 1 Principal radii of curvature, ρ_1 and ρ_2 for the s-l interface.

1 F.C. Frank, Acta Cryst. 4, 497 (1951).

2 J.P. Hirth and J. Lothe, Theory of Dislocations (McGraw-Hill 1968) p.62.

3 ibid., p.78.

At a temperature T near but below T_m the increments in chemical potentials of liquid and solid from their values at T_m are

$$\Delta\mu_l = - S_l (T - T_m) \quad , \tag{E1}$$

and

$$\Delta\mu_s = - S_s (T - T_m) + V_s \gamma_{sl} (\rho_1^{-1} - \rho_2^{-1}) + V_s \mu b^2 / 8 \pi r^2 , \tag{E2}$$

where we assume all strain energy associated with the dislocation is relieved in the melt. At equilibrium the chemical potentials areequal giving

$$\rho_1^{-1} - \rho_2^{-1} + r_d r^{-2} = r_m^{-1} \quad , \tag{E3}$$

where

$$r_d = \mu b^2 / 8 \pi^2 \gamma_{sl} \quad \text{and} \quad r_m = V_s T_m \gamma_{sl} / \Delta_m T \Delta H_m . \tag{E4}$$

Now ρ_1 and ρ_2 are given by

$$\rho_1 = \frac{1}{r''} \left[1 + (r')^2 \right]^{3/2} = - \frac{1}{z''} \left[1 + (z')^2 \right]^{3/2} , \tag{E5}$$

and

$$\rho_2 = r \left[1 + (r')^2 \right]^{\frac{1}{2}} = \frac{r}{z'} \left[1 + (z')^2 \right]^{\frac{1}{2}} . \tag{E6}$$

Well down the core $r' \ll 1$ so that eqn. (E3) becomes

$$r^2 r'' - r - r^2 / r_m = - r_d \tag{E7}$$

This describes the shape of the funnel as it first opens up. Well away from the surface in the core $r'' = 0$ and consequently the radius r_∞ of the molten part of the core is readily seen to be

$$r_\infty = \tfrac{1}{2} \left\{ - r_m + \sqrt{r_m^2 + 4 r_m r_d} \right\} . \tag{E8}$$

Now for NaCl near its melting temperature $r_d = 0.19$ nm while at a temperature 5 K below T_m, $r_m = 19.3$ nm which means that $r_\infty \approx r_d$ and therefore the core is molten to a radius less than one ion spacing. This of course means that the core is not molten and we assume rather that the energy density there is constant and, according to Frank, equal to

$\mu/200$ for $r < r_c = 5b/\pi$. This being the case, the s-l interface in this region must be the cap of a sphere of radius ρ_p given by

$$\rho_p^{-1} = r_d/\, 2r_c^{\,2} - r_m^{-1} \qquad \text{(E9)}$$

and the surface of the sphere has the equation

$$z = (r^2 - r_c^{\,2})\, /2\rho_p \;;\; r \leq r_c. \qquad \text{(E10)}$$

The interface for $r > r_c$ is obtained by solving equations (E3), (E5) and (E6). It will be shown that in this region $z' \ll 1$ with the result that these equations approximate to

$$r^2 z'' + r\, z' + r^2/r_m = r_d \qquad \text{(E11)}$$

which has the solution

$$z = \tfrac{1}{2} r_d \left\{\ln(r/r_1)\right\}^2 + M \ln(r/r_1) - \tfrac{1}{4}\, r^2/r_m + N \qquad \text{(E12)}$$

The constants are determined by matching this curve with the core curve eqn. (E10) both in value and gradient, and setting $z = 0$ when $r = r_c$. The final solution is

$$z = \tfrac{1}{2}\left[r_d - r_c^{\,2}/r_m\right]\ln(r/r_c) + \tfrac{1}{2} r_d \left\{\ln(r/r_c)\right\}^2 - \tfrac{1}{4}\left[r^2 - r_c^{\,2}\right]/r_m. \qquad \text{(E13)}$$

The full interface curve given by eqns. (E10) and (E13) is plotted in fig. E2 and is seen to be a broad shallow pit which meets the surface tangentially at the pit radius r_p given by

$$r_p^{\,2} + r_c^{\,2} = r_m r_d \left\{1 + 2 \ln(r_p/r_c)\right\} \qquad \text{(E14)}$$

Therefore, the pit radius increases approximately as $(\Delta_m T)^{-\frac{1}{2}}$ as T_m is approached. On the other hand, the pit depth d_p is given by the sum of depth of the spherical cap at the core and $z(r_p)$, i.e.

$$d_p = \tfrac{1}{4}\left[r_d - 2r_c^{\,2}/r_m\right] + z(r_p), \qquad \text{(E15)}$$

and the total volume of melt in the pit is

$$v_p\,(\Delta_m T) = \int_0^{r_c} (z_p - z)\, 2\pi\, r\, dr + \int_{r_c}^{r_p} (z_p - z)\, 2\pi\, r\, dr$$

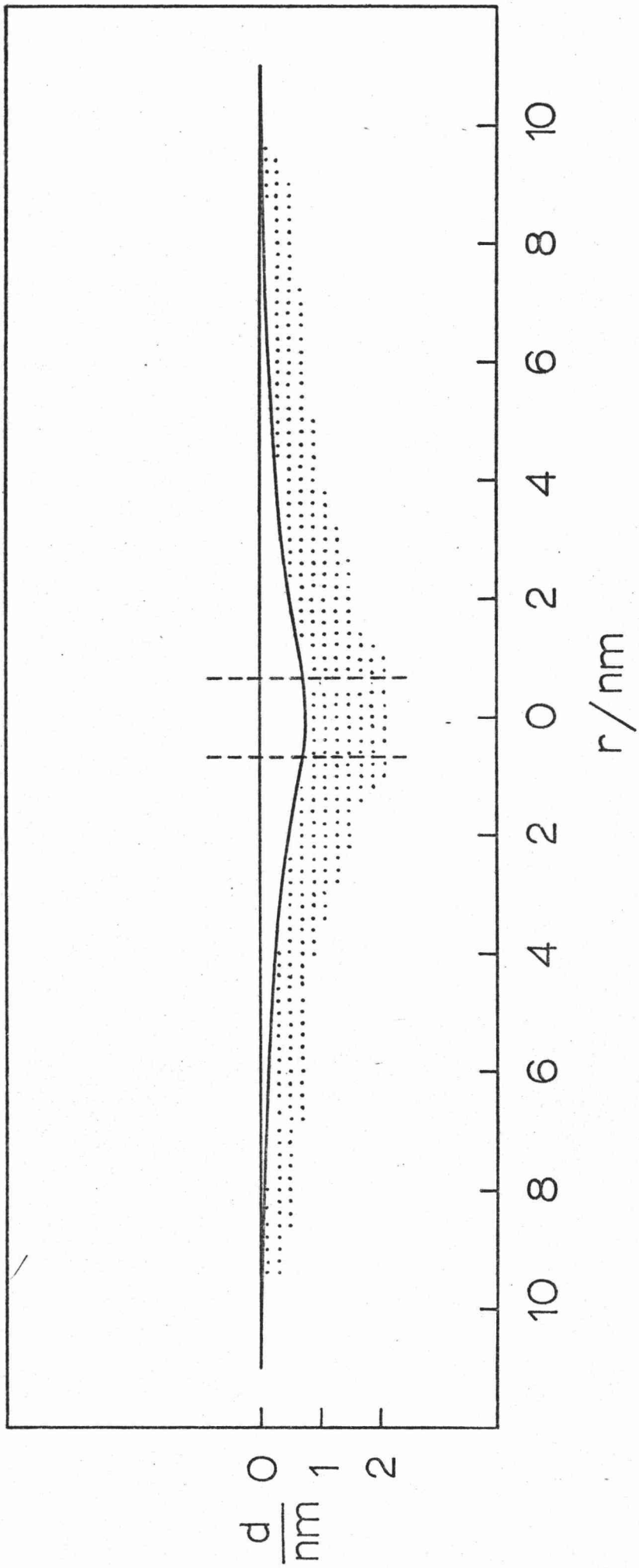

Fig. E2 Shape of the s-1 interface in a dislocation melt pit, 1 K below the melting point. The dashed lines mark the extent of the core.

$$= \tfrac{1}{2}\pi r_p^2 r_d \ln(r_p/r_c) + \tfrac{1}{8}\pi r_c^2 r_d - \tfrac{1}{8}\frac{\pi}{r_m}(r_p^4 + 2r_p^2 r_c^2 - r_c^4) \qquad \text{(E16)}$$

The pit radius, depth and volume are entered in Table E1 for a range of values of $\Delta_m T$ for NaCl and the radius and volume are seen to increase rapidly as T_m is approached, and quite apart from considerations of strain energy density under the flat surfaces, at a finite temperature below T_m all melt pits will eventually overlap and the entire crystal surface will be sheathed in melt. Presumably due to the strain energy under all surfaces this will occur anyway and at a somewhat lower temperature. The temperature dependence of the melt volume in the pit is given fairly accurately by

$$v_p \; m^{-3} = 4.26 \times 10^{-26} \; \Delta_m T^{-4/3} \; . \qquad \text{(E17)}$$

$\Delta_m T$	r_p/nm	d_p/nm	$v_p/(\text{nm})^3$
5	4.07	0.31	3.16
2	7.26	0.54	14.8
1	11.0	0.75	41.7
0.5	16.5	0.99	110.
0.2	27.9	1.33	376.
0.1	41.2	1.63	922.
0.05	60.7	1.95	2210.

Table E1. Temperature dependence of the radius, depth and volume of a melt pit at the exit of a dislocation in NaCl.

We have assumed in the analysis that $z' \ll 1$ and we will now justify this. The maximum gradient is at $r=r_c$ where $z' = r_c/\rho = r_d/2r_c - r_c/r_m$. For NaCl $r_d/2r_c \sim .14$ and because z' is less than this, the assumption is valid.

The equilibrium thermal etch pit exposed by sublimation is given by the same equations (E10) and (E13) except that r_m^{-1} is set equal to zero. Both equations now reduce to those given by Frank, viz.

$$z = (r^2 - r_c^2) r_d / 4 r_c^2 \qquad r \leq r_c, \qquad \text{(E18)}$$

and

$$z = \tfrac{1}{2} r_d \ln (r/r_c) + \tfrac{1}{2} r_d \left[\ln(r/r_c)\right]^2 \qquad r \geq r_c, \qquad \text{(E19)}$$

In contrast to the melt case, the volume of the pit is infinite as, for $r > r_c$, z increases indefinitely with r. This is because the dislocation is a non-equilibrium defect and a crystal with just one dislocation will sublime preferentially onto a perfect crystal. We can, however, introduce the natural cut-off radius R_c equal to half the average spacing of dislocations and within this radius the volume is finite, although this volume is a steady state volume and sublimation will continue over the whole surface. If n_d is the dislocation line density

$$R_c = (\pi n_d)^{-\frac{1}{2}} \qquad \text{(E20)}$$

and in terms of R_c the volume of the thermal etch pit is

$$v_p = \tfrac{1}{2} \pi r_d R_c^2 \ln(R_c/r_c) + \tfrac{1}{8} \pi r_c^2 r_d. \qquad \text{(E21)}$$

In all cases the second term is negligible. Because r_m is absent, the shape and volume of the etch pit are independent of temperature and now only the rate of sublimation changes with temperature. If $n_d = 10^{11}$ lines/m^2, $R_c = 1.8$ μm and $v_p = 7.51 \times 10^{-21}$ m^3 i.e. a factor of 1000 greater than the melt volume .05 K below T_m. Therefore, provided the sublimation rate is sufficiently high, thermal etching should provide a much greater heat absorbtion than pit melting.

APPENDIX F

The Shear Contribution to the Vibrational Entropy of a Dislocation.

The shear components of the vibrational entropy of a lattice are given in eqn. (4.10) as

$$\Delta S_s = 3R \sum_{j=1}^{5} g_s(j)\ e_j^{\,2} \ . \qquad \text{(F1)}$$

For an array of dislocations of density n_d, the total molar entropy is

$$\Delta S_s = 3Rn_d \sum_{j=1}^{5} g_s(j) \int_{r_o}^{R_c}\int_{0}^{2\pi} e_j^{\,2}\ r\,dr\,d\theta \ , \qquad \text{(F2)}$$

where r_o and R_c are the usual core radius and cut-off radius. For a screw dislocation $\sigma_{12} = \sigma_{11} = \sigma_{22} = \sigma_{33} = 0$ and[1]

$$\sigma_{13} = -\frac{\mu b}{2\pi} \cdot \frac{y}{x^2+y^2} \quad \text{and} \quad \sigma_{23} = \frac{\mu b}{2\pi} \cdot \frac{x}{x^2+y^2} \ . \qquad \text{(F3)}$$

Therefore, noting that $e_5 = \mu^{-1}\sigma_{13}$ and $e_4 = \mu^{-1}\sigma_{23}$, one may readily obtain for eqn. (F2)

$$\Delta S_s = 3R\ n_d\ g_s(3) \left(\frac{b^2}{2\pi}\right) \ln\left[\frac{R_c}{r_o}\right] \ ,$$

$$= 6\mu^{-1}\ R\ n_d\ g_s(3)\ U\ (\text{screw}), \qquad \text{(F4)}$$

where U(screw) is the elastic strain energy of a screw dislocation. A screw dislocation has no dilatation and therefore the total molar free energy is

$$\Delta G = \Delta U - T\Delta S_s = n_d\ U(\text{screw}) \left\{V - 6\mu^{-1} RT\ g_s(3)\right\}, \qquad \text{(F5)}$$

where V is the molar volume of the solid. For NaCl near the melting point $6\mu^{-1}\ RT\ g_s(3) = 9.4 \times 10^{-6}$ m^3. mol.$^{-1}$ while $V = 3.0 \times 10^{-5}$ m^3. mol.$^{-1}$. Clearly then the shear vibrational entropy has a very significant contribution to the Gibbs function, however it is not so great in the case of screw

1 J.P. Hirth and J. Lothe, loc. cit., p.60.

dislocations that they could participate in the melting process by spontaneous generation. Edge dislocations are more likely candidates in that both dilatation and shear contributions to the entropy obtain. The stresses about a $\langle 100 \rangle \{100\}$ edge dislocation from isotropic elasticity are[1]:

$$\sigma_{11} = -\frac{\mu_e b}{2\pi} \cdot \frac{y(3x^2+y^2)}{(x^2+y^2)^2} \; ; \; \sigma_{22} = \frac{\mu_e b}{2\pi} \cdot \frac{y(x^2-y^2)}{(x^2+y^2)^2}$$

$$\sigma_{33} = -\frac{\mu_e b \nu}{\pi} \cdot \frac{y}{x^2+y^2} \; ; \; \sigma_{12} = \frac{\mu_e b}{2\pi} \cdot \frac{x(x^2-y^2)}{x^2+y^2)^2} \qquad \text{(F6)}$$

$$\text{and} \quad \sigma_{13} = \sigma_{23} = 0$$

Rather more lengthy manipulation in this case yields

$$\Delta S_s = 3\, RU(\text{edge})\, (2\mu_e)^{-1} \left\{ \left[1 + \tfrac{2}{3}(1-2\nu)^2\right] g_s(1) \left(\frac{\mu_e}{\mu'}\right)^2 + g_s(3) \left(\frac{\mu_e}{\mu}\right)^2 \right\} \qquad \text{(F7)}$$

where the edge dislocation energy is given by

$$U(\text{edge}) = \frac{\mu_e b^2}{4\pi} \cdot \ln \left[\frac{R_c}{r_o}\right]. \qquad \text{(F8)}$$

Since $g_s(1)$ is negative and greater in magnitude than $g_s(3) = g$, the shear entropy of an edge dislocation with Burgers vector in a $\langle 100 \rangle$ direction is negative. For an edge dislocation with a $\langle 110 \rangle$ Burgers vector $g_s(1)$ and $g_s(3)$ with their appropriate ratios of shear moduli should be interchanged in eqn. (F7) so that, due to the factor, $\left[1 + \frac{2}{3}(1 - 2\nu)^2\right]$, ΔS_s is a little less negative. Combining this with the fact that $\langle 100 \rangle$ Burgers vector dislocations have twice the elastic energy of $\langle 110 \rangle$ Burgers vector dislocations, none of the former dislocations will be operating in the melting process, and flow in the melt will be confined to local $\{110\}$ type slip. This is consistent with

1 ibid. p.74

the ideas developed in § 4.4. Another possible slip system on $\{110\}$ planes is $\langle 100\rangle\{110\}$ and this is best dealt with by transforming the stresses to the normal $[100],[010],[001]$ co-ordinate system. This is achieved by a $\pi/4$ rotation about the 1 axis (x-axis) which transforms the stresses given by eqns. (F6) to the following

$$\sigma_{12} = \frac{\mu_e' b}{2\sqrt{2}\pi} \cdot \frac{x(x^2 - y^2)}{(x^2 + y^2)^2} = - \sigma_{13}$$

$$\sigma_{23} = - \frac{\mu_e' b}{2\pi} \left\{ \tfrac{1}{2} \frac{y(x^2 - y^2)}{(x^2 + y^2)^2} + \nu \frac{y}{x^2 + y^2} \right\}$$

$$\sigma_{11} = - \frac{\mu_e' b}{2\pi} \cdot \frac{y\,(3x^2 + y^2)}{(x^2 + y^2)^2} \qquad \text{(F9)}$$

$$\sigma_{22} = \sigma_{33} = 0$$

$$\frac{1}{2\sqrt{3}} (2\sigma_{11} - \sigma_{22} - \sigma_{33}) = - \frac{\mu_e' b}{4\sqrt{3}\pi} \left\{ \frac{y(7x^2 + y^2)}{(x^2 + y^2)^2} - 2\nu \frac{y}{x^2 + y^2} \right\}$$

Here $\mu_e' = (c_{11}' + c_{12}) \cdot \sqrt{\dfrac{c_{44}(c_{11}' - c_{12})}{c_{11}'(c_{11}' + c_{12} + 2c_{44})}}$

where $c_{11}' = \tfrac{1}{2}(c_{11} + c_{12} + 2c_{44})$ (F10)

If the strains e_j derived from these stresses are entered in eqn. (F2) the shear vibrational entropy is calculated to be

$$\Delta S = \frac{R n_d\, U(\text{edge})}{4\mu_e'} \left\{ 3 g_s(3) \left(\frac{\mu_e'}{\mu}\right)^2 (5/8 + \tfrac{1}{2}\nu + \nu^2) + g_s(1) \left(\frac{\mu_e'}{\mu'}\right)^2 (17/2 - 10\nu + 4\nu^2) \right\} \qquad \text{(F11)}$$

Here $\{100\}$ shear contributes positively to ΔS however the $\{110\}$ shear vibration entropy is strongly negative so that the total ΔS_{shear} is large and negative. Furthermore, the Burgers vector b = a and consequently the core energy is at least twice that for $\langle 110\rangle\{110\}$ dislocations. In the light of these two facts it is clear that $\langle 100\rangle\{110\}$ dislocations will neither contribute to surface melting nor to bulk melting.

AUTHOR INDEX